Amplifier front-end design in dry-electrode electrocardiography

A thesis submitted to the University of Dublin
for the degree of Doctor of Philosophy

Cédric E. Assambo
Trinity College Dublin, June 2011

Department of Electronic and Electrical Engineering
Trinity College Dublin

Declaration

I hereby declare that this thesis has not been submitted as an exercise for a degree at this or any other University and that it is entirely my own work.

I agree that the Library may lend or copy this thesis upon request.

Signed,

To my family.

Abstract

This thesis presents an analytical approach to some key issues related to the design of biopotential amplifiers for use in long-term ambulatory recording of the electrocardiogram (ECG) employing pasteless or dry electrodes. The two principal problems of low-frequency distortion and immunity to common-mode interfering signals are analysed in detail. There is also an algorithm for the identification of the model parameters of a group of systems simulated as a double-time-constant network in an attempt to characterise the interface composed of the skin and the sensing electrodes. In the case of low-frequency distortion, new input impedance specifications for dry-electrode electrocardiography are derived from the analysis of performance requirements issued in international standards and recommendations. This is necessary if the low-frequency components in the ECG that contain valuable clinical information about the condition of the cardiovascular system are to be faithfully reproduced. The factors defining the ability of the recording system to effectively reject external unwanted voltages are then determined to allow the suitability of a small number of amplifier circuit configurations to be assessed. The design of new instrumentation amplifiers is finally outlined and their performance evaluated in a worst-case scenario.

It is important to recognise that high fidelity in the reproduction of the ECG waveform requires a measurement system that preserves the ECG features and provides amplification selective to the physiological signal while rejecting external interference and noise. The most obvious implication is that the presence of a frequency-dependent skin-electrode interface introduces distortion to the signal in its propagation from its source to the input of the recording amplifier, which may lead to misdiagnosis of serious cardiac conditions unless the front-end stage is adapted to the source impedance. Therefore, attention is given to investigating the close relationship between the low-frequency response of the skin-electrode-amplifier network and the input impedance characteristics of electrocardiographs.

A prototype was built and tested. Fourteen volunteers (4 females, 10 males) were recruited for actual ECG measurements acquired at rest and while subjects were moving and exercising. No noticeable difference existed between ECG tracings recorded using dry and wet electrodes. Semiconductor noise affected all waveforms but did not significantly degrade the signal. The common-mode rejection ratio (CMRR) was measured at 97 dB at mains frequency, 50 Hz, and 89 dB at 100 Hz for the amplifier alone, meeting current requirements.

Securing high immunity to external interference has been the subject of extensive research in instrumentation amplifier design in the last decade. Several novel circuit structures have been proposed in an attempt to enhance the performance of the "classical" circuit configuration. Analysis of existing solutions indicates that improvement is not guaranteed in worst-case conditions without adjustment either manually or using automatic control circuits. Another contribution brought about by this thesis is the invention of a novel voltage amplifier struc-

ture that achieves enhanced immunity to external contaminating signals without requiring adjustment or high-precision passive components, therefore allowing high performance to be obtained at low cost. The new structure is created by revisiting the theory underlying the operation of the standard approach, identifying its limitations and proposing an alternative implementation that solves specific equations at critical nodes in the circuit. Worst-case simulation results indicate that the minimum CMRR obtainable can be 30 dB greater than that of the "classical" circuit structure, but this comes at the expense of increased power consumption. It is intended as part of future development to improve, construct and test the new circuit structure to assess performance in real-life conditions.

There are several remaining issues in dry-electrode ECG recording not answered in this thesis. In particular, motion artefact and the problem of poor contact between electrode and skin are severe obstacles to the provision of high-quality ECG signals. Motion artefact that occupies the ECG spectrum cannot be detected successfully by the amplifiers presented and so cannot be removed efficiently. Motion detection requires the use of accelerometers at the electrode site to allow voltage changes associated with cardiac activity and those caused by movement of muscle and limbs to be distinguished. These difficulties provide ample opportunity for further research.

Acknowledgements

I must thank first and foremost Dr. Anthony Quinn and the teaching staff at the National Institute of Applied Science (INSA) in Lyon for making my "Trinity Experience" possible.

I would like to thank all former and present members of the research group led by Dr. Martin Burke who have helped me over the years. In particular, I am greatly indebted to my two research companions, Adeshina Baba and Roberta Dozio, who joined me for several months in an obsessive quest for a speculated character named "double-peak" at the highly unpredictable frontier between skin and electrodes. I have said many times, including at a conference my mother attended, that I would marry the woman who brings me this character alive by providing two peaks in the phase response of her skin coupled to dry electrodes. I said dry, not wet or pre-gelled, we only do dry in this house! Since then, Mum has been trying to convince me that there exists in my motherland of Central Africa a place where all women are born with this much desired feature, among many more. I would not have enough words to express how grateful I am to my mother and all members of my family for the support and love they show every day. But, I have to confess that my long-term girlfriend really is the only one considered for this question, double-peak on her skin or not! Sigita has participated in many measurements in the last months of this project and has supported me emotionally over the past three years; she earns my favour and my deep gratitude.

Many thanks to Gavin Shorten and Craig Berry for sharing valuable data and interesting research ideas.

I wish to express my sincere appreciation to my supervisor Dr. Martin Burke for his support and guidance over the duration of my research project. Despite some energetic discussions on the mathematics and notation, Martin's experience and eye for detail have been invaluable. He helped me to grow as a researcher and mature as a person by presenting challenging tasks to complete and by giving me the freedom to explore my own ideas and go my own way.

My thanks also go out to all the staff in the Department of Electronic & Electrical Engineering, particularly to Bernadette Clerkin, Shane Hunt, Sean O'Callaghan, Robbie Dempsey and Conor Nolan for their technical support. Many thanks to Teresa Lawlor for her kindness and precious help in my daily life as a postgraduate student.

I would like to acknowledge the valuable contribution provided by the Dean of Graduate Studies and Enterprise Ireland that has enabled me to carry out this research and to present my work to a wide international audience.

Contents

List of Abbreviations

ac alternating current

ADC Analog-to-Digital Converter

AECG Ambulatory Electrocardiogram

AV Atrio-Ventricular

CMRR Common-Mode Rejection Ratio

dc direct current

ECG Electrocardiogram

GBP Gain Bandwidth Product

LA Left Atrium

LV Left Ventricle

op-amp Operational Amplifier

pk peak

p-p peak-to-peak

RA Right Atrium

RV Right Ventricle

rms root-mean-square

rti referred to input

SA Sino-Atrial

List of Figures

List of Tables

Chapter 1

Introduction

Device-based methods are nowadays regarded by health care providers and public finance administrators as the foundation of the prevention and therapy of heart failure. In particular, the value of the information provided by ECGs is praised in the detection of cardiac abnormalities [1–4]. The ECG profile is obtained by recording the electrical activity of the heart from the surface of the body, enabling the detection of subtle physiological changes associated with aggravating conditions in the heart and impending cardiac failure. An ECG usually measures the regularity of the heart rate, the size and the position of the chambers, the presence of any damage to the muscles and tissues of the heart and the effect of drugs or devices used to regulate its function. As a result, the diagnosis and treatment of many cardiovascular diseases relies heavily upon an inspection of the recorded ECG signal profile.

1.1 A growing demand for ambulatory ECG monitoring

Ambulatory electrocardiography has been available since the early 1950s, when Holter introduced the first portable 24-h ECG monitor [5–7]. Ambulatory monitoring has the potential to considerably improve the management of heart diseases in terms of successful clinical outcomes and economic savings since more patients can be monitored and treated outside of the hospital [1, 8]. Studies of cardiac dysfunctions in the elderly tend to emphasise the importance of management of patients in their own environment because hospitals can be a disorientating experience for the very elderly. Responding to the substantial growth of ambulatory monitoring of outpatients in the past two or three decades, Holter monitors have decreased in size and weight and increased in sophistication. Furthermore, advances in miniaturisation of electronic instrumentation in recent times have extended ECG monitoring out of the conventional clinical environment into other areas such as cardiac rehabilitation, sports physiology, drug studies and monitoring of infants at risk of Sudden Infant Death

Syndrome (SIDS) [3, 4, 9, 10]. For example, modern ambulatory methods make possible the monitoring of the performance of implantable electrical devices such as defibrillators or pacemakers and the control of patient-device interaction. Regular verification of the operation of an implanted pacemaker and its leads allows the detection of lead failure and pulse generator exhaustion or malfunction [2].

The main advantage of continuous ECG recording is its ability to quantify and classify various physiological events over prolonged periods of time. It is therefore the preferred approach in the assessment of electrophysiological changes and the effectiveness of drugs and devices in the treatment of cardiac conditions. However, several problems associated with the standard methods of ECG monitoring remain unsolved.

1.2 The limitations of conventional ambulatory ECG monitoring

In conventional recording of the ECG, a coupling gel is used with sensing electrodes which must be placed correctly on the subject's body by a professional medic. Many advances have been made in the quality and performance of disposable gelled electrodes or adhesive electrodes in everyday use [11]. Nevertheless, some patients develop allergic reaction and skin irritation because of the gel which also dries out over wearing time, reducing signal quality and the performance of the recording system [12]. While the lifetime of modern adhesive electrodes has improved substantially, this is still limited to several days after which the quality of the ECG signal obtained becomes unacceptable. Even in the event of monitoring for periods of days, it is usually impossible for patients to shower or bathe. Lack of hygiene may be clinically inadvisable in some cases, for example, where healing wounds need to be cleaned and dressed. Moreover, in many patients, particularly those having much body hair, the skin must be prepared by shaving or abrasion to get good electrical contact [13–15]. This in turn can lead to increased proneness to skin irritation or adverse reaction to prolonged contact with a coupling gel or adhesive.

1.3 Opportunities offered by dry electrodes

In more recent years, there has been a growing interest in the area of ambulatory ECG recording using dry or unjelled electrodes for long term physiological monitoring [16–40]. The key advantage of dry electrodes is the elimination of allergic reactions or other forms of skin irritation commonly associated with electrolyte gels [37–42]. It results in the improvement of patient comfort and compliance, allowing the recording technique to cater for a wider range of users such as elderly, the long-term ill, cardiac rehabilitation patients, paediatrics

and neonates [43]. Furthermore, dry-electrode recording does not require preparation of the electrodes before or after application apart from cleaning and they can be re-used almost indefinitely. The durability of dry electrodes over gel-based ones permits their shelf-life to be extended and considerably increases the length of time for which they can be worn, allowing long-term ambulatory ECG recording at much lower cost. Embedded in remote telemetry systems, dry electrode ECG recording can thus contribute to the improvement of health care delivery [40].

1.4 Signal quality

Signal fidelity in the reproduction of the ECG waveform is of primary importance for accurate diagnosis and treatment of cardiovascular ailments. This requires the ability of the recording amplifier to reproduce the morphology of the detected signal with as high a degree of accuracy as possible. The frequency response and impedance characteristics of the amplifier used to interface with the electrodes can cause significant distortion of the recorded signal, which can have serious diagnostic implications [44]. Few ECG amplifiers are suitable for interfacing with all adhesive or disposable electrodes. Very often the precise properties of the electrodes must be known when designing the front-end stages of the amplifier. Much is often assumed which is not known, and this can also have diagnostic implications if the overall performance requirements of the recording system do not meet the specifications of international standards [45].

The amount of published work in field of instrumentation amplification applied to ambulatory dry-electrode ECG recording is quite limited due to the difficulty of acquiring an ECG signal of diagnostic quality without a conductive gel and the much more stringent demands placed on the recording amplifier. Much higher performance requirements are needed in the case of dry-electrode ECG monitoring than in conventional recording to compensate the lower electrical conductivity and greater polarisation potential associated with dry electrodes as well as their vastly different electrical properties.

1.5 The aim of the project

This thesis concerns itself with the investigation of the primary issues associated with the design of such a recording amplifier. The dissertation aims to present a rigorous analytical strategy for designing a high-performance, low-power, low-cost portable instrumentation amplifier for use in ambulatory dry-electrode ECG recording. The focus is to utilise international standards defining the performance criteria for monitoring systems and to identify other requirements imposed by the recording environment in order to design an optimised

interfacing amplifier that ensures accurate ECG signal reproduction. In particular, criteria and recommendations published by the International Electrotechnical Commission (IEC), the American National Standards Institute (ANSI) and the American Heart Association (AHA) are used to establish and evaluate the requirements of the amplifier stages.

So far many dry-electrode ECG recorders have used identical instrumentation to that used in gel-based applications. Furthermore, much of the work in bio-potential recording has concentrated on the design of amplifiers the performance of which is based on standard working conditions. The approach taken in the work reported in this thesis considers worst-case scenarios and the harshest operating conditions. The thesis addresses the problems of a frequency dependent skin-electrode-amplifier interface, common-mode interference rejection, component mismatch, dc offset conditions, stability issues, and low-power design in physiological measurements.

There are generally several stages of amplification and these can be divided into three main blocks:

1. The front-end stage provides the high input impedance necessary to compensate the source impedance composed of the tissue, skin and electrodes. High input impedance prevents signal attenuation and distortion;

2. The fully differential amplification stages amplify the difference between the two electrode potentials and suppress common-mode interference;

3. The differential-to-single-ended stage provides a single-ended output signal adequate for monitoring, further conditioning, processing or storage.

Because of mismatch in manufactured components and the limitation of common-mode rejection ratio (CMRR) of the operational amplifiers used in differential configurations, common-mode signals cannot be completely suppressed. The thesis therefore spends some effort in assessing the effects of these imperfections on the single-ended output and presents a new circuit structure that dramatically improves performance while limiting cost. An important innovation resides therefore in a novel fully differential stage which surpasses the performance of traditional implementations and introduces an improved means of suppressing common-mode interference.

1.6 Thesis outline

The two primary issues impacting on the design of amplifiers for dry-electrode recording addressed in this dissertation are:

1. the preservation of low-frequency components in the ECG signal in the presence of a frequency-dependent skin-electrode interface;

2. the provision of high immunity to external interference in the harshest recording conditions.

In-depth analysis of the amplifier performance is carried out to establish the needs for dry-electrode recording and a review of the work of other researchers relevant to these key issues are incorporated to the discussions. The design of new instrumentation amplifiers is then presented in detail. The circuits are simulated using PSpice and their performance are evaluated in a worst-case scenario. Bench testing and actual ECG recordings are then carried out on a constructed prototype of the ultra-low-power dry-electrode preamplifier. The following is a brief outline of each subsequent chapter.

Chapter 2: Requirements for a faithful reproduction of the ECG signal

This chapter outlines the source of the electrocardiogram signal and its measurement at the surface of the body. Several electrical models that relate the voltage sensed at the input of the recording amplifier to the biological signal generated within the heart are presented. A realistic representation of the ECG volume conductor is retained based on experimental results reported with dry electrodes. The importance of preserving the signal profile is pointed out and the major international standards and recommendations for ECG recording equipment are reviewed. Performance requirements are interpreted in the light of dry-electrode electrocardiography and their implications for the design of the front-end amplifier used for this measurement. It is concluded that international performance specifications have not been drawn up with dry-electrode recording in mind and therefore fall short of providing the standards needed in this scenario.

Chapter 3: Low-frequency response and the skin-electrode interface

The third chapter deals with the nature of the skin-electrode-amplifier interface and its effect on the low-frequency performance of dry-electrode recording. Analysis of previous related work suggests that high-pass filtering can affect the quality of the recorded ECG waveform and that the risk of distortion is exacerbated by the presence of a frequency-dependent skin-electrode impedance. New approaches for the determination of the model parameters of the skin-electrode interface and new input impedance requirements for dry-electrode ECG recording are then presented.

Chapter 4: Interference suppression and CMRR

Chapter 4 concerns itself with the rejection of interfering signals and the requirements of common-mode rejection ratio of the amplifier and its resulting design constraints. The need for securing high immunity to common-mode signals is justified and a number of existing

amplifier structures designed with these issues in mind are examined and assessed in order to identify an appropriate circuit structure.

Chapter 5: Design of a very-low-power single-supply dry-electrode ECG preamplifier

This chapter presents the undertaken approach in designing an ultra-low power ECG preamplifier operating from a single-rail supply for use with the pasteless electrodes characterised in Chapter 3. An instrumentation amplifier structure optimised for high rejection of unwanted external voltages and enhanced low-frequency performance is proposed. Worst-case simulation results suggest that the proposed amplifier features excellent performance in terms of input impedance, frequency response and CMRR value at the expense of an increase in power consumption. Practical test results suggest that the low-frequency performance of the constructed prototype is in accordance with simulation results. However, the amplifier's response at high frequency is limited by the presence of stray capacitance on the circuit board. Actual physiological measurements acquired using dry and wet electrodes return waveforms of satisfactory quality. No significant difference is noticeable between results obtained with wet and dry electrodes and the ECG signal can be clearly identified from the interference present in all recordings.

Chapter 6: A novel instrumentation amplifier circuit structure

In this chapter, a novel instrumentation amplifier circuit structure that allows enhanced CMRR performance without requiring trimming or high-precision resistors is presented. The solution is obtained by revisiting the fundamental equations that underly the operation of the "classical" instrumentation amplifier. The circuit configuration is then modified to allow common-mode voltages to be rejected further. Circuit simulations are run with PSpice to assess improvement when worst-case mismatches in resistor values are considered. The limitations imposed by imperfections in real op-amps are taken into account and two circuit implementations are then presented and simulated.

Chapter 7: Conclusion and Further Work

The conclusion summarises the main findings reported in this thesis. This chapter highlights the added knowledge in the field of instrumentation amplification applied to dry-electrode ECG recording. The limitations of the undertaken approach are pointed out and several problems that have not been addressed or solved in the dissertation are discussed as well as possible methods for investigating their solution in future research.

1.7 Publications

Associated with this thesis are the following publications:

[46] C. Assambo and M. J. Burke, *Low-frequency response and the skin-electrode interface in dry-electrode electrocardiography, in: Electrocardiograms.* InTech, 2011 (invited book chapter, to appear)..

[47] C. Assambo and M. J. Burke, "Amplifier Input Impedance in Dry Electrode ECG Recording," in *Conf Proc IEEE Eng Med Biol Soc*, Minneapolis, MN, USA, Sept. 2009, pp. 1774-1777.

[48] R. Dozio, A. Baba, C. Assambo, and M. J. Burke, "Time Based Measurement of the Impedance of the Skin-Electrode Interface for Dry Electrode ECG Recording," in *Conf Proc IEEE Eng Med Biol Soc*, Lyon, France, Aug. 2007, pp. 5001-5004.

[49] C. Assambo and M. J. Burke,"Determination of the Parameters of the Skin Electrode Impedance Model for ECG Measurement," in *Proc WSEAS EHAC*, Feb. 2007, pp. 90-95.

[50] C. Assambo and M. J. Burke, "An Improved Very-Low Power Pre-amplifier for use with Un-gelled Electrodes in ECG Recording," *Int J Biol Biomed Eng*, vol. 1, pp. 25-31, 2007.

[51] M. J. Burke and C. Assambo, "An Improved Micro-power Pre-amplifier for Dry-electrode ECG Recording," in *ELE COM ENG*, vol. 11, July 2007, pp. 234-239.

[52] C. Assambo, A. Baba, R. Dozio, and M. J. Burke, "Parameter Estimation of the Skin-Electrode Interface Model for High-Impedance Bio-Electrodes" *WSEAS T Biol Biomed*, vol. 3, pp. 573-580, Aug. 2006.

Chapter 2

Requirements for a faithful reproduction of the ECG signal

2.1 Physiological background

2.1.1 Function and anatomy of the heart

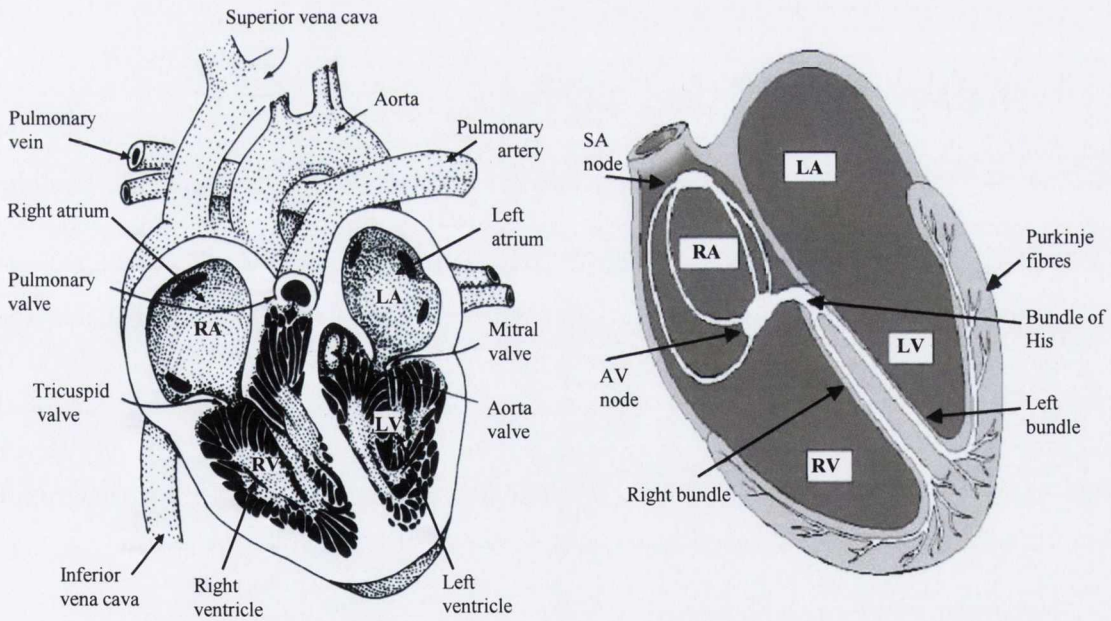

(a) A cross section of the human heart (from [53]) (b) Conduction system of the heart (from [54]).

Figure 2.1: Schematics showing (a) a cross-section of the human heart and (b) its specialised conduction system.

The study reported in this Chapter has been published in part in [47–52]

Fig. 2.1(a) illustrates the major anatomical parts of the human heart, from which we can clearly distinguish four chambers: two large thick-walled ventricles, and two small thin-walled atria. The heart muscle (myocardium) can be regarded as an electrically activated mechanical pump. Oxygenated blood arrives from the lungs into the left atrium via the pulmonary vein. This blood is then passed onto the left ventricle that pumps it into the systemic circulation, responsible for providing oxygen and nutrients to rest of the body. The right atrium receives deoxygenated blood from the systemic circulation, and then passes it on to the right ventricle. The ventricle on this side pumps deoxygenated blood into the pulmonary artery that will then be reoxygenated in the lungs and returned to the left atrium [55]. The resting or filling phase of the cardiac cycle is referred to as diastole while the contractile or ejecting phase is called systole [56]. During diastole, the inner electrochemical potential of the cardiac cell membranes is lower than the external potential, contributing to an overall resting potential of between -80 and -90 mV. Hence cardiac cells in the resting state are electrically polarised [56, 57].

The conduction of electrical excitation in the heart

The blood pumping mechanisms are accompanied by periodic electrical activity in the heart. More precisely, the origin of the heartbeat is an electrical event and each time the heart muscle contracts, electrical currents flow through it [55]. The specialised conduction system of the heart is depicted in Fig. 2.1(b).

Although the heart has four chambers, from an electrical point of view it can be regarded as having only two since both ventricles contract together, as do the two atria [58]. Systole is triggered spontaneously by electrical excitations generated regularly in the sino-atrial (SA) node. Because the SA node initiates the heartbeat, it is essentially a pacemaker and it sets the heart rate. Excitation quickly spreads through the tissues of atria, causing their contraction, and then reaches the atrio-ventricular (AV) node. The AV node conducts the impulse very slowly, imposing a delay between the excitation of the atria and that of the ventricles. This region is the sole electrical connection between atrium and ventricle. Beyond the AV node, currents spread to the Purkinje bundles, branches of large fibres that rapidly conduct the impulse to the muscle fibres in the walls of the two ventricles [53, 55].

Cardiac action potential

The flow of blood travelling through the heart causes certain cell membranes to become permeable at given times. Changes in membrane permittivity are accompanied by an inversion of the inner cell potential. Potentials can become $+20$ to $+30$ mV higher inside the cells, relative to the outside [57]. The change of membrane potential polarity is called depolarisation and the variations in transmembrane potential during cell activity are called action

potentials. A typical action potential of a ventricular cell is shown in Fig. 2.2(a). The shape of the action potential is mainly dependent on the membrane permeability of the specific heart cell. Its amplitude can reach levels between 100 and 120 mV peak-to-peak (p-p). A rapid depolarisation phase is followed by a steady state, the duration of which varies from cell to cell. Then, membrane potentials recover their resting levels in the repolarisation phase. In the resting condition, cells are in the passive state awaiting re-excitation [55]. The currents accompanying the depolarisation of a cell are generally large enough to excite neighbouring cells and their return path to the source normally involves the entire body. This yields currents and associated electric fields everywhere in the body [57, 59]. The resulting potential differences on the surface of the skin can therefore be measured and recorded. A close correlation between the changes in cellular action potential and body surface potential exists in the case of ventricular cells, as shown in Fig. 2.2(b).

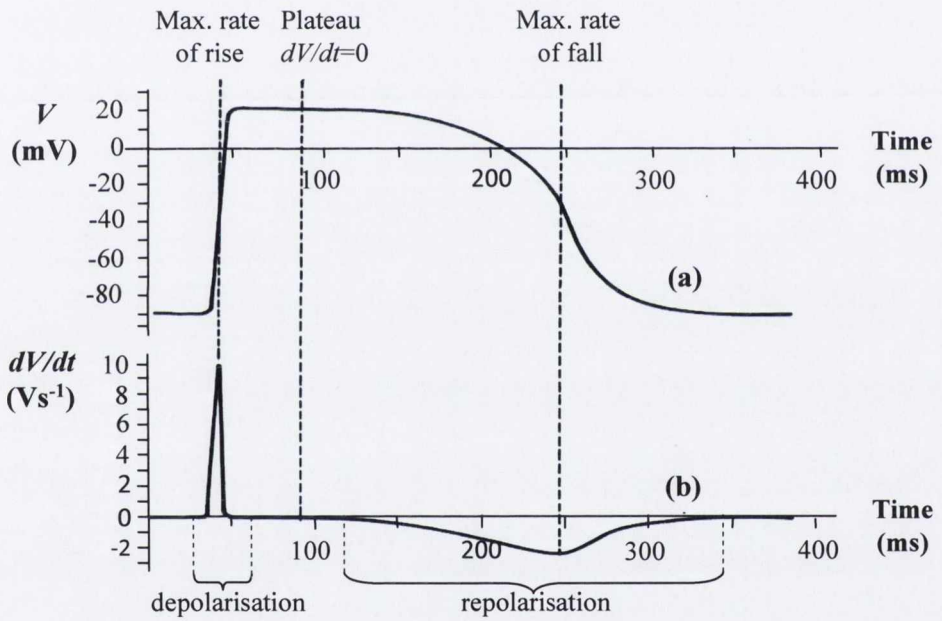

Figure 2.2: Schematic representation of (a) the action potential of a ventricular cell and (b) its first derivative against time (modified from [55]).

2.1.2 Electrocardiography

Electrocardiography refers to the recording of the changes in the electrical field resulting from cardiac activity with time. The most common form of electrocardiography is the surface electrocardiogram in which measurements are made using contact electrodes positioned at prescribed locations on the skin [53, 55, 56]. A dipole moment, known as the cardiac vector, resulting from the electrical activity of the heart can be represented along several axes made

up of different permutations of electrodes.

A typical ECG profile

The potential measured between any two electrodes is termed an ECG lead. Three ECG leads make up the basis the cardiac vector on a frontal plane passing through the four limbs. Electrodes located on the left arm (LA), right arm (RA) and left leg (LL) form the Einthoven triangle, shown in Fig. 2.3. A ground electrode can be connected to the right leg (RL). However, very often the electrode placed on the right leg is connected to a circuit known as right-leg-drive that detects the common-mode signal and feeds it back to the body.

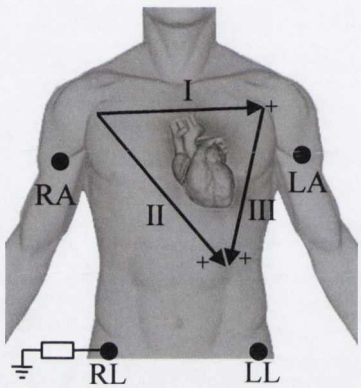

Figure 2.3: Three basic ECG leads(modified from [60, 61]).

As illustrated in Fig. 2.3, the Einthoven triangle is associated with three lead vectors: lead I is oriented from RA to LA, lead II goes from RA to LL and lead III is assigned to the direction LA to LL. Fig. 2.4 shows the profile and frequency spectrum of a typical lead II ECG recording.

Einthoven defined three successive waves in the ECG which he labelled "P", "QRS" and "T" [55, 62, 63].

- The P wave corresponds to the depolarisation of atrial cells causing the contraction of the atria. The wave is about 90 ms in duration and its amplitude generally not greater than 0.2 mV;
- The QRS complex is associated with ventricular depolarisation and lasts typically between 85 and 95 ms;
- The T wave occurs when ventricular cells repolarise and regain their resting potential levels. Its amplitude is normally a good deal lower than that of the QRS complex.

The repolarisation of the atria is masked by the large QRS complex and so is not identified by an individual wave. A small deflection, named "U", can sometimes be detected following

the T wave. Several hypotheses have been proposed to explain the genesis of the U wave [64–66], but none of them have received universal acceptance and its physiological origin remains uncertain [67, 68].

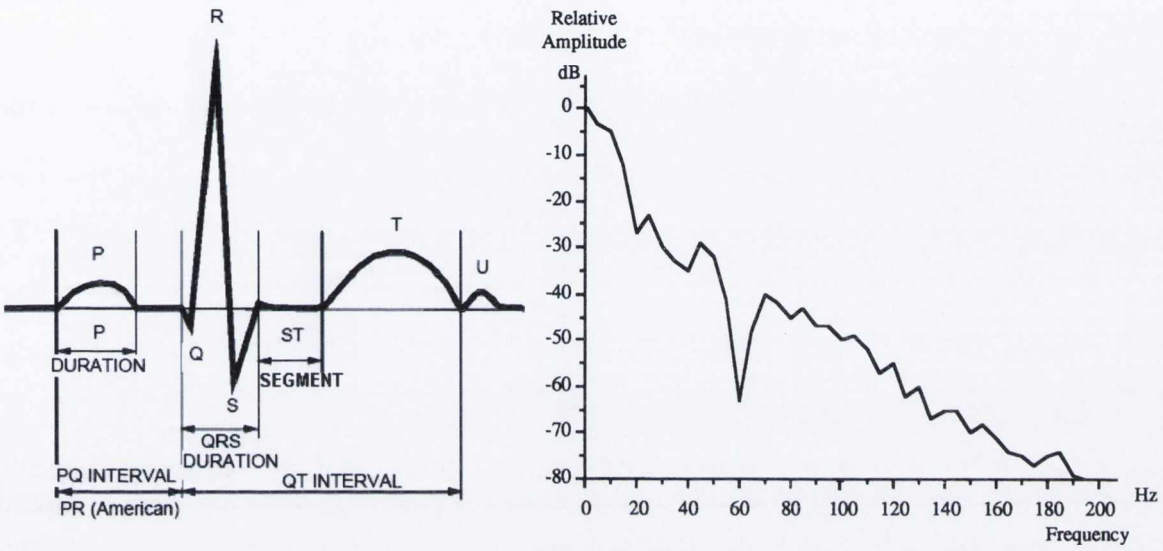

(a) A normal ECG profile (from [69]).

(b) ECG frequency spectrum mesured experimentally by Burke ([70]).

Figure 2.4: Plots of (a) the time representation and (b) frequency spectrum of a typical lead II ECG signal.

What can be learnt from the ECG?

Despite the absence of consensus on the interpretation of the U wave, essential physiological information can be obtained from a study of the PQ and QT intervals of the electrocardiogram. Surface electrocardiography therefore offers a powerful and affordable diagnostic tool, combining three major advantages: it is rapid, non-invasive and non-traumatic [57, 59, 71]. When longer recording periods are required, ECGs are adapted and integrated into ambulatory systems.

Changes in the ECG of cardiac origin having diagnostic implications may be categorised as follows.

- Injury to regions of the heart may be observed in the ECG as a shift away from the baseline level of the ST segment [44, 45, 59];

- Changes in the shape or position of the heart may be deduced from the amplitude and duration of the P wave, the QRS complex and the length of the ST segment [36].

- Disease of any of the structures comprising the specialised conduction system may be associated with several ECG patterns. For example, studies reported in [72] relate conduction defects in the muscle fibres to changes in the duration and amplitude of the QRS complex. Other evidence may include anomalies in the P wave such as delay, change of shape and the presence of an additional wave [36].

- Significant changes in the number of ECG cycles per minute infer irregularities of the heart rhythm.

- Ionic and drug effects may alter segments and interval durations, as well as wave morphology [73, 74].

2.2 An electrical model of the ECG

The ability to detect and measure electrical events occurring within the heart relies primarily on the conductive properties of the volume surrounding it. The bioelectric current produced during ventricular activation may then be measured at the outer surface of the medium as shown in Fig. 2.5. Hence, a complete electrical model of the electrocardiogram defines two independent parts: the generator and its electrical load. For this purpose the electrical properties of cardiac muscle and other body tissue must be considered.

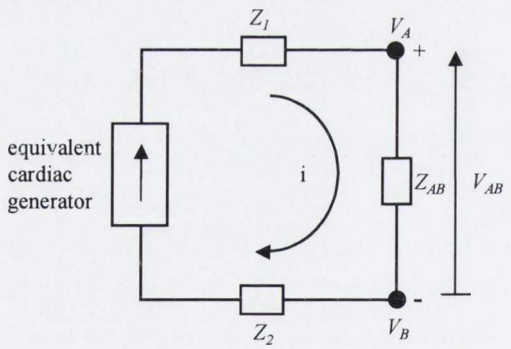

Figure 2.5: A simple lumped electrical model of the electrocardiogram between two arbitrary points on the torso (modified from [56]). Z_1 and Z_2 are the impedances between the source and points A and B respectively. Z_{AB} is the impedance seen between A and B. V_{AB} is the bipolar ECG lead voltage $V_A - V_B$.

2.2.1 The bioelectric source

In the electrocardiogram model, the heart is viewed as an electrical equivalent generator [56]. At any given time, the combined effect of all active cells generates an electrical field

the strength and direction of which depend on the potential difference and distance between the excited and resting cells of the myocardium. Einthoven postulated that, at least to a first approximation, the distribution of sources throughout the heart during the cardiac cycle could be represented by a single lumped time-varying dipole source at a fixed location, as shown in Fig. 2.6 [56, 59, 62, 75].

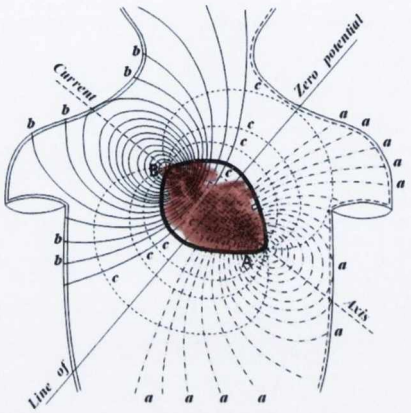

Figure 2.6: Representation of the heart as a dipole source having the positive pole located at lower end of the ventricles'wall (point A) and the negative pole at the SA node (point B) [75]. The thick line gives the approximate position of the heart, curves (a) show the positive isopotential lines, curves (b) give the negative lines and curves (c) represent the current flux lines.

More accurate computational models that include the inhomogeneity of the cardiac muscle and its motion have been considered for several decades. In the mid-1950s, Brody analysed the effect of the blood mass inside the heart in relation to the field generated by single current source in the myocardium. He concluded that dipoles whose poles are oriented tangentially to the internal blood mass are reduced by it but not perpendicular poles [57, 76]. Later, Appleton et al. presented a computer model of the heart incorporating real geometry and motion obtained from magnetic resonance imaging [77]. The simulated ECG demonstrated that the motion of the heart shifts the onset of the T wave to the left. More recently, Norian offered a two-dimension model of cardiac cells that accounts for deflections of electrical fields within the myocardium. The model, designed for educational purposes, allows atrial and ventricular activity at cellular level to be distinguished [78]. In the early 1980s, Spach and Kootsey studied the effects of discontinuity in axial resistance associated with inhomogeneity and electrical interconnections between cells in cardiac muscles [79]. On a microscopic scale, they discovered that conduction discontinuities can modify the shape of the intracellular action potential. However, at macroscopic level, the application of continuous models that do not include discontinuity, but rather consider an average representation of cardiac muscle bundles, returned valid and valuable information. Their conclusion confirmed that the simple

electrical representation proposed by Einthoven is an excellent approximation of the heart, at a macroscopic scale.

2.2.2 The impedance of body tissue

The strength of the electric field generated in the myocardium gradually decreases with increasing distance from the source. A simple model of the volume conductor approximates the thoracic medium as a homogeneous, linear and purely passive conductor, free of electrical sources or sinks. This model represents the thorax as a resistive load on the equivalent cardiac generator [56, 80]. Fig. 2.7 shows a schematic representation of the electrical equivalent of the human body and gives typical resistance values measured at the torso and the four limbs.

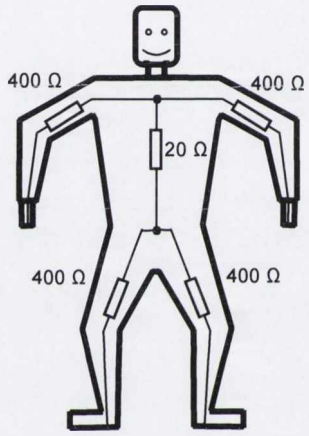

Figure 2.7: Simplified schematic diagram for the lumped internal resistance of the human body (modified from [81, 82]).

A more detailed representation of body tissue models cell membranes as leaky insulators, introducing capacitive effects to the impedance of the volume conductor [59]. In the mid-1950s, experiments led by Schwan and Kay demonstrated that in the frequency range up to 1000 Hz, an electromagnetic plane wave moving in the thoracic medium from the heart to the body surface would undergo negligible attenuation and phase shift [80]. They concluded that at frequencies of interest for bioelectric phenomena the reactive components of the model could be neglected. The average thoracic impedance was confirmed to an excellent approximation as being resistive [59].

At the time, little importance was attached to the impedance of the skin which was generally reduced by abrasion for ECG measurement. Such aggressive techniques of dealing with this are not ideal for patient populations such as elderly, allergenic and paediatric subjects. Results obtained from ECG measurement, without preliminary skin preparation, suggested that the assumption of linearity of the electrical model must be reconsidered at the skin-

electrode interface [44, 45]. Moreover, recent experiments have confirmed that the skin-electrode interface is a major contributor to the overall source impedance in dry-electrode ECG recording [47, 48, 83, 84].

2.2.3 The skin-electrode interface

Surface electrodes convert the ionic current within the body into electronic current in metal connecting leads. Experiments of Swanson & Webster in the mid-1970s demonstrated a dominant effect of the skin layers on the skin-electrode impedance [85]. They originally proposed a model of the skin-electrode interface as a parallel combination of a resistor and a capacitor in series with a second resistor. However, experimental results obtained by the research group of which the author is a member indicate that the three element model is not applicable in the case of dry electrodes [47–49, 52, 83, 84].

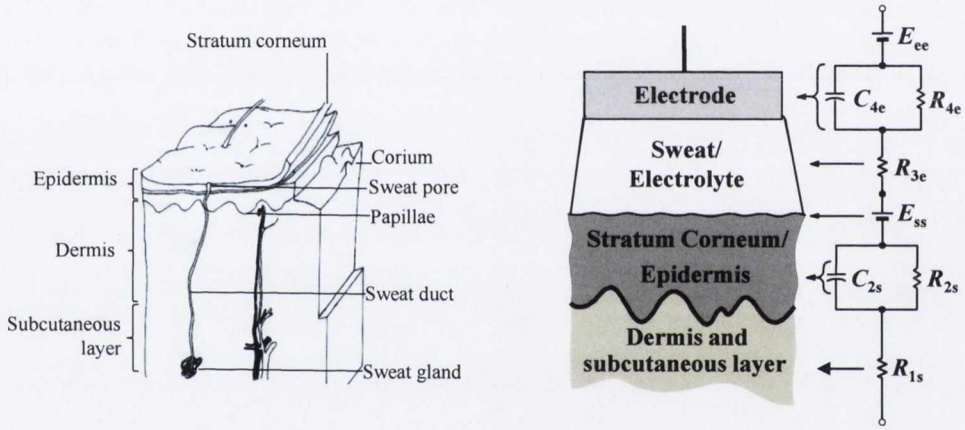

(a) Anatomy of the skin.

(b) Equivalent electrical model of the skin-electrode interface.

Figure 2.8: Schematics of (a) the anatomy of the skin and (b) the electrical model of the skin-electrode interface (modified from [86]). The half-cell potential of the electrode is labelled E_{ee}. R_{4e} and C_{4e} constitute the impedance associated with the interface between electrode and electrolyte. The series resistance R_{3e} is the effective resistance due to electrolyte between the electrode and the skin (largely perspiration in the case of dry electrodes). E_{ss} represents the potential difference across the membrane of the stratum corneum, and R_{2s} and C_{2s} make up the impedance of the epidermal layer. The dermis, subcutaneous layer and deeper tissues are generally purely resistive and modeled by a lumped resistance R_{1s}.

A more accurate model, proposed by Kaczmarek & Webster in 1989, was considered. The skin-electrode interface is described as a double-time-constant system with probably time-varying parameters [86, 87]. Because of complex current-dependent voltage sources, capacitances, and ohmic resistances, the interface acts as a non-linear second-order high-pass

filter. Neumann has given an electrical equivalent circuit of an eight-element skin-electrode interface model, shown in Fig. 2.8. Wet and dry electrodes have the same electrical model but the parameter values are significantly different [48, 83, 88, 89].

2.3 Principle of ECG signal amplification

ECG monitoring involves the measurement of low-level voltages as small as 0.1 mV, that must be amplified before their display and processing. However, the associated high source impedance and superimposed high-level interfering signals and noise tend to degrade the quality of the recorded ECG waveform.

2.3.1 Measurement of a lead II ECG

The characterisation of the equivalent electrical properties of the cardiac muscle, its volume conductor and the recording electrodes allows a complete model of the ECG that relates the voltage measured at the inputs of a biopotential amplifier to the signal generated within the heart to be established. A set-up, showing the detection of an ECG signal from the body surface using a pair of identical electrodes and a differential amplifier is schematically illustrated in Fig. 2.9.

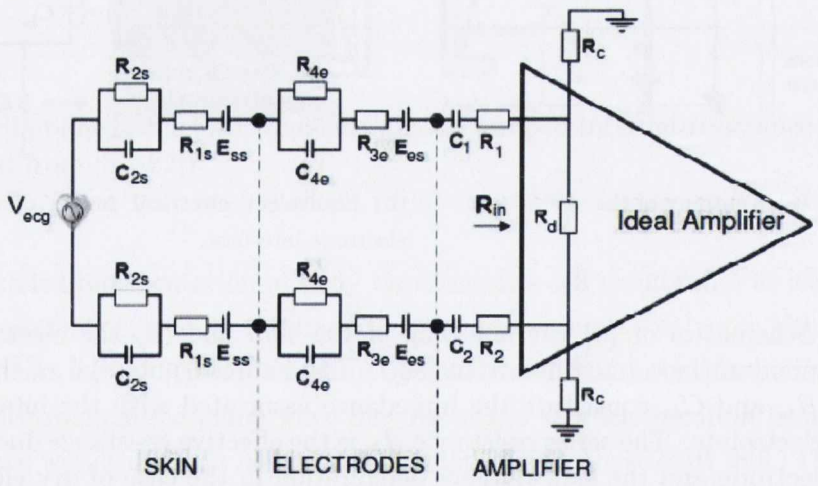

Figure 2.9: Principle of ECG measurement with identical electrodes and a differential amplifier.

The common-mode input resistances, R_c, are the equivalent resistances of both inputs of the differential amplifier with respect to ground (or analogue common) while the differential input resistance, R_d, is the equivalent resistance between the two inputs. The dc polarisation potential of dry electrodes can be much higher than is the case with conventional electrodes

[12] and is best eliminated by using dc-blocking capacitors, C_1 and C_2, in series with the electrodes. In addition, resistors R_1 and R_2 are inserted to limit transient current spikes or the current due to fault conditions which may reach the subject. The intensity of direct current is generally limited to 0.1 μA for any patient-electrode connection that serves as an amplifier input.
If R_c and R_d are taken as purely resistive, the transfer function of the combined skin-electrode-amplifier network as measured at the amplifier input is given as:

$$H(s) = \frac{R_{in}}{R_{in} + 2\left(Z_e + R_1 + \frac{1}{sC_1}\right)} \tag{2.1}$$

with

$$R_{in} = R_d//(2R_c) \tag{2.2}$$

$$Z_e = R_{1s} + R_{3s} + \frac{R_{2s}}{1 + sR_{2s}C_{2s}} + \frac{R_{4e}}{1 + sR_{4e}C_{4e}} \tag{2.3}$$

The ideal biopotential amplifier represented schematically in Fig. 2.9 should exactly reproduce the differential voltage, as sensed by the two electrodes. In practice, deviation from an exact representation of the ECG occurs due to several sources of interference caused by unwanted external voltages.

2.3.2 Sources of interference

Motion artefact

Movement of the subject during exercise induces stretch variations at the skin-electrode interface, which generates artefact in the signal present at the amplifier input [90, 91]. In addition, changes in the skin-electrode impedance and its polarisation potential are generated by triboelectric effect from electrode and skin friction [13, 14, 92]. Tam & Webster have observed variations in offset potential of about 20 mV when the skin stretches and shown that motion artefact is significantly reduced by skin abrasion with about 20 strokes of sandpaper [13]. However skin irritation and occasionally some bleeding were observed after abrasion [14].

Slow changes in the skin-electrode polarisation potential do not cause noticeable variation of the ECG base line because they are suppressed by the use of ac coupling as described above. However, high-rate changes in offset potential produce artefacts within the ECG bandwidth that cannot be removed by filtering. Motion artefact is therefore best minimised when electrode movement is prevented by the use of an elasticated belt or vest that holds them on the skin [36, 93].

Electrical interference

Other sources of electrical interference exist which occupy the spectrum of the signal. These include ac wiring and outlets, industrial and medical equipment operating in the vicinity of the electrocardiograph and domestic appliances [36, 81, 94]. Unwanted in-band signals can be superimposed on the wanted ECG signal at the amplifier input by means of electrical interference, particularly that caused by the mains power supply [95]. Mains hum can be introduced into the ECG by two means, namely electromagnetic induction and electrostatic induction [60]. In the case of electromagnetic induction, the magnetic field associated with mains supply current flowing in nearby electrical equipment cuts the loop enclosed by the subject, the electrode leads and the amplifier and induces an electromotive force in the leads, as shown in Fig. 2.10. The induced emf is directly proportional to the area of the loop, which can be minimised by twisting the leads or using coaxial cables [60]. In the case of electrodes and a preamplifier mounted in a belt or vest worn by the subject, there is little or no loop area present and hence this type of interference is not prevalent.

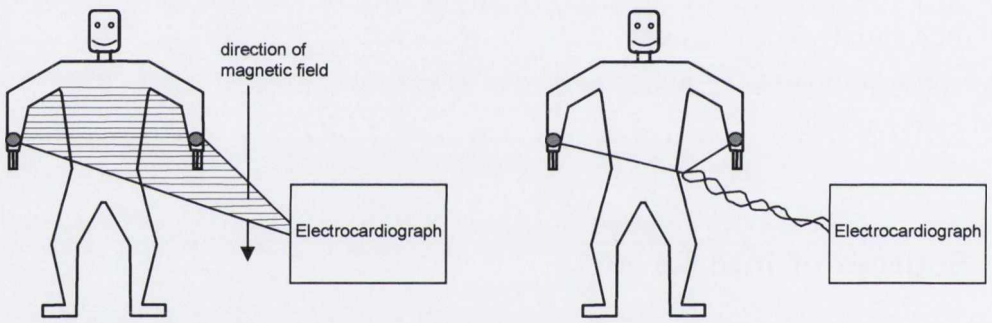

(a) Electromagnetic induction.

(b) Minimising the effect of electromagnetic induction.

Figure 2.10: Diagram showing (a) the principle of electromagnetic induction and (b) its minimisation in ECG measurement (modified from [60]).

In the case of electrostatic induction, the electric field associated with the mains supply is capacitively coupled to the subject who is also coupled to ground via their body capacitance [60, 96, 97]. With battery-operated instruments, when the common supply line of the amplifier is not at true earth potential, there is also an isolation capacitance present [36, 96, 97]. A displacement current then flows through the subject to ground, developing an interfering signal at the input to the recording amplifier, as shown in Fig. 2.11. When the electrodes are mounted close together on the subject, the interference is predominantly common-mode. Displacement currents of the order of 0.5 μA have been measured generating a typical interfering signal level of 40 mV [34, 35]. Measurement error due to common-mode interference is a major problem in electrocardiography and the common-mode rejection ratio

(CMRR) of the amplifier must be relied upon to suppress it [34, 35, 50, 51].

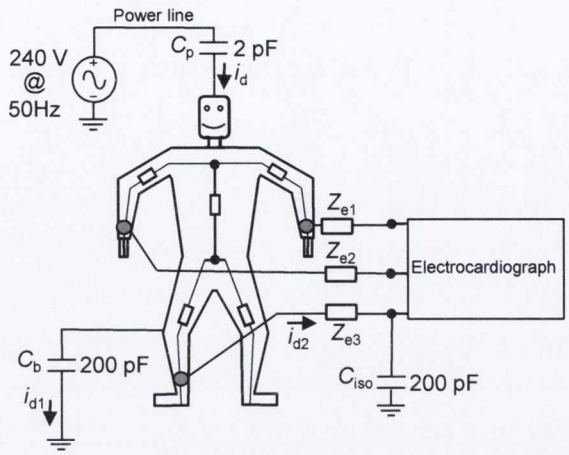

Figure 2.11: Diagram showing how the electric field from the power line can be coupled to the body (modified from [36, 60, 97]). Z_{e1}, Z_{e2} and Z_{e3} represente the electrode impedances.

2.4 Essential performance requirements

Lack of fidelity in the reproduction of the ECG limits the ability of the cardiologist or an automated interpreter to faithfully measure signal amplitudes, time relationships and waveform characteristics, and may have serious clinical consequences. To ensure that the amplifier functions well in this regard, international standards dictate essential performance requirements [69, 82, 98–114]. The International Electrotechnical Commission (IEC) is the source of the majority of standards in electrocardiography applied world-wide. The most recent documents specifying the performance requirements of electrocardiographic monitoring equipment were approved as European standards without modification in 2001 for ambulatory ECG (AECG) [102] and in 2005 for non-ambulatory diagnostic ECG and heart monitors [101]. Despite the fact that standards in place in the U.S.A. are initially based on IEC documents, American standards generally consider the recommendations of the American Heart Association (AHA) for their final texts [104, 105]. This explains why differences appear between criteria endorsed by the American National Standards Institute (ANSI) and these followed in Europe, for example. The standards and recommendations considered in this thesis have been issued by the three organisations cited above:

- the International Electrotechnical Commission (IEC);
- the American Heart Association (AHA);
- and the American National Standards Institute (ANSI).

2.4.1 Safe current limits

Specification limits related to patient's safety relevant in a low-voltage battery-powered application are listed in Table 2.1. International standards specify the safe current limit that can flow through patient-connected leads under normal condition as 10 μA rms from dc to 1 kHz [82, 103, 106]. Under single-fault conditions, the maximum current is defined as 50 μA rms over the same frequency range. However, the more relaxed limit under single-fault conditions is not supported by the AHA which recommends that the "ECG apparatus shall be designed so that no more than 10 μA root mean square, from direct current to the tenth harmonic of power line frequency, shall flow through any patient-connected lead under either normal or single-fault conditions" [115]. The more stringent requirement issued by the AHA is justified by studies reporting dangerous physiological changes for patients connected to a 50 μA rms signal at 60 Hz over 5 s [115].

Table 2.1: Safe current limits flowing through patient-connected leads.

	Ambulatory & non-ambulatory ECG	
	AHA	ANSI & IEC
Max. current under normal condition	10 μA rms	10 μA rms
Max. current under single-fault condition	10 μA rms	50 μA rms

The presence of multilayer ceramic capacitors in series with the sensing electrodes prevent dc current from reaching the patient's body. In addition, the current-limiting resistors, R_1 and R_2 in Fig. 2.9, can be selected so that no more than 10 μA rms, or 28 μA pp, reach the body in a worst-case scenario. Operating from a 3 V single-supply, patient safety is secured with $R_1 = R_2 = 100$ kΩ.

2.4.2 ECG input dynamic range

Knowledge of the input signal dynamic range is of primary importance for appropriate design of the amplification stages of an electrocardiograph. The differential input signal range, its maximum rate of variation and the level of dc offset voltage specifications are given in table 2.2 for both ambulatory and non-ambulatory ECG recording.

Table 2.2: Input dynamic range and differential offset voltage requirements.

	Ambulatory ECG	Non-ambulatory ECG
	ANSI & IEC	ANSI & IEC
input range	± 3 mV	± 5 mV
min. feature size	50 μV p-p @ 10 Hz	N.A.
slew rate	125 mVs^{-1}	320 mVs^{-1}
dc offset voltage	± 300 mV	± 300 mV

Considering the most stringent requirements, a new dry-electrode ECG amplifier must be capable of recording differential input signal voltages of ±5 mV varying at rates of up 320 mVs^{-1}, in the presence of dc offset voltage in the range ±300 mV. For ambulatory electrocardiography, a minimum feature size of 50 μV p-p at 10 Hz shall be detected to ensure that low-amplitude P waves are reproduced. However, this specification is not included in the more recent standards for non-ambulatory ECG issued in 2005 by the IEC [101] and in 2007 by the ANSI [104].

Consequently, if the preamplifier is to provide a 1-V p-p output to the subsequent amplification stages, the required voltage gain in the frequency bandwidth of the signal must be 100, or 40 dB. In addition, the maximum input variation rate must be considered for the selection of operational amplifiers having sufficient slew-rate performance. It also gives an indication of the level of transient current that may arise through capacitors. Finally, the presence of a significant skin-electrode polarisation voltage justifies the need for inserting dc-blocking capacitors, C_1 and C_2 in Fig. 2.9, in series with the dry contact electrodes as suggested in [34–36]. The dc-blocking capacitors have been placed in some amplifier designs after moderate amplification [116, 117]. However, such configuration allows op-amps bias current to flow back to the subject body, which is inadvisable in dry-electrode ECG recording due to the nature of the skin-electrode-interface, as discussed in detail in Section 4.3.2, page 88.

It can be noted that reduced dynamic range requirements are specified for AECG because it was assumed that AECG interpretations do not ordinarily involve analysis of the QRS in fine morphological detail [102].

2.4.3 System noise

Noise is arguably the most challenging obstacle to the detection of a diagnostic quality ECG signal. The main sources of interference were identified in the previous section, yet noise is also generated internally by recording systems and prevents the observation of small signals. Thus, biopotential amplifiers must keep intrinsic noise to a minimum and provide the ability to reject unwanted external voltages which appear simultaneously at both inputs. However, this ability is often limited by the finite value of the common-mode impedance seen at the amplifier's input and the imbalance of skin-to-electrode impedance, allowing the conversion of common-mode input signals into differential signals. A 51 kΩ resistor in parallel with a 47-nF capacitor simulate skin-to-electrode impedance imbalance in all international ECG standards considered. Under this condition, intrinsic noise shall not exceed 30 μV p-p referred to the amplifier input. The equivalent common-mode rejection ratio requirements are given in Table 2.3 for ambulatory and non-ambulatory ECG.

Measurements of bioelectric signals using Nasicon ceramic dry electrodes have proven the

Table 2.3: System noise requirements.

	Ambulatory ECG ANSI & IEC	Non-ambulatory ECG ANSI	Non-ambulatory ECG IEC
max. intrinsic noise	50 μV ptp	30 μV ptp	30 μV ptp
min. CMRR @ mains freq.	60 dB	95 dB	89 dB
min. CMRR @ twice mains freq.	45 dB	N.A.	N.A.

existence of significant noise attributable to electrochemical features of the skin-electrode interface [118]. The noise in the bandwidth 1 Hz - 100 Hz was found to be more intense than the thermal noise of the resistive part of the electrode plus the amplifier voltage and current noise combined. Since the published ECG standards apply to measurement equipment after the signal is sensed by the electrodes, the criteria regarding the rejection of common-mode signals shown in Table 2.3 do not account for the additional noise associated with the electrodes. As a result, the design of a new dry-electrode ECG amplifier shall target a minimum value CMRR of 95 dB, not restricted to the power supply frequency but extending to over 100 Hz, the noise bandwidth.

2.4.4 Input impedance requirement

All standards reviewed specify a single-ended input impedance magnitude at the amplifier's front-end greater than 2.5 MΩ for non-ambulatory ECG and 10 MΩ for AECG. This common-mode input impedance, R_c in Fig. 2.9, must be large enough to compensate the effective skin-to-electrode impedance over the frequency range of the signal and to guarantee that all subjects will be monitored with minimum attenuation and reproduction error. The effect of the skin-electrode interface is simulated by means of a 620 kΩ resistor connected in parallel with a 4.7 nF capacitor. To reduce the skin-electrode impedance, preferably below 2 kΩ at 10 Hz, the AHA recommends the removal of hair from electrode sites and skin abrasion with sandpaper [109, 112]. At 10 Hz, the impedance of the combination should not cause significant attenuation of the ECG signal. The maximum level of signal attenuation is determined relative to the amplitude obtained without the simulated impedance. A 20% signal reduction is tolerated for non-ambulatory monitoring while only 6% attenuation is accepted in ambulatory recording, leading to the values shown in Table 2.4. As part of the design of the dry-electrode ECG amplifier, the input impedance requirements will be reviewed to suit the more realistic ECG model illustrated in Fig. 2.9.

2.4.5 Frequency response

Requirements for reproduction accuracy, summarised in Table 2.5, must be considered at every stage of the design of an ECG amplifier. It has been proven that inadequate high-

Table 2.4: Input impedance requirements.

	Ambulatory ECG ANSI & IEC	Non-ambulatory ECG ANSI & IEC
assumed skin-to-electrode impedance	4.7 nF capacitor // 620 kΩ resistor	
max. attenuation @ 10 Hz	6 %	20 %
min. single-ended input impedance	10 MΩ	2.5 MΩ

frequency response rounds off the sharp features of the ECG waveform and diminishes the amplitude of the QRS complex while distortion in the slow varying detail such as the T wave occurs due to poor low-frequency performance, degrading the reproduction of the ST segment [44, 45, 119]. Therefore, reproduction fidelity necessitates sufficient frequency bandwidth and adequate phase characteristic to prevent signal distortion.

Table 2.5: Accuracy of input signal reproduction.

	Ambulatory ECG		Non-ambulatory ECG		
	AHA	ANSI & IEC	AHA	ANSI	IEC
max. output error:					
max. % error	±10 %	±10 %	±5 %	±5 %	±20 %
max. absolute error	±50 μV	N.A.	±25 μV	±40 μV	±100 μV
3-dB bandwidth:					
upper cut-off freq.	60 Hz	55 Hz	250 Hz	150 Hz	40 Hz
lower cut-off freq.	0.05 Hz	0.05 Hz	0.05 Hz	0.67 Hz	0.67 Hz
impulse response:					
rectangular test input	1 mVs	0.3 mVs	1 mVs	0.3 mVs	0.3 mVs
max. undershoot	0.3 mV	0.1 mV	0.3 mV	0.1 mV	0.1 mV
max. slope	1 mVs^{-1}	0.3 mVs^{-1}	1 mVs^{-1}	0.3 mVs^{-1}	0.3 mVs^{-1}

Maximum output error

The maximum overall output error tolerated in the reproduction of input signals varying at rates of up to 125 mVs^{-1} are given in Table 2.5. The AHA recommends the highest reproduction accuracy, limiting the error at the output to the greater of ±5% or ±25 μV, relative to a ±5 mV input signal level [108, 110]. The ANSI restricts the maximum reproduction error to below ±5 % but accepts absolute errors of up ±40 μV, obtained by adding one half of the maximum system noise (±15 μV) to the limit recommended by the AHA. The precision requirement is relaxed to ±10 % when errors due to electrode impedance imbalance are included [104].

High-frequency response

IEC standards for AECG require that the 3 dB high-frequency cut-off be greater than 40 Hz and extend it to 55 Hz for infants weighing less than 10 kg. A 40 Hz bandwidth is selected by the IEC for non-ambulatory ECG, assuming that the primary purpose of monitoring the ECG is the identification of the heart rate, which can be accomplished with this bandwidth [101]. Besides, the 40-Hz cut-off reduces interference from mains power-lines and high-frequency muscle artefact. However, this cut-off frequency is not endorsed by the AHA that stresses the need for reproducing more accurately the higher frequency features in the signal [108, 110]. American standards aim for a higher cut-off frequency of 150 Hz for adults, adolescents and children in non-ambulatory ECG and an even higher bandwidth of 250 Hz when applied to infants [108]. A novel high-performance dry-electrode ECG amplifier should therefore provide a 3-dB bandwidth greater than 250 Hz, as recommended by the AHA.

Low-frequency response

A 0.67-Hz low-frequency cut-off is the current standard for non-ambulatory ECG. It finds its justification in the results of studies led by Simmonson [120, 121] suggesting a lower heart rate of 40 bits per minute (equivalent to 0.67 Hz) for over 99 % of resting adults, for more than 99 % of the time. However, the AHA insists upon 3-dB cut-off frequency lower than 0.05 Hz in AECG to accurately measure ST segments and recommends that the amplitude response should be flat to within ±6 % (0.5 dB) over the range 0.14 to 30 Hz [102, 112].

Frequency response recommendations have been traditionally completed with phase distortion criteria, particularly important in the low-frequency response. The AHA have recommended that ECG amplifiers should introduce no more phase shift into the signal than that which would be introduced by a 0.05-Hz, single-pole high-pass filter [108, 110]. More recently, low-frequency criteria have been more precisely defined in terms of the system impulse response, as suggested by the AHA since 1990. As shown in Fig. 2.12, IEC and ANSI standards state that a 300-μVs impulse shall not yield an offset on the ECG record from the isoelectric line of greater than 100 μV, and shall not produce a recovery slope of greater than 300 μVs^{-1} following the end of the impulse [98, 101, 102, 104]. The AHA recommended that a 1-mVs input impulse should not generate a displacement greater than 300 μV. The slope of the response outside the region of the impulse should nowhere exceed 1 mVs^{-1} [110].

The amplifier front-end shall therefore be adapted to prevent dc-blocking capacitors in series with the electrodes from giving rise to significant phase distortion on the ECG signal.

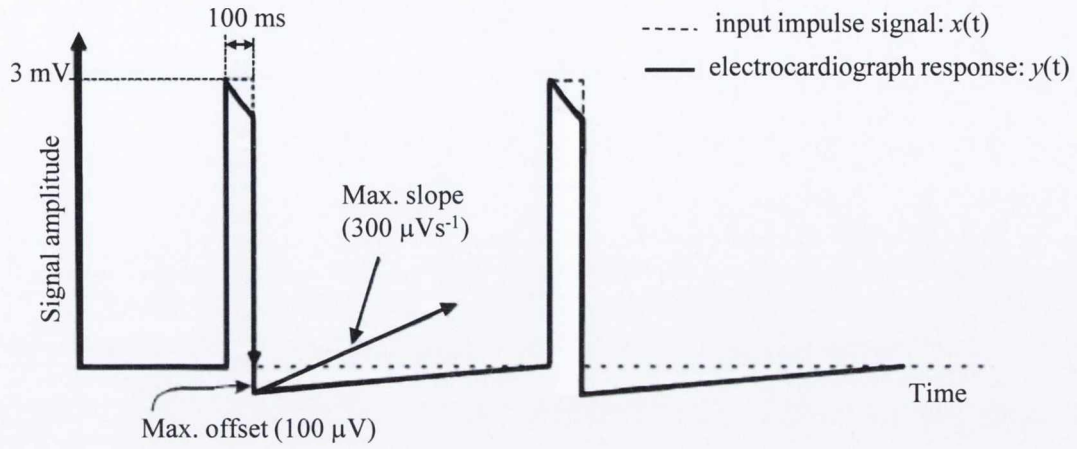

Figure 2.12: Plots of the impulse response requirements (from [98, 101, 102, 104]).

2.5 Discussion

The model of the skin-electrode interface and the associated parameter values utilised in the international standards reviewed rely on results obtained with wet electrodes, for which signal sensing is facilitated by the presence of a conductive gel. Therefore, wet electrodes exhibit relatively small resistance to current, allowing a single-time-constant RC network to simulate the effect of the skin-to-electrode impedance. New versions of the standards for ambulatory and non-ambulatory electrocardiographic equipment are due to be published before the end of 2010 by the IEC. Drafts, made available in advance for public review do not, however, address issues specific to dry electrodes and minimum requirements for input impedance and rejection of common-mode signals are not expected to change [98–100]. As indicated in section 2.2.3, a single-time-constant model is not suitable for dry electrode recording because the absence of electrolytic gel reduces electrode conductivity and therefore increases its resistance to current. This yields higher voltage drops at the skin-electrode interface and hence greater signal attenuation, unless the magnitude of the amplifier's input impedance is significantly increased. Furthermore, since the model for dry electrodes simulates the skin-electrode interface as a second-order high-pass filter, the ECG may suffer low-frequency distortion in a different manner than predicted by the simpler model. The overall input impedance, R_{in} in Fig. 2.9, provided by the amplifier front-end must be chosen so that amplitude, phase and impulse response criteria are fulfilled. In an effort to design a new dry-electrode, low-power, ECG pre-amplifier suitable for operating in ambulatory and non-ambulatory environments, the most stringent requirements among all reviewed standards are retained. A target performance specification for the amplifier to be designed is given in table 2.6.

Table 2.6: Target performance specification.

Input signal:	
signal amplitude	0.05 mV - 10 mV p-p
max. rate of variation	320 ms^{-1}
dc offset voltage	$\pm$ 300 mV
Output signal:	
Output signal amplitude	1 V p-p
max. output error	the greater of $\pm$10 % or 50 μV
System noise:	
intrinsic noise	30 μV max. (referred to input)
CMRR	95 dB min. in 0.5 - 100 Hz bandwidth
Input impedance:	TO BE DETERMINED
Frequency response:	
3-dB bandwidth	0.05 - 2500 Hz (1 decade above the max. frequency in ECG)
Differential gain	$\geq$40 dB
amplitude response	flat to within $\pm$0.5 dB over the range 0.14 to 30 Hz
phase response	phase characteristic of 0.05 Hz single-pole high-pass filter
impulse response	0.1 mV max. undershoot after 0.3 mVs impulse
recovery slope	0.3 mVs^{-1} max.
Power supply:	
Supply voltage	3 V nominal single supply
Supply current	50 μA max.

Considering recommendations issued by the AHA for infant weighing less than 10 kg, the target 3-dB bandwidth is extended to 0.05 - 2500 Hz in order to keep the phase shift introduced by the pre-amplifier below 6° within an ECG signal bandwidth of 0.5 - 250 Hz.

As for all battery-powered equipment, an acceptable compromise must be found between performance and power consumption. Low-cost 3 V lithium coin cell batteries providing 1 Ah capacity are available today and therefore a portable ECG system that draws 100 μA in current would operate continuously for up to 10,000 h. Despite not being rechargeable, these batteries offer, at 3 V, excellent shelf-life for relatively small sizes [122]. If only 50% of the power is allocated to the preamplifier, physiological monitoring can be safely performed over

several years without changing the battery. Signal conditioning stages after filtering may then be implemented digitally using an embedded microcontroller. For example, Microchip has recently applied their nanoWatt Technology to Programmable Interface Controllers (PICs) operating from less than 3 μA at 32 kHz and costing less than 1 euro [123].

2.6 Conclusion

In this chapter the principles of ECG reproduction were examined. The electrocardiographic problem was shown to involve bioelectrical currents generated within the heart and the creation of electrical fields that can be measured on the surface of the skin using sensing electrodes. The volume conductor surrounding the heart is composed of body tissues the impedance of which is mainly resistive. However, the skin-electrode interface acts as an high-pass filter and is therefore a potential source of distortion of the low-frequency components in the ECG signal. Other factors limiting the ability of the recorder to faithfully reproduce the ECG waveform include interfering signals caused by external unwanted voltages, motion artefact and additional perturbation intrinsic to the amplifier.

International standards and recommendations provide essential performance requirements for ECG recorders, although the absence of criteria adapted to dry electrodes makes current specifications regarding input impedance and common-mode-rejection inadequate. The author will therefore review some key issues that dictate the quality of the ECG signal at the output of the dry-electrode preamplifier in the following chapters.

Chapter 3

Low-frequency response and the skin-electrode interface

Initiated during the space-age era of the 1960s, the investigation of the use of dry electrodes for ECG monitoring has led to the development of several pasteless electrode systems which overcome the disadvantages associated with traditional approaches employing wet electrodes. The following question, however, was immediately raised: how should the recording amplifier be adapted to the high source impedance commonly associated with dry electrodes? Optimised designs of the amplifier front-end have usually involved measuring the impedance of the skin-electrode interface [19–39, 124–134]. Some solutions have then inserted resistors in series with unbalanced electrodes to match the effective impedance seen at each input of the recording amplifier [30, 31]. Others have fabricated dry electrodes having impedances lower in magnitude than those of conventional Ag/AgCl wet electrodes [19, 20, 134]. Commercial dry-electrode Holter monitors providing diagnostic quality ECGs are, however, not available to date. The recent development in 2009 of a wearable two channel dry electrode ECG system called *care.mon* has shown some prospects in the realisation of long-term telemetric application in the near future [18]. The designers have admitted, however, that their prototype cannot get a signal of the same quality as that of a standard electrode Holter system.
A critical source of error was soon identified as low-frequency distortion introduced at the amplifier's front-end. In this chapter, the author shows how high-pass filtering can affect the quality of the recorded ECG waveform and demonstrates that the risk of distortion is exacerbated by the presence of a frequency dependent skin-electrode impedance. New approaches for the determination of the model parameters of the skin-electrode interface and new input impedance requirements for dry-electrode ECG recording are then presented.

Results from this chapter have been published in [46–49, 52]

3.1 Importance of the recorder's low-frequency response in diagnostic quality electrocardiography

To ensure that the electrocardiograph's output signal is an accurate representation of the physiological input waveform, the amplifier must faithfully reproduce all frequency components of the ECG signal. Out-of-band high frequency interfering signals are normally removed from the preamplifier's output by implementing linear-phase low-pass filters [36]. However, distortion introduced by an inadequate low-frequency response cannot generally be corrected in real time by simple filtering in the subsequent amplification stages [45]. The quality of the recorder's low-frequency response relies therefore on the performance of the preamplifier's front-end. To prevent recording error caused by the electrocardiograph, the preamplifier must preserve the ECG signal by providing flat amplitude response and linear or zero phase within the ECG bandwidth [44, 45]. Failure to fulfil these requirements can have serious clinical implications.

3.1.1 Diagnostic implications of a poor low-frequency response

Berson & Pipberger have demonstrated that ECG preamplifiers implementing high-pass filters with a poor low-frequency amplitude response are a potential source of recording error that may lead to misdiagnosis of serious cardiac conditions [44]. They concluded that an increase of the filter's cutoff frequency above 0.05 Hz or a roll-off greater than 6 dB per octave causes distortion of the S-T segment and the T wave of the ECG waveform. Yet, accurate measurement of slow deflections, especially in the first quarter of the ST-T complex, is usually crucial for assessing the condition of the heart and its response to therapy [59, 73, 74, 135]. For example, acute myocardial infarction, commonly known as heart attack, is frequently accompanied by an elevation of the ST segment but inadequate low-frequency response reduces this elevation and can produce an inversion of the terminal part of the T wave, as shown in Fig. 3.1(a). In addition, it was reported that the ECG of patients who had suffered damage to the surface of the heart, referred to as an old infarct, usually shows a downward sloping S-T segment [44]. Fig. 3.1(b) illustrates how poor high-pass filtering can modify the S-T segment by converting a downward slope into an upward slope, which has a different clinical interpretation.

It was found that low-frequency distortion is generally greater for abnormal than for normal ECG waveforms and for records having essentially monophasic QRS patterns than for those having biphasic QRS complexes. Besides, it was observed that the increase in heart rate associated with exercise can alter recording error in an unpredictable manner [44].

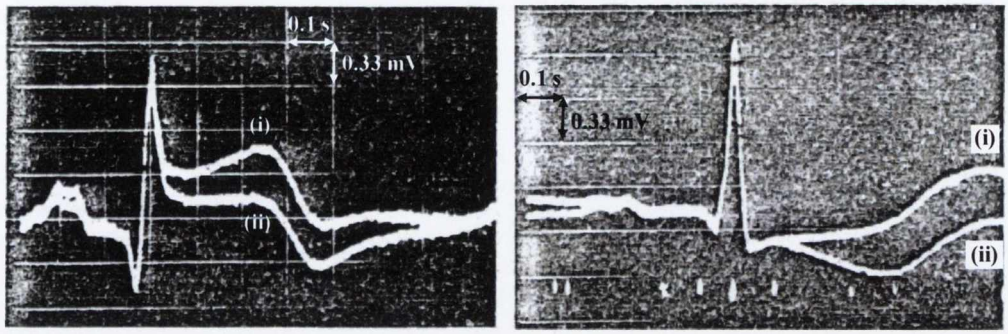

(a) Acute infarct record.

(b) Old infarct record.

Figure 3.1: Oscilloscope photographs of the electrocardiogram of patients suffering from (a) acute myocardial infarction and (b) an old infarct (from [44]). In both pictures, the upper record, labelled (i), is obtained with a simulated dc amplifier system while the lower record , (ii), is the output of a high-pass filter having a 0.5-Hz cutoff and 24-dB-per-octave roll-off.

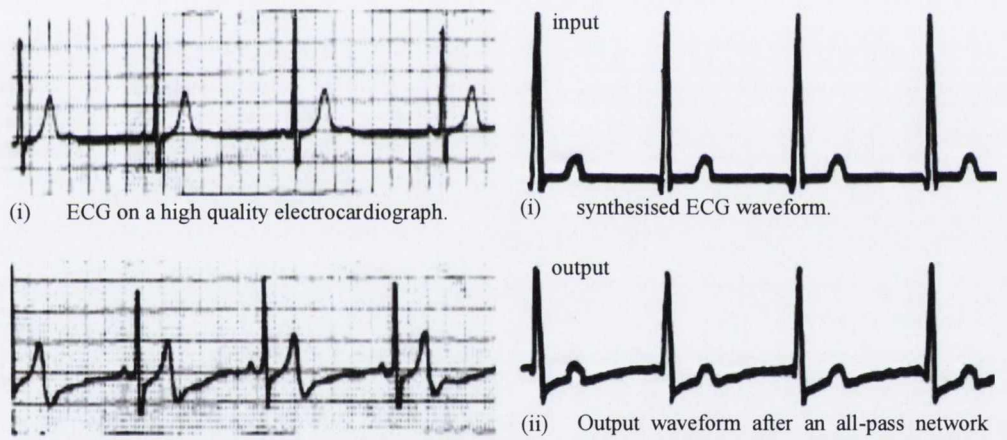

(a) Effect of phase distortion on a patient's ECG.

(b) Effect of an all-pass network with nonlinear phase response.

Figure 3.2: Electrocardiograms showing the effect of low-frequency distortion caused by nonlinear phase response in the bandwidth of the ECG signal from (a) a patient's record and (b) a synthesised ECG waveform (modified from [45]). In (b), the input waveform is filtered by an all-pass network with flat amplitude response from dc to 10 kHz ($\pm$ 1 dB), but a nonlinear phase response with a breaking point approaching the fundamental frequency of the input waveform.

The works of Berson & Pipberger were followed by studies led by Tayler & Vincent on the low-frequency phase response of filters used in ECG recording [45]. They concluded that phase nonlinearity is also a major source of recording error and misdiagnosis. For example, myocardial ischaemia is a disease that reduces the supply of blood to the heart muscle and normally manifests itself in the ECG record as elevation or depression of ST segments [59, 135]. However, false ST segment shifts such as those depicted in Fig. 3.2(a) have been noted with ambulatory ECG recorders exhibiting a nonlinear phase response at low frequency. Results revealed that the ST segment is more readily affected by distortion when the point of maximum phase nonlinearity approaches the fundamental frequency of the ECG signal, as shown in Fig. 3.2(b). Once phase nonlinearity is introduced at the preamplifier front stage, its effects on the ST-T complex cannot be corrected subsequently without distorting other portions of the ECG waveform [45].

3.1.2 Low-frequency performance requirements of ECG recorders

The empirical findings reported in [44] and [45] have played a key role in defining the frequency response requirements of ECG recorders utilised today and can be considered as part of the classical publications in ECG signal conditioning. As reviewed in chapter 2, the traditional performance criteria have been enhanced by the addition of specifications in the time domain. The evolution of the low-frequency performance requirements in electrocardiography can be summarised as follows:

1. In the mid 1960s, to ensure that recording errors are kept under 50 μV in the early portion of the ST-T complex, Berson & Pipberger recommended that ECG preamplifiers provide a 0.05-Hz low-frequency cutoff with a 6-dB-per-octave roll-off [44], as achieved for example by a single-pole high-pass filter. The AHA has endorsed this low-frequency cutoff since 1967 [113, 114] and added in 1985 that the amplitude response should be flat to within ±6 % (0.5 dB) over the range 0.14 to 30 Hz [112], as shown in Fig. 3.3(a).

2. In the early 1980s, Tayler & Vincent recommended that phase linearity must be maintained down to the fundamental frequency of the physiological signal to allow high fidelity in the reproduction of the ECG waveform [45]. The AHA has adopted this recommendation since 1985 by specifying that the phase shift introduced by the amplifier should not be greater than that introduced by a 0.05-Hz, single-pole high-pass filter [112], as depicted in Fig. 3.3(b).

3. In more recent years, specification of the low-frequency performance of electrocardiographs based on the system's impulse response have been introduced. The International Electrotechnical Committee (IEC) and the American National Standard Institute (ANSI) have indicated that a 300-μVs impulse shall not yield an undershoot on

the ECG record from the isoelectric line of greater than 100 μV, and shall not produce a recovery slope of greater than 300 μVs^{-1} following the end of the impulse [102, 104], as illustrated in Fig. 3.4.

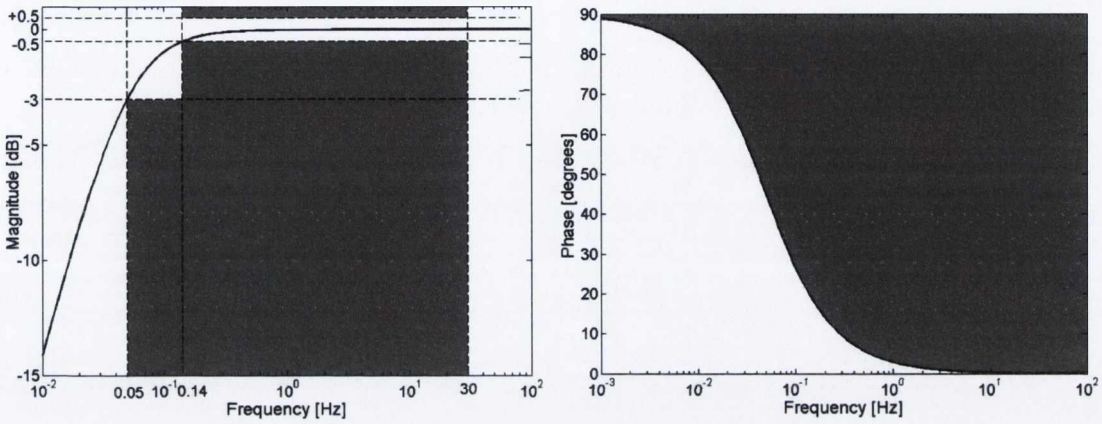

(a) Amplitude response criterion

(b) Phase response criterion

Figure 3.3: Plots of the low-frequency (a) amplitude and (b) phase criteria illustrated with a 0.05-Hz single-pole high-pass filter. The shaded areas indicate the "forbidden" areas as specified by the AHA [112].

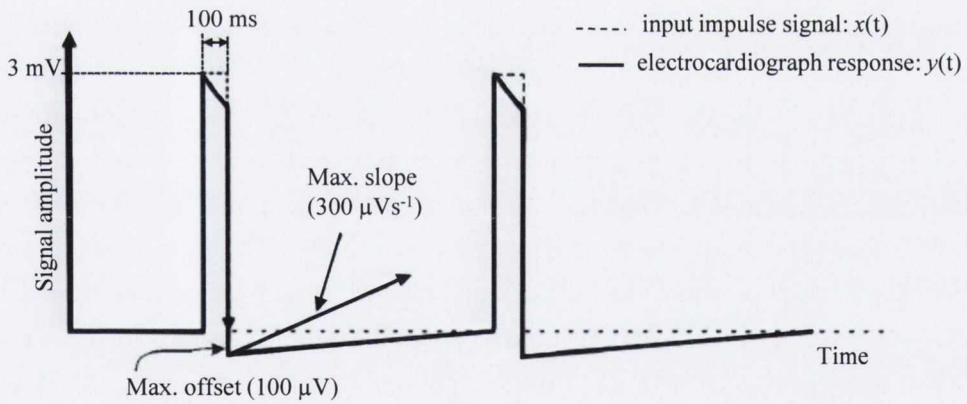

Figure 3.4: Plots of the impulse response requirements (from [101, 102, 104]).

3.1.3 The effect of high-pass filtering on the ECG signal

The performance requirements can be explained from a simple mathematical model of the physiological signal and the recording system. From a signal viewpoint, the ECG waveform

may be regarded as a periodic time function represented by the following Fourier series:

$$f(t) = \sum_{n=0}^{\infty} \left[a_{\mathrm{n}} cos\left(\frac{2\pi nt}{T_{\mathrm{R\text{-}R}}}\right) + b_{\mathrm{n}} sin\left(\frac{2\pi nt}{T_{\mathrm{R\text{-}R}}}\right) \right] \tag{3.1}$$

where $T_{\mathrm{R\text{-}R}}$ is the $R-R$ interval or cardiac cycle time and a_{n} and b_{n} are the Fourier coefficients. The fundamental frequency of the ECG signal is therefore determined by $1/T_{\mathrm{R\text{-}R}}$ and defines the heart rate while its dc component is given by a_0.

If $A(s)$ represents the preamplifier's transfer function, its response to the ECG signal defined in eq. (3.1) can then be modelled in the Laplace domain by the following product:

$$V_{\mathrm{out}}(s) = A(s) \int_0^{\infty} f(t) e^{-st}\, dt \tag{3.2}$$

$V_{\mathrm{out}}(t)$, the preamplifier's response to $f(t)$ in the time domain, is obtained from the inverse Laplace transform of eq. (3.2) by convolution once $A(s)$ is known.

Taking $s = j\omega$, the preamplifier response may also be specified in the frequency domain as follows:

$$A(j\omega) = |G(\omega)|\, e^{j\theta(\omega)} \tag{3.3}$$

with $|G(\omega)|$ its amplitude response and $\theta(\omega)$ its phase response. An ideal amplitude response is achieved when $|G(\omega)|$ is frequency-independent, which in practice would require the ECG recorder to be dc-coupled to the source signal. This approach is, however, inadvisable due to excessive base-line wander and artefacts commonly associated with dc-coupled recording equipment. In addition, the large dc offset inherently present with dry electrodes would quickly limit the obtainable gain of the amplification stages due to saturation. AC-coupling is therefore unavoidable in diagnostic quality ECG recording but it comes at the cost of potential amplitude and phase distortion as experienced in [44] and [45]. Because of phase nonlinearity, a non-constant group delay is introduced into the ECG waveform. Consequently the low-frequency components of the QRS complex are affected by a greater time delay than its high-frequency components and can therefore become superimposed on the ST complex [45]. Low-frequency phase distortion is avoided if the phase shift or the group delay is made negligible. For example, the phase shift introduced by a first order high-pass filter is less than 6° from a decade above the cutoff frequency, f_{c}. Therefore, if frequencies in the vicinity of the fundamental ECG frequency are to be reproduced, the 3-dB low-frequency point must be about 10 times lower than $1/T_{\mathrm{R\text{-}R}}$. Considering a lower limit heart rate of 30 beats per minute gives $1/T_{\mathrm{R\text{-}R}} = 0.5$ Hz and thus $f_{\mathrm{c}} = 0.05$ Hz.

The impulse response requirements complement the frequency response specifications to ensure that the fast varying signals in the ECG, such as the QRS complex and P wave, do not generate noticeable depressions as result of filtering. A visible undershoot could, in fact, be

misinterpreted as an additional ECG component. The Common Standards for Quantitative Electrocardiography (CSE) issued by the European Union defines the presence of a QRS deflection as a waveform having an amplitude greater than or equal to 20 μV and a duration greater than or equal to 6 ms [104]. Moreover, the slope of the response after the end of the input impulse must be minimised to preserve base line stability and allow accurate amplitude measurement of the P wave and the QRS complex.

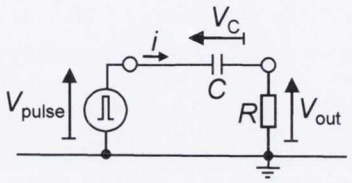

Figure 3.5: Test set up for the measurement of the impulse response of a passive single-pole high-pass filter.

Fig. 3.5 shows a passive single-pole high-pass filter connected to a generator supplying a rectangular pulse, V_{pulse}, of amplitude V_{m} and duration T. Considering V_{C}, the potential across the capacitor C, and V_{out} the output voltage across the resistor R, Kirchhoff's law allows V_{pulse} to be expressed as follows:

$$V_{\text{pulse}}(t) = V_{\text{C}}(t) + V_{\text{out}}(t) \tag{3.4}$$

The current $i(t)$ that flows through the RC network is defined as

$$i(t) = C\frac{dV_{\text{C}}(t)}{dt} \tag{3.5}$$

The output voltage is therefore given by $V_{\text{out}}(t) = Ri(t)$ as:

$$V_{\text{out}}(t) = RC\frac{dV_{\text{C}}(t)}{dt} \tag{3.6}$$

The time origin, $t = 0$, is taken as the instant when V_{pulse} reaches its maximum amplitude, V_{m}. The input impulse is then given for $0 < t < T$ by $V_{\text{pulse}} = V_{\text{m}}$. It can be shown that during this time interval, the voltage across the capacitor in its charging phase is characterised by:

$$V_{\text{C}}(t)|_{0<t<T} = V_{\text{m}}\left[1 - e^{-\left(\frac{t}{RC}\right)}\right] \tag{3.7}$$

and

$$\left.\frac{dV_{\text{C}}(t)}{dt}\right|_{0<t<T} = \frac{V_{\text{m}}}{RC}e^{-\left(\frac{t}{RC}\right)} \tag{3.8}$$

The output voltage, V_{out}, and its slope, V'_{out}, can therefore be deduced from eqs. (3.6) to

(3.8) as:

$$V_{\text{out}}(t)|_{0<t<T} = V_{\text{m}} e^{-\left(\frac{t}{RC}\right)} \tag{3.9}$$

and

$$V'_{\text{out}}(t)|_{0<t<T} = \left.\frac{dV_{\text{out}}(t)}{dt}\right|_{0<t<T} = -\frac{V_{\text{m}}}{RC} e^{-\left(\frac{t}{RC}\right)} \tag{3.10}$$

After the end of the pulse, $t > T$ with $V_{\text{pulse}} = 0$, Kirchhoff's law gives:

$$0 = V_{\text{C}}(t) + V_{\text{out}}(t) = V_{\text{C}}(t) + RC\frac{dV_{\text{C}}(t)}{dt} \tag{3.11}$$

Solving eq. (3.11) yields:

$$V_{\text{C}}(t)|_{t>T} = Ke^{-\left(\frac{t}{RC}\right)} \tag{3.12}$$

where K is a constant. Continuity in the charge and discharge characterisctics of the capacitor requires that at $t = T$, V_{C} must simultaneously satisfy eqs. (3.7) and (3.12), allowing K to be evalutated as:

$$K = V_{\text{m}}\left[e^{\left(\frac{T}{RC}\right)} - 1\right] \tag{3.13}$$

Taking $f_{\text{c}} = \frac{1}{2\pi RC}$, the filter's response and its recovery slope after the end of the input impulse can therefore be expressed as follows:

$$V_{\text{out}}(t)|_{t>T} = -V_{\text{m}}\left[e^{\left(\frac{T}{RC}\right)} - 1\right] e^{-\left(\frac{t}{RC}\right)} = -V_{\text{m}}\left[e^{(2\pi f_{\text{c}}T)} - 1\right] e^{-(2\pi f_{\text{c}}t)} \tag{3.14}$$

and

$$V'_{\text{out}}(t)|_{t>T} = \left.\frac{dV_{\text{out}}(t)}{dt}\right|_{t>T} = \frac{V_{\text{m}}}{RC}\left[e^{\left(\frac{T}{RC}\right)} - 1\right] e^{-\left(\frac{t}{RC}\right)} = 2\pi f_{\text{c}} V_{\text{m}}\left[e^{(2\pi f_{\text{c}}T)} - 1\right] e^{-(2\pi f_{\text{c}}t)} \tag{3.15}$$

Eqs. (3.14) and (3.15) indicate that for $V_{\text{out}}(t)$ and $V'_{\text{out}}(t)$ to approach zero after the end of the input impulse, f_{c} should also tend towards zero, supporting the call for low-frequency cut-off at 0.05 Hz or below. It must be noted that the slope of the response after the end of the impulse is a function of the pulse duration, T. Eqs. (3.8) and (3.10) indicate, however, that during the charging phase of the capacitor the rate at which energy is dissipated in the resistor is independent of T. The energy stored in the capacitor at the end of the charging phase at time $t = T$ is given by:

$$W_{max} = C\frac{[V_{\text{C}}(T)]^2}{2} = CV_{\text{m}}^2\frac{\left[1 - e^{-\left(\frac{T}{RC}\right)}\right]^2}{2} \tag{3.16}$$

For $T << RC$, this energy is dissipated during the recovery phase at a much lower rate than the rate at which it was accumulated during the pulse. The slope of the impulse response before and after the end of impulse are therefore expected to be significantly different, as

depicted in Fig. 3.6 for $T = 0.1$ s and $RC = 3.2$ s, corresponding to $f_c = 0.05$ Hz. Fig. 3.6 shows that there is a very slow recovery slope after the pulse.

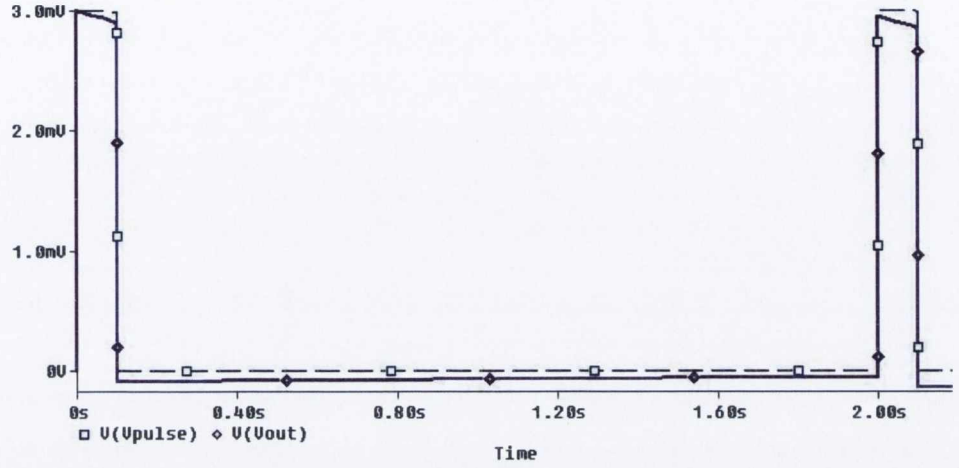

Figure 3.6: Impulse response of a 0.05-Hz single-pole high-pass filter simulated wih PSpice. The pulse is repeated after two seconds to simulate a lower limit heart rate of 0.5 Hz. $V_m = 3$ mV, $T = 0.1$ s, $R = 10$ MΩ and $C = 0.33$ μF.

3.2 Effect of the skin-electrode interface on the low-frequency performance of ECG recording systems

High pass-filtering is commonly achieved in dry-electrode ECG recording by inserting a dc-blocking capacitor, C_{in}, in series with each sensing electrode as shown in Fig. 3.7. Z_e simulates the skin-electrode impedance and R_{in} is the input impedance of the recording amplifier. Two electrical models of have been principally used to simulate the skin-electrode interface at the preamplifier's input: a simple single-time-constant RC network and a more complete double-time-constant model.

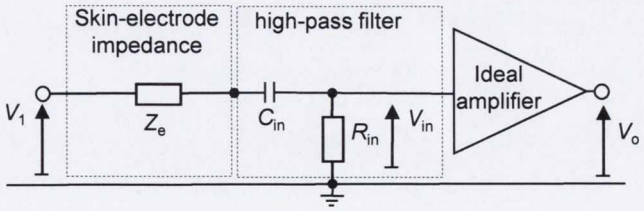

Figure 3.7: Schematic representation of a simple high-pass filter at the amplifier's front-end. AC-coupling achieved this way allows dc offset voltages associated with polarisation effects at the skin-electrode interface to be blocked from the amplifier input.

3.2.1 Non-intrusive biopotential measurement using capacitive dry electrodes

Since the beginning of research in dry electrode biopotential recording, it was suggested that the input stage of the recording amplifier is ideally designed when the source impedance of the electrodes in combination with the human body is determined. Several researchers therefore investigated the opportunities offered by impedance transforming capacitive dry active electrodes for long-term biopotential recording. Fig. 3.8 shows the principle of operation of an active capacitive electrode.

Impedance matching issues have then not been limited to ECG recording but have rather extended to applications measuring other bio signals without the use of a conductive gel [26, 125, 129]. For example, experiences in electroencephalography (EEG) have shown how the effect of changing skin impedance can be minimised by inserting an insulating electrode the capacitance of which should be at least two orders of magnitude less than that of the skin. The effective capacitance of a thin dielectric layer at the surface of the electrodes was reduced to 150 pF which required an recording amplifier having an input impedance of 10^{15} Ω to preserve the low-frequency components of the EEG signal [129]. When applied to ECG recording, capacitive electrodes ranging from 50 nF to 1 fF (1f= 10^{-15}) have been coupled to buffer amplifiers having 10^{8} Ω to 10^{18} Ω input impedance [128, 130–133, 136–140].

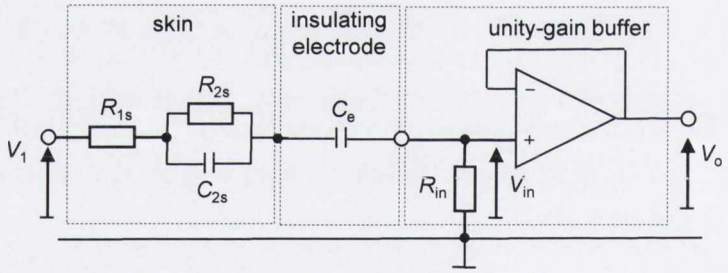

Figure 3.8: Schematic representation of an active insulating electrode for capacitively coupled ECG measurement. C_e represents the electrode capacitance, R_{2s} and C_{2s} make up the impedance of the epidermal skin layer and deeper tissues are modeled by a lumped resistance R_{1s}. An impedance transforming unity-gain buffer is incorporated at the electrode site, with resistor R_{in} providing a path for the op-amp bias current.

Lim et al. have recently demonstrated the feasibility of long-term physiological monitoring using non-intrusive sensors embedded in everyday equipment [136–138]. In 2006, Lim, Kim & Park presented a recording system for ECG measurement without conductive contact while subjects sit on a chair wearing normal clothes [136]. Two active insulating electrodes sensed the potential variation on the subject's body relative to a conductive ground plane, also capacitively coupled to the body. The electrode capacitance was estimated at 30 pF

and a 3 GΩ-input-impedance preamplifier was inserted at the electrode site. The proposed method had the advantage of easy use on a daily basis. However, excessive sensitivity to motion artefact resulted in signal quality classified as poorer than that obtained with conventional wet electrodes [136]. They later published in 2007 a revised method for monitoring ECG during sleep relying on an array of high-input-impedance capacitive active electrodes fixed on a mattress [137]. The value for R_{in} was reduced to 1.6 GΩ to prevent output saturation caused by large motion artefact when coupled to the same electrodes as used in [136]. The selection of the value of R_{in} was reported as intuitive with observation in [136] and yielded ECG recordings affected by noticeable low-frequency distortion. In February 2011, Lim et al. reported results of ECG measurements carried out using active insulated electrodes equipped with 50 GΩ-input-impedance buffer amplifiers embedded in chairs, beds, belts and toilet seats. The recorded bio signals were not affected by low-frequency distortion but the authors admitted that capacitively coupled ECG measurement presents higher sensitivity to motion artefact and lower signal to noise-ratio compared to Ag/AgCl ECG electrodes that require direct skin contact [138]. Similar experiments were reported in 2008 by Beak et al. who assessed the efficacy and practicality of ECG measurement on a toilet seat using capacitively coupled electrodes [139]. It was concluded that clear R peaks could be detected allowing the heart rate to be calculated but large common-mode noise and motion artefact limited the ability of the recording system to provide an ECG signal of diagnostic quality. In September 2010, results published by Spinelli & Haberman demonstrated that an amplifier having a bias resistor of 3 TΩ coupled to capacitive electrodes of 10 pF can be used to acquire an ECG signal with a similar quality to that of wet electrodes when applied to bare skin [140]. Unfortunately breathing artefacts of capacitive electrodes placed over clothes were much higher than in the case of Ag/AgCl contact electrodes [140].

The results reported in [136–140] show some prospects in the provision of non-intrusive ubiquitous health monitoring relying on non-contact capacitive electrodes in the near future. However, the method currently presents serious limitations. Insulating electrodes having extremely low coupling capacitance require ultra-high input impedance amplifiers, which are highly susceptible to external electrostatic and electromagnetic interference unless shielding is used around the electrodes [12, 127]. Their reported lack of robustness has thus made insulated electrodes unsuitable for functional clothes [39]. Therefore, wearable long-term ECG applications have generally employed dry flexible contact electrodes that rely on perspiration built on the surface of the skin to facilitate electrical conduction [39, 93].

3.2.2 A single-time-constant model of the skin-electrode interface for contact electrodes

Fig. 3.9 shows the general form of the single-time-constant skin-electrode model for contact electrodes which represents the impedance of the electrode with a resistor, R_e, in parallel with a capacitor, C_e, while the lumped resistance of the skin and body tissue is simulated by a resistor, R_s. However, because of its relatively low value, R_s is often omitted. The electrode polarisation potential is modelled with a dc voltage source, V_{DC}.

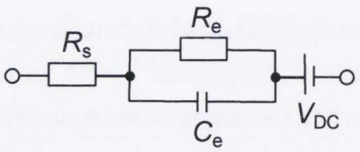

Figure 3.9: A standard single-time-constant representation of the skin-electrode interface. The half-cell potential, V_{DC}, introduces a dc offset but does not contribute to the ac impedance of the interface.

The parameter values stipulated in international standards issued by both IEC and ANSI are R_e =0.62 MΩ and C_e=4.7 nF [82, 98–102, 104, 105]. In all standards, including the most recent documents dating from 2009 [98–100], it is stated that the skin-electrode impedance in series with any patient-electrode connection must not result in a signal reduction of more than 6% of that obtained without the simulated impedance. The standards specify that the preamplifier must provide an input impedance of at least 10 MΩ at 10 Hz, since the magnitude of the simulated source impedance would be equal to 0.6 MΩ at this frequency [102]. In addition, a low-frequency cutoff at 0.05 Hz or lower must be achieved by the amplifier, with the simulated skin-electrode impedance disconnected. Given R_{in} = 10 MΩ, an input capacitance C_{in} = 0.33 μF is required to implement a 0.05-Hz single-pole high-pass filter at the amplifier input. It must be noted, however, that the input impedance specification does not take into account phase response, impulse response or attenuation below 10 Hz.

In 2004, considering the amplitude and phase criteria recommended by the AHA [110], the relationship between input impedance requirement and source impedance was analytically studied by Valverde et al [25] who suggested that for frequencies below 100 Hz, the interface can be approximated by the electrode resistance, R_e. It was concluded that an amplifier having a low-frequency input impedance $R_{in} > 17R_e$ would not cause more than 6% attenuation at 0.14 Hz nor introduce a phase shift of greater than 6° at 0.5 Hz. Based on electrode resistance R_e = 150 kΩ, R_{in} was estimated at 2.4 MΩ at 0.14 Hz and the dc-blocking capacitor was chosen as C_{in} = 2.2 μF.

In 2000, Burke & Gleeson [34, 35] estimated the component values of the skin-electrode

interface as R_s = 10 kΩ, R_e = 1.4 MΩ and C_e= 20 nF. The preamplifier front-end was designed so that its input impedance would be significantly larger than that of the skin-electrode impedance to minimise interference caused by motion artefact and unwanted common-mode voltages. It was reported that the attenuation caused by R_s is limited to 1% for $R_{in} > 100R_s$ and the phase shift introduced by R_e and C_e is kept below 1° in the bandwidth of the ECG signal for $R_{in} > 60R_e$. The designed low-power preamplifier achieved an input impedance of 260 MΩ and was coupled with a 1 μF dc-blocking capacitor.

Emphasis must be placed on the fact that input impedance requirements have not traditionally included impulse response criteria. The author has therefore evaluated the performance of simulated high-pass filters based on the models outlined above to assess whether or not amplitude, phase and impulse response criteria would be simultaneously met when the electrode impedance is taken into account. A program was written in MATLAB to determine and plot the low-frequency response of the skin-electrode-amplifier networks based on the provided skin-electrode model and the amplifier's front-end design. Plots of the simulated amplitude, phase and impulse responses, together with the recovery slope are shown in Fig. 3.10. Results are compared with the response of a 0.05-Hz single-pole high-pass filter equivalent to the amplifier operating with a dc-blocking capacitor but omitting the skin-electrode impedance, as previously discussed in Section 3.1.3. A summary is given in Table 3.1.

Table 3.1: Low-frequency performance of simulated skin-electrode-amplifier networks compared to that of a single-pole 0.05-Hz high-pass filter. Bold case indicates that performance requirement is not met.

	max. magitude 0.14-30 Hz [dB]	phase @ 0.5 Hz [°]	max. undershoot after impulse [mV]	max. slope [mVs^{-1}]
specification limit	-0.5	6	-0.1	0.3
0.5-Hz single-pole high-pass filter	-0.5	5.8	-0.093	0.03
IEC minimum input impedance requirements	**−0.96**	5.3	**−0.25**	**53.6**
solution proposed by Valverde et al	-0.5	4.1	**−0.11**	**0.49**
solution proposed by Burke & Gleeson	-0.05	0.1	-0.02	**0.55**

Columns 2 and 3 indicate the maximum attenuation in the frequency range 0.14 to 30 Hz and the phase shift at 0.5 Hz, respectively. Plots of the frequency response are presented in Figs. 3.10(a) and 3.10(b), which suggest that the amplitude and phase criteria would not be met if the IEC minimum input impedance requirement was applied with the electrodes used in international standards. It can be observed that the capacitive component of the simulated

skin-electrode introduces additional phase shift into the signal for frequencies above 10 Hz. However, these criteria are fulfilled in the case of designs suggested by Valverde et al. and Burke & Gleeson.

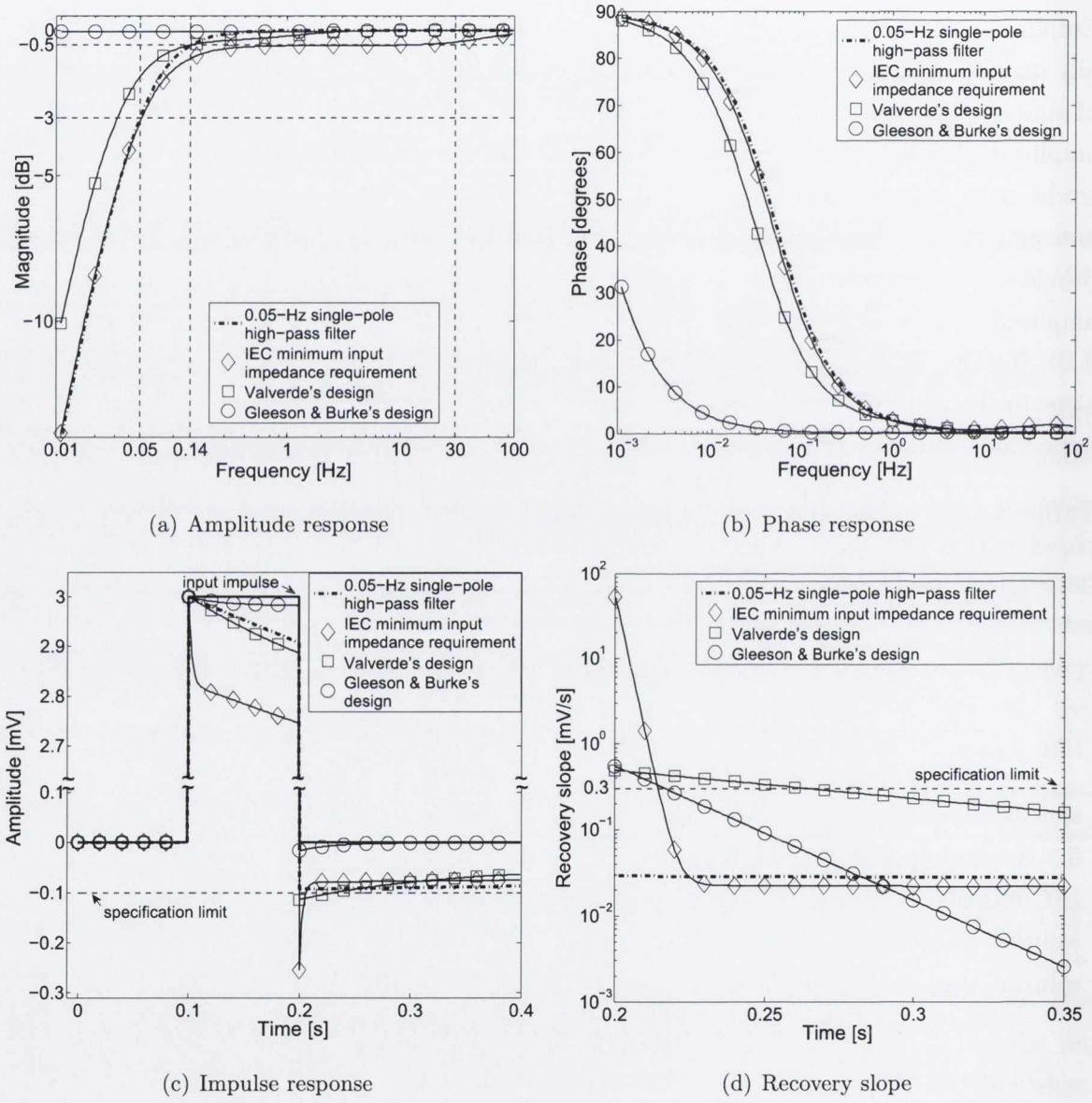

(a) Amplitude response

(b) Phase response

(c) Impulse response

(d) Recovery slope

Figure 3.10: Plots of (a) the amplitude response, (b) phase response, (c) impulse response and (d) recovery slope of the simulated skin-electrode-amplifier networks compared to that of a single-pole 0.05-Hz high-pass filter.

3.2.3 A double-time-constant model of the skin-electrode interface for dry contact electrodes

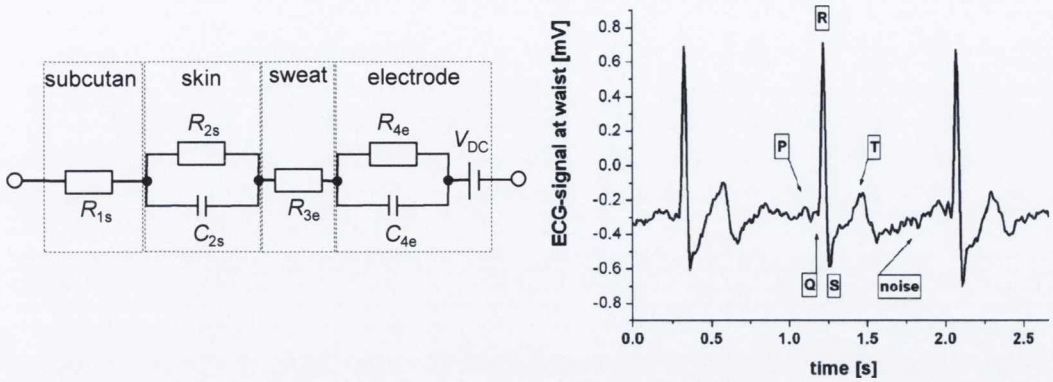

(a) A double-time-constant model equivalent to that presented in Section 2.2.3.

(b) Sample ECG recording with dry electrodes in equilibrium.

Figure 3.11: Figures showing (a) the equivalent electrical representation of the skin-electrode assumed by Mühlsteff et al and (b) a sample ECG recording (from [39]).

Using the double-time-constant model depicted in Fig. 3.11(a), Mühlsteff et al. investigated in 2004 the complex impedance of the skin-electrode interface of silicone rubber dry electrodes [39]. Measurements, taken in the frequency range 0.1 to 1000 Hz indicated that the ac behaviour of the skin-electrode contact interface is not accurately simulated by a single parallel RC-model. They proposed a double RC model with parameter values in equilibrium estimated as: $R_{1s}+R_{3e} = 8\,\text{k}\Omega$, $R_{2s} = 140\,\text{k}\Omega$, $C_{2s} = 3\mu\text{F}$, $R_{4e} = 150\text{k}\Omega$ and $C_{4e} = 180\,\text{nF}$. An instrumentation amplifier having 10 MΩ input impedance was then used by Mühlsteff et al. for recording the ECG shown in Fig. 3.11(b). The record clearly displays the QRS complex and the T wave. The P wave can also be identified despite its low amplitude. However, it can be observed that the baseline is not horizontal, especially immediately following abrupt voltage variations associated with the QRS complex and the T wave. Such effects can be attributed to low-frequency distortion similar to that reported by Tayler & Vincent [45].

The author has investigated the origin of the observed distortion by reproducing the low-frequency response of the dry-electrode design suggested Mühlsteff et al. Several different input capacitance values available in non-electrolytic form were used, ranging from 0.33 to 3.3 μF. Given $R_{\text{in}} = 10\,\text{M}\Omega$, the 3-dB point of the simulated high-pass filters varies between 0.05 and 0.005 Hz, and therefore meets AHA recommendations. This allows assessment of whether or not the low-frequency distortion suspected on the ECG recording of Fig. 3.11(b) might be caused by a degradation of the frequency response due to the presence of the double-time-constant skin-electrode interface.

Table 3.2: Low-frequency performance of simulated transfer functions based on the design model by Mühlsteff et al. compared to that of a single-pole 0.05-Hz high-pass filter: $R_{in} = 10$ MΩ, $R_{1s} + R_{3e} = 8$ kΩ, $R_{2s} = 140$ kΩ, $C_{2s} = 3$ μF, $C_{4e} = 0.18$ μF. Bold case indicates that the requirement is not met.

	max. magnitude 0.14-30 Hz [dB]	phase @ 0.5 Hz [°]	max. undershoot after impulse [mV]	max. slope [mVs^{-1}]
specification limit	-0.5	6	-0.1	0.3
0.5-Hz single-pole high-pass filter	-0.5	5.8	-0.093	0.03
C_{in}=0.33 μF	**−0.72**	5.9	**−0.14**	**1.68**
C_{in}=0.47 μF	-0.49	4.3	**−0.11**	**1.65**
C_{in}=1 μF	-0.29	2.3	-0.08	**1.63**
C_{in}=2.2 μF	-0.25	1.3	-0.07	**1.62**
C_{in}=3.3 μF	-0.25	1	-0.06	**1.62**

Results are presented in Fig. 3.12 and Table 3.2. Results from the simulated skin-electrode-amplifier network using the double-time-constant model indicate that for $R_{in} = 10$ MΩ, a cutoff frequency of about 0.03 Hz or lower is needed to fulfil both amplitude and phase requirements ($C_{in} \geq 0.47$ μF). It suggests that the presence of the modelled skin-electrode interface impedance has increased the effective 3-dB point of the skin-electrode-amplifier network. However, this increase alone cannot explain the level of distortion observed on the ECG of Fig. 3.11(b). Frequency response plots shown in Figs. 3.12(a) and 3.12(b) suggest that the amplitude and phase response would remain very close to that of a 0.05-Hz single-pole high-pass filter if C_{in} was equal to 0.33 μF.

Fig. 3.12(c) gives plots of the systems' response to a 3-mV pulse of 100-ms duration. As R_{in} remains constant, the offset following the input impulse is less than 0.1 mV for $C_{in} \geq 1$ μF, suggesting that in the presence of the skin-electrode impedance defined above, a lower 3-dB point of about 16 mHz is needed to meet the requirement of maximum undershoot. Fig. 3.12(d) is a graph of the recovery slope after the 300-mVs input impulse. The maximum slope of the response immediately after the impulse is about 1.6 mVs^{-1}, five times the allowed limit, and shows little variation when C_{in} is increased from 0.33 μF to 3.3 μF. In comparison, the recovery slope exhibited by a 0.05 Hz high-pass filter is not greater than 0.03 mVs^{-1}. Consequently, the slope of the impulse response is not satisfactory for the range of input capacitances simulated. Excessively high recovery slope therefore explains why the baseline of the ECG recording of Fig. 3.11(b) is not horizontal, immediately following abrupt voltage variations.

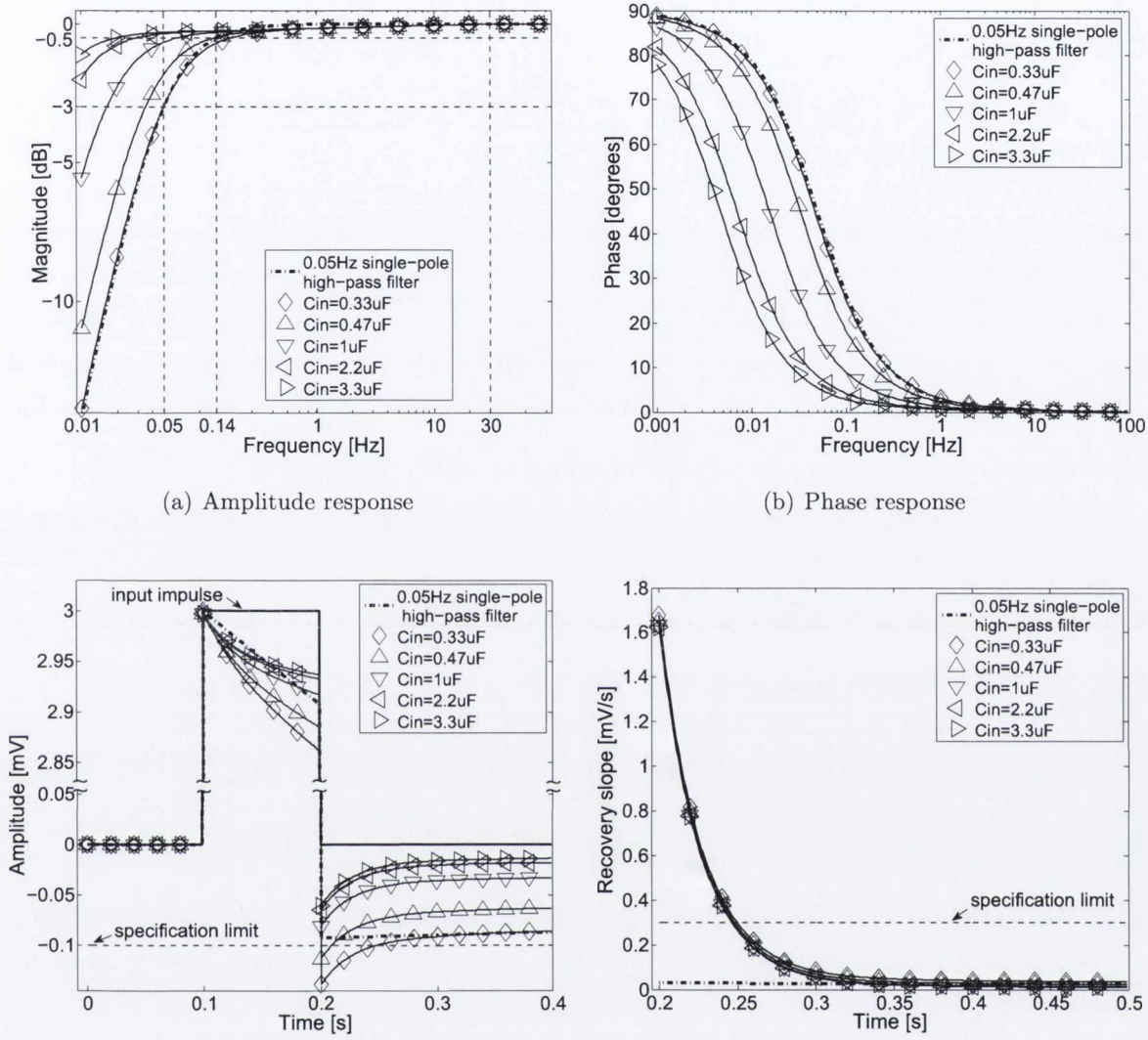

(a) Amplitude response

(b) Phase response

(c) Impulse response

(d) Recovery slope

Figure 3.12: Plots of (a) the amplitude response, (b) phase response, (c) impulse response and (d) recovery slope of simulated transfer functions based on the design suggested by Mühlsteff et al. compared to that of a 0.05-Hz single-pole high-pass filter.

These results confirm that amplitude and phase requirements provide necessary conditions for the reproduction of low-frequency components of the ECG but they are not sufficient to prevent distortion and possible clinical misinterpretation of the waveform.

3.2.4 Discussion

Simulation results have shown that the input impedance specification stated in international standards is not consistent with the accompanying low-frequency performance requirements. In addition, despite fulfilling both amplitude and phase criteria, some designs may fall short of meeting the impulse response requirements when the skin-electrode impedance is taken into account for dry-electrode recording. For the range of input capacitance values used, simulations based on the double-time-constant skin-electrode model indicate that the recovery slope is not significantly affected by a change of C_{in}. This can be explained by the presence of capacitive elements as small as 0.18 μF in the skin-electrode interface. The reactance of the electrode impedance is therefore considerably greater than that of C_{in} and dominates the reactance of the skin-electrode-amplifier network. It can therefore be concluded that:

1. Impulse response considerations must be included as an inherent part of the design strategy of new dry-electrode preamplifiers.

2. A complete characterisation of the skin-electrode interface is fundamental for the appropriate design of the amplifier front-end.

3. Meeting the impulse response specifications implies tighter requirements than compliance with the amplitude and phase criteria when the electrode impedance is taken into account.

4. The optimum values of R_{in} and C_{in} must be determined in relation to the parameter values of the skin-electrode interface so that all low-frequency requirements are simultaneously fulfilled.

3.3 New methods of characterisation of the skin-electrode interface

Previous studies have demonstrated that measurement of the dc skin-electrode impedance does not provide sufficient information. Because of the capacitive components, corresponding to the epidermal layer and the electrodes permittivity, ac measurement is needed to obtain an accurate estimate of the skin-electrode impedance [124]. The research group of which the author is a member has attempted to measure the resistive and capacitive properties of wet and dry electrodes using two experimental approaches, namely frequency-domain based and time-domain based measurement. Several identification algorithms were also considered by the group: an asymptotic method requiring only five points extracted from the frequency response and curve fitting based on least squares error minimisation algorithms.

3.3.1 Instrumentation set-up

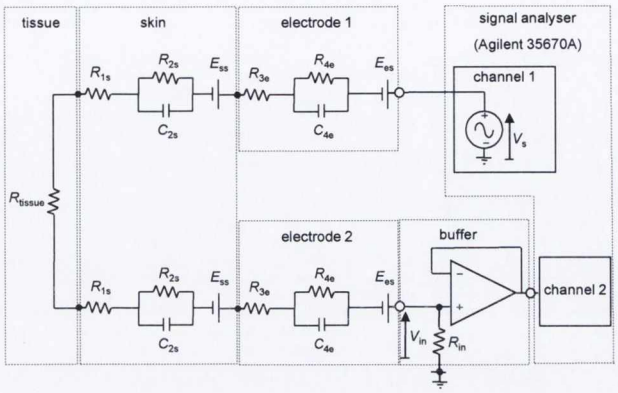

Figure 3.13: Schematic representation of the measurement set-up assuming a double-time-constant model.

Impedance spectroscopy is generally the method applied to characterise the skin-electrode interface in the frequency range 0.05 Hz to 1 MHz [19–39, 88, 124–134]. The measured impedance is then fitted to an equivalent electrical model to identify the resistive and capacitive elements of the interface. Fig. 3.13 shows the instrumentation set-up considered by the author for measuring the frequency response of the skin-electrode interface which consists of a dual electrode configuration connected to a resistive load, R_{in}. One electrode is fed with a sinusoidal voltage from a signal analyser (Agilent 35670A) and connected to the body. A second electrode is used to detect the resulting signal from the skin and feeds it to the input of the analyser. The selected signal analyser can generate sinusoidal signals in the frequency range 15 mHz to 51 kHz.

3.3.2 The proposed identification method

Fig. 3.14 shows the asymptotic bode diagram and the simulated frequency response of the interface based on the parameter values reported by Mühlsteff et al. ($R_{1\text{s}} + R_{3\text{e}} = 8$ kΩ, $R_{2\text{s}} = 140$ kΩ, $C_{2\text{s}} = 3$ μF, $R_{4\text{e}} = 150$ kΩ , $C_{4\text{e}} = 180$ nF and $R_{\text{in}} = 10$ MΩ) [39]. For the model provided, the phase response exhibits three local extrema at $f_1 = 0.45$ Hz, $f_2 = 1.40$ Hz and $f_3 = 5.26$ Hz. The author has published a novel method for the characterisation of the interface that relies upon knowledge of these three frequencies, and the attenuation introduced by the interface at low and high frequency.

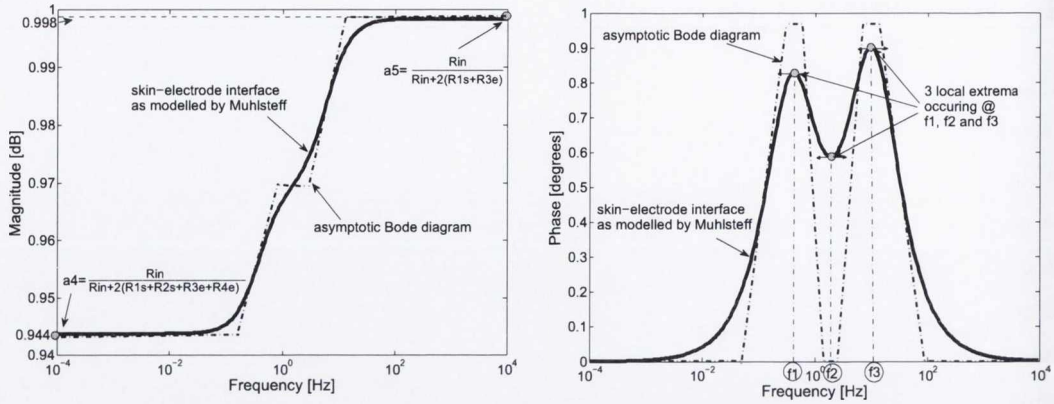

(a) Amplitude response

(b) Phase response

Figure 3.14: Plots of (a) the magnitude response and (b) the phase response of the skin-electrode interface as defined by Mühlsteff et al. for $R_{\text{in}} = 10\ \text{M}\Omega$.

Taking $\tau_{2\text{s}} = R_{2\text{s}}C_{2\text{s}}$ and $R_{4\text{e}} = R_{4\text{e}}C_{4\text{e}}$, the phase measured at the amplifier input and its first derivative with respect to the angular frequency ω are given in eqs. (3.17) and (3.18) as:

$$\varphi(\omega) = tan^{-1}\left(\frac{\omega\frac{R_{2\text{s}}\tau_{2\text{s}}+R_{4\text{e}}R_{4\text{e}}}{R_{\text{in}}+2(R_{1\text{s}}+R_{2\text{s}}+R_{3\text{e}}+R_{4\text{e}})} + \omega^3\tau_{2\text{s}}R_{4\text{e}}\frac{R_{4\text{e}}\tau_2+R_{2\text{s}}R_{4\text{e}}}{R_{\text{in}}+2(R_{1\text{s}}+R_{2\text{s}}+R_{3\text{e}}+R_{4\text{e}})}}{1+\omega^2\frac{\tau_{2\text{s}}^2[R_{\text{in}}+2(R_{1\text{s}}+R_{3\text{e}}+R_{4\text{e}})]+R_{4\text{e}}^2[R_{\text{in}}+2(R_{1\text{s}}+R_{3\text{e}}+R_{4\text{e}})]}{R_{\text{in}}+2(R_{1\text{s}}+R_{2\text{s}}+R_{3\text{e}}+R_{4\text{e}})} + \omega^4\frac{[R_{\text{in}}+2(R_{1\text{s}}+R_{3\text{e}})]\tau_{2\text{s}}^2R_{4\text{e}}^2}{R_{\text{in}}+2(R_{1\text{s}}+R_{2\text{s}}+R_{3\text{e}}+R_{4\text{e}})}}\right) \tag{3.17}$$

$$\begin{aligned}&\frac{d\varphi(\omega)}{d\omega}\\ &= \frac{1+a_1\omega^2+a_2\omega^4+a_3\omega^6}{\left[1+\left[\frac{\tau_{2\text{s}}^2[R_{\text{in}}+2(R_{1\text{s}}+R_{3\text{e}}+R_{4\text{e}})]+R_{4\text{e}}^2[R_{\text{in}}+2(R_{1\text{s}}+R_{2\text{s}}+R_{3\text{e}})]}{R_{\text{in}}+2(R_{1\text{s}}+R_{2\text{s}}+R_{3\text{e}}+R_{4\text{e}})}\right]\omega^2+\left[\frac{R_{\text{in}}+2(R_{1\text{s}}+R_{3\text{e}})}{R_{\text{in}}+2(R_{1\text{s}}+R_{2\text{s}}+R_{3\text{e}}+R_{4\text{e}})}\tau_{2\text{s}}^2R_{4\text{e}}^2\right]\omega^4\right]^2}\\ &\qquad + \left[\left[\frac{2R_{2\text{s}}\tau_{2\text{s}}+2R_{4\text{e}}R_{4\text{e}}}{R_{\text{in}}+2(R_{1\text{s}}+R_{2\text{s}}+R_{3\text{e}}+R_{4\text{e}})}\right]\omega+\left[\frac{2R_{2\text{s}}R_{4\text{e}}+2R_{4\text{e}}\tau_{2\text{s}}}{R_{\text{in}}+2(R_{1\text{s}}+R_{2\text{s}}+R_{3\text{e}}+R_{4\text{e}})}\tau_{2\text{s}}R_{4\text{e}}\right]\omega^3\right]^2\end{aligned} \tag{3.18}$$

where

$$\begin{aligned}a_1 = &\frac{3\left(R_{4\text{e}}\tau_{2\text{s}}+R_{2\text{s}}R_{4\text{e}}\right)\tau_{2\text{s}}R_{4\text{e}}}{R_{2\text{s}}\tau_{2\text{s}}+R_{4\text{e}}R_{4\text{e}}}\\ &-\frac{\tau_{2\text{s}}^2\left[R_{\text{in}}+2\left(R_{1\text{s}}+R_{3\text{e}}+R_{4\text{e}}\right)\right]+R_{4\text{e}}^2\left[R_{\text{in}}+2\left(R_{1\text{s}}+R_{2\text{s}}+R_{4\text{e}}\right)\right]}{R_{\text{in}}+2\left(R_{1\text{s}}+R_{2\text{s}}+R_{3\text{e}}+R_{4\text{e}}\right)}\end{aligned} \tag{3.19}$$

$$a_2 = \frac{\tau_{2s}R_{4e}\left[\tau_{2s}^2\left[R_{in}+2\left(R_{1s}+R_{3e}+R_{4e}\right)\right]+R_{4e}^2\left[R_{in}+2\left(R_{1s}+R_{2s}+R_{3e}\right)\right]\right]\left(\tau_{2s}R_{4e}+R_{4e}R_{2s}\right)}{\left[R_{in}+2\left(R_{1s}+R_{2s}+R_{3e}+R_{4e}\right)\right]\left(R_{2s}\tau_{2s}+R_{4e}R_{4e}\right)} - \frac{3\tau_{2s}^2R_{4e}^2\left[R_{in}+2\left(R_{1s}+R_{3e}\right)\right]}{R_{in}+2\left(R_{1s}+R_{2s}+R_{3e}+R_{4e}\right)} \quad (3.20)$$

$$a_3 = -\frac{\tau_{2s}^3R_{4e}^3\left[R_{in}+2\left(R_{1s}+R_{3e}+R_{4e}\right)\right]\left(R_{4e}\tau_{2s}+R_{2s}R_{4e}\right)}{\left[R_{in}+2\left(R_{1s}+R_{2s}+R_{3e}+R_{4e}\right)\right]\left(R_{2s}\tau_{2s}+R_{4e}R_{4e}\right)} \quad (3.21)$$

The three frequencies f_1, f_2 and f_3 identified in Fig. 3.14(b) are associated with three angular frequencies $\omega_1 = 2\pi f_1$, $\omega_2 = 2\pi f_2$ and $\omega_3 = 2\pi f_3$ that correspond to the positive and real solutions of $\frac{d\varphi(\omega)}{d\omega} = 0$. The following system of equations is then obtained:

$$\begin{cases} 1 + a_1\omega_1^2 + a_2\omega_1^4 + a_3\omega_1^6 = 0 & (3.22) \\ 1 + a_1\omega_2^2 + a_2\omega_2^4 + a_3\omega_2^6 = 0 & (3.23) \\ 1 + a_1\omega_3^2 + a_2\omega_3^4 + a_3\omega_3^6 = 0 & (3.24) \end{cases}$$

It can be shown that the system defined in eqs. (3.22) to (3.24) can be rearranged to give the coefficients as:

$$\begin{cases} a_1 = -\dfrac{1}{\omega_1^2} - \dfrac{1}{\omega_2^2} - \dfrac{1}{\omega_3^2} & (3.25) \\ a_2 = \dfrac{\omega_1^2+\omega_2^2+\omega_3^2}{\omega_1^2\omega_2^2\omega_3^2} & (3.26) \\ a_3 = -\dfrac{1}{\omega_1^2\omega_2^2\omega_3^2} & (3.27) \end{cases}$$

In addition, the magnitude response shown in Fig. 3.14(a) exhibits two asymptotes at low and high frequency corresponding to:

$$a_4 = \lim_{\omega\to 0}\left|\frac{V_{in}(\omega)}{V_s(\omega)}\right| = \frac{R_{in}}{R_{in}+2\left(R_{1s}+R_{2s}+R_{3e}+R_{4e}\right)} \quad (3.28)$$

and

$$a_5 = \lim_{\omega\to \infty}\left|\frac{V_{in}(\omega)}{V_s(\omega)}\right| = \frac{R_{in}}{R_{in}+2\left(R_{1s}+R_{3e}\right)} \quad (3.29)$$

It can be noted that the magnitude response reaches more than 99.99% of its asymptotic values at 15 mHz and 1 kHz, giving good estimates of a_4 and a_5. The coefficients defined in eqs. (3.25) to (3.29) provide sufficient information for the identification of $q = \tau_{2s}R_{4e}$ as the positive and real solution of the following polynomial equation:

$$-\frac{3a_3^2a_5^2}{a_4^2} - \frac{a_1a_3a_5}{a_4^2}q^2 + \frac{a_2}{a_4}q^4 + \frac{3}{a_5}q^6 = 0 \quad (3.30)$$

After solving eq. (3.30), the time constants are obtained from the positive solutions of the

following equation:

$$1 + \frac{(a_1 a_4 q^2 + 3a_3 a_5)(a_3 a_5 - a_4 q^3) a_5 - (a_4 - a_5) q^3 (a_4 q^3 + a_3 a_5) a_4}{a_4 (a_3 a_5^2 - a_4^2 q^3) q^4} \tau^2 + \frac{1}{q^2} \tau^4 = 0 \quad (3.31)$$

Two valid solutions are then available for τ. In previous literature the skin contribution is considered to be dominant, therefore the larger of the two solutions can be allocated to τ_{2s}, the second one being R_{4e}. Eqs. (3.25) to (3.31) are then utilised to determine the model parameters as:

$$R_{4e} = \frac{R_{in}}{2} \frac{(a_5 - a_4)(a_4 q^4 + a_5 a_3 \tau_{2s}^2)}{(a_3 a_5 - a_4 q^3) a_4 a_5 (\tau_{2s}^2 - q)} \quad (3.32)$$

$$R_{2s} = \frac{R_{in}}{2} \frac{(a_5 - a_4)}{a_4 a_5} - R_{4e} \quad (3.33)$$

$$C_{2s} = \frac{\tau_{2s}}{R_{2s}} \quad (3.34)$$

$$C_{4e} = \frac{q}{\tau_{2s} R_{4e}} \quad (3.35)$$

$$R_{1s} + R_{3e} = \frac{R_{in}}{2} \frac{(1 - a_5)}{a_5} \quad (3.36)$$

Only solutions that are real and positive are relevant for the purpose of parameter identification. For example, the five reference points indicated in the bode plot of Fig. 3.14 suggest the following coefficient values:

$$a_1 = -0.14 \mathrm{s}^2 \mathrm{rad}^{-2} \quad (3.37)$$

$$a_2 = 1.7 \mathrm{s}^2 \mathrm{rad}^{-2} \quad (3.38)$$

$$a_3 = -1.48 \mathrm{s}^2 \mathrm{rad}^{-2} \quad (3.39)$$

$$a_4 = 0.998 \quad (3.40)$$

$$a_5 = 0.944 \quad (3.41)$$

Applying theses values to eq. (3.30) yields:

$$-7.78 \text{ x } 10^{-12} - 2.30 \text{ x } 10^{-7} q^2 + 1.8 \text{ x } 10^{-3} q^4 + 3q^6 = 0 \quad (3.42)$$

Eq. (3.42) has a unique positive real solution at $q = \tau_{2s} R_{4e} = 0.0114 \text{ s}^2$. This value is then inserted into eq. (3.31) to solve the following equation:

$$1 - 1.39 \text{ x } 10^3 \tau^2 + 7.71 \text{ x } 10^3 \tau^4 = 0 \quad (3.43)$$

The two positive solutions are: $\tau_{2s} = 0.423$ s and $R_{4e} = 0.027$ s. Taking $R_{in} = 10$ MΩ, the

model parameters can then be deduced from eqs. (3.32) to (3.36) as:

$$R_{4e} \simeq 148 \text{ k}\Omega,\ R_{2s} \simeq 139 \text{ k}\Omega,\ C_{2s} \simeq 3 \text{ } \mu\text{F},\ C_{4e} \simeq 182 \text{ nF and } R_{1s} + R_{3e} \simeq 10 \text{ k}\Omega.$$

The small discrepancy observed between the estimated values and the simulated parameters is due to floating point approximation error in solving eqs. (3.30) and (3.31) and the limited precision with which a_4 and a_5 can be measured. The resolution method is described in more detail by the author in [50] and [52] and detailed derivations are given in Appendix A.

3.3.3 Measurement results

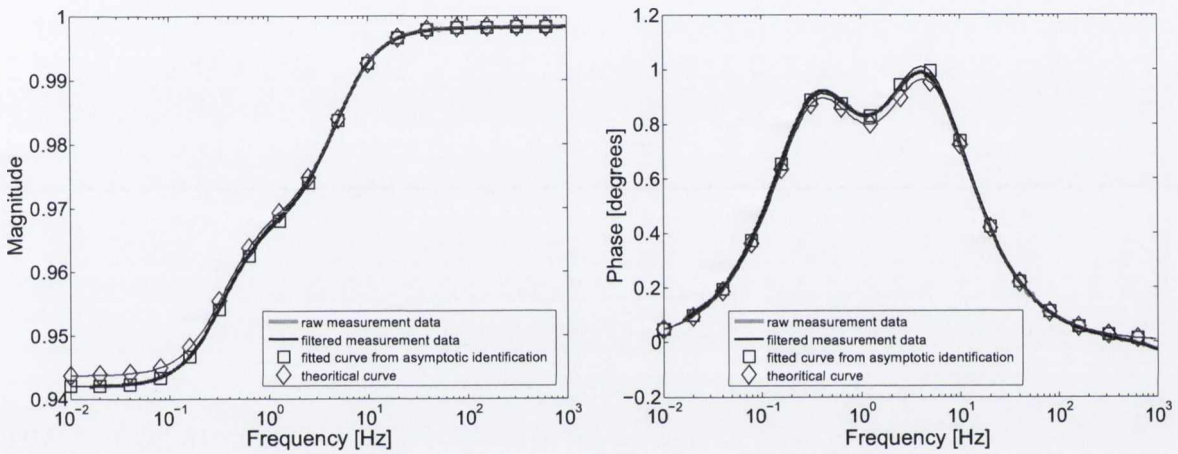

(a) Amplitude response

(b) Phase response

Figure 3.15: Comparison between the measured data ((a) magnitude and (b) phase) and data obtained as a result of the novel identification procedure for a constructed hardware model defined in Table 3.3.

A hardware model of the skin-electrode interface was constructed using actual resistors and capacitors, based on the model provided by Mühlsteff et al. to assess the ability of the signal analyser to reproduce the simulated results shown in Fig. 3.14. A pair of 3.3-μF and 220-nF multi-layer ceramic capacitors simulated the effects of C_{2s} and C_{4e}, respectively, the original capacitance values (3 μF and 180 nF) being unavailable. Fig. 3.15 compares the measurement of magnitude and phase to that obtained as a result of the new identification method. Raw measurement data are filtered to remove measurement noise and to facilitate the detection of the two peaks and the trough in the phase response. The frequency of the three local extrema in the phase response and the two extremum values in the magnitude response allow the five identification coefficients to be estimated and and the frequency response of the network to be simulated. A theoretical curve is included to assess the precision

of the measurement and the accuracy of the fitted model. The accuracy of the method can be appreciated from the results shown in Table 3.3, which suggest that if the skin-electrode interface in equilibrium behaves in a similar way as that measured by Mühlsteff et al., the proposed method would then provide a fast and accurate identification tool.

Table 3.3: Accuracy of the new identification method assessed from a constructed hardware model.

	actual component value	estimated value	% error
$R_{1s} + R_{3e}$ [kΩ]	8.20	8.47	+3.3 %
R_{2s} [kΩ]	140.00	141.21	+0.9%
R_{4e} [kΩ]	150.45	157.99	+5.1 %
C_{2s} [μF]	3.340	3.395	+1.6%
C_{4e} [μF]	0.219	0.218	-0.4 %

In 1988, Rosell et al. reported values of skin impedance ranging from 10 kΩ to 1 MΩ at 1 Hz when measured using standard Ag/AgCl electrodes [141]. The skin resistance value indicated in Table 3.3 is therefore in accordance with these previous measurements.
Two conductive silicon rubber dry electrodes of 2.56 cm in diameter (Pro Carbone, C5005PF) were connected to one another to estimate their dc impedance using an ohmmeter. Electrode resistance was measured at 4 kΩ, which is well under the value of 150 kΩ reported in [39]. This suggests that a speculative model that consists of a double-time-constant RC network for the skin and a lumped resistance for the electrode may be considered. In addition, as pointed out by Kaczmarek & Webster in 1989, an accurate model of the skin-electrode interface is likely to have time-varying parameters [87].

Fig. 3.16(a) shows sample phase characteristics of the skin-electrode interface using wet and dry electrodes measured on a female subject. It was observed that very often the phase response did not display two distinct peaks but only a single peak. This means that the polynomial $f(\omega) = 1 + a_1\omega^2 + a_2\omega^4 + a_3\omega^6$ has one real and positive root (ω_i), one real and negative root ($-\omega_i$) and four complex conjugate roots (ω_j, ω_j^*, $-\omega_j$ and $-\omega_j^*$). Similar results have been obtained from simulation when the time constant τ_{2s} and R_{4e} differ by less than one order of magnitude, as shown in Fig. 3.17.

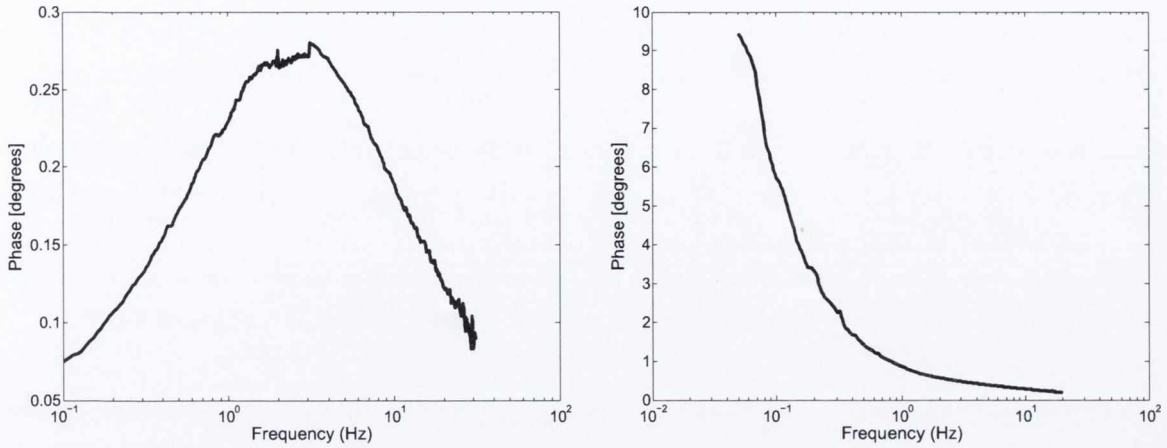

(a) wet electrodes (Wandy, E-50mm Hydrogel).

(b) dry electrodes (Wandy, E-45).

Figure 3.16: Typical phase response measurements obtained in vivo from (a) wet electrodes and (b) dry electrodes on the same subject (female, aged 26).

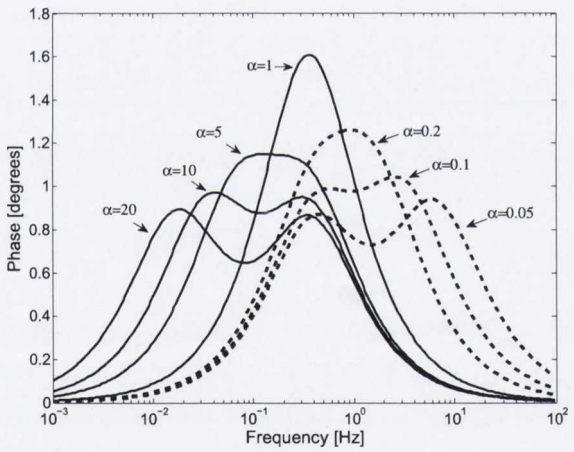

Figure 3.17: Plot of the phase against frequency for different values of the ratio $\alpha = \frac{\tau_{2s}}{R_{4e}}$ when $R_{in} = 10$ MΩ, $R_{1s} + R_{3e} = 8$ kΩ, $R_{2s} = 140$ kΩ and $R_{4e} = 150$ kΩ.

3.3.4 Alternative approaches

Alternative approaches have been investigated to solve the parameter estimation problem in situations where the phase response does not display the expected double-peak behaviour. Dozio and Baba considered different fitting algorithms and measurement set-ups and concluded that time-domain measurements combined with least squares error minimisation were the most appropriate [48, 49, 52, 83, 84].

Fitting magnitude and phase

Dozio et al. first developed a least squares error minimisation program for fitting both the magnitude and phase response [50, 52]. The algorithm successfully converged when applied to a pair of adhesive electrodes (Wandy, E-50mm Hydrogel) placed on the lower abdomen and returned the the following model parameters:

$$R_{1s} + R_{3e} = 3.6\ \text{k}\Omega,\ R_{2s} = 35.2\ \text{k}\Omega,\ C_{2s} = 0.9\ \mu\text{F},\ R_{4e} = 29.5\ \text{k}\Omega,\ C_{4e} = 5.8\ \mu\text{F}.$$

The experiment also confirmed that a simple 3-parameter model is not suitable for describing the skin-electrode impedance. The curve fitting algorithm did not however converge in the case of dry, pasteless electrodes (WANDY, W-45) for which the phase response exhibited no peak in the frequency range 0.05 to 30 Hz, as shown in Fig. 3.16(b). This was thought to be because the peak existed at a frequency below the minimum range of the analyser.

Time-based measurement

Frequency-based measurements have been unsuccessful when applied to dry electrodes since the characteristic frequencies are too low to allow reliable steady state measurement. To overcome this limitation time-based measurements have been developed. Baba et al. implemented a novel measurement technique that relies upon the time response of the skin-electrode interface to a current source [48, 52, 83, 84]. A constant current is fed through the body while measuring the skin-electrode impedance and a high frequency sine wave input current is used to determine $R_{1s} + R_{3e}$. The knowledge of $R_{1s} + R_{3e}$ reduces the complexity of the fitting procedure to only four parameters and improves the accuracy of the results. Measurements were taken on seven subjects, using seven different types of dry electrodes, under variable conditions of contact pressure, electrode settling time and current level. Dozio developed a curve fitting program for the time-based data acquired. The time-domain measurement procedure and the results obtained are discussed in detail in references [83] and [84].

Table 3.4 gives a summary of values for each component, measured across all subjects, electrodes, locations and contact pressures as published by Baba & Burke [83]. The identification of the skin-electrode interface model parameters from two hundred and sixty eight measurements returned values of resistance ranging from 23 kΩ to 1.85 MΩ and of capacitance ranging from 0.1 μF to 65 μF, while values of the time constants $\tau_{2s} = C_{2s}R_{2s}$ and $R_{4e} = C_{4e}R_{4e}$ varied from 0.02 s to 7.2 s. It was also discovered that there were substantial differences in the component values and the time constants between the rise and the fall phases in the step response of the skin-electrode interface. Worst-case parameter values obtained can now be used in the design of the input differential amplifier in ECG recording equipment to prevent low-frequency distortion of the ECG signal.

Table 3.4: Summary of parameter values published by Baba & Burke from 268 measurements [83].

	Current rise phase		Current fall phase	
	min.	max.	min.	max.
$R_{1s} + R_{3e}$ [kΩ]	0.64	12	0.64	12
R_{2s} [kΩ]	4.94	1760.24	23.87	2540.93
R_{4e} [kΩ]	23.26	1840.52	84.78	1380.00
C_{2s} [μF]	0.01	21.51	0.04	21.88
C_{4e} [μF]	0.10	432.35	0.69	65.15
$R_{1s} + R_{2s} + R_{3e} + R_{4e}$ [kΩ]	161.24	3616.83	125.82	3326.10
τ_{2s} [s]	0.02	1.84	0.06	1.17
R_{4e} [s]	0.18	31.29	0.77	7.19

3.4 New amplifier input impedance requirements for dry-electrode ECG recording

As seen in previous sections, the front-end amplifier plays a crucial role in the ability of the ECG recorder to preserve the low-frequency components of the signal. The low-frequency performance achieved by the amplifier in the presence of the electrode impedance is principally determined by the magnitude of the input impedance of the recording system. Fig. 2.9 shows the equivalent impedance seen at the amplifier input when the skin-electrode interface, the current limiting resistance and the dc-blocking capacitors are taken into account.

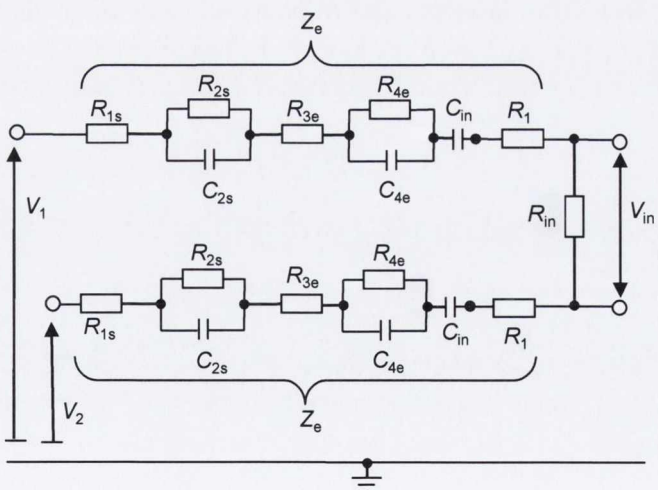

Figure 3.18: Schematic representation of the equivalent impedance seen at the amplifier input.

The transfer function of the skin-electrode-amplifier network in this configuration is defined as follows:

$$H_{\mathrm{d}}(s) = \frac{V_{\mathrm{in}}(s)}{V_1(s) - V_2(s)} = R_{\mathrm{in}} \frac{C_{\mathrm{in}}}{2} \left[\frac{\tau_{2\mathrm{s}} R_{4\mathrm{e}} s^3 + (\tau_{2\mathrm{s}} + R_{4\mathrm{e}})\, s^2 + s}{d_3 s^3 + d_2 s^2 + d_1 s + 1} \right] \tag{3.44}$$

where:

$$d_1 = \left[R_{\mathrm{in}} + 2\left(R_1 + R_{1\mathrm{s}} + R_{2\mathrm{s}} + R_{3\mathrm{e}} + R_{4\mathrm{e}}\right)\right] \frac{C_{\mathrm{in}}}{2} + \tau_{2\mathrm{s}} + R_{4\mathrm{e}} \tag{3.45}$$

$$d_2 = \left[\left[R_{\mathrm{in}} + 2\left(R_1 + R_{1\mathrm{s}} + R_{3\mathrm{e}}\right)\right](\tau_{2\mathrm{s}} + R_{4\mathrm{e}}) + 2R_{2\mathrm{s}}R_{4\mathrm{e}} + 2R_{4\mathrm{e}}\tau_{2\mathrm{s}}\right] \frac{C_{\mathrm{in}}}{2} + \tau_{2\mathrm{s}} R_{4\mathrm{e}} \tag{3.46}$$

$$d_3 = \left[R_{\mathrm{in}} + 2\left(R_1 + R_{1\mathrm{s}} + R_{3\mathrm{e}}\right)\right] \frac{C_{\mathrm{in}}}{2} \tau_{2\mathrm{s}} R_{4\mathrm{e}} \tag{3.47}$$

In the following sections, the author establishes new input impedance requirements for use in dry-electrode ECG recording.

3.4.1 Frequency response criteria

Amplitude response

The equivalent skin-electrode impedance, shown in Fig. 3.18, is responsible for a reduction in the signal amplitude before reaching the amplifier input. Minimum attenuation is obtained at high frequencies for which the impedance of capacitive elements in the electrode impedance tends toward zero, ensuring:

$$|H_{\mathrm{d}}(\omega)| < \frac{R_{\mathrm{in}}}{R_{\mathrm{in}} + 2\left(R_1 + R_{1\mathrm{s}} + R_{3\mathrm{e}}\right)} < 1 \tag{3.48}$$

At low frequencies, the source impedance is given by:

$$Z_{\mathrm{e}}(\omega) = R_{1\mathrm{s}} + R_{3s} + \frac{R_{2\mathrm{s}}}{1 + j\omega R_{2\mathrm{s}} C_{2\mathrm{s}}} + \frac{R_{4\mathrm{e}}}{1 + j\omega R_{4\mathrm{e}} C_{4\mathrm{e}}} + \frac{1}{j\omega C_1} + R_1 \tag{3.49}$$

The AHA recommends a maximum attenuation of 0.5 dB (or 6%) at 0.14 Hz, which establishes the requirement:

$$\frac{R_{\mathrm{in}}}{\left|R_{\mathrm{in}} + 2Z_{\mathrm{e}}\left(\omega_{0.14}\right)\right|} > 0.94 \tag{3.50}$$

where $\omega_{0.14} = 0.28\pi$.

It can be shown that the condition specified in eq. (3.50) implies the following relationship

between R_{in} and the parameters of the skin-electrode interface:

$$R_{\text{in}}^2\frac{1-0.94^2}{0.94^2}-4R_{\text{in}}\left[R_1+R_{1\text{s}}+R_{3\text{e}}+\frac{R_{2\text{s}}}{1+\tau_{2\text{s}}^2\omega_{0.14}^2}+\frac{R_{4\text{e}}}{1+R_{4\text{e}}^2\omega_{0.14}^2}\right]$$
$$-4\left[R_1+R_{1\text{s}}+R_{3\text{e}}+\frac{R_{2\text{s}}\tau_{2\text{s}}\omega_{0.14}}{1+\tau_{2\text{s}}^2\omega_{0.14}^2}+\frac{R_{4\text{e}}R_{4\text{e}}\omega_{0.14}}{1+R_{4\text{e}}^2\omega_{0.14}^2}+\frac{1}{\omega_{0.14}C_{\text{in}}}\right]^2$$
$$-4\left[R_1+R_{1\text{s}}+R_{3\text{e}}+\frac{R_{2\text{s}}}{1+\tau_{2\text{s}}^2\omega_{0.14}^2}+\frac{R_{4\text{e}}}{1+R_{4\text{e}}^2\omega_{0.14}^2}\right]^2>0 \quad (3.51)$$

The amplitude response criterion is then fulfilled for R_{in} selected as follows:

$$R_{\text{in}}>\frac{2*0.94^2}{1-0.94^2}\sqrt{\begin{array}{l}\left(R_1+R_{1\text{s}}+R_{3\text{e}}+\frac{R_{2\text{s}}}{1+\tau_{2\text{s}}^2\omega_{0.14}^2}+\frac{R_{4\text{e}}}{1+R_{4\text{e}}^2\omega_{0.14}^2}\right)^2\\+(1-0.94^2)\left(R_1+R_{1\text{s}}+R_{3\text{e}}+\frac{R_{2\text{s}}\tau_{2\text{s}}\omega_{0.14}}{1+\tau_{2\text{s}}^2\omega_{0.14}^2}+\frac{R_{4\text{e}}R_{4\text{e}}\omega_{0.14}}{1+R_{4\text{e}}^2\omega_{0.14}^2}+\frac{1}{\omega_{0.14}C_{\text{in}}}\right)^2\\+\frac{2*0.94^2}{1-0.94^2}\left(R_1+R_{1\text{s}}+R_{3\text{e}}+\frac{R_{2\text{s}}}{1+\tau_{2\text{s}}^2\omega_{0.14}^2}+\frac{R_{4\text{e}}}{1+R_{4\text{e}}^2\omega_{0.14}^2}\right)\end{array}} \quad (3.52)$$

Phase response

The transfer function defined in eq. (3.44) can be rearranged so that real and imaginary parts are more easily identified:

$$H_{\text{d}}(\omega)=R_{\text{in}}\frac{C_{\text{in}}}{2}\left[\frac{\begin{array}{l}\left[(d_1-\tau_{2\text{s}}-R_{4\text{e}})\,\omega^2+\left[d_2\left(\tau_{2\text{s}}+R_{4\text{e}}\right)-d_3\right]\omega^4+d_1d_3\tau_{2\text{s}}R_{4\text{e}}\omega^6\right]\\+j\left[\omega+\left(d_1\tau_{2\text{s}}+d_1R_{4\text{e}}-\tau_{2\text{s}}R_{4\text{e}}\right)\omega^3+\left[d_2\tau_{2\text{s}}R_{4\text{e}}-d_3\left(\tau_{2\text{s}}+R_{4\text{e}}\right)\right]\omega^5\right]\end{array}}{\left(1-d_2\omega^2\right)^2+\left(d_1\omega-d_3\omega^3\right)^2}\right] \quad (3.53)$$

Replacing d_1, d_2 and d_3 by their expressions as given in eq.(3.45) to (3.47) yields the following:

$$H_{\text{d}}(\omega)=R_{\text{in}}\frac{C_{\text{in}}}{2}\omega\left[\frac{\begin{array}{l}R_T\frac{C_{\text{in}}}{2}\omega+\left[R_T\frac{C_{\text{in}}}{2}\left(\tau_{2\text{s}}^2+R_{4\text{e}}^2\right)+2\tau_{2\text{s}}R_{4\text{e}}\left(R_{2\text{s}}+R_{4\text{e}}\right)\frac{C_{\text{in}}}{2}\right]\omega^3\\+R_{13}\frac{C_{\text{in}}}{2}\tau_{2\text{s}}^2R_{4\text{e}}^2\omega^5\\+j[1+\left[2\left(R_{2\text{s}}\tau_{2\text{s}}+R_{4\text{e}}R_{4\text{e}}\right)\frac{C_{\text{in}}}{2}+\tau_{2\text{s}}^2+\tau_{4s}^2\right]\omega^2]\\+j[\tau_{2\text{s}}R_{4\text{e}}\left[2\left(R_{2\text{s}}R_{4\text{e}}+R_{4\text{e}}\tau_{2\text{s}}\right)\frac{C_{\text{in}}}{2}+\tau_{2\text{s}}R_{4\text{e}}\right]\omega^4]\end{array}}{\begin{array}{l}\left[1-\left[\left[R_{13}\left(\tau_{2\text{s}}+R_{4\text{e}}\right)+2R_{2\text{s}}R_{4\text{e}}+2R_{4\text{e}}\tau_{2\text{s}}\right]\frac{C_{\text{in}}}{2}+\tau_{2\text{s}}R_{4\text{e}}\right]\omega^2\right]^2\\+\left[\left(R_T\frac{C_{\text{in}}}{2}+\tau_{2\text{s}}+R_{4\text{e}}\right)\omega-R_{13}\frac{C_{\text{in}}}{2}\tau_{2\text{s}}R_{4\text{e}}\omega^3\right]^2\end{array}}\right] \quad (3.54)$$

where

$$R_{\text{T}}=R_{\text{in}}+2\left(R_1+R_{1\text{s}}+R_{2\text{s}}+R_{3\text{e}}+R_{4\text{e}}\right) \quad (3.55)$$

and

$$R_{13} = R_{\text{in}} + 2\left(R_1 + R_{1\text{s}} + R_{3\text{e}}\right) \tag{3.56}$$

Since both imaginary and real parts of $H_{\text{d}}(\omega)$ are positive, an expression for the phase response can then be extracted from (3.54) as:

$$\varphi_{\text{d}}(\omega) = tan^{-1}\left(\frac{1 + \left[\left(R_{2\text{s}}\tau_{2\text{s}} + R_{4\text{e}}R_{4\text{e}}\right)C_{\text{in}} + \tau_{2\text{s}}^2 + \tau_{4s}^2\right]\omega^2 + \tau_{2\text{s}}R_{4\text{e}}\left[\left(R_{2\text{s}}R_{4\text{e}} + R_{4\text{e}}\tau_{2\text{s}}\right)C_{\text{in}} + \tau_{2\text{s}}R_{4\text{e}}\right]\omega^4}{R_T\frac{C_{\text{in}}}{2}\omega + \left[R_T\frac{C_{\text{in}}}{2}\left(\tau_{2\text{s}}^2 + R_{4\text{e}}^2\right) + \tau_{2\text{s}}R_{4\text{e}}\left(R_{2\text{s}} + R_{4\text{e}}\right)C_{\text{in}}\right]\omega^3 + R_{13}\frac{C_{\text{in}}}{2}\tau_{2\text{s}}^2R_{4\text{e}}^2\omega^5}\right) \tag{3.57}$$

Eq. (3.57) indicates that all positive frequencies:

$$0 < \varphi_{\text{d}}(\omega) < 90^\circ \ , \ \forall\omega \in \Re^{+*} \tag{3.58}$$

The phase introduced by a single-pole high-pass filter having a cutoff frequency f_{c} is given by:

$$\Phi(\omega) = tan^{-1}\left(\frac{2\pi f_{\text{c}}}{\omega}\right) \tag{3.59}$$

The AHA recommends that the amplifier should introduce no more phase shift into the signal than that which would be introduced by a linear 0.05-Hz, single-pole filter. This condition is respected for $\varphi(\omega) < \Phi(\omega)$, therefore :

$$\tan^{-1}\left(\frac{1 + \left[\left(R_{2\text{s}}\tau_{2\text{s}} + R_{4\text{e}}R_{4\text{e}}\right)C_{\text{in}} + \tau_{2\text{s}}^2 + \tau_{4s}^2\right]\omega^2 + \tau_{2\text{s}}R_{4\text{e}}\left[\left(R_{2\text{s}}R_{4\text{e}} + R_{4\text{e}}\tau_{2\text{s}}\right)C_{\text{in}} + \tau_{2\text{s}}R_{4\text{e}}\right]\omega^4}{R_T\frac{C_{\text{in}}}{2}\omega + \left[R_T\frac{C_{\text{in}}}{2}\left(\tau_{2\text{s}}^2 + R_{4\text{e}}^2\right) + \tau_{2\text{s}}R_{4\text{e}}\left(R_{2\text{s}} + R_{4\text{e}}\right)C_{\text{in}}\right]\omega^3 + R_{13}\frac{C_{\text{in}}}{2}\tau_{2\text{s}}^2R_{4\text{e}}^2\omega^5}\right) < \tan^{-1}\left(\frac{2\pi f_{\text{c}}}{\omega}\right) \tag{3.60}$$

Both phase shifts belong to the interval $]0, \frac{\pi}{2}[$, in which the function tan is strictly increasing. The condition specified in eq. (3.60) is therefore equivalent to:

$$\frac{1 + \left[\left(R_{2\text{s}}\tau_{2\text{s}} + R_{4\text{e}}R_{4\text{e}}\right)C_{\text{in}} + \tau_{2\text{s}}^2 + \tau_{4s}^2\right]\omega^2 + \tau_{2\text{s}}R_{4\text{e}}\left[\left(R_{2\text{s}}R_{4\text{e}} + R_{4\text{e}}\tau_{2\text{s}}\right)C_{\text{in}} + \tau_{2\text{s}}R_{4\text{e}}\right]\omega^4}{R_T\frac{C_{\text{in}}}{2}\omega + \left[R_T\frac{C_{\text{in}}}{2}\left(\tau_{2\text{s}}^2 + R_{4\text{e}}^2\right) + \tau_{2\text{s}}R_{4\text{e}}\left(R_{2\text{s}} + R_{4\text{e}}\right)C_{\text{in}}\right]\omega^3 + R_{13}\frac{C_{\text{in}}}{2}\tau_{2\text{s}}^2R_{4\text{e}}^2\omega^5} < \frac{2\pi f_{\text{c}}}{\omega} \tag{3.61}$$

Taking $\omega_c = 2\pi f_c$, the phase criterion is met for:

$$\left[\omega_c R_{13}\frac{C_{in}}{2}\tau_{2s}^2 R_{4e}^2 - \tau_{2s}R_{4e}\left[\left(R_{2s}R_{4e} + R_{4e}\tau_{2s}\right)C_{in} + \tau_{2s}R_{4e}\right]\right]\omega^4$$
$$+\left[\omega_c\left[R_T\frac{C_{in}}{2}\left(\tau_{2s}^2 + R_{4e}^2\right) + \tau_{2s}R_{4e}\left(R_{2s} + R_{4e}\right)C_{in}\right] - \left[\left(R_{2s}\tau_{2s} + R_{4e}R_{4e}\right)C_{in} + \tau_{2s}^2 + \tau_{4s}^2\right]\right]\omega^2$$
$$+\omega_c R_T\frac{C_{in}}{2} - 1 > 0 \quad (3.62)$$

The polynomial function of eq. (3.62) is positive when two conditions are satisfied: (i) the coefficient of the highest power of ω is positive and (ii) there is no positive root. All roots must therefore be negative or complex. Both conditions are simultaneously met when:

$$\begin{cases} \omega_c R_{13}\dfrac{C_{in}}{2}\tau_{2s}^2 R_{4e}^2 - \tau_{2s}R_{4e}\left[\left(R_{2s}R_{4e} + R_{4e}\tau_{2s}\right)C_{in} + \tau_{2s}R_{4e}\right] > 0 & (3.63) \\ \omega_c R_T\dfrac{C_{in}}{2} - 1 > 0 & (3.64) \end{cases}$$

Substituting $\tau_{2s} = R_{2s}C_{2s}$, $R_{4e} = R_{4e}C_{4e}$, $R_{13} = R_{in} + 2\left(R_1 + R_{1s} + R_{3e}\right)$ and $R_T = R_{13} + 2\left(R_{2s} + R_{4e}\right)$, eqs. (3.63) and (3.64) become:

$$\begin{cases} R_{in} > \dfrac{2}{\omega_c}\left(\dfrac{1}{C_{2s}} + \dfrac{1}{C_{4e}} + \dfrac{1}{C_{in}}\right) - 2\left(R_1 + R_{1s} + R_{3e}\right) & (3.65) \\ R_{in} > \dfrac{2}{C_{in}\omega_c} - 2\left(R_1 + R_{1s} + R_{2s} + R_{3e} + R_{4e}\right) & (3.66) \end{cases}$$

Eq. (3.66) establishes the phase criterion at low frequency, when the reactance of the capacitive effects in the skin-electrode interface tends towards infinity. At these frequencies C_{2s} and C_{4e} are equivalent to open switches making the skin-electrode impedance purely resistive. Phase shift is therefore solely introduced by the input capacitance C_{in}. This result is consistent with traditional design strategies which state that low-frequency distortion can be prevented if $R_{in}C_{in} > 1/\omega_c$, since other capacitive effects are neglected [25, 127].
As frequency increases, the effects of C_{2s} and C_{4e} must be considered and eq. (3.65) ensures that the phase of the combined skin-electrode-amplifier network will not be greater than that introduced by a high-pass filter having a single pole at $f_c = \omega_c/2\pi$. As seen in Section 3.2.1, the effect of changing skin impedance have be minimised by making the coupling capacitance of insulating electrodes at least two orders of magnitude smaller than those of the skin. Coupling capacitance values ranging from 50 nF to 1 fF have thus been used with buffer amplifiers having 10^8 to 10^{18} Ω input impedance [128–133, 136–140]. Eq. (3.65) confirms that for $C_{in} << \{C_{2s}, C_{4e}\}$, the reactance of the skin-electrode interface can be neglected, and therefore selecting $R_{in}C_{in} > 1/\omega_c$ would prevent distortion. However, this approach involves the use of ultra-high input impedance amplifiers, whereas, the input impedance requirement can be relaxed if eq. (3.65) is applied instead.

With $f_c = 0.05$ Hz, the phase requirement is satisfied at all frequencies when the input impedance is chosen such that for the worst-case values of skin-electrode parameters:

$$R_{in} > \frac{20}{\pi}\left(\frac{1}{C_{2s}} + \frac{1}{C_{4e}} + \frac{1}{C_{in}}\right) \tag{3.67}$$

3.4.2 Impulse response requirements

In more recent years, the IEC have defined more precisely the low-frequency criteria for ECG signal reproduction in terms of the system impulse response. The response to a rectangular pulse $x(t)$ of amplitude V_m and duration T is limited to a maximum offset, ΔV_{max}, and a maximum slope, s_{max}. Fig. 3.19 shows in a generic form the impulse response requirement defined by the international standards reviewed in Chapter 2.

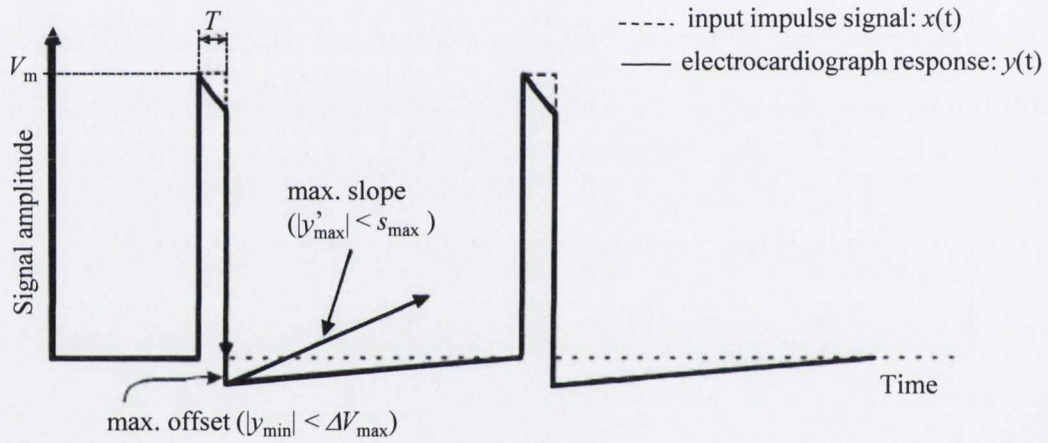

Figure 3.19: Schematic illustrating the impulse response requirements.

The rectangular pulse $x(t)$ is ideally modelled using the Heaviside unit step function u as:

$$x(t) = V_m\,[u(t) - u(t-T)] \tag{3.68}$$

The Laplace transform of $x(t)$ is therefore given by:

$$X(s) = \frac{V_m}{s}\left(1 - e^{-sT}\right) \tag{3.69}$$

Using the transfer function $H_d(s)$ defined in eq. (3.44), the frequency response $y_d(s)$ of the skin-electrode-amplifier network to the pulse $X(s)$ is:

$$y_d(s) = X(s)H_d(s) = V_m\left(1 - e^{-Ts}\right) R_{in}\frac{C_{in}}{2}\tau_{2s}R_{4e}\left[\frac{\left(s + \frac{1}{\tau_{2s}}\right)\left(s + \frac{1}{R_{4e}}\right)}{d_3s^3 + d_2s^2 + d_1s + 1}\right] \tag{3.70}$$

$Y(s)$ can then be expanded by partial fractions as:

$$y_{\mathrm{d}}(s) = V_{\mathrm{m}}\left(1 - e^{-Ts}\right) R_{\mathrm{in}} \frac{C_{\mathrm{in}}}{2} \tau_{2\mathrm{s}} R_{4\mathrm{e}} \left[\frac{A_0}{(s-p_0)} + \frac{A_1}{(s-p_1)} + \frac{A_2}{(s-p_2)}\right] \tag{3.71}$$

where p_0, p_1 and p_2 are the poles of $H_{\mathrm{d}}(s)$. The three poles and three coefficients A_0, A_1 and A_2 are functions of the parameters of the skin-electrode-amplifier network. Eqs. (3.70) and (3.71) imply:

$$\begin{aligned} y_{\mathrm{d}}(s)(s-p_0) &= V_{\mathrm{m}}\left(1 - e^{-Ts}\right) R_{\mathrm{in}} \frac{C_{\mathrm{in}}}{2} \tau_{2\mathrm{s}} R_{4\mathrm{e}} \left[A_0 + (s-p_0)\frac{A_1}{(s-p_1)} + (s-p_0)\frac{A_2}{(s-p_2)}\right] \\ &= V_{\mathrm{m}}\left(1 - e^{-Ts}\right) R_{\mathrm{in}} \frac{C_{\mathrm{in}}}{2} \tau_{2\mathrm{s}} R_{4\mathrm{e}} \left[\frac{\left(s + \frac{1}{\tau_{2\mathrm{s}}}\right)\left(s + \frac{1}{R_{4\mathrm{e}}}\right)}{(s-p_1)(s-p_2)}\right] \end{aligned} \tag{3.72}$$

Evaluating eq. (3.72) at $s = p_0$ yields:

$$A_0 = \frac{\left(p_0 + \frac{1}{\tau_{2\mathrm{s}}}\right)\left(p_0 + \frac{1}{R_{4\mathrm{e}}}\right)}{(p_0 - p_1)(p_0 - p_2)} \tag{3.73}$$

A similar approach leads to expressions for A_1 and A_2 as follows:

$$A_1 = \frac{\left(p_1 + \frac{1}{\tau_{2\mathrm{s}}}\right)\left(p_1 + \frac{1}{R_{4\mathrm{e}}}\right)}{(p_1 - p_0)(p_1 - p_2)} \tag{3.74}$$

$$A_2 = \frac{\left(p_2 + \frac{1}{\tau_{2\mathrm{s}}}\right)\left(p_2 + \frac{1}{R_{4\mathrm{e}}}\right)}{(p_2 - p_0)(p_2 - p_1)} \tag{3.75}$$

The inverse Laplace transform of $y_{\mathrm{d}}(s)$ gives the corresponding response in time $y_{\mathrm{d}}(t)$ as:

$$\begin{aligned} y_{\mathrm{d}}(t) = V_{\mathrm{m}} R_{\mathrm{in}} \frac{C_{\mathrm{in}}}{2} \varphi \tau_{2\mathrm{s}} R_{4\mathrm{e}} \big[&\left(A_0 e^{-p_0 t} + A_1 e^{-p_1 t} + A_2 e^{-p_2 t}\right) u(t) \\ &- \left(A_0 e^{-p_0(t-T)} + A_1 e^{-p_1(t-T)} + A_2 e^{-p_2(t-T)}\right) u(t-T)\big] \end{aligned} \tag{3.76}$$

If $x(t)$ is an ideal pulse, the amplitude of the response following the end of the impulse is given by:

$$y_{\mathrm{d}}(t)|_{t>T} = -V_{\mathrm{m}} R_{\mathrm{in}} \frac{C_{\mathrm{in}}}{2} \tau_{2\mathrm{s}} R_{4\mathrm{e}} \sum_{k=0}^{2} \left[A_{\mathrm{k}}(e^{-p_{\mathrm{k}}T} - 1)e^{-p_{\mathrm{k}}t}\right] \tag{3.77}$$

The derivative of $y(t)$ at $t > T$ defines the slope of the impulse response following the impulse:

$$y'_{\mathrm{d}}(t)|_{t>T} = \left.\frac{dy_{\mathrm{d}}(t)}{dt}\right|_{t>T} = V_{\mathrm{m}} R_{\mathrm{in}} \frac{C_{\mathrm{in}}}{2} \tau_{2\mathrm{s}} \tau_{4\mathrm{e}} \sum_{k=0}^{2} \left[p_{\mathrm{k}} A_{\mathrm{k}}(e^{-p_{\mathrm{k}}T} - 1)e^{-p_{\mathrm{k}}t}\right] \tag{3.78}$$

The poles p_0, p_1 and p_2 are obtained by solving the polynomial $d_3s^3 + d_2s^2 + d_1s + 1 = 0$. Computing the equation with *Mathematica* returns the following solutions:

$$p_0 = -\frac{d_2}{3d_3} - \frac{2^{1/3}\left(-d_2^2+3d_1d_3\right)}{3d_3\left[-2d_2^3+9d_1d_2d_3-27d_3^2+\sqrt{4\left(-d_2^2+3d_1d_3\right)^3+\left(-2d_2^3+9d_1d_2d_3-27d_3^2\right)^2}\right]^{1/3}} + \frac{\left[-2d_2^3+9d_1d_2d_3-27d_3^2+\sqrt{4\left(-d_2^2+3d_1d_3\right)^3+\left(-2d_2^3+9d_1d_2d_3-27d_3^2\right)^2}\right]^{1/3}}{32^{1/3}d_3} \tag{3.79}$$

$$p_1 = -\frac{d_2}{3d_3} - \frac{\left(1+j\sqrt{3}\right)\left(-d_2^2+3d_1d_3\right)}{32^{1/3}d_3\left[-2d_2^3+9d_1d_2d_3-27d_3^2+\sqrt{4\left(-d_2^2+3d_1d_3\right)^3+\left(-2d_2^3+9d_1d_2d_3-27d_3^2\right)^2}\right]^{1/3}} - \frac{\left(1-j\sqrt{3}\right)\left[-2d_2^3+9d_1d_2d_3-27d_3^2+\sqrt{4\left(-d_2^2+3d_1d_3\right)^3+\left(-2d_2^3+9d_1d_2d_3-27d_3^2\right)^2}\right]^{1/3}}{62^{1/3}d_3} \tag{3.80}$$

$$p_2 = -\frac{d_2}{3d_3} - \frac{\left(1-j\sqrt{3}\right)\left(-d_2^2+3d_1d_3\right)}{32^{1/3}d_3\left[-2d_2^3+9d_1d_2d_3-27d_3^2+\sqrt{4\left(-d_2^2+3d_1d_3\right)^3+\left(-2d_2^3+9d_1d_2d_3-27d_3^2\right)^2}\right]^{1/3}} - \frac{\left(1+j\sqrt{3}\right)\left[-2d_2^3+9d_1d_2d_3-27d_3^2+\sqrt{4\left(-d_2^2+3d_1d_3\right)^3+\left(-2d_2^3+9d_1d_2d_3-27d_3^2\right)^2}\right]^{1/3}}{62^{1/3}d_3} \tag{3.81}$$

The terms d_1, d_2 and d_3 may be substituted with their expressions given in eqs. (3.45) to (3.47) to evaluate p_0, p_1 and p_2. This would allow $y_d(t)$ and $y'_d(t)$ to be represented in terms of the parameters of the skin-electrode-amplifier network and the input impedance requirement to be identified. However, this method involves solving non-linear functions in the complex domain for which analytical solutions are not available. An alternative approach consists of implementing a numerical algorithm to find the minimum value of R_{in} for which the recording system meets the impulse response requirements. An algorithm was developed in *MATLAB* to test the maximum undershoot and recovery slope for a range of values of R_{in}.

3.4.3 Results

Data collected from two hundred and sixty eight measurements of the skin-electrode interface are analysed using the proposed methods. Measurements were taken on seven subjects, using seven different types of dry electrodes, under variable conditions of contact pressure, electrode settling time and current level. As for simulations referred to in Section 3.1.1, the input capacitance is initially set at $C_{in} = 0.33$ µF. The current limiting resistor was chosen as $R_1 = 100$ kΩ, as recommended in previous literature [34–36].

Amplitude and phase criteria

Fig. 3.20(a) shows the frequency response of the skin-electrode interface when the input impedance is selected following the amplitude response criterion defined in eq. (3.52). For all measurements, the minimum input impedance that fulfils the amplitude response recommendation varies from 21 MΩ to 115 MΩ. Fig. 3.20(b) gives the corresponding results when

the front-end is designed according to the phase response requirement indicated in eq. (3.67). Meeting the phase criterion requires an input impedance between 21 MΩ and 750 MΩ.

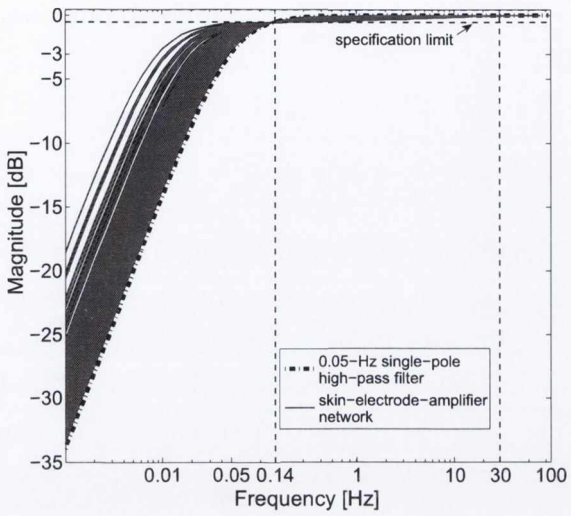

(a) Amplitude response with R_{in} as defined by eq. (3.52).

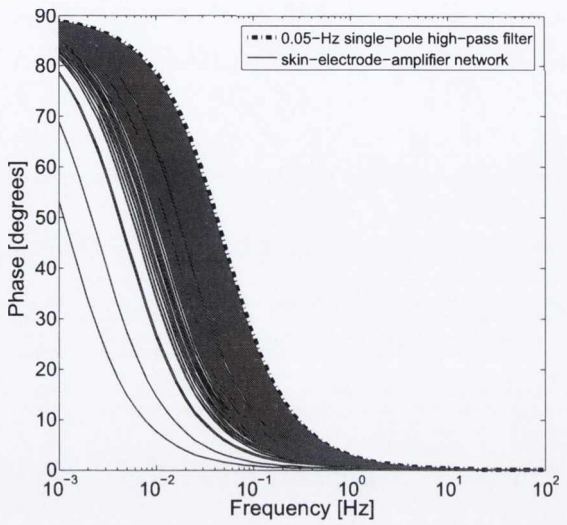

(b) Phase response with R_{in} as defined by eq. (3.67).

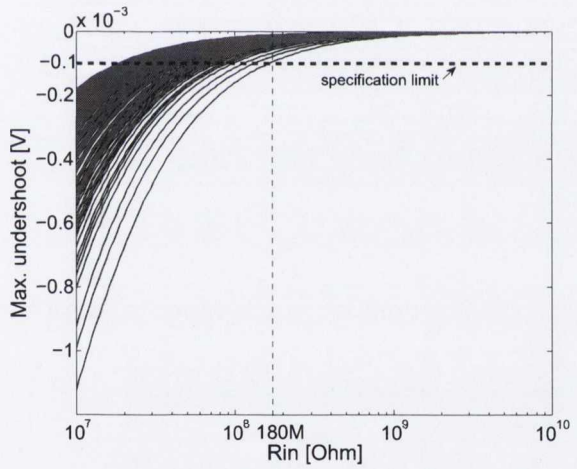

(c) Maximum undershoot vs. R_{in}.

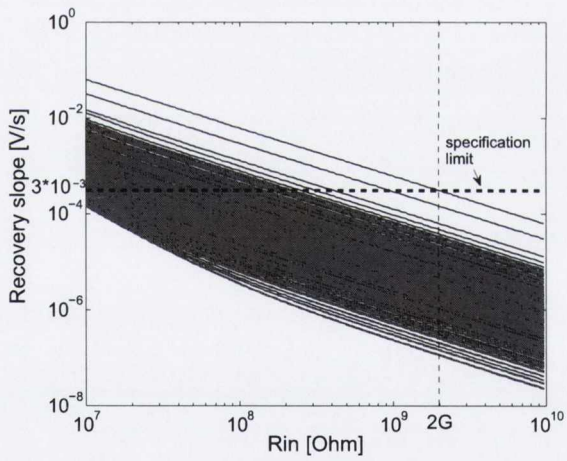

(d) Maximum slope absolute value vs. R_{in}.

Figure 3.20: Plots of (a) the amplitude response, (b) phase response, (c) the maximum undershoot and (d) the maximum recovery slope for 268 measurements of skin-electrode interface impedance with $C_{\text{in}} = 0.33$ µF and $R_1 = 100$ kΩ.

Impulse response criteria

Results from the analysis of the impulse response for all measurements are presented in Fig. 3.20. A rectangular wave of amplitude 3 mV and duration 100 ms is used as input. The response is analysed over a 2 s period. Fig. 3.20(c) shows a plot of the maximum offset

produced for a range of input impedance values between 10 MΩ and 10 GΩ. In Fig. 3.20(d), the maximum absolute values of the slope of the responses following the impulse are shown over the same range of input impedance values. With $C_{in} = 0.33$ μF, the required minimum input impedance varies between 20 MΩ and 2 GΩ.

Influence of the coupling capacitance

Tables 3.5 and 3.6 compare the values of input impedance suggested by the frequency response and impulse response criteria. The values of R_{in} are given in both tables for a range of non-electrolytic capacitance values of C_{in} varying from 0.1 μF to 3.3 μF, available in multilayer ceramic forms. Table 3.5 gives the maximum values of input impedance suggested by all measurements. When one pair of outlying values is removed from the results, the requirements suggested by 99.2% of the data are shown in Table 3.6.

Table 3.5: Worst-case input impedance requirements as a function of the capacitance of the dc-blocking capacitor C_{in} for all 268 measurements.

C_{in} [μF]	0.1	0.22	0.33	0.47	1	2.2	3.3
amplitude response: R_{in} [MΩ]	139	119	115	114	112	112	112
phase response: R_{in} [MΩ]	764	730	720	714	707	704	703
impulse response: R_{in} [MΩ]	2040	2040	2040	2040	2040	2040	2040

Table 3.6: Worst-case input impedance requirements as a function of the capacitance of the dc-blocking capacitor C_{in} for 99.2% of measurements.

C_{in} [μF]	0.1	0.22	0.33	0.47	1	2.2	3.3
amplitude response: R_{in} [MΩ]	120	96	91	89	87	86	86
phase response: R_{in} [MΩ]	236	201	192	185	180	175	174
impulse response: R_{in} [MΩ]	429	429	429	429	429	429	429

Results for both tables indicate that the value of R_{in} levels out at around a value of $C_{in} = 1$ μF. As suggested by eq. (3.67), with increasing dc-blocking capacitance value, the parameters of the skin-electrode interface become the limiting factor. All results confirm that meeting the impulse response involves the highest values of input impedance, which are selected as the target design value. This is seen to be 2 GΩ, well above the IEC specification value of 10 MΩ. This again highlights the inappropriateness of this impedance specification for dry electrodes.

3.5 Conclusion

In this chapter, poor low-frequency response was shown to be a primary source of measurement error that jeopardises the ability of the ECG recording to provide reliable diagnostic clinical information. Despite being necessary to prevent base line wander, high-pass filtering can also cause distortion in the ECG signal if implemented inadequately. A numerical tool was developed by the author to assess the performance of passive high-pass filters up to fourth order against standards requirements. Simulation results have highlighted the lack of consistency between minimum input impedance requirement and low-frequency specifications in ECG standards. It was also demonstrated that the input impulse criteria imply more stringent requirements than the traditional amplitude and phase specifications. In particular, it was shown that recording systems for which the impulse response exhibits an unsatisfactory recovery slope may distort the ECG waveform despite providing acceptable amplitude and phase characteristics in the signal bandwidth. The need for new input impedance requirements that rely upon a complete characterisation of the skin-electrode interface was therefore identified.

Different approaches have been undertaken to model the skin-electrode interface. Experiences with self-adhesive electrodes confirmed that an early model which describes the interface as a single-time-constant RC network is inadequate. A model involving two time constants proves more accurate. Based on the latter model, an algorithm has been implemented to identify the parameters of any double-time-constant system the phase response of which displays a double-peak. Simulations returned highly accurate results when the two time constants forming the system are in a ratio of greater than 10 to 1. The method reaches its limits, however, when the time constants are close to each other and the difference in the phase of the two peaks in the response becomes too small to be accurately measured by the instruments available. Time-domain measurements were employed to obtain parameter values for dry, pasteless electrodes. The fitting procedure converged when the rise and fall phases of the response were analysed separately, producing two estimates of the model parameters. The author has then derived, using a combination of analytical and numerical methods, a set of input impedance requirements which ensure that performance specifications are met in dry-electrode recording. The minimum requirement for the input resistance of the amplifier is determined as 2 GΩ over a range of electrodes, measurement conditions and the value of dc-blocking capacitors used. However, 99.2% of measurements suggested that a value of R_{in} of 500 MΩ would meet requirements.

Chapter 4

Interference suppression and CMRR

Early biopotential amplification was performed using single op-amp configurations because op-amps were expensive [142]. Single-ended biopotential amplifiers are used today in earth-ground-free recording and offer the advantage of simplicity. However, lack of immunity to common-mode interference requires other means of reducing external unwanted voltages [142, 143]. Notch filters are commonly inserted to suppress interference at the power line frequency but this comes at the cost of introducing amplitude and phase distortion into the physiological signal [144]. Single op-amp biopotential differential amplifiers generally exhibit better immunity to surrounding noise. This requires the gain defining resistors to be perfectly matched. Nevertheless, imbalance at the skin-electrode interface causes a gain error and rapidly reduces the ability of the recording system to suppress external contaminating signals. In addition, single op-amp difference amplifiers suffer severe restrictions on the input impedance, which is limited by the input resistors, also responsible for setting the gain of the circuit. Practical circuit considerations therefore limit the range of value for these resistors. That is why the use of instrumentation amplifier circuits proves to be a more suitable solution.

In this chapter, the author explains the need for securing high immunity to common-mode signals and analyses the performance of existing instrumentation amplifier circuits, in light of the actual measurements of skin-electrode impedance presented in Chapter 3.

4.1 Importance of common-mode rejection in diagnostic quality ECG recording

The ECG waveform is recorded as a potential difference between sensing electrodes. If the distance between two measuring electrodes is small, the amplitude and phase characteristics of power line signals are identical on both sides, resulting in a voltage common to the two input terminals of the recording system. The amplitude of the biosignal, ranging from 100 μV to 10 mV, is far smaller than that of the interfering common voltage and must be

augmented above the interfering signal before display or further processing. It is the role of the instrumentation amplifier to carry out amplification selective to the physiological signal while at the same time suppressing common voltages.

4.1.1 Common-mode signal as a source of interference

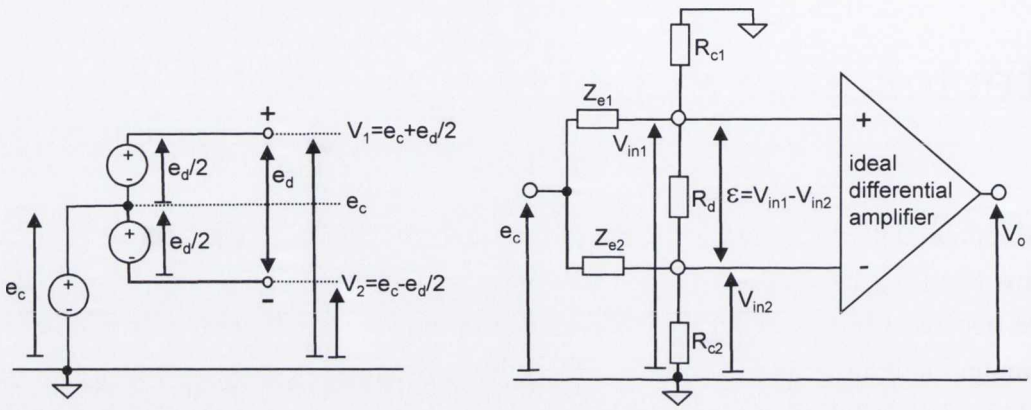

(a) Voltages at the input of an ECG recording system.

(b) Conversion of e_c into a differential component $\epsilon = V_{in1} - V_{in2}$ due to impedance mismatch.

Figure 4.1: Schematics showing (a) the electrical potentials at the input of an ECG recording system and (b) the mechanism of conversion of a common-mode interfering voltage into a differential signal.

Fig. 4.1(a) is a schematic representation of the potentials sensed by two bioelectrodes. These potentials can be expressed in terms of the voltages, V_1 and V_2, at the input of the recording system as:

$$e_d = V_1 - V_2 \tag{4.1}$$

$$e_c = \frac{V_1 + V_2}{2} \tag{4.2}$$

Physiological information is contained in the differential signal, e_d, while the common-mode voltage, e_c, is associated with unwanted external interference principally originating from power lines connected to electrical equipment and appliances. However, mismatch in the impedances on either side of the amplifier allows a common-mode signal to be converted into a differential component at the amplifier input, as shown in Fig. 4.1(b). The effect of common-mode interference on a recorded ECG waveform is illustrated in Fig. 4.2. The QRS complex is visible on the ECG record, but accurate measurement of the amplitude of the P wave and ST segments is not possible due to poor signal-to-noise ratio. Securing a high level of immunity to common-mode interference is therefore crucial in diagnostic quality ECG recording.

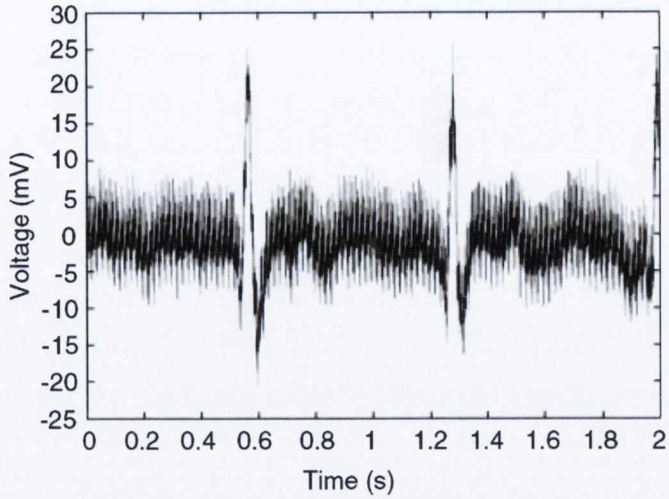

Figure 4.2: Sample ECG recording affected by mains interference (from [29]).

4.1.2 The Common-Mode Rejection Ratio

If A_d and A_c represent the differential gain and common-mode gain of the instrumentation amplifier, respectively, the voltage at its single-ended output can be written as:

$$V_o = A_d e_d + A_c e_c \tag{4.3}$$

The right-hand term of eq. (4.3) is an error introduced at the output by the conversion of common-mode voltages into a differential signal. The ability of the amplifier to suppress common-mode interference is measured by its common-mode rejection ratio (CMRR) as "the ratio of the output voltage produced by a differential voltage compared to the output voltage produced by a common-mode signal of equal amplitude" [143, 145]:

$$\text{CMRR} = \frac{A_d}{A_c} \tag{4.4}$$

There are three primary factors which limit the CMRR obtainable, namely: common-mode impedance mismatch at the amplifier input, $\text{CMRR}_{\Delta Z}$; manufacturing tolerances in the gain-determining resistors, $\text{CMRR}_{\Delta R}$; and the finite CMRR_{op} of the op-amps used for implementing the circuit. The overall CMRR of the amplifier is determined by the combination of these effects as:

$$\frac{1}{\text{CMRR}} = \frac{1}{\text{CMRR}_{\Delta Z}} + \frac{1}{\text{CMRR}_{\Delta R}} + \frac{1}{\text{CMRR}_{op}} \tag{4.5}$$

CMRR specifications have been issued by international standards in variable forms that can be summarised as follows:

- For ambulatory ECG, the International Electrotechnical Commission (IEC) defines the common-mode rejection capability of an ECG recording system as "the ratio of the peak-to-valley value of the interfering supply mains frequency to the peak-to-valley value of the resulting signal in any ECG input channel, referred to input" [102]. The CMRR as defined must exceed 60 dB at mains frequency and 45 dB at twice the mains frequency [102].

- When applied in a non-ambulatory context, the IEC indicates that a 10 V rms (or 28.28 V peak-to-peak) common-mode input signal at mains frequency must not produce an output signal greater than 1 mV peak-to-valley referred to the input [101]. Considering the peak-to-valley and peak-to-peak voltages as being equivalent over a short period of time allows the minimum CMRR requirement to be expressed in dB as $\text{CMRR}_{\text{min}} = |A_{\text{d}}/A_{\text{c}}|_{\text{dB}} = |e_{\text{ci}}/e_{\text{co}_{\text{rti}}}|_{\text{dB}} = 89$ dB, where $e_{\text{ci}} = 28.28$ V p-p is the common-mode input voltage and $e_{\text{co}_{\text{rti}}}$=1 mV p-p is the resulting common-mode output voltage, referred-to-input.

- American standards for non-ambulatory ECG are more stringent since the common-mode test signal is taken as 20 V rms (or 56.57 V p-p) and shall not result in an output signal exceeding 1 mV p-p referred-to-input [104]. This requirement is equivalent to CMRR $\geq$ 95 dB.

As previously indicated in section 2.4.3 of Chapter 2, to take into account additional noise in the bandwidth 1 - 100 Hz inherent with the use of dry electrodes, the author has targeted a CMRR greater than 95 dB in this frequency range.

4.1.3 Interference rejection capability of popular biopotential instrumentation amplifier structures

Fig. 4.3 shows three different realisations of ac-coupled instrumentation amplifiers commonly found in ECG recording. The instrumentation amplifier shown in Fig. 4.3(a) utilises impedance transforming unity-gain buffers at the input terminals of a difference amplifier. This configuration is mainly implemented on recording systems equipped with active electrodes [23–26, 125–133, 146]. The chief advantage of the voltage follower input stage over a single op-amp approach resides in the fact that its input impedance is independent of the differential gain of the circuit. However, due to the finite values for R_{c1} and R_{c2}, common-mode signals are present at the input of the second stage. The absence of differential amplification at the front-end stage means that the overall CMRR heavily relies upon the use of very precise resistors in the differential-to-single-end stage.

Fig. 4.3(b) presents a standard instrumentation amplifier configuration that constitutes an improved, and very popular, version of the three-op-amp implementation of Fig. 4.3(a).

The front-end op-amps, A_1 and A_2, ensure high differential amplification while keeping common-mode gain to unity, despite any mismatch due to manufacturing tolerances in the gain-defining resistors R_{2A} and R_{2B}. The differential signal is therefore augmented at the output of the first stage, relative to the common-mode signal. Common-mode components are further rejected by the second stage built around the output op-amp, A_3. It can be shown that the CMRR of op-amp A_3 and the precision with which resistors are matched are not as critical in this circuit as in the case of the follower type instrumentation amplifier of Fig. 4.3(a).

Fig. 4.3(c) shows an alternative configuration based on only two op-amps. This solution is attractive in amplifier designs interested in a minimum number of components [147]. However, the overall CMRR is more dependent on precise resistor matching than in the case of the standard three-op-amp structure of Fig. 4.3(b).

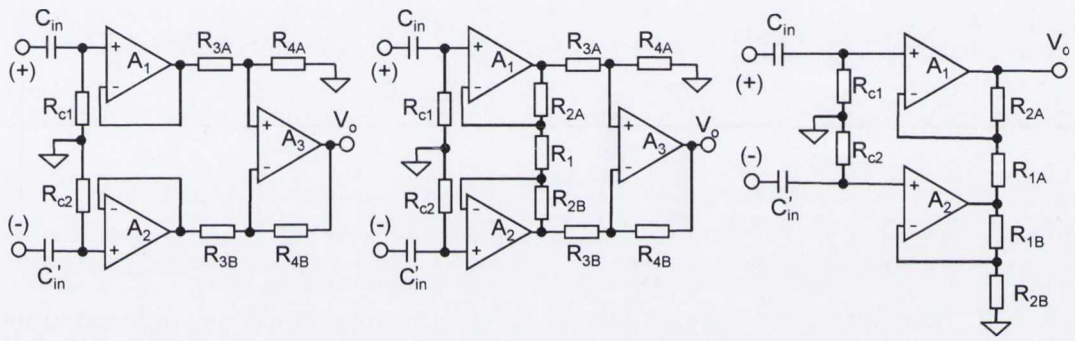

(a) Voltage follower input stage. (b) The "classical" three-op-amp IA. (c) A standard two-op-amp IA.

Figure 4.3: Circuit diagram of three different implementations of ac-coupled instrumentation amplifiers (IAs) utilised in ECG recording including (a) the voltage follower input stage, (b) the improved "classical" amplifying input stage and (c) its two-op-amp version (modified from [148]).

It can be concluded that the "classical" instrumentation amplifier arrangement exhibits superior immunity to common-mode interference when compared to the voltage follower and the two-op-amp configurations.

4.2 Analysis of the CMRR of the standard three op-amp instrumentation amplifier

A schematic diagram of the standard three-op-amp instrumentation amplifier coupled to imbalanced electrode impedances, Z_{e1} and Z_{e2}, is shown in Fig. 4.4. Several analyses of the CMRR of this "classical" structure have been published [34–36, 149–158], but a study

that considers actual measurements of skin-electrode impedance and includes a rigorous assessment of the worst-case scenario is a shortfall of the work in this area.

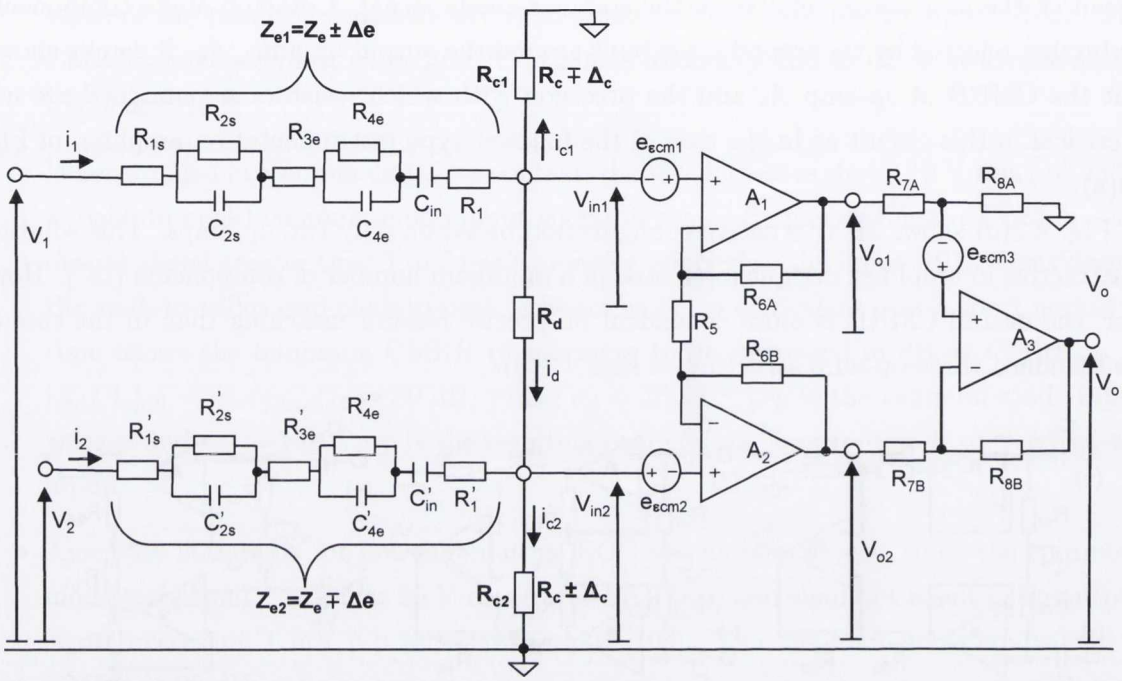

Figure 4.4: Schematic modelling the mechanisms of common-mode to differential-mode conversion in a standard three-op-amp instrumentation amplifier. The voltage sources $e_{\epsilon cm1}$, $e_{\epsilon cm2}$ and $e_{\epsilon cm3}$ represent the equivalent input common-mode error voltages due to the limited CMRR of op-amps A_1, A_2 and A_3, respectively, modelled as differential sources.

4.2.1 CMRR due to common-mode impedance mismatch at the amplifier input

In the absence of a differential input signal, the voltages at the input terminals of the recording system are equal ($V_1 = V_2 = e_c$), resulting ideally in $V_o = 0$ V at the output. However, imbalanced electrode impedances, Z_{e1} and Z_{e2}, and finite values of input impedance, $R_{in} = R_d // (R_{c1} + R_{c2})$, generate a differential signal, V_{id}, that can be expressed as:

$$V_{id} = V_{in1} - V_{in2} = (e_c - Z_{e1} i_1) - (e_c - Z_{e2} i_2) \tag{4.6}$$

with

$$i_1 = i_{c1} + i_d = \frac{V_{in1}}{R_{c1}} + \frac{V_{id}}{R_d} \tag{4.7}$$

$$i_2 = i_{c2} - i_d = \frac{V_{in2}}{R_{c2}} - \frac{V_{id}}{R_d} \tag{4.8}$$

Therefore, eq. 4.6 can be written as:

$$V_{\mathrm{id}} = \frac{\frac{Z_{\mathrm{e2}}}{R_{\mathrm{c2}}} V_{\mathrm{in2}} - \frac{Z_{\mathrm{e1}}}{R_{\mathrm{c1}}} V_{\mathrm{in1}}}{1 + \frac{Z_{\mathrm{e1}} + Z_{\mathrm{e2}}}{R_{\mathrm{d}}}} \tag{4.9}$$

where

$$V_{\mathrm{in1}} = e_{\mathrm{c}} \left[Z_{\mathrm{e1}} // R_{\mathrm{c1}} // \left(R_{\mathrm{d}} + Z_{\mathrm{e2}} // R_{\mathrm{c2}} \right) \right] \left[\frac{1}{Z_{\mathrm{e1}}} + \frac{R_{\mathrm{c2}}}{\left(Z_{\mathrm{e2}} + R_{\mathrm{c2}} \right) \left(R_{\mathrm{d}} + R_{\mathrm{c2}} // Z_{\mathrm{e2}} \right)} \right] \tag{4.10}$$

$$V_{\mathrm{in2}} = e_{\mathrm{c}} \left[Z_{\mathrm{e2}} // R_{\mathrm{c2}} // \left(R_{\mathrm{d}} + Z_{\mathrm{e1}} // R_{\mathrm{c1}} \right) \right] \left[\frac{1}{Z_{\mathrm{e2}}} + \frac{R_{\mathrm{c1}}}{\left(Z_{\mathrm{e1}} + R_{\mathrm{c1}} \right) \left(R_{\mathrm{d}} + R_{\mathrm{c1}} // Z_{\mathrm{e1}} \right)} \right] \tag{4.11}$$

For $|R_{\mathrm{in}}| >> \{|Z_{\mathrm{e1}}|, |Z_{\mathrm{e2}}|\}$, eq. (4.9) can be approximated by:

$$V_{\mathrm{id}} \simeq \left(\frac{Z_{\mathrm{e2}}}{R_{\mathrm{c2}}} - \frac{Z_{\mathrm{e1}}}{R_{\mathrm{c1}}} \right) e_{\mathrm{c}} \tag{4.12}$$

The CMRR due to impedance mismatch is then given by:

$$\mathrm{CMRR}_{\Delta Z} = \left| \frac{e_{\mathrm{c}}}{V_{\mathrm{id}}} \right| \tag{4.13}$$

The minimum value for $\mathrm{CMRR}_{\Delta Z}$ is obtained when the impedance mismatch is maximum. If Δ_{e} and Δ_{c} are the variations in Z_{e} and R_{c} respectively, the worst-case scenario occurs for:

$$R_{\mathrm{c1}} = R_{\mathrm{c}} \left(1 - \Delta_{\mathrm{c}} \right) \tag{4.14}$$

$$R_{\mathrm{c2}} = R_{\mathrm{c}} \left(1 + \Delta_{\mathrm{c}} \right) \tag{4.15}$$

$$Z_{\mathrm{e1}} = Z_{\mathrm{e}} \left(1 + \Delta_{\mathrm{e}} \right) \tag{4.16}$$

$$Z_{\mathrm{e2}} = Z_{\mathrm{e}} \left(1 - \Delta_{\mathrm{e}} \right) \tag{4.17}$$

Assuming a purely resistive input impedance, $\mathrm{CMRR}_{\Delta Z}$ can hence be expressed in terms of the nominal impedances and their variation as follows:

$$\mathrm{CMRR}_{\Delta Z}|_{\mathrm{dB}} \simeq 20\log_{10} \left(\left| \frac{R_{\mathrm{c1}} R_{\mathrm{c2}}}{R_{\mathrm{c1}} Z_{\mathrm{e2}} - R_{\mathrm{c2}} Z_{\mathrm{e1}}} \right| \right) \simeq 20\log_{10} \left(\frac{R_{\mathrm{c}}}{|Z_{\mathrm{e}}|} \right) + 20\log_{10} \left(\frac{1 - \Delta_{\mathrm{c}}^2}{2 \left(\Delta_{\mathrm{c}} + \Delta_{\mathrm{e}} \right)} \right) \tag{4.18}$$

where $|Z_e|$ is defined as:

$$|Z_e| = \sqrt{\left[R_{1s} + R_{3e} + \frac{R_{2s}}{1+(R_{2s}C_{2s}\omega)^2} + \frac{R_{4e}}{1+(R_{4e}C_{4e}\omega)^2} + R_1\right]^2 + \left[\frac{1}{C_{in}\omega} + \frac{R_{2s}^2 C_{2s}\omega}{1+(R_{2s}C_{2s}\omega)^2} + \frac{R_{4e}^2 C_{4e}\omega}{1+(R_{4e}C_{4e}\omega)^2}\right]^2} \tag{4.19}$$

4.2.2 CMRR due to manufacturing tolerances in the gain-determining resistors

The amplification stages of the "classical" three op-amp configuration are shown in Fig. 4.5.

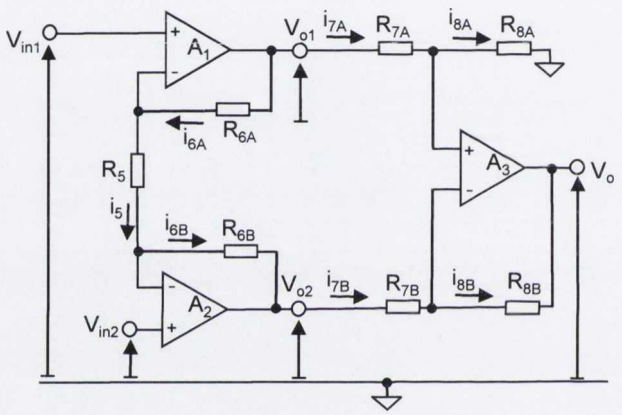

Figure 4.5: Simplified circuit schematic of the "classical" three-op-amp IA considering exclusively the conversion of common-mode signal to differential component due to manufacturing tolerances in the gain-determining resistors.

Referring to Fig. 4.5, potential V_{o1} is equal to V_{in1} augmented by the voltage drop across resistor R_{6A} while V_{o2} is V_{in2} reduced by the voltage drop across resistor R_{6B}, so that:

$$V_{o1} = V_{in1} + R_{6A} i_{6A} \tag{4.20}$$

$$V_{o2} = V_{in2} - R_{6B} i_{6B} \tag{4.21}$$

Under the assumption of ideal op-amps, it can be said that:

$$i_{6A} = i_{6B} = i_5 = \frac{V_{in1} - V_{in2}}{R_5} \tag{4.22}$$

Eqs. (4.20) to (4.22) yield the following expressions for the differential and common-mode

voltages at the output of the cross-coupled stage:

$$V_{o1} - V_{o2} = \left(1 + \frac{R_{6A} + R_{6B}}{R_5}\right)(V_{in1} - V_{in2}) \tag{4.23}$$

$$\frac{(V_{o1} + V_{o2})}{2} = \frac{(V_{in1} + V_{in2})}{2} + \frac{(R_{6A} - R_{6B})}{2R_5}(V_{in1} - V_{in2}) \tag{4.24}$$

Eqs. (4.23) and (4.24) demonstrate an important feature of the standard IA structure that resides in the absence of conversion of common-mode input into differential output at the front-end stage. This allows the common-mode gain of the differential-input-differential-output stage to be unity while its nominal differential gain, when the corresponding A and B values are matched, is set by:

$$G_1 = 1 + 2\frac{R_6}{R_5} \tag{4.25}$$

The final amplification stage transforms V_{o1} and V_{o2} into a single-ended signal V_o defined as follows:

$$V_o = \frac{R_{7B} + R_{8B}}{R_{7A} + R_{8A}} \frac{R_{8A}}{R_{7B}} V_{01} - \frac{R_{8B}}{R_{7B}} V_{02} \tag{4.26}$$

The nominal differential gain of the output stage is then given as:

$$G_2 = \frac{R_8}{R_7} \tag{4.27}$$

Imbalance introduced in the circuit by mismatch in the values of the gain-defining resistors is considered by expressing each paired resistor, R_{xy}, in terms of its nominal value, R_x, and an error due to manufacturing tolerances, Δ_{xy}, so that:

$$R_{xy} = R_x (1 + \Delta_{xy})|_{x=\{6,7,8\}, y=\{A,B\}} \tag{4.28}$$

Eqs. (4.23) to (4.24) can be rewritten as follows:

$$V_{o1} - V_{o2} = \left[1 + \frac{R_6}{R_5}(2 + \Delta_{6A} + \Delta_{6B})\right](V_{in1} - V_{in2}) \tag{4.29}$$

$$\frac{(V_{o1} + V_{o2})}{2} = \frac{(V_{in1} + V_{in2})}{2} + \frac{R_6(\Delta_{6A} - \Delta_{6B})}{2R_5}(V_{in1} - V_{in2}) \tag{4.30}$$

and

$$V_o \simeq \frac{R_8}{R_7}\left[1 + \frac{R_7(\Delta_{8A} + \Delta_{8B} - \Delta_{7A} - \Delta_{7B}) + 2R_8(\Delta_{8B} - \Delta_{7B})}{(R_7 + R_8)}\right](V_{o1} - V_{o2}) + \frac{R_8}{R_7 + R_8}(\Delta_{7B} - \Delta_{7A} + \Delta_{8A} - \Delta_{8B})\left(\frac{V_{o1} + V_{o2}}{2}\right) \tag{4.31}$$

The worst-case scenario corresponds to the mismatch in resistor values that yields the largest common-mode voltage at the single-ended output. Referring to eqs. (4.29) to (4.31), this situation occurs with the following configuration:

$$R_{6A} = R_6 \left(1 + \Delta_{R_{max}}\right) \tag{4.32}$$

$$R_{6B} = R_6 \left(1 - \Delta_{R_{max}}\right) \tag{4.33}$$

$$R_{7A} = R_7 \left(1 - \Delta_{R_{max}}\right) \tag{4.34}$$

$$R_{7B} = R_7 \left(1 + \Delta_{R_{max}}\right) \tag{4.35}$$

$$R_{8A} = R_8 \left(1 + \Delta_{R_{max}}\right) \tag{4.36}$$

$$R_{8B} = R_8 \left(1 - \Delta_{R_{max}}\right) \tag{4.37}$$

where $\Delta_{R_{max}}$ is the manufacturing tolerance. The final output voltage can therefore be expressed as:

$$\begin{aligned} V_o \simeq \frac{R_8}{R_7}\left[1 + 2\Delta_{R_{max}}\frac{R_8}{(R_7+R_8)}\right]\left(1 + 2\frac{R_6}{R_5}\right)(V_{in1} - V_{in2}) \\ + 4\Delta_{R_{max}}\frac{R_8}{R_7+R_8}\frac{(V_{in1}+V_{in2})}{2} + 4\Delta^2_{R_{max}}\frac{R_6}{R_5}\frac{R_8}{(R_7+R_8)}(V_{in1} - V_{in2}) \end{aligned} \tag{4.38}$$

Eq. (4.38) is an expression of V_o in terms of a differential component, $V_{id} = V_{in1} - V_{in2}$, and a common-mode component, $V_{ic} = (V_{in1} + V_{in2})/2$, each respectively scaled by a multiplying factor ,A_d and A_c, defined as follows:

$$A_d = \left(1 + 2\frac{R_6}{R_5}\right)\frac{R_8}{R_7}\left[1 + 2\Delta_{R_{max}}\frac{R_8}{(R_7+R_8)}\right] + 4\left(\frac{R_6}{R_5}\right)\frac{R_8}{(R_7+R_8)}\Delta^2_{R_{max}} \tag{4.39}$$

and

$$A_c = \frac{R_8}{R_7+R_8}\left(4\Delta_{R_{max}}\right) \tag{4.40}$$

Considering $\Delta_{R_{max}} << 1$ and $R_7 \leq R_8$, the minimum common-mode rejection ratio due to manufacturing tolerances in the gain-determining resistors can be closely approximated by:

$$\text{CMRR}_{\Delta R_{min}} = \left|\frac{A_d}{A_c}\right| = \left(1 + 2\frac{R_6}{R_5}\right)\left(1 + \frac{R_8}{R_7}\right)\left(\frac{1}{4\Delta_{R_{max}}}\right) \tag{4.41}$$

Referring to eqs. (4.25) and (4.27), the nominal differential gain of the circuit is given by:

$$A_{d0} = \left(1 + 2\frac{R_6}{R_5}\right)\frac{R_8}{R_7} = G_1 G_2 \tag{4.42}$$

Eq. (4.41) can therefore be rewritten as:

$$\mathrm{CMRR}_{\Delta R_{min}} = \frac{G_1\,(1+G_2)}{4\Delta_{\mathrm{R_{max}}}} = \frac{G_1 + A_{\mathrm{d0}}}{4\Delta_{\mathrm{R_{max}}}} \tag{4.43}$$

The CMRR of the three-op-amp IA can also be defined as the product of the CMRRs provided by the two amplification stages and is commonly approximated by $A_{\mathrm{d0}}/4\Delta_{\mathrm{R_{max}}}$. Consequently, the use of high gain in both stages of the circuit is often recommended for achieving high CMRR performance [34, 35]. For a given nominal gain $A_{\mathrm{d0}} = G_1 G_2$, with $1 \leq G_1 \leq A_{\mathrm{d0}}$ and $1 \leq G_2 \leq A_{\mathrm{d0}}$, eq. (4.41) indicates, however, that an optimal value for $\mathrm{CMRR}_{\Delta R}$ is obtained with $G_1 = A_{\mathrm{d0}}$ and $G_2 = 1$. This result suggests therefore that the differential gain should be allocated exclusively to the differential-to-differential stage when possible. The gain of differential-to-single-ended stage is then made unity by selecting $R_7 = R_8$.

It can be concluded that the worst-case common-mode rejection ratio due to manufacturing tolerances in the gain-determining resistors is given by:

$$\mathrm{CMRR}_{\Delta \mathrm{R_{min}}} = \left.\frac{A_{\mathrm{d0}}}{2\Delta_{\mathrm{R_{max}}}}\right|_{G_1 = A_{\mathrm{d0}}, G_2 = 1} \tag{4.44}$$

Similar results have been reported by Chevallier [150] and Français [151].

4.2.3 Limitation due to the finite CMRR of op-amps

Ideally, a differential op-amp should only respond to the differential potential applied at its input terminals and reject all common voltages. In practice, the suppression of common-mode signals is restricted by the finite value of the CMMR of real op-amps. The limitation is due to a slight mismatch in the gains of the inverting and non-inverting channels, resulting in a common-mode error for op-amps used in a differential configuration [159, 160]. The CMRR of an op-amp is defined as the ratio of its differential gain to the common-mode gain. Fig. 4.6 is a circuit diagram of the standard IA structure modelling the effect of the limited CMRR of the three op-amps. The effect of resistors mismatch and imbalanced electrode impedances are ignored in this model, since they have been investigated earlier.

The common-mode ouput error signal is generally referred to the op-amp input as an equivalent voltage source $e_{\epsilon\mathrm{cm}}$, as shown in Fig. 4.6. For a given op-amp, A_i, a common-mode voltage e_{cmi} applied to its input terminals results in a common-mode error $e_{\epsilon\mathrm{cmi}}$ referred to its non-inverting input as:

$$e_{\epsilon\mathrm{cmi}} = \frac{e_{\mathrm{cmi}}}{\mathrm{CMRR}_{\mathrm{op}i}} \tag{4.45}$$

The front-end stage of the circuit shown in Fig. 4.6 is designed to provide high differen-

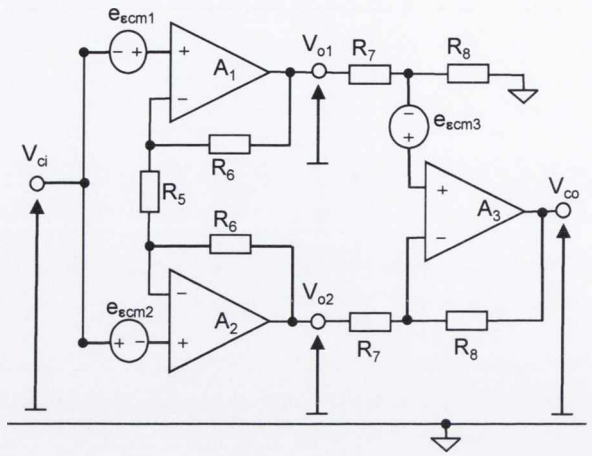

Figure 4.6: Circuit diagram of the standard IA structure modelling the effect of limited CMRR of the three op-amps.

tial gain while maintaining the common-mode gain at unity. However, the introduction of common-mode error voltages at the op-amp input makes the common-mode output voltage dependent on the op-amps' finite CMRRs. Consequently, a differential signal is produced due to imbalanced common-mode error voltages present at op-amps A_1 and A_2. The resulting differential component is subject to the differential gain of the circuit, leading to:

$$V_{o1} - V_{o2} = \left(1 + 2\frac{R_6}{R_5}\right)(e_{ecm1} - e_{ecm2}) = \left(1 + 2\frac{R_6}{R_5}\right)\left(\frac{V_{ci}}{\text{CMRR}_{op1}} - \frac{V_{ci}}{\text{CMRR}_{op2}}\right) \tag{4.46}$$

$$\frac{V_{o1} + V_{o2}}{2} = V_{ci} + \frac{e_{ecm1} + e_{ecm2}}{2} = V_{ci}\left[1 + \frac{1}{2}\left(\frac{1}{\text{CMRR}_{op1}} + \frac{1}{\text{CMRR}_{op2}}\right)\right] \tag{4.47}$$

where V_{ci} is the common-mode input voltage of the circuit as depicted in Fig. 4.6. It can be shown that the potential at the output of the differential-to-single-ended stage built around op-amp A_3 is given by:

$$V_{co} = \frac{R_8}{R_7}(V_{o1} - V_{o2}) + \left(1 + \frac{R_8}{R_7}\right)e_{ecm3} = G_1G_2\left(\frac{V_{ci}}{\text{CMRR}_{op1}} - \frac{V_{ci}}{\text{CMRR}_{op2}}\right) + \frac{(1 + G_2)\left(\frac{V_{o1}+V_{o2}}{2}\right)}{\text{CMRR}_{op3}} \tag{4.48}$$

where G_1 and G_2 refer to the resistor ratios previously defined in Section 4.2.2. Eqs. (4.45) to (4.48) allow the common-mode gain to be expressed in terms of the $CMRRs$ as:

$$A_c = \left|\frac{V_{co}}{V_{ci}}\right| = G_1G_2\left|\frac{1}{\text{CMRR}_{op1}} - \frac{1}{\text{CMRR}_{op2}}\right| + (1 + G_2)\left(\frac{1 + \frac{1}{2\text{CMRR}_{op1}} + \frac{1}{2\text{CMRR}_{op2}}}{\text{CMRR}_{op3}}\right) \tag{4.49}$$

Taking $\text{CMRR}_{opi} >> 1$ and $A_{d0} = G_1G_2$, the Common-Mode Rejection Ratio due to the

finite CMRR of the three op-amps is closely approximated by:

$$\frac{A_{d0}}{A_c} \simeq \left| \frac{1}{\frac{\pm 1}{|\mathrm{CMRR_{op1}}|} + \frac{\mp 1}{|\mathrm{CMRR_{op2}}|} + \frac{(1+G_2)}{A_{d0}} \frac{\pm 1}{|\mathrm{CMRR_{op3}}|}} \right| \tag{4.50}$$

For $G_2 = 1$, the worst-case CMRR is therefore identified as:

$$\frac{1}{\mathrm{CMRR_{op}}} = \frac{1}{|\mathrm{CMRR_{op1}}|} + \frac{1}{|\mathrm{CMRR_{op2}}|} + \frac{1}{\frac{A_{d0}}{2}|\mathrm{CMRR_{op3}}|} \tag{4.51}$$

4.2.4 Results

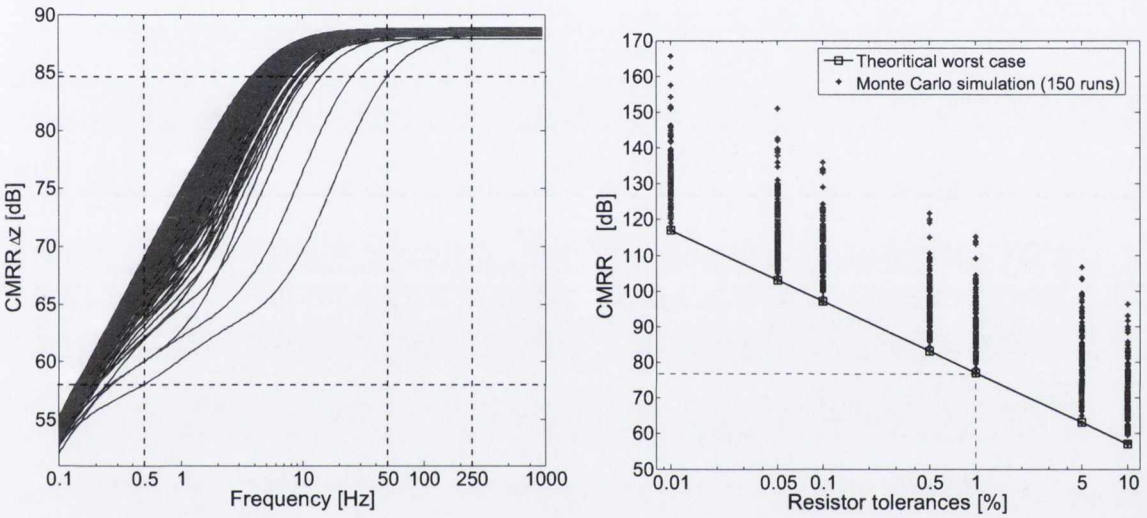

(a) $\mathrm{CMRR}_{\Delta Z}$ vs. frequency.

(b) $\mathrm{CMRR}_{\Delta R}$ vs. $\Delta_{R_{max}}$.

Figure 4.7: Plots of (a) $\mathrm{CMRR}_{\Delta Z}$ and (b) $\mathrm{CMRR}_{\Delta R}$ for the "classical" three op-amp IA structure. $\mathrm{CMRR}_{\Delta Z}$ is plotted against frequency for 268 measurements of skin-electrode impedance assuming $\Delta_e = 0.33$, $\Delta_c = 0.03$, $R_c = 2$ GΩ, $R_1 = 100$ kΩ and $C_{in} = 0.33$ μF. $\mathrm{CMRR}_{\Delta R}$ is simulated for $A_{d0} = G_1 = 40$ dB using ideal op-amps and different resistor tolerances. The theoretical worst-case value defined in eq. (4.44) is compared with Monte Carlo simulation results compiled from 150 runs using PSpice.

Measurements of skin-electrode impedance on seven subjects, using seven different types of dry electrodes, under variable conditions of contact pressure, electrode settling time and current level presented in Chapter 3 have allowed the minimum input impedance requirement for preventing low-frequency distortion to be identified as $R_{in} = R_d//(2R_c) = 2$ GΩ. This can be achieved by selecting $R_c = 2$ GΩ and $R_d = 4$ GΩ. The dominant variation in the impedances seen at the amplifier input is that of the skin-electrode which, if considered to be mismatched by a factor of 2:1 between electrodes gives $\Delta_e = 0.33$ and with $\Delta_c = 0.03$, as

reported in [34–36], yields the plots of $\text{CMRR}_{\Delta Z}$ shown in Fig. 4.7(a), for all two hundred and sixty eight measurements of skin-electrode impedance. Results suggest a minimum $\text{CMRR}_{\Delta Z}$ at 58 dB considering the worst-case electrode impedance magnitude $|Z_e|$= 3.8 MΩ and mismatch $\Delta_e = 33\%$.

Fig. 4.7(b) shows the predicted $\text{CMRR}_{\Delta R}$ simulated with PSpice for different values of resistor tolerance varying in the range 0.01% to 10%. Results indicate that if 1% manufacturing tolerance is assumed for all resistors, a differential mid-band gain of 43 dB guarantees in the worst-case scenario $\text{CMRR}_{\Delta R} \geq 77$ dB.

Table 4.1: CMRR and gain bandwidth product (GBP) performance of low-power op-amps suitable for the implementation of the standard three-op-amp instrumentation amplifier circuit shown in Fig. 4.6.

		Manufacturer	part number	supply current [μA] typical	supply current [μA] max.	CMRR [dB] typical	CMRR [dB] min.	GBP [kHz]
Op-amps	A_1 & A_2	Analog Devices	OP281	3	4	90	65	100
		Linear Technology	LT2178	13	18	103	93	60
		Maxim	MAX409A	1	1.2	80	70	150
		Maxim	MAX9910	4	5.5	80	70	200
		Texas Instruments	OPA2379	2.9	5.5	100	55	90
Op-amp	A_3	Analog Devices	AD8500	0.75	1	90	75	7
		Linear Technology	LT6003	1	1.2	115	88	2
		Maxim	MAX406A	1	1.2	80	70	8
		Texas Instruments	OPA369	0.8	1.2	110	75	12

Table 4.1 presents a list of suitable low-power op-amps, selected for their CMRR and gain-bandwidth product (GBP) performance. Since the front-end op-amps, A_1 and A_2, are responsible for setting the gain of the circuit, gain-bandwidth product characteristics must be taken into account to secure amplification without phase distortion over the entire frequency bandwidth of the ECG signal. CMRR and GBP requirements are less stringent for the unity-gain output stage built around A_3, as indicated by eq. (4.51).

Table 4.1 indicates that the MAX409A and AD8500 provide the best low-power performance while the two op-amps from Linear Technology, LT2178 and LT6003, offer the highest CMRR values. Assuming a mid-band differential gain of 43 dB, eq. (4.51) allows the minimum CMRR_{op} to be estimated at 64 dB for an ultra-low power design requiring a total quiescent current of 3.4 μA. Values for CMRR_{op} exceeding 86 dB can be expected by using op-amps LT2178 and LT6003, but this comes at the cost of a significant increase in power consumption, since up to 37.2 μA may be drawn from the supply.

Considering a design aiming for ultra-low power consumption, the overall CMRR of the standard three-op IA is obtained by combining the effects of $\mathrm{CMRR}_{\Delta Z}$, $\mathrm{CMRR}_{\Delta R}$ and $\mathrm{CMRR}_{\mathrm{op}}$, as follows:

$$\begin{aligned}\frac{1}{\mathrm{CMRR}_{min}} &= \frac{1}{\mathrm{CMRR}_{\Delta Z}} + \frac{1}{\mathrm{CMRR}_{\Delta R}} + \frac{1}{\mathrm{CMRR}_{\mathrm{op}}} \\ &= \frac{2\left|Z_{\mathrm{e}}\right|\left(\Delta_{\mathrm{c}} + \Delta_{\mathrm{e}}\right)}{R_{\mathrm{c}}\left(1 - \Delta_{\mathrm{c}}^{2}\right)} + \frac{2\Delta_{\mathrm{R_{max}}}}{A_{\mathrm{d0}}} + \frac{1}{\left|\mathrm{CMRR}_{\mathrm{op1}}\right|} + \frac{1}{\left|\mathrm{CMRR}_{\mathrm{op2}}\right|} + \frac{1}{\frac{A_{\mathrm{d0}}}{2}\left|\mathrm{CMRR}_{\mathrm{op3}}\right|}\end{aligned} \tag{4.52}$$

Evaluating (4.52) with $\mathrm{CMRR}_{\Delta Z_{min}} = 58$ dB, $\mathrm{CMRR}_{\Delta R_{min}} = 77$ dB and $\mathrm{CMRR}_{op_{min}} = 64$ dB returns an overall CMRR_{min} of 54 dB, which is 41 dB below the minimum performance requirement specified by American standards. This result indicates that $\mathrm{CMRR}_{\Delta Z}$ is the principal limiting factor of the overall CMRR obtainable. Unless electrodes with lower impedance are used or a higher input impedance can be provided by the amplifier, improving $\mathrm{CMRR}_{\Delta R}$ or $\mathrm{CMRR}_{\mathrm{op}}$ would have negligible effect on the overall CMRR. The standard three-op-amp IA structure must therefore be significantly improved if CMRR performance requirements are to be fulfilled.

4.3 A brief review of existing CMRR enhancement techniques

Several schemes have been put forward for optimising the common-mode rejection performance of instrumentation amplifiers. Some circuit designers have improved the CMRR due to impedance imbalance by enhancing the amplifier input impedance, others have concentrated their effort in correcting the effects of resistor mismatch and the limited CMRR provided by op-amps. A small number of circuits have been adapted to single-rail supply while high input impedance performance and low power consumption were maintained. The effectiveness of body potential drivers in increasing the overall CMRR of instrumentation amplifiers has also been demonstrated in ECG recording performed in a three-electrode configuration. In this section, the author evaluates the performance of a selection of CMRR enhancement techniques found in ECG recording which are the most promising for use with dry electrodes.

4.3.1 Trimming techniques

Trimming mechanisms constitute a first-step approach in the compensation of imbalances caused by mismatched resistors and op-amps. CMRR performance of greater than 100 dB has been reported with instrumentation amplifiers employing an adjustment resistor trimmed either manually or via an active trim technique, without requiring either precision resistors

or high-CMRR op-amps. Figs. 4.8 and 4.9 present two examples in which the value of the adjustment resistor is optimised for cancelling the common-mode voltage at the amplifier output stage.

Introduction of a deliberate mismatch

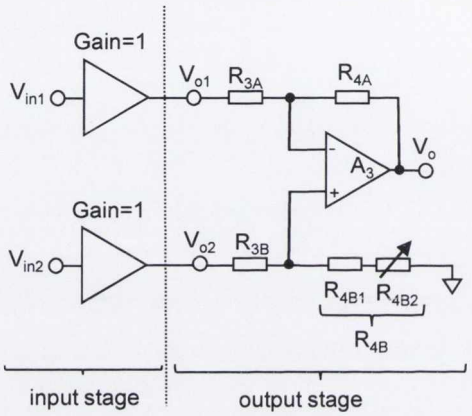

Figure 4.8: Schematic showing a circuit including a potentiometer that can be adjusted to cancel the effect of common-mode interference on the output signal (modified from [143]).

The circuit shown in Fig. 4.8 comprises a potentiometer inserted into the non-inverting input side of a difference amplifier. Pallás-Areny and Webster [143] have shown that the CMRR of the circuit can be maximised by introducing a deliberate mismatch between the ratios R_{3A}/R_{4A} and R_{3B}/R_{4B} so that:

$$\frac{R_{3B}}{R_{4B}} - \frac{R_{3A}}{R_{4A}} = \frac{1}{\mathrm{CMRR_{op}}|_{\omega=0}} \tag{4.53}$$

After adjusting the resistor ratio as indicated in eq. (4.53), the CMRR of the output stage becomes:

$$\frac{A_d}{A_c} = \frac{1}{\frac{1}{\mathrm{CMRR_{op}}} - \frac{1}{\mathrm{CMRR_{op}}|_{\omega=0}}} \tag{4.54}$$

Eq. (4.54) suggests that the CMRR of the amplifier is ideally infinite if $\mathrm{CMRR_{op}}$ has no phase shift in the frequency bandwidth of interest. This adjustment thus simultaneously compensates the imbalance due to resistor tolerances and the limited CMRR of the op-amps. In practice, however, the dependency of $\mathrm{CMRR_{op}}$ on frequency imposes an upper limit on the CMRR obtainable. Measurements of CMRR exceeding 106 dB at 100 Hz have been reported using 5% resistors and a 741 op-amp, known for the limited bandwidth characteristic of

its CMRR. CMRR performance increased to 126 dB with the use of op-amps with higher bandwidth. In both cases the measured CMRR exceeded the CMRR of the op-amp alone.

Solution proposed by Kellogg in 1980

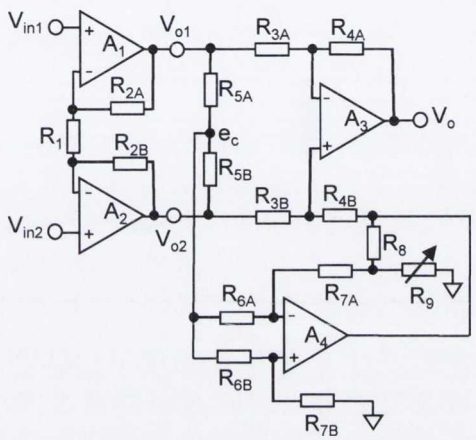

Figure 4.9: Circuit diagram of an wide band instrumentation amplifier with high common-mode rejection, patented by Kellogg in 1980 (modified from [161]).

Fig. 4.9 is the circuit diagram of an instrumentation amplifier adapted to provide high common-mode rejection while preserving the amplifier frequency bandwidth [161]. The technique, patented by Kellog in 1980, includes a compensation channel dedicated to the cancellation of common-mode components from the output voltage, which can be expressed as follows:

$$V_o = A_d\,(V_{in1} - V_{in2}) + (A_c - A'_c)\,\frac{(V_{in1} + V_{in2})}{2} \tag{4.55}$$

where A_c and A'_c denote the common-mode gains of the amplification channel and the compensation channel, respectively. The CMRR is optimised by adjusting a variable resistor, R_9, responsible for balancing the effective impedances at the inverting and non-inverting input terminals of op-amp A_4 to yield $A_c = A'_c$. If op-amps are built on the same chip, good matching between A_c and A'_c would allow high CMRR performance to be achieved over a wider bandwidth than that of the solution shown in Fig. 4.8. CMRR values as high as 160 dB have been reported within the bandwidth over which the common-mode responses of the two channels track [161].

Appraisal of trimming techniques

Trimming techniques present a simple means for improving the CMRR characteristics of a differential amplifier because they rely on a minimum number of parts and are effective with off-the shelf components [162, 163]. This approach is, however, time consuming and therefore involves additional cost and resources when implemented for very large scale production. Automatic trimming mechanisms are available, although their realisation usually requires the combination of analogue and digital circuits for conditioning the biopotential signal [164, 165]. This comes at the expense of increased circuit complexity, additional cost and power consumption.

4.3.2 Amplification performed without input ground reference

The standard instrumentation amplifiers shown in Figs. 4.3 and 4.4 are ac-coupled at their input to eliminate large dc electrode polarisation potentials. The input capacitor also stops the op-amp bias current from flowing back to the electrode and the patient body. Resistors R_{c1} and R_{c2} must therefore be inserted to provide a path for bias current to ground, limiting the input impedance of the circuit and therefore degrading the common-mode rejection ratio due to impedance mismatch, as seen previously. Figs. 4.10 and 4.11 present two instrumentation amplifier circuits that provide ac-coupling without requiring grounded input resistors. The common-mode input impedance of the circuit relies therefore upon the input resistance of the front-end op-amps, which can reach up to 2 TΩ for some low-power amplifiers considered in section 4.2.3. The obtainable $\mathrm{CMRR}_{\Delta Z_{min}}$ would then be close to 100 dB, for the electrode impedances previously measured.

Instrumentation amplifiers providing amplification and integration at the output stage

Fig. 4.10 is an instrumentation amplifier that blocks low-frequency signals at the differential-to-single-ended stage [116]. An integrator built around op-amp A_4 is inserted in THE positive feedback loop of the output stage to filter the output signal. In order to prevent saturation caused by large dc offset voltages, the gain of the differential-input-to-differential-output stage must therefore be limited to low values. To compensate the low gain of the front-end stage, the negative feedback loop of the output stage is modified so that its ac gain can be increased while unwanted dc offset is blocked.

Referring to Fig. 4.10, the potentials at the inputs of op-amp A_3 are given by:

$$V_{\mathrm{A_3}}^{+} = V_{\mathrm{a}} = \frac{\frac{V_{\mathrm{o1}}}{R_{\mathrm{3A}}} + \frac{V_x}{R_{\mathrm{4A}}}}{\frac{1}{R_{\mathrm{3A}}} + \frac{1}{R_{\mathrm{4A}}}} \tag{4.56}$$

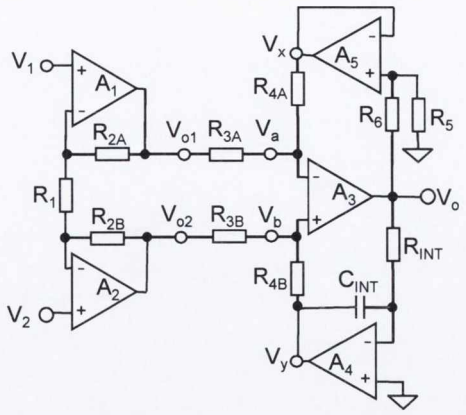

Figure 4.10: Circuit schematic of an instrumentation amplifier that provides amplification and filtering at the differential-to-single-ended stage (modified from [116]).

$$V_{A_3}^{-} = V_b = \frac{\frac{V_{o2}}{R_{3B}} + \frac{V_y}{R_{4B}}}{\frac{1}{R_{3B}} + \frac{1}{R_{4B}}} \tag{4.57}$$

where

$$V_x = \frac{R_5}{R_5 + R_6} V_o \tag{4.58}$$

and

$$V_y = -\frac{1}{sR_{INT}C_{INT}} V_o \tag{4.59}$$

If resistor mismatch is neglected and the op-amps are taken as ideal, eqs. (4.56) to (4.59) would lead to:

$$V_o(s) = \frac{R_4}{R_3}(1 + \frac{R_6}{R_5})(V_{o2} - V_{o1})\frac{s/\omega_c}{1 + s/\omega_c} = \frac{R_4}{R_3}\left(1 + \frac{R_6}{R_5}\right)\left(1 + 2\frac{R_2}{R_1}\right)\frac{(V_2(s) - V_1(s))\, s/\omega_c}{1 + s/\omega_c} \tag{4.60}$$

where

$$\omega_c = \frac{1 + \frac{R_6}{R_5}}{R_{INT}C_{INT}} \tag{4.61}$$

Eq. (4.60) demonstrates how the ac differential gain is increased while dc offset is eliminated. Eq. (4.61) indicates however that the low-frequency cutoff is multiplied by the gain introduced by the negative feedback loop, which requires the time constant $R_{INT}C_{INT}$ to be multiplied by the same ratio to prevent signal distortion. Assuming a mid-band gain of 43 dB, a low-frequency cutoff below 0.05 Hz would suggest prohibitive values for R_{INT} and C_{INT}.

A differential amplifier having two ac-coupling stages

An alternative approach for obtaining large common-mode input impedance and large values of $\mathrm{CMRR}_{\Delta Z_{min}}$ is suggested in the circuit diagram given in Fig. 4.11. This solution, proposed

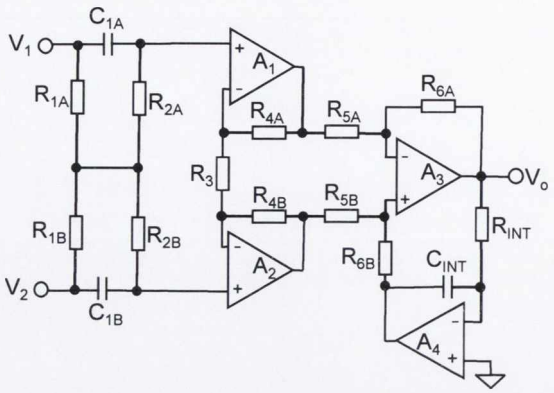

Figure 4.11: Circuit drawing of an instrumentation amplifier having two ac-coupling stages: a passive input stage and an active dc suppression circuit (modified from [166]).

by Spinelli et al in 2004 [166], has two ac-coupled stages and provides a bias path through the electrodes and the subject's body without grounded a resistor. A common biopotential electrode then drains the bias current from the patient's body to ground. The output voltage is therefore ideally given by:

$$V_o(s) = \left(1 + 2\frac{R_4}{R_3}\right)\left(\frac{R_5}{R_6}\right)\left(\frac{sR_2C_1}{1 + sR_2C_1}\right)\left(\frac{sR_{\mathrm{INT}}C_{\mathrm{INT}}}{1 + sR_{\mathrm{INT}}C_{\mathrm{INT}}}\right)(V_2(s) - V_1(s)) \qquad (4.62)$$

Active dc offset removal is performed at the output stage while electrode polarisation potentials are blocked at the input, enabling high differential gain to be implemented in the front-end stage. Because of the absence of grounded resistor, the fully differential passive network exhibits little sensitivity to matching conditions allowing CMRR performance greater than 120 dB at 50 Hz to be measured [166].

Appraisal of differential amplifiers without input ground reference

Amplification performed without input grounded resistors allows dc offset voltages originating at the skin-electrode interface to be eliminated while the circuit input impedance is preserved [16, 162, 167–171]. In fact, allowing bias currents to flow through the patient's body enables high CMRR values to be obtained, as is the case in dc-coupled ultra-high-input-impedance instrumentation amplifiers. Nevertheless, any bias current flowing through a subject's body will cause a voltage drop across the skin-electrode impedance, the magnitude of which can attain several MΩ in the case of dry electrodes. This dc current, which varies from a fraction of pA to several nA for some low-power op-amps, can also charge the capacitance of the electrodes generating additional unwanted in-band noise associated with motion and changes in the skin-electrode interface [172]. Differential amplifiers without input

ground resistors would therefore be difficult to implement with dry electrodes, considering the electrode characteristics previously measured.

4.3.3 Fully differential instrumentation amplifiers and differential ADCs

Fully differential instrumentation amplifiers are becoming increasing popular due to their high immunity to common-mode interference [117, 173–179]. Fully differential circuits provide a differential output that presents a higher dynamic range than their single-ended counterparts, which allows the differential gain to be doubled and results in further CMRR improvement. Pallás-Areny et al. have shown that the later the differential to single-ended stage is placed in the measurement chain, the higher the obtainable CMRR [152–155, 180]. A differential output can be obtained from a single-ended amplifier by creating a 180° out-of-phase copy of the single-ended output signal [181]. This strategy however requires multiple conversions that inevitably degrades signal quality and reduces dynamic range [117, 173]. The recent development of high-resolution analog-to-digital converters (ADCs) having differential inputs eliminates the need for single-ended conversion in the analogue signal processing chain. The following sections present two examples of fully differential amplifiers recently published by Spinelli et al [117, 173].

A fully differential ECG amplifier with active dc suppression

Ac-coupling is inevitable in dry-electrode ECG recording in order to block large dc offset voltages generated at the skin-electrode interface. This is commonly achieved with input dc-blocking capacitors and grounded resistors. However, in order to preserve the high immunity to common-mode interference provided by fully differential amplifiers, unmatched grounded components should be avoided. In addition, input serial capacitors do not remove the output offset voltage arising from op-amp offset voltages and bias currents following the ac-coupling stage. The solution presented in Section 4.3.2 including an integrator in the feedback loop of a differential to single-ended stage cannot obviously be considered in a fully differential topology. Fig. 4.12(a) is a block diagram of a fully differential ECG amplifier proposed by Spinelli et al. in 2004 that includes an active dc suppression circuit. The circuit implementation, given in Fig. 4.12(b) features a mechanism for fast recovery and startup.

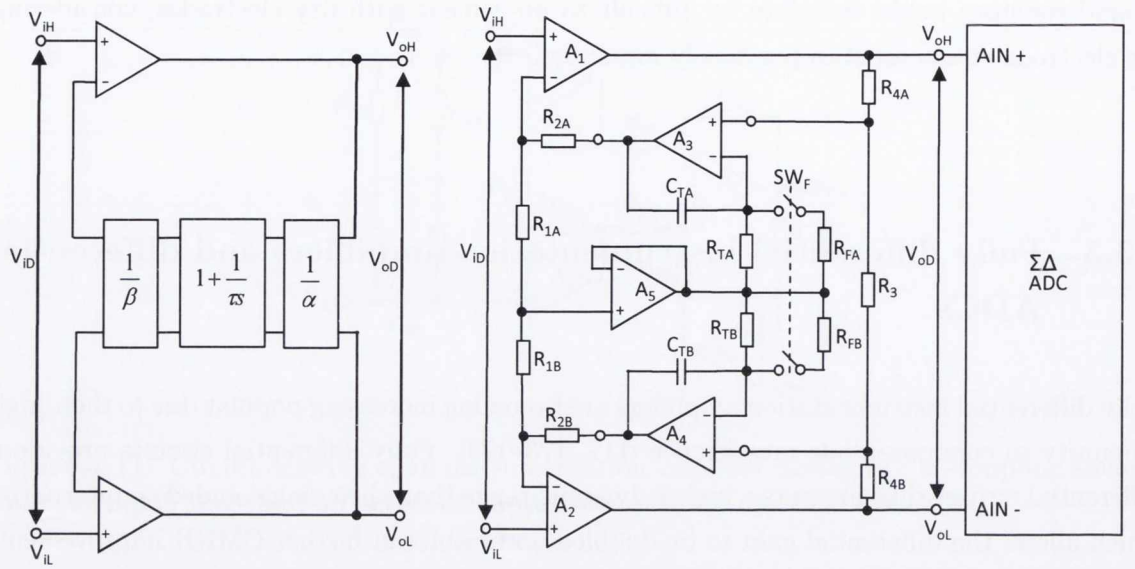

(a) Topology of a fully differential circuit for dc suppression.

(b) Implemented ECG amplifier based on the topoloy proposed by Spinelli et al.

Figure 4.12: Schematic diagrams of (a) the circuit topology and (b) the implementation of a fully differential ac-coupled ECG amplifier optimised for high CMRR value [117]. When switch SW_F is closed, the low resistance of $R_{\mathrm{TA}}//R_{\mathrm{FA}}$ and $R_{\mathrm{TB}}//R_{\mathrm{FB}}$ allows operation in "fast-recovery" mode since a reduced time constant is achieved.

Referring to Fig. 4.12(a), the transfer function of the fully differential stage is given as:

$$\frac{V_{\mathrm{oD}}(s)}{V_{\mathrm{id}}(s)} = \frac{\alpha\beta s\tau}{1+s\tau} \tag{4.63}$$

The mid-band gain is determined by $A_{\mathrm{d0}} = \alpha\beta$ and the low frequency cutoff is given as $\omega_c = 1/\tau$. The circuit implementation shown in Fig. 4.12(b) allows α, β and τ to be identified as follows:

$$\alpha = 1 + \frac{2R_4}{R_3} \tag{4.64}$$

$$\beta = 1 + \frac{2R_2}{R_1} \tag{4.65}$$

and

$$\tau = R_T C_T \tag{4.66}$$

where $R_1 = R_{1A} = R_{1B}$, $R_2 = R_{2\mathrm{A}} = R_{2B}$, $R_4 = R_{4\mathrm{A}} = R_{4\mathrm{B}}$, $R_T = R_{\mathrm{TA}} = R_{\mathrm{TB}}$ and $C_T = C_{\mathrm{TA}} = C_{\mathrm{TB}}$ under nominal condition. It is reported that, disregarding stray capacitance, the absence of connection to ground prevents common-mode voltages from being converted into differential components because the common-mode current is null. It results in a CMRR which is ideally infinite for the fully differential stage, despite passive component mismatch, as

in the case of the cross-coupling stage of the "classical" three-op-amp IA. In practice, however, the CMRR of this stage is limited by the performance of the op-amps. The proposed circuit having unity common-mode gain, the overall CMRR is determined by the performance of the differential ADC. A circuit was implemented with a single 5-V power supply, 1% tolerance resistors for R_1 to R_4, 10% tolerance resistors for R_T and 10% tolerance capacitors, aiming at a differential gain $A_{d0} = 56$ dB. The CMRR measured at the output of the differential ADC in the configuration shown in Fig. 4.12(b) was reported as 102 dB at 50 Hz.

A dual-mode conditioning circuit for differential ADCs

Fig. 4.13 shows the circuit diagram of a fully differential conditioning circuit that allows both common-mode and differential-mode components to be adapted to the signal levels and bandwidth suitable for a selected differential ADC. The circuit, presented by Spinelli et al. in January 2010, comprises a non-inverting fully differential front-end stage that provides high input impedance and high differential gain, and a dual-mode processing stage [173]. The first stage amplifies differential voltages by a nominal gain $A_{d0} = 1 + 2R_2/R_1$ but provides unity-gain for the common-mode components. The second stage maintains unity-gain for differential signals but attenuates common-mode signals. Capacitors C_{1A} and C_{1B} are inserted to provide bandwidth limitation for both modes, thus securing circuit stability.

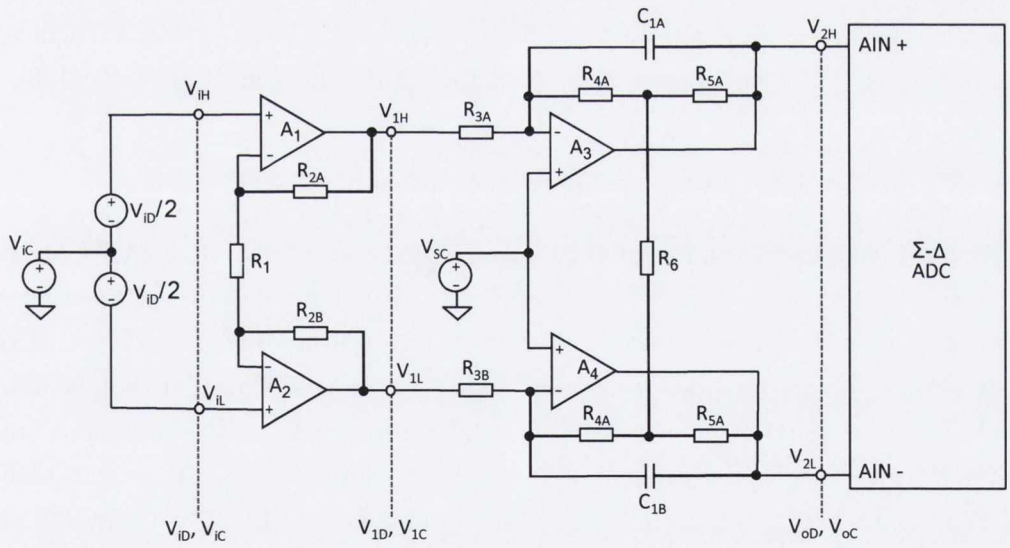

Figure 4.13: Schematic diagram of a dual-mode conditioning circuit for differential ADCs proposed by Spinelli et al. in 2010 [173]. V_{id} and V_{ic} are the differential and common-mode input voltages, respectively. V_{SC} is an auxilary dc source added to shift the dc common-mode at the amplifier output to a level compatible with the input common-mode range of the differential ADC. $V_{SC} = 2.9$ V for the published implementation.

Referring to Fig. 4.13, the differential and common-mode voltages at the output of the second stage are described as:

$$V_{\mathrm{oD}}(s) = V_{2H}(s) - V_{2L}(s)$$
$$= -V_{\mathrm{id}}(s)\left(1+\frac{2R_2}{R_1}\right)\left(\frac{R_4+R_5+2R_4R_5/R_6}{R_3}\right)\left[\frac{1}{1+s\left(R_4+R_5+2\frac{R_4R_5}{R_6}\right)C_1}\right] \quad (4.67)$$

and

$$V_{\mathrm{oc}}(s) = \frac{V_{2H}(s)+V_{2L}(s)}{2}$$
$$= -V_{\mathrm{ic}}\left(\frac{R_4+R_5}{R_3}\right)\left[\frac{1}{1+s\left(R_4+R_5\right)C_1}\right] + V_{\mathrm{SC}}\left(1+\frac{R_4+R_5}{R_3}\right) \quad (4.68)$$

The mid-band common-mode gain of the second stage is determined by $A_{\mathrm{c0}} = -\frac{(R_4+R_5)}{R_3}$. Making $R_3 >> (R_4+R_5)$ therefore allows common-mode voltages to be attenuated, while adjusting R_6 permits the differential gain to be controlled. However, residual common-mode signals are reproduced at the output due to the conversion of common-mode signals into a differential component, limiting the overall CMRR obtainable. The worst-case CMRR of the dual-mode conditioning circuit is given as $A_{\mathrm{d0}}/4\Delta_{\mathrm{R_{max}}}$, where $\Delta_{\mathrm{R_{max}}}$ is the manufacturing tolerance of the gain-determining resistors. A circuit providing $A_{\mathrm{d0}} = 200$ and $A_{\mathrm{c0}} = -1/5$ was constructed using 1% tolerance resistors and 5% tolerance capacitors. The CMRR measured at the output of the ADC was reported as 102 dB at 10 Hz and 106 dB at 1 Hz [173].

Appraisal of fully differential amplifiers and differential ADCs

Fully differential instrumentation amplifiers have been shown to exhibit higher CMRR performance than single-ended amplifiers when employed with high-resolution differential ADCs and some examples of their use have been reported in the literature [117, 173, 179]. $\mathrm{CMRR_{ADC}}$, the common-mode rejection ratio of a differential ADC, is generally greater than 90 dB. This is 56 dB higher than $\mathrm{CMRR}_{\Delta R}$ provided by a difference amplifier at the output stage of the "classical" three-op-amp instrumentation amplifier analysed in Section 4.2.2, assuming 1% tolerance resistors. Given a nominal differential gain A_{d0} provided by a fully differential amplifier, the CMRR obtainable at the output of a differential ADC is given by the product $A_{\mathrm{d0}}\mathrm{CMRR_{ADC}}$. Since higher differential gains can be implemented with fully differential amplifiers, ultra-high CMRR performance is theoretically conceivable. For similar CMRR performance to be obtained with the standard three-op-amp IA structure, manufacturing tolerance in the gain-defining resistors would need to be lower than 0.0001%.

In addition, low-cost high-resolution differential ADCs that operate at low voltage from a

single-rail supply are commonly available today, making them suitable for portable battery-powered applications. Nevertheless, several limitations to the performance of such techniques exist:

1. Securing high immunity to common-mode interference requires amplification without grounded resistors. As discussed in the previous section, this approach necessitates bias currents to flow back into the patient's body, which is inadvisable in dry-electrode ECG recording due to the nature of the skin-electrode interface characterised in Chapter 3.

2. Single-supply operation without grounded resistors requires the body to be biased at half-rail. Consequently, any variation of the dc level on the subject will result in unwanted changes in the ECG base line.

3. High-resolution fully differential ADCs available today dissipate more power than their single-ended counterparts, which presents a major limitation for designs aiming at ultra-low power.

4.3.4 Bootstrapping techniques

Other circuit designs have allowed the amplifier's input impedance to be increased by reducing the magnitude of the input current via positive feedback, as shown in Figs. 4.14 to 4.16. These techniques are referred to as bootstrapping and can be achieved using capacitive or resistive feedback [33–36, 126, 143, 152, 156, 164, 182–190].

Composite instrumentation amplifiers

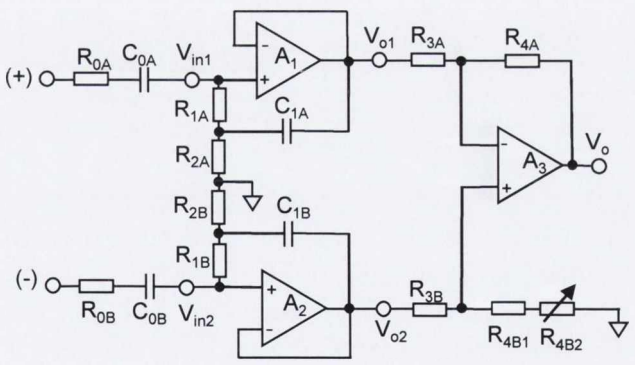

Figure 4.14: Circuit drawing of a composite amplifier [143, 156, 188].

Fig. 4.14 is the schematic diagram of a composite instrumentation amplifier presented by Pallás-Areny & Webster in 1990 [143]. Op-amps A_1 and A_2 operate as impedance transform-

ing unity-gain buffers providing a frequency-dependent input impedance defined as:

$$Z_{\text{in}}(s) = R_1 + R_2 + sC_1R_1R_2 \tag{4.69}$$

Eq. (4.69) indicates that the magnitude of the input impedance increases linearly with frequency, allowing very large values to be obtained at 50 or 60 Hz. The conversion of common-mode signal into differential components due to electrode impedance imbalance is therefore significantly reduced at the power line frequency. Values of CMRR as high as 126 dB at 60 Hz have been reported for this circuit, achieved by the adjustment of resistor R_{4B2}, as outlined earlier in Section 4.3.1 [143].

It must be noted, however, that the input impedance is closely approximated by $R_1 + R_2$ at low-frequency. As discussed in Chapter 3, fulfilling the low-frequency performance requirements specified in international standards would therefore necessitate the resistance of each resistor to be greater than 1 GΩ. Alternatively, the capacitance of feedback capacitor C_2 can be increased, but this would quickly lead to prohibitive values, not available in non-electrolytic form.

Dc bootstrapped amplifiers

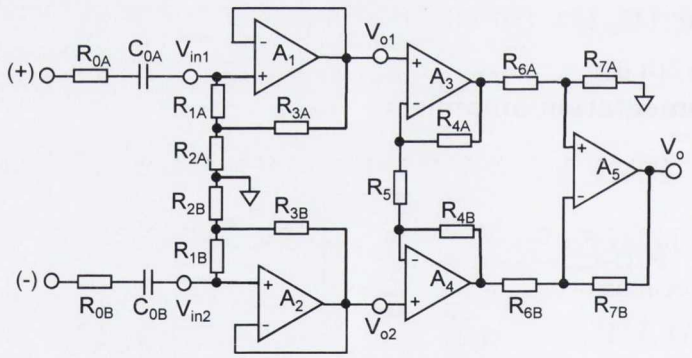

Figure 4.15: Schematic showing an IA employing two bootstrapped buffers with biasing resistor at its front-end stage (modified from [185]).

The circuit diagram shown in Fig. 4.15 allows the input impedance to be increased at all frequencies, down to dc. It can be shown that impedance seen at each input of the amplifier is purely resistive and is given by:

$$R_{\text{in}} = R_1 + R_2 + \frac{R_1R_2}{R_3} \tag{4.70}$$

Taking $R_3 << \{R_1, R_2\}$ yields ultra high values for R_{in}, allowing both the input impedance and the CMRR to be significantly increased at all frequencies. Lányi & Pisani reported values of input resistance as high as 350 GΩ with this structure [185]. The obtainable CMRR of the buffer stage was therefore principally limited by the finite CMRR of the op-ams employed.

A single-rail supply purely resistive bootstrapped amplifier

Burke & Gleeson have presented a purely resistive bootstrapped amplifier operating from a single-rail supply, illustrated in Fig. 4.16 [34–36].

It can be shown that the nominal input impedance achieved by this circuit is closely approximated by:

$$R_{\text{in}} = R_1 \left[1 + \frac{R_2 // (R_3 + R_2 // R_4)}{R_4} \right] \tag{4.71}$$

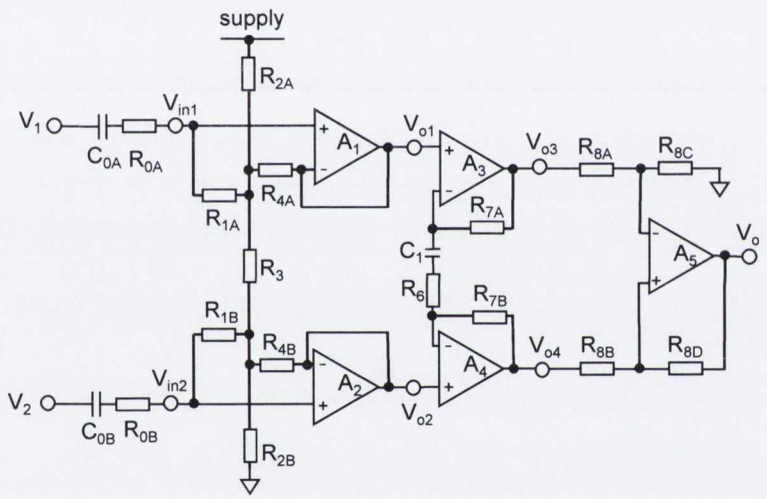

Figure 4.16: Circuit diagram of the amplification channel of an IA implementing a purely resistive input resistance multiplication mechanism at its front-end stage. The circuit, operating from a single-rail supply, was presented by Burke & Gleeson in 1999 (modified from [34–36]).

The main advantage of this solution resides in the ability to define the dc-bias voltage at each input via the biasing resistors $R_{2\text{A}}$, R_3 and $R_{2\text{B}}$ without degrading the amplifier's input impedance, allowing $\text{CMRR}_{\Delta Z}$ to be preserved. Another feature of the design suggested by Burke & Gleeson is the distribution of the differential gain over three amplification stages. The front-end stage, the second differential-to-differential stage and the final differential-to-single-ended stage provide gains of 13 dB, 25.6 dB and 6 dB, respectively. The overall mid-band gain is therefore 44.6 dB. However, as suggested earlier in Section 4.2.2, the repartition of the differential gain over three stages degrades the CMRR due to manufacturer tolerances

in the gain-determining resistors.

Appraisal of bootstrapping techniques

Several variations of the fundamental bootstrapping structures discussed above have been published [126, 182–184, 186, 187, 190]. In general, bootstrapping techniques offer the advantage of augmenting the amplifier input impedance without requiring excessively large resistor values and allow the effect of varying electrode impedance to be minimised. Ac bootstrapped amplifiers achieve high common-mode rejection at power-line frequency while the common-mode input impedance at dc remains small. This permits the effect of common-mode displacement currents resulting from unwanted external voltages to be minimised at low frequency and the offset voltages due to op-amp bias currents to be limited to low values. However, performance related to the frequency response of the skin-electrode-amplifier network is difficult to fulfil with this arrangement, particularly with dry electrodes.

Bootstrapping which relies on positive resistive feedback facilitates compliance with both low-frequency performance requirements and CMRR specifications. Bootstrapped amplifiers with resistive feedback as shown in Fig. 4.15 can easily be implemented with circuits operating from symmetrical dual supply, while the solution proposed by Burke & Gleeson offers the facility to operate at ultra-low power from a single-rail supply. The overall CMRR of the amplifier is limited by errors introduced by imbalanced electrodes and resistors. The recording system designed by Burke & Gleeson requires a driven-right-leg circuit to enhance the rejection of common-mode voltages.

4.3.5 Driven-right-leg circuits

Because power line and other external unwanted voltages are capacitively coupled to the subject being monitored, they produce a displacement current that flows through the body. The conducting nature of the body causes a potential difference to appear at any two points on the surface of the skin. An effective method for improving the suppression of common-mode contaminating signals in ECG recording consists therefore of using one or more CMRR enhancement techniques discussed above concurrently with a body potential driver. Driven-right-leg circuits are the most commonly employed body potential drivers in three-electrode ECG recording [34–36, 60, 147, 168, 191–194]. The common-mode voltage is sensed and fed back to the body via a third (common) electrode after inversion and amplification, as depicted in Fig. 4.17.

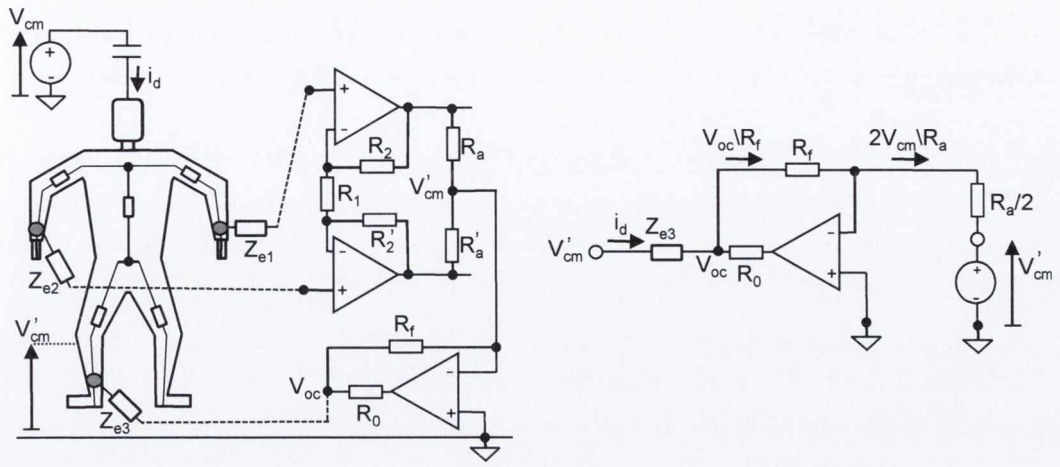

(a) Right-leg-drive arrangement for minimising common-mode interference.

(b) Equivalent driven-right-leg circuit.

Figure 4.17: Diagrams showing (a) the principle of operation of a driven-right-leg system and (b) its equivalent circuit (modified from [60]).

Referring to Fig. 4.17 the potential at the output of the driven-right-leg circuit is given in terms of the common-mode voltage, V'_{cm}, and the resulting displacement current, i_d, as:

$$V_{\mathrm{oc}} = V'_{\mathrm{cm}} - Z_{\mathrm{e3}} i_d \tag{4.72}$$

where Z_{e3} is the impedance of the common electrode. A second expression for V_{oc} can be obtained as a function of the gain of the inverting amplifier:

$$V_{\mathrm{oc}} = -\frac{R_{\mathrm{f}}}{R_{\mathrm{a}}/2} V'_{\mathrm{cm}} \tag{4.73}$$

Equating eqs. (4.72) and (4.73) results in a definition of the amplitude of the common-mode voltage given by:

$$V'_{\mathrm{cm}} = \left(\frac{Z_{\mathrm{e3}}}{1 + 2R_{\mathrm{f}}/R_{\mathrm{a}}} \right) i_{\mathrm{d}} \tag{4.74}$$

The method is therefore effective in improving the overall CMRR of the recording system by allowing the common-mode signal on the body, V'_{cm}, to be reduced by the gain of the driven-right-leg circuit compared to the common-mode voltage which exists without the right-leg-drive.

4.3.6 CMRR enhancement of two-electrode instrumentation amplifiers

Ambulatory ECG recording obtained from two electrodes is attractive because of the simplicity of electrode placement. A large number of ECG amplifiers have thus been designed to provide high CMRR performance in a two-electrode configuration [164, 184, 189, 195–198]. This approach, however, would be difficult to implement with most dry electrodes previously tested because of the inherently high electrode impedance that limits the CMRR obtainable. Two-electrode ECG amplifiers have therefore been reserved to recording systems employing wet electrodes which exhibit low resistance to current.

New prospects offered by the development of ultra-low-impedance dry electrodes

The recent development of ultra-low-impedance dry electrodes has shown new prospects in the realisation of long-term AECG monitoring in the near future. Measurement results published in May 2010 by Chang et al. [19] are shown in Fig. 4.18. It is suggested that the magnitude of the skin-electrode impedance using the novel dry electrode without skin preparation (i) does not exceed 10 kΩ in the frequency range 0.5 Hz to 10 kHz and (ii) is consistently lower than that measured from wet electrodes after skin abrasion.

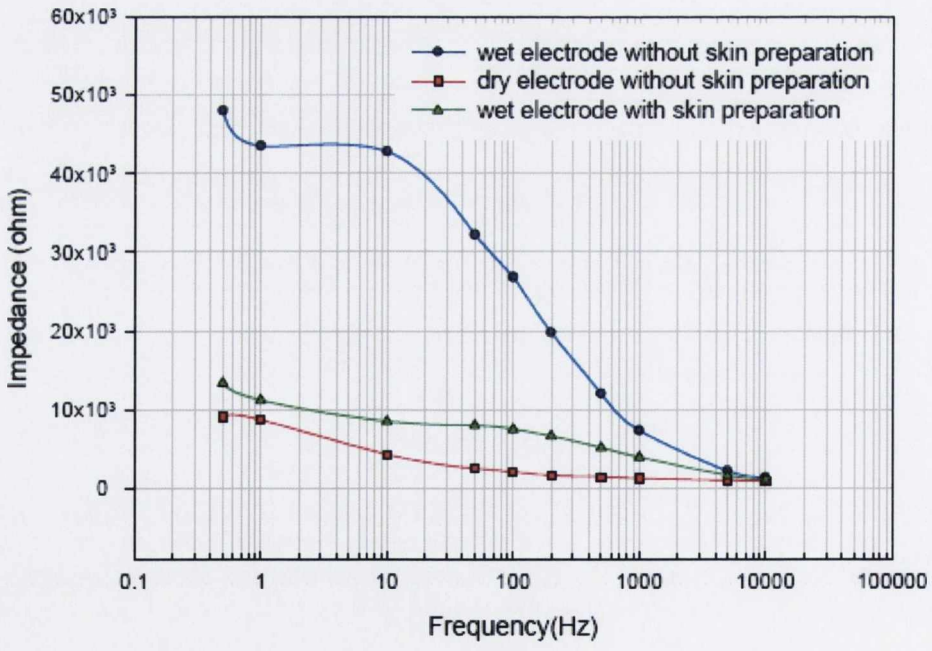

Figure 4.18: Measurement of skin-electrode impedance published by Chang et al. using a novel microelectromechanical dry electrodes compared with results obtained with standard wet electrodes [19].

As previously derived in Section 4.2.1, the common-mode rejection ratio due to impedance imbalance is given by:

$$|\text{CMRR}_{\Delta Z}|_{\text{dB}} = 20\log_{10}\left(\frac{R_{\text{c}}}{|Z_{\text{e}}|}\right) + 20\log_{10}\left(\frac{1-\Delta_{\text{c}}^2}{2\left(\Delta_{\text{c}}+\Delta_{\text{e}}\right)}\right) \tag{4.75}$$

In ac-coupled ECG recording, the impedance of the dc-blocking capacitor, C_{in}, and the current limiting resistor, R_1, must be included in $|Z_{\text{e}}|$. Two approaches are therefore possible for maximising $\text{CMRR}_{\Delta Z}$:

1. The impedance associated with C_{in} and R_1 can be made large to limit the variation Δ_{e} to component tolerances. For example, taking $\Delta_{\text{e}} = \Delta_{\text{c}} = 3\%$, $R_{\text{c}} = 2$ GΩ and $|Z_{\text{e}}| =$ 500 kΩ at 0.5 Hz would result in $\text{CMRR}_{\Delta Z} \geq 90$ dB.

2. Alternatively, the impedance associated with C_{in} and R_1 can be made small to reduce $|Z_{\text{e}}|$. For example, assuming $\Delta_{\text{e}} = 10\%$, $\Delta_{\text{c}} = 3\%$, $R_{\text{c}} = 2$ GΩ and $|Z_{\text{e}}| = 50$ kΩ at 0.5 Hz yields $\text{CMRR}_{\Delta\text{Z}} \geq 93$ dB.

For safety reasons, the first solution is therefore preferable since R_1 must be sufficiently large to protect the patient against electrical faults that might originate in the recording equipment. This can easily be achieved with $R_1 = 100$ kΩ and $C_{\text{in}} = 0.47$ µF, for example.

Using ultra-low-impedance electrodes is therefore an effective means of enhancing the CMRR due to impedance imbalance.

A two-electrode ECG amplifier circuit concept proposed by Dobrev

Fig. 4.19 shows the shematic diagram of a low-voltage, low-power, two-electrode instrumentation amplifier, designed to achieve a differential gain in the range 46 to 60 dB and a CMRR greater than 60 dB from 0.05 Hz to 100 Hz using 1 % resistors.

The amplifier circuit concept, published in 2004 by Dobrev, includes a capacitor that prevents amplification of the electrode polarisation potential. The 3-dB response is determined by resistor R_3 and capacitor C_1 while the differential gain is essentially set by the ratio $\frac{R_1}{R_2//R_3}$, as indicated in eq. (4.76):

$$A_{\text{d}} = \left(1+\frac{R_1}{R_2//R_3}\right)\frac{2R_3Cs}{1+2R_3Cs} \tag{4.76}$$

For $R_2 << R_3$, the nominal differential gain can be closely approximated by $A_{\text{d0}} = 1+R_1/R_2$. The minimum common-mode rejection ratio due to manufacturing tolerances in the gain-determining resistors is given as:

$$\text{CMRR}_{\Delta\text{R}_{\text{min}}} = 1.5\left(\frac{A_{\text{d0}}}{4\Delta_{max}}\right) \tag{4.77}$$

Eq. (4.77) suggests that $CMRR_{\Delta R_{min}}$ is 3.5 dB greater than that of a two-op-amp IA but 2.5 dB less than what is achieved by the standard three-op-amp IA. The selected op-amps providing a minimum CMRR of 75 dB, the resulting CMRR of the constructed circuit was measured at 66 dB for a mid-band differential gain of 46 dB.

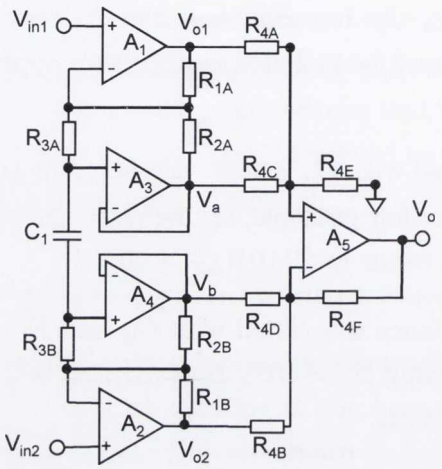

Figure 4.19: Schematic diagram of a two-electrode ECG amplifier proposed by Dobrev (modified from [197]).

Appraisal of two-electrode amplification

Two-electrode ECG recording is possible in dry-electrode AECG if low-impedance electrodes are employed, which ensures high values of $CMRR_{\Delta Z}$. When op-amps with high CMRR performance are used, the limiting factor of the overall obtainable CMRR of the circuit resides in imbalance caused by mismatched resistors. The solution proposed by Dobrev includes an attractive ac-gain stage that effectively prevents the amplification of electrode polarisation potentials without requiring large capacitor values. Nevertheless, the following shortcomings must be ponited out:

1. This configuration permits bias current to flow through the subject's body.

2. The solution presented suffers from a small reduction in $CMRR_{\Delta R}$.

4.3.7 Discussion

Considering the contribution of the three factors responsible for the overall CMRR of the recording system ($CMRR_{\Delta Z} = 58$ dB, $CMRR_{\Delta R} = 74$ dB and $CMRR_{op} = 64$ dB), the CMRR was estimated at 54 dB. Given the magnitude of the electrode impedance previously measured, the common-mode rejection ratio due to impedance mismatch has been identified as

the principal limitation of the overall CMRR obtainable. Therefore employing high precision resistors, high CMRR op-amps or trimming techniques would provide little CMRR enhancement at the expense of additional cost and power consumption, since the improvement would be limited to 4 dB if $\text{CMRR}_{\Delta R}$ and CMRR_{op} were made infinite.

Bootstrapping mechanisms present a suitable solution for obtaining high values of input impedance without requiring prohibitive resistor values. An amplifier employing a bootstrapped buffer with biasing resistors may exhibit input impedance performance in the order of hundreds of GΩ if operating from dual supply-rail. The modification suggested by Burke & Glesson offers, however, a more attractive solution for a design aiming for low-power consumption and operation from a single-rail supply. The allocation of the gain among the differential amplification stages must be revisited in order to prevent degradation of the CMRR due to resistor mismatch.

Although, ultra high input impedance is not advisable since it may result in large dc offsets due to the op-amps bias currents. For example, the maximum bias current is 10 pA in low-power op-amps from the MAX400 series. A maximum input offset current $I_{OS_{max}} = 20$ pA may therefore result from imbalance between the two op-amps at the front-end, causing a resulting input offset voltage $V_{OS_{max}} = R_{\text{in}} I_{OS_{max}}$. Considering the input impedance requirement established in Chapter 3 ($R_{\text{in}} \geq 2$ GΩ) yields $V_{OS_{max}} = 40$ mV. In practice, the input offset current is reduced by having the two op-amps fabricated on the same chip. Nevertheless, any increase in the value of R_{in} increases the input offset voltage proportionally, which may then be amplified in the subsequent gain stages. It is therefore preferable to restrict R_{in} to 2GΩ and improve the CMRR of the recording system by implementing a driven-right-leg circuit so that:

$$\text{CMRR} = 20\log_{10}(\text{G}) + \frac{1}{\frac{1}{\text{CMRR}_{\Delta\text{Z}}} + \frac{1}{\text{CMRR}_{\Delta\text{R}}} + \frac{1}{\text{CMRR}_{\text{op}}}} \tag{4.78}$$

where G is the gain of the inverting amplifier in the driven-right-leg circuit, which must exceed 41 dB if $CMRR > 95$ dB is to be obtained.

New opportunities will be made available in the near future with the development of low-impedance dry electrodes, constituting a very effective means of securing high CMRR values. Consequently, performance will no longer be dictated by impedance imbalance at the amplifier input but will reside to a greater extent in the circuit amplification channel. The use of op-amps having high CMRR performance together with low-tolerance resistors and capacitors will therefore have a noticeable impact on the rejection of common-mode interfering signals. This, however, shall involve increased power consumption and additional cost.

4.4 Conclusion

This chapter has put the emphasis on the necessity for the recording amplifier to suppress contaminating common-mode components in order to obtain an ECG signal of diagnostic quality. The common-mode rejection ratio was defined as a measure of the performance of the recording system in this regard and several amplifier structures were considered. The analysis of the CMRR of the "classical" three-op-amp instrumentation amplifier has allowed limiting factors to be quantified based on previous measurements. It was concluded that modification of the standard structure is necessary for performance requirements to be met. A non-exhaustive review of existing circuits has allowed the effectiveness of a limited number of approaches that may be employed for enhancing the common-mode rejection performance of ECG preamplifiers to be evaluated. The following developments are therefore proposed by the author:

- A design aiming for ultra-low power consumption and single-rail supply operation will be based on the amplifier structure invented by Burke & Gleeson. The amplification stages will be modified and the driven-right-leg stage will be revisited to maximise the CMRR obtainable. This solution will target a mid-band differential gain of 40 dB and a CMRR of 95 dB when coupled with the dry electrodes previously tested.

- Taking into account recent developments in dry electrodes technology, alternative instrumentation amplifier structures that offer the possibility of operating in either two- or three-electrode configurations will be explored, in an effort to enhance the CMRR limited by manufacturing tolerances in the gain-determining resistors.

Chapter 5

Design of a very-low-power single-supply dry-electrode ECG preamplifier

Despite the development of digital integrated circuits, op-amps remain the primary building block for the implementation of instrumentation amplifiers used in biopotential measurements. Because op-amps are conventionally intended for dual supply operation, dc-dc converters are generally employed in battery-powered portable systems for providing a dual supply rail without requiring the use of an additional battery cell [199–203]. This solution is attractive for consumer devices because it eliminates the need for replacing or recharging multiple batteries. However, charge-pumps and other commonly used voltage converters and regulators require additional space on the circuit board and usually come at the expense of increased cost and power consumption, which presents major inconveniences for designs aiming at ultra-low power. The use of a single-rail supply therefore constitutes a more effective solution. Equipment operating from a single voltage supply allows cost and circuit complexity to be reduced, since a single supply source can provide power to all components of the system. The need for a dc-dc converter is hence eliminated, offering the opportunity for additional savings in power consumption and reduction in circuit size. Battery life can be further extended by minimising the quiescent current drawn by the circuit. This is achieved by increasing the values of bias resistors and selecting ultra-low-power op-amps. In general, adapting op-amps designed for dual supply to operate from a single rail permits a lower supply voltage to be used, which further reduces power dissipation [202, 204, 205]. In addition, circuit reliability is improved because components operating at voltage levels much lower than the maximum rating generally last longer [204]. However, performance has occasionally been sacrificed for the convenience of working from a single supply [199–205]. The

This work has been published in part in [50, 51]

reduction of the operating supply voltage introduces additional design constraints caused by possible "headroom" problems limiting the op-amp input dynamic range. Furthermore, the input common-mode range becomes a more critical parameter when op-amps designed for dual rail operation are used in a single-supply configuration [204]. These limitations have been overcome by the development of op-amps designed and fabricated for a single supply that provide rail-to-rail input and output voltage swing [204, 205]. Nevertheless, performance related to bandwidth, slew rate and CMRR remain restricted in devices optimised for low supply voltage and ultra-low quiescent current.

This chapter presents the approach undertaken by the author in designing an ultra-low-power ECG preamplifier operating from a single-rail supply for use with the pasteless electrodes previously characterised in Chapter 3. The author proposes an instrumentation amplifier structure optimised for high rejection of unwanted external voltages and enhanced low-frequency performance. Op-amps are selected and component values determined on the basis of essential performance requirements related to frequency response considerations, input impedance, CMRR, dc bias conditions, power consumption and intrinsic noise discussed in previous chapters. The design strategy therefore comprises the following stages:

1. Selection of an instrumentation amplifier structure adapted for single-rail supply. The solution published by Burke & Gleeson in 2000 combines high-input impedance and ultra-low power consumption [34–36].

2. Modification of the circuit structure and selection of op-amps. Redistribution of the differential gain allows common-mode to differential signal conversion to be minimised and dc offset variations to be reduced. Suitable low-cost ultra-low-power high-precision op-amps currently available are retained.

3. Determination of the input impedance characteristics of the circuit and identification of the required values of resistors at the front-end stage.

4. Establishment of the CMRR performance of the recording system coupled to imbalanced skin-electrode impedances.

5. Determination of the amplifier frequency response and implementation of a compensation scheme for preventing instability and ringing in the impulse response.

6. Estimation of the range of dc offset variation of the output voltage to assess the risk of saturation.

7. Validation: Simulation results using PSpice allow the performance of the recording system to be assessed considering worst-case operating conditions.

5.1 Selection of a suitable amplifier circuit structure

5.1.1 A micropower dry-electrode ECG preamplifier proposed by Burke & Gleeson

A number of instrumentation amplifier circuit structures were reviewed in Section 4.3 of Chapter 4 and a suitable solution for single-supply operation was identified as the circuit arrangement suggested by Burke & Gleeson, shown in detail in Fig. 5.1 [34–36].

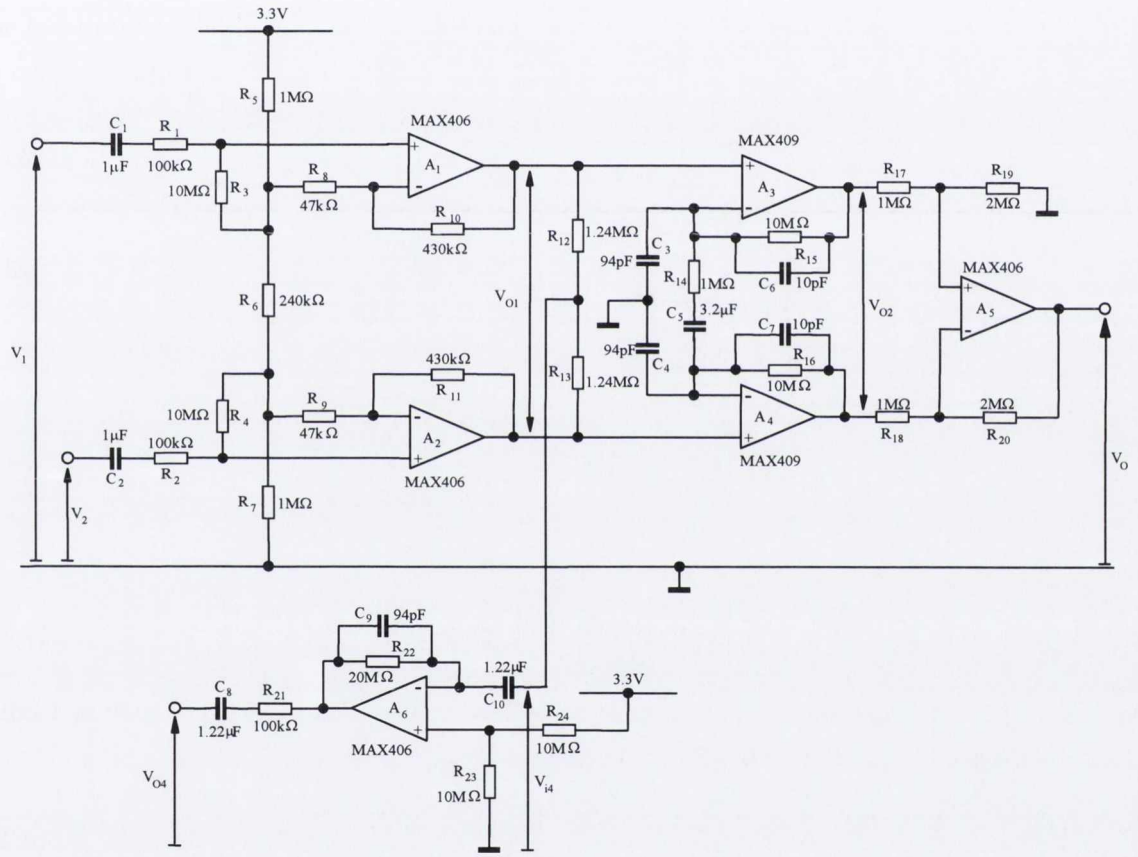

Figure 5.1: Schematic diagram of the micropower dry-electrode ECG preamplifier designed and constructed by Burke & Gleeson [34–36].

The ECG amplifier presented in Fig. 5.1 dissipates less than 30 μW in power operating from a 3.3-V battery. Detailed description of the circuit structure is given in [34–36, 50, 51] and the main features are summarised below.

The front-end stage

A key advantage of the front-end stage invented by Burke & Gleeson over other bootstrapping techniques reviewed in Section 4.3.4 of Chapter 4 resides in its ability to combine very high input impedance and single-supply operation without requiring unduly large values of resistors. Resistors R_5, R_6 and R_7 allow the operating bias voltages at the input terminals of op-amps A_1 and A_2 to be defined as 1.826 V and 1.473 V, respectively [36]. Resistors R_3 and R_4 are used to define the input resistance on each side of the amplifier. The lower ends of these resistors are connected to either side of resistor R_6 which receives positive feedback from the outputs of op-amps A_1 and A_2 via resistors R_8 and R_9, respectively [34, 35, 50, 51]. This bootstrapping mechanism allows the magnitude of the currents flowing across R_3 and R_4 to be reduced, making their resistance appear much higher at the amplifier inputs. The common-mode input resistance is given as $R_c = 260$ MΩ and the differential input resistance is set at $R_d = 75$ MΩ, obtained with standard off-the-shelf 1% resistors. Referring to Fig. 5.1, the transfer function of this stage for a differential input $V_{id} = V_1 - V_2$ is determined by:

$$\frac{V_{o1}(s)}{V_{id}(s)} = \left[1 + \frac{R_{10}}{R_8 + \frac{R_5 R_6}{2R_5+R_6}}\right]\left[\frac{sC_1\left(\frac{R_c R_d}{2R_c+R_d}\right)}{1 + sC_1\left(\frac{R_c R_d}{2R_c+R_d}\right)}\right] \tag{5.1}$$

where R_c and R_d given as follows:

$$R_c = R_3\left[\frac{R_8 + \frac{R_5(R_6+R_8)}{R_5+R_6+R_8}}{R_8}\right]\left(1 + \frac{R_5}{R_6+R_8}\right) \tag{5.2}$$

and

$$R_d = R_3\left[\frac{R_8 + \frac{R_5(R_6+R_8)}{R_5+R_6+R_8}}{R_8}\right]\left(1 + \frac{R_6+R_8}{R_5}\right) \tag{5.3}$$

This stage acts therefore as a high-pass filter providing a mid-band differential gain of 13 dB and a low-frequency cutoff at 0.002 Hz defined by:

$$\omega_{c1} = \frac{1}{\left(\frac{R_c R_d}{2R_c+R_d}\right)C_1} \tag{5.4}$$

The second fully differential stage

The second stage of the amplifier is a differential-input-differential-output stage that provides a differential mid-band gain of 25 dB. The presence of capacitor C_5 in series with the gain defining resistor R_{14} limits the dc gain to unity, resulting in a transfer function given by:

$$\frac{V_{o2}(s)}{V_{o1}(s)} = 1 + \frac{2sC_5R_{15}\left(1 + s\frac{C_3R_{14}}{2}\right)}{\left(1 + sC_6R_{15}\right)\left(1 + s\frac{C_3R_{14}}{2}\right)} \tag{5.5}$$

Unwanted peaking in the frequency response within the amplifier 3-dB bandwidth was previously reported by Burke & Gleeson [34–36]. The problem was identified being caused by parasitic capacitances at the input of op-amps A_3 and A_4 introducing a zero in the amplifier transfer function. Capacitors C_6 and C_7 are added at the op-amp non-inverting inputs to define the zeros more reliably [34–36, 50, 51]. Capacitors C_{15} and C_{16} are then included in parallel with resistors R_{15} and R_{16} to introduce poles which cancel these zeros by making $2C_6R_{15} = 2C_7R_{16} = C_3R_{14} = C_4R_{14}$. This allows eq. (5.5) to be reduced to:

$$\frac{V_{o2}(s)}{V_{o1}(s)} = \left(1 + \frac{2R_{15}}{R_{14}}\right)\left(\frac{s + \frac{\omega_{c2}}{1+2R_{15}/R_{14}}}{s + \omega_{c2}}\right) \tag{5.6}$$

Where ω_{c2} is defined by:

$$\omega_{c2} = \frac{1}{R_{14}C_5} = 0.284 \text{ rad/s} \tag{5.7}$$

Capacitors C_1, C_2 and C_5 are chosen to achieve $\omega_{c1} = \omega_{c2}/\left(1 + 2R_{15}/R_{14}\right)$ which permits the low-frequency response of the combined first and second stages to be that of single-pole at 0.05 Hz [34–36, 50, 51], resulting in a transfer function given by:

$$\frac{V_{o2}(s)}{V_{id}(s)} = \left(1 + \frac{2R_{15}}{R_{14}}\right)\left(1 + \frac{R_{10}}{R_8 + \frac{R_5R_6}{2R_5+R_6}}\right)\left(\frac{s}{s + \omega_{c2}}\right) \tag{5.8}$$

The final output stage

A standard dc-coupled difference amplifier is built around op-amp A_5 to provide a single-ended output signal to the subsequent conditioning stages. The gain of this final output stage is given by $R_{19}/R_{17} = 6$ dB. The output voltage resulting from a differential input V_{id} is determined by the combined effect of the three differential stages and is described as:

$$\frac{V_o(s)}{V_{id}(s)} = \frac{R_{19}}{R_{17}}\left(1 + \frac{2R_{15}}{R_{14}}\right)\left(1 + \frac{R_{10}}{R_8 + \frac{R_5R_6}{2R_5+R_6}}\right)\left(\frac{s}{s + \omega_{c2}}\right) \tag{5.9}$$

The driven-right-leg stage

The CMRR of the ECG recording system is enhanced by the use of a driven common electrode, as previously demonstrated in Section 4.3.5 of Chapter 4. Resistors R_{12} and R_{13} sense the common-mode output signal from the first stage of the amplifier. The common-mode voltage is inverted and amplified in the stage built around op-amp A_6 and is then fed back to the right leg electrode via resistor R_{21} and capacitor C_8. This signal is therefore effectively subtracted from the common-mode interfering signal present at the amplifier input and has the effect of increasing the rejection of common-mode input signals by a factor equal to the gain of the inverting stage, which is set at 30 dB [34–36]. The non-inverting input terminal

of op-amp A_6 is connected to a virtual ground defined as 1.65 V by resistors R_{23} and R_{24}, enabling the amplifier to operate from a single-rail supply. Capacitor C_{10} blocks dc voltages present at the input of the inverting amplifier while capacitor C_9 limits its bandwidth in order to prevent instability at high frequency.

5.1.2 Limitations of the original design

The recording system designed and constructed by Burke & Gleeson was optimised for ultra-low power consumption and secured linear magnitude and phase response within the ECG bandwidth. However, performance related to the system impulse response was not considered, resulting in characteristics that fall short of meeting the recommendations issued by the AHA in 1990 [110]. In addition, a number of shortcomings related to the amplifier CMRR performance and dc offset variation under worst-case conditions must be addressed.

Limited input impedance characteristics

A new minimum input resistance requirement for dry-electrode electrocardiography was derived in Chapter 3 as 2 G Ω for low-frequency components in the ECG signal to be preserved in the presence of the skin-electrode interface. Given $R_c = 260$ MΩ and $R_d = 75$ MΩ, it results in an overall resistance seen at the input of the circuit shown in Fig. 5.1 defined by $R_d//(2R_c) \simeq 66$ MΩ. It can be concluded that the original solution presented by Burke & Gleeson is not readily adapted to the dry electrodes previously characterised.

Limited worst-case CMRR

Limited common-mode input impedance results in reduced values for $CMRR_{\Delta Z}$, the common-mode rejection ratio due to impedance imbalance at the amplifier input. Considering a worst-case magnitude of approximately 4 MΩ for the electrode impedance and a worst-case imbalance of 33% at the skin-electrode interface yields a minimum value for $CMRR_{\Delta Z}$ inferior to 40 dB, given $R_c = 260$ MΩ. The right-leg-drive circuit should then provide a gain greater than 55 dB if an overall CMRR performance of 95 dB is to be achieved from 0.5 Hz to 100 Hz, as established in Chapter 4. Gains of this magnitude are difficult to implement because of the limited gain-bandwidth product of op-amp A_6 which is given by the manufacturer as 4 kHz (min.). The 3-dB bandwidth of the inverted amplifier would therefore be limited to 6.5 Hz with a gain of 55 dB. Moreover, such practice is not advisable since studies published by Winter and Webster suggest that instability may be experienced at the bandwidth limit of driven-right-leg circuits when large gains are implemented [194].

In addition, the allocation of the differential gain among three amplification stages diminishes $CMRR_{\Delta R}$, the common-mode rejection ratio due to manufacturing tolerances in

the gain-defining resistors. Referring to Fig. (5.1), the differential voltage at the output of the front-end stage is described in eq. (5.10) by:

$$\begin{aligned} V_{o1} = V_1 & \left[1 + \frac{R_{10}\left[\left(R_5+R_8\right)\left(R_7+R_9\right)+R_5R_8\right]+R_{11}R_7R_9}{R_7R_9\left(R_5+R_8\right)+R_5R_8\left(R_7+R_9\right)+R_3\left(R_5+R_8\right)\left(R_7+R_9\right)}\right] \\ & - V_2\left[1 + \frac{R_{11}\left[\left(R_5+R_8\right)\left(R_7+R_9\right)+R_7R_9\right]+R_{10}R_5R_8}{R_7R_9\left(R_5+R_8\right)+R_5R_8\left(R_7+R_9\right)+R_3\left(R_5+R_8\right)\left(R_7+R_9\right)}\right] \\ & = \left[1 + \frac{R_{10}}{R_8 + \frac{R_5R_6}{2R_5+R_6}}\right]\left(V_1 - V_2\right) + \epsilon\left(\Delta_{R_{max}}\right)\frac{\left(V_1+V_2\right)}{2} \end{aligned} \tag{5.10}$$

where $\epsilon\left(\Delta_{R_{max}}\right)$ is an error resulting from mismatch in resistor values. Eq. (5.10) suggests that imbalance on either side of the amplifier leads to the conversion of a common-mode voltage into a differential component. This interfering signal is then subject to the gain of the subsequent stages, which degrades the CMRR of the circuit. In addition, the differential gain achieved by the output stage comes at the cost of further loss of CMRR. The common-mode gain is in fact augmented by 3 dB compared to a structure that allocates the full differential gain to the second fully differential stage built around A_3 and A_4, as previously demonstrated by the author in Section ?? of Chapter 4.

Effect of the gain distribution on dc bias conditions

The original design published by Burke & Gleeson uses op-amps entirely from the MAX400 series because they offered the best low-power characteristics available at the time, combined with low input offset voltages [34–36]. In addition, very small bias current, typically less than 0.1 pA, means that the impedance multiplication effect accomplished by the bootstrapped front-end does not cause significant offset variation under nominal conditions. Minimising changes in the dc bias conditions is, in fact, particularly important for preventing dc levels from exceeding the input common-mode range (V_{CM}) of the op-amps, limited at 1.1 V below the positive supply voltage for the MAX400 series. Ideally, the output signal should sit at half-rail, 1.65 V, to maximise the differential output swing but because of the reduced common-mode input range of the op-amps, the bias output voltage was set instead at 0.7 V [36].

Furthermore, a differential offset voltage can result from the combined effects of the biasing resistors R_5, R_6 and R_7, the dc gain of the amplifier, and the difference in the op-amp input offset voltages and bias currents when the two sides of the amplifier are imbalanced. The circuit provides an overall dc gain of 19 dB, hence any differential variation in offset levels is amplified accordingly. It was reported that dc offset variation reaches ± 244 mV at the output, the contribution of op-amp's bias currents being neglected [36].

5.1.3 Modifications suggested by the author

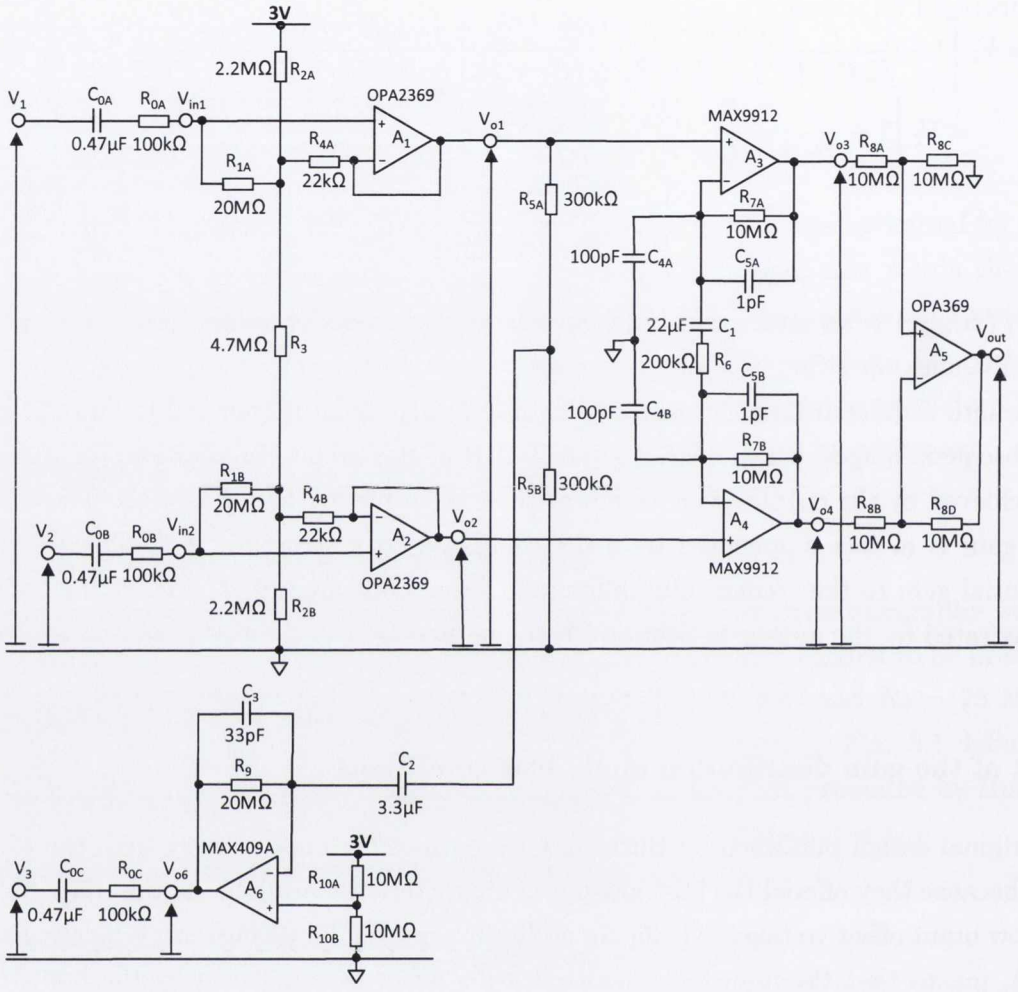

Figure 5.2: Schematic diagram of the new design proposed by the author.

Fig. 5.2 shows a new version of the instrumentation amplifier structure published by Burke & Gleeson, modified for enhanced CMRR and low-frequency performance. The difference between this and the original design resides essentially in the distribution of the gain within the amplification channel and the redesign of the circuit structure to improve input impedance characteristics and to cope with the effects of offsets. In light of results presented in Chapter 4, the author has allocated the differential gain exclusively to the second fully differential amplification stage built around op-amps A_3 and A_4. The front-end acts as an impedance defining unity-gain buffer stage. Input bias currents are blocked from reaching the patient body by capacitors C_{0A}, C_{0B}, C_{0C} and C_2, and only a very small amount can enter the input pins of op-amps. Therefore, the dc-current that flows from the power supply to the analogue

ground finds its path through resistors R_{2A}, R_3 and R_{2B} in series. Each resistor yields a constant voltage drop that defines the dc voltage levels at the input terminals of op-amps A_1 and A_2 at $3V_{cc}/4$ and $V_{cc}/4$, respectively. This is achieved by selecting $R_{2A} = R_{2B} = R_3/2$, resulting in an input differential dc bias voltage equal to $V_{cc}/2$ that is subject to unity-gain in all stages of the amplification channel, up to the final output. The final stage provides a single-ended output without amplification as $R_{8A} = R_{8B} = R_{8C} = R_{8D} = R_8$. The principal limitation of the overall CMRR obtainable was identified in Chapter 4 as the magnitude of the skin-electrode impedance associated with the dry electrodes previously characterised. The circuit arrangement of the amplification stage and the right-leg-drive have therefore not been modified since they constitute two standard configurations proven effective in securing high immunity to common-mode interference in the presence of high source impedance [34–36, 60, 194, 206].

Table 5.1: Electrical characteristics of the selected op-amps.

Parameter	Unity-gain stages op-amps A_1, A_2 & A_5 OPA2369/OPA369 Texas Instruments Inc.			Amplification stage op-amps A_3 & A_4 MAX9912 Maxim Inc.			Driven-Right-Leg op-amp A_6 MAX409A Maxim Inc.		
	min.	typ.	max.	min.	typ.	max.	min.	typ.	max.
A_{VOL} (dB)	114	134		95	120		106	120	
GBP (kHz)		12			200		80	150	
Slew rate ($V\mu s^{-1}$)		0.005			0.1		0.08	0.04	
Gain stability	1			1			10		
V_{CM} input range	V^-		V^+	V^-		V^+	V^-		V^+-1.1 V
CMRR @ dc (dB)	100	114		70	80		70	80	
Com. mode input res.		10^{13} Ω||3 pF			10^9 Ω			undefined	
Diff. mode input res.		10^{13} Ω||3 pF			10^{10} Ω			undefined	
Bias current I_B (pA)		10	50		1	10		< 0.1	10
Offset current I_{os} (pA)		10	50		1	10		undefined	
In. offset volt. V_{io} (mV)		0.25	0.75		0.2	1		0.25	0.5
Volt. noise density V_{nd_0}		220 nV$\sqrt{\text{Hz}}$			400 nV$\sqrt{\text{Hz}}$			150 nV$\sqrt{\text{Hz}}$	
Cur. noise density I_{nd_0}		1fA$\sqrt{Hz}$			1fA$\sqrt{Hz}$			undefined	
Quiescent cur. I_{cc} (μA)		0.8	1.2		3.5	4.5		1	1.2

Table 5.1 gives a summary of the essential electrical characteristics considered in the selection of suitable op-amps for implementing the single-supply instrumentation amplifier proposed by the author. In an effort to maintain the total dc current drawn by the circuit below 50 μA, the investigation has targeted ultra-low-power products currently available. The

selection of op-amps for the proposed new design was then motivated by the performance criteria outlined below.

Common-mode input and output range

The circuit design presented by the author requires the dc bias voltage at the input of op-amps A_1 and A_3 to be set at $3V_{cc}/4$, which is outside the input common-mode range of op-amps from the MAX400 series. Alternatively the OPA369 series was chosen for op-amps A_1, A_2 and A_5 and the MAX9912 was selected for op-amps A_3 and A_4 as they provide rail-to-rail input and output swing.

Gain and bandwidth characteristics

Because the two op-amps of the second stage provide the differential gain for the circuit, it is crucial that their open-loop gain (A_{VOL}) and gain-bandwidth product (GBP) are sufficiently large to secure amplification of the input signal without amplitude or phase distortion within the ECG bandwidth. Op-amps from the MAX9910 series were retained for this purpose since $A_{VOL} > 95$ dB and GBP = 200 kHz. A mid-band differential gain $A_{d0} = 40$ dB for this stage offers the possibility of extending the 3-dB bandwidth of the amplifier to approximately 5.5 kHz. The two unity-gain stages at the front-end and at the output are built around op-amps from the OPA369 series for which the frequency characteristics exceed the bandwidth of interest given GBP = 12 kHz and $A_{VOL} > 114$ dB.

Stability considerations

All five op-amps composing the differential amplification channel are unity-gain stable. Unity-gain stability is required at the front-end stage and the output stage for which the differential gain is one. In addition, as recommended by Gasulla et al. and White [180, 207], the second fully differential stage is also unity-gain stable as the common-mode gain is unity.

Input impedance and CMRR parameters

Immunity to external interfering signals relies on the ability of the amplifier to reject common-mode voltages. This is achieved by securing high input impedance and selecting op-amps providing high CMRR performance. The front-end op-amps must therefore have sufficiently large input resistance and open loop gain characteristics so that the input impedance of the amplifier can be determined by the bootstrapping mechanism. With 10 TΩ common-mode and differential-mode input resistances and $A_{VOL} > 114$ dB, op-amps from the OPA369 series satisfy these requirements. Input resistance performance is less stringent at the second stage which is dc-coupled to the front-end stage.

5.2 Characterisation of the proposed new amplifier circuit

5.2.1 Input impedance characteristics

Fig. 5.3 is a simplified representation of the impedances at the input of an instrumentation amplifier showing a differential input resistance, R_d, and two common-mode input resistances, R_{c1} and R_{c2}. R_d is the equivalent resistance between the two input terminals while R_{c1} and R_{c2} are the equivalent resistances of both inputs with respect to the analogue ground.

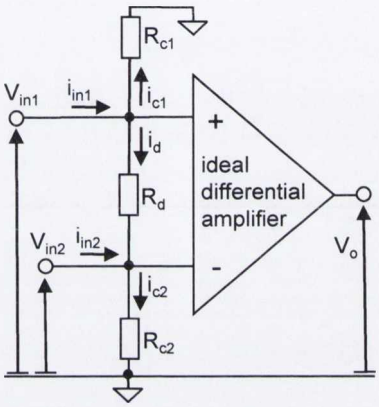

Figure 5.3: Schematic diagram of the equivalent impedances seen at the input of an instrumentation amplifier.

Referring to Fig. 5.3, differential and common-mode input resistances can be expressed in terms of the input voltages and input currents as follows:

$$R_d = \left.\frac{V_{in1} - V_{in2}}{i_d}\right|_{V_{in1}=-V_{in2}} \tag{5.11}$$

$$R_{c1} = \left.\frac{V_{in1}}{i_{in1}}\right|_{V_{in1}=V_{in2}=V_c} \tag{5.12}$$

$$R_{c2} = \left.\frac{V_{in2}}{i_{in2}}\right|_{V_{in1}=V_{in2}=V_c} \tag{5.13}$$

Balancing both sides of the front-end stage yields R_{c1}=R_{c2}=R_c. The overall input impedance of an instrumentation amplifier in a differential configuration is therefore given by:

$$R_{in} = R_d // (2R_c) = \frac{2R_dR_c}{R_d + 2R_c} \tag{5.14}$$

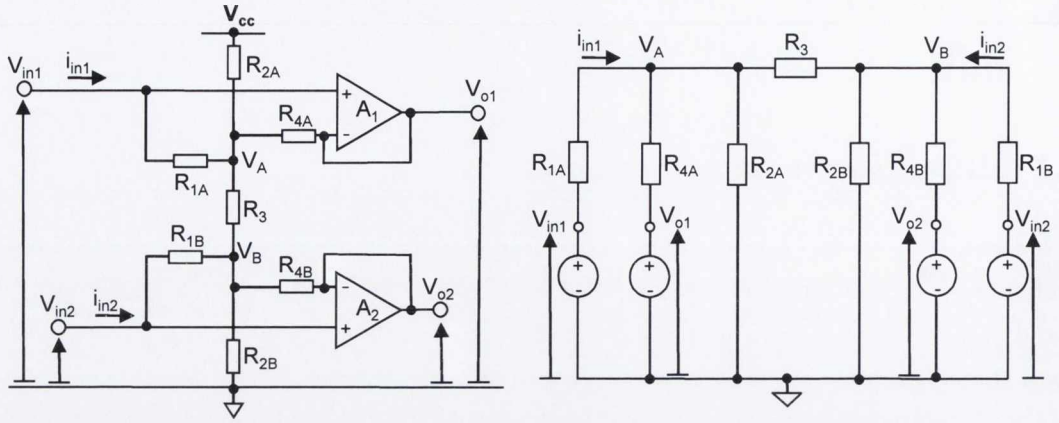

(a) The amplifier front-end stage.

(b) Equivalent representation.

Figure 5.4: Simplified circuit schematics of (a) the amplifier front-end stage and (b) its equivalent representation assuming ideal op-amps and omitting the effects of the skin-electrode impedance, dc-blocking capacitance and current limiting resistance. These components contribute to the electrode impedance Z_e, considered in subsequent sections.

Fig. 5.4 shows a simplified equivalent model of the resistances seen at the input of op-amps A_1 and A_2 at the front-end stage. Referring to Figs. 5.4(a) and 5.4(b), the input currents i_{in1} and i_{in2} are defined as:

$$i_{in1} = \frac{V_{in1} - V_A}{R_{1A}} \tag{5.15}$$

and

$$i_{in2} = \frac{V_{in2} - V_B}{R_{1B}} \tag{5.16}$$

where V_A and V_B are given by:

$$V_A = [R_{1A}//R_{2A}//R_{4A}//(R_3 + R_{1B}//R_{2B}//R_{4B})] \left[\frac{V_{in1}}{R_{1A}//R_{4A}} + \frac{\frac{R_{2B}}{R_{2B}+R_{1B}//R_{4B}} V_{in2}}{R_3 + R_{1B}//R_{2B}//R_{4B}} \right] \tag{5.17}$$

and

$$V_B = [R_{1B}//R_{2B}//R_{4B}//(R_3 + R_{1A}//R_{2A}//R_{4A})] \left[\frac{V_{in2}}{R_{1B}//R_{4B}} + \frac{\frac{R_{2A}}{R_{2A}+R_{1A}//R_{4A}} V_{in1}}{R_3 + R_{1A}//R_{2A}//R_{4A}} \right] \tag{5.18}$$

Single-ended input resistance

The single-ended input resistances seen at each input terminal of the instrumentation amplifier are defined as follows:

$$R'_{in1} = R_d//R_{c1} = \left.\frac{V_{in1}}{i_{in1}}\right|_{V_{in2}=0} = \frac{R_{1A}}{1-\frac{V'_A}{V_{in1}}} \tag{5.19}$$

and

$$R'_{in2} = R_d//R_{c2} = \left.\frac{V_{in2}}{i_{in2}}\right|_{V_{in1}=0} = \frac{R_{1B}}{1-\frac{V'_B}{V_{in2}}} \tag{5.20}$$

where V'_A and V'_B are given by:

$$V'_A = V_A|_{V_{in2}=0} = \left[\frac{R_{1A}//R_{2A}//R_{4A}//\left(R_3+R_{1B}//R_{2B}//R_{4B}\right)}{R_{1A}//R_{4A}}\right]V_{in1} \tag{5.21}$$

and

$$V'_B = V_B|_{V_{in1}=0} = \left[\frac{R_{1B}//R_{2B}//R_{4B}//\left(R_3+R_{1A}//R_{2A}//R_{4A}\right)}{R_{1B}//R_{4B}}\right]V_{in2} \tag{5.22}$$

Eqs. (5.19) and (5.20) can therefore be rewritten as:

$$R'_{in1} = R_{1A}\left[1+\frac{R_{2A}//\left(R_3+R_{1B}//R_{2B}//R_{4B}\right)}{R_{1A}//R_{4A}}\right] \tag{5.23}$$

and

$$R'_{in2} = R_{1B}\left[1+\frac{R_{2B}//\left(R_3+R_{1A}//R_{2A}//R_{4A}\right)}{R_{1B}//R_{4B}}\right] \tag{5.24}$$

In the ideal scenario of perfect matching at both sides of the amplifier, the nominal single-ended input impedance is determined by:

$$R'_{in} = R_1\left[1+\frac{R_2//\left(R_3+R_1//R_2//R_4\right)}{R_1//R_4}\right] \tag{5.25}$$

where $R_1 = R_{1A} = R_{1B}$, $R_2 = R_{2A} = R_{2B}$ and $R_4 = R_{4A} = R_{4B}$. Eq. (5.25) demonstrates the resistance multiplication effect achieved by the bootstrapping mechanism at the amplifier front-end and indicates that if resistor values are selected such that $R_1 >> \{R_2, R_4\}$, the single-ended input resistance is then closely approximated by:

$$R'_{in} \simeq R_1\left[1+\frac{R_2//\left(R_3+R_2//R_4\right)}{R_4}\right] \tag{5.26}$$

Common-mode input resistance

The common-mode input resistances at each input of the amplifier are determined by applying a common-mode input voltage V_c=V_{in1}=V_{in2} as follows:

$$R_{c1} = \left.\frac{V_c}{i_{in1}}\right|_{V_c=V_{in1}=V_{in2}} = \frac{R_{1A}}{1-\frac{V''_A}{V_c}} \tag{5.27}$$

and

$$R_{c2} = \left.\frac{V_c}{i_{in2}}\right|_{V_c=V_{in1}=V_{in2}} = \frac{R_{1B}}{1-\frac{V''_B}{V_c}} \tag{5.28}$$

with

$$\begin{aligned} V''_A &= V_A|_{V_c=V_{in1}=V_{in2}} \\ &= [R_{1A}//R_{2A}//R_{4A}//(R_3+R_{1B}//R_{2B}//R_{4B})]\left(\frac{1}{R_{1A}//R_{4A}}+\frac{\frac{R_{2B}}{R_{2B}+R_{1B}//R_{4B}}}{R_3+R_{1B}//R_{2B}//R_{4B}}\right)V_c \end{aligned} \tag{5.29}$$

and

$$\begin{aligned} V''_B &= V_B|_{V_c=V_{in1}=V_{in2}} \\ &= [R_{1B}//R_{2B}//R_{4B}//(R_3+R_{1A}//R_{2A}//R_{4A})]\left(\frac{1}{R_{1B}//R_{4B}}+\frac{\frac{R_{2A}}{R_{2A}+R_{1A}//R_{4A}}}{R_3+R_{1A}//R_{2A}//R_{4A}}\right)V_c \end{aligned} \tag{5.30}$$

Selecting $R_{1A} >> \{R_{2A}, R_{4A}\}$ and $R_{1B} >> \{R_{2B}, R_{4B}\}$ as previously stated, allows R_{c1} and R_{c2} to be closely approximated by:

$$R_{c1} = R_{1A}\left[1+\frac{R_{2A}}{R_{4A}}\left(\frac{R_{2B}R_{4B}+R_{2B}R_3+R_3R_{4A}+R_{4A}R_{2B}}{R_{2B}R_{4B}+R_{2B}R_3+R_3R_{4A}+R_{4B}R_{2A}}\right)\right] \tag{5.31}$$

and

$$R_{c2} = R_{1B}\left[1+\frac{R_{2B}}{R_{4B}}\left(\frac{R_{2A}R_{4A}+R_{2A}R_3+R_3R_{4B}+R_{4B}R_{2A}}{R_{2A}R_{4A}+R_{2A}R_3+R_3R_{4B}+R_{4A}R_{2B}}\right)\right] \tag{5.32}$$

Each paired resistor, R_{xy}, can be expressed in terms of its nominal value, R_x, and an error due to manufacturing tolerances, Δ_{xy}, so that:

$$R_{xy} = R_x\left(1+\Delta_{xy}\right)|_{x\in\{1,2,4,5,6,7,8,10\},y\in\{A,B,C,D\}} \tag{5.33}$$

Eqs. (5.31) and (5.32) can therefore be expanded as follows:

$$R_{c1} = R_1 (1 \pm \Delta_{1A}) \left[1 + \frac{R_2 (1 \pm \Delta_{2A})}{R_4 (1 \pm \Delta_{4A})} \left[\frac{\begin{array}{c} R_2 (1 \pm \Delta_{2B}) R_4 (1 \pm \Delta_{4B}) + R_2 (1 \pm \Delta_{2B}) R_3 \\ + R_3 R_4 (1 \pm \Delta_{4A}) + R_4 (1 \pm \Delta_{4A}) R_2 (1 \pm \Delta_{2B}) \end{array}}{\begin{array}{c} R_2 (1 \pm \Delta_{2B}) R_4 (1 \pm \Delta_{4B}) + R_2 (1 \pm \Delta_{2B}) R_3 \\ + R_3 R_4 (1 \pm \Delta_{4A}) + R_4 (1 \pm \Delta_{4B}) R_2 (1 \pm \Delta_{2A}) \end{array}} \right] \right] \tag{5.34}$$

and

$$R_{c2} = R_1 (1 \pm \Delta_{1B}) \left[1 + \frac{R_2 (1 \pm \Delta_{2B})}{R_4 (1 \pm \Delta_{4B})} \left[\frac{\begin{array}{c} R_2 (1 \pm \Delta_{2A}) R_4 (1 \pm \Delta_{4A}) + R_2 (1 \pm \Delta_{2A}) R_3 \\ + R_3 R_4 (1 \pm \Delta_{4B}) + R_4 (1 \pm \Delta_{4B}) R_2 (1 \pm \Delta_{2A}) \end{array}}{\begin{array}{c} R_2 (1 \pm \Delta_{2A}) R_4 (1 \pm \Delta_{4A}) + R_2 (1 \pm \Delta_{2A}) R_3 \\ + R_3 R_4 (1 \pm \Delta_{4B}) + R_4 (1 \pm \Delta_{4A}) R_2 (1 \pm \Delta_{2B}) \end{array}} \right] \right] \tag{5.35}$$

It can be shown that the mismatch in the common-mode resistances seen on each side of the amplifier is maximum with the following combination of mismatches of individual resistors:

$$\Delta_{1A} = \Delta_{2A} = \Delta_{4B} = \Delta_{R_{max}} \tag{5.36}$$

and

$$\Delta_{1B} = \Delta_{2B} = \Delta_{4A} = -\Delta_{R_{max}} \tag{5.37}$$

The common-mode resistance can then be expressed in terms of its nominal value, R_c, and an error, Δ_c, caused by manufacturing tolerances in the resistor values, as follows:

$$R_c = R_1 \left(1 + \frac{R_2}{R_4} \right) \tag{5.38}$$

$$\Delta_c = \frac{R_4}{R_2 + R_4} \left[1 + \frac{R_2}{R_4} \left[\frac{2R_4^2 + 3R_3 (R_2 + R_4)}{2R_2 R_4 + R_3 (R_2 + R_4)} \right] \right] \Delta_{R_{max}} \tag{5.39}$$

R_{c1} and R_{c2} are therefore given in the worst-case scenario as:

$$R_{c1} = R_c (1 - \Delta_c) \tag{5.40}$$

and

$$R_{c2} = R_c (1 + \Delta_c) \tag{5.41}$$

Differential input resistance

The single-ended input resistance being defined as $R'_{in} = R_d//R_c$, the differential input resistance can therefore be deduced as:

$$R_d = \frac{R_c R'_{in}}{R_c - R_{in}} \tag{5.42}$$

Substituting the nominal expressions for R_c and R'_{in} given by eqs. (5.26) and (5.38) into eq. (5.42) yields the nominal value of R_d as:

$$R_d \simeq R_1 \left(2 + \frac{R_3}{R_4//R_2}\right)\left(1 + \frac{R_4}{R_2}\right) \tag{5.43}$$

Selection of the resistor values at the amplifier front-end stage

The overall input resistance in a differential configuration is defined nominally as $R_{in} = R_d//(2R_c)$. It has been established in earlier chapters that R_{in} must be greater than 2 GΩ for the frequency performance requirements of the skin-electrode-amplifier network to be fulfilled at low-frequencies. This can be achieved by selecting $R_c = 2$ GΩ and $R_d = 4$ GΩ. Low cost 1% resistors are currently available in surface mount form for resistance values up 20 MΩ, which is the value used for R_1. This requires the impedance multiplication factors to be 100 and 200 for R_c and R_d, respectively. Considering the expression for R_c derived in eq. (5.38) leads to:

$$1 + \frac{R_2}{R_4} \geq 100 \tag{5.44}$$

Taking $R_2 = 2.2$ MΩ and $R_4 = 22$ kΩ satisfies the condition indicated in eq. (5.44) while ensuring $R_1 >> \{R_2, R_4\}$, as previously indicated. The selection of large resistor values allows the quiescent current that flows in the dc path to be minimised. In addition, dc-bias conditions inherent in single-supply operation imply $R_3 = 2R_2$ in order to set the dc output voltage at half-rail. The closest normalised value available is $R_3 = 4.7$ MΩ resulting in:

$$R_d \simeq R_1 \left(2 + \frac{R_3}{R_4}\right) \simeq 4.31 \text{ GΩ} \tag{5.45}$$

$$R_c \simeq R_1 \left(1 + \frac{R_2}{R_4}\right) \simeq 2.02 \text{ GΩ} \tag{5.46}$$

$$R_{in} = \frac{2R_d R_c}{R_d + 2R_c} = 2.08 \text{ GΩ} \tag{5.47}$$

Δ_c is estimated for $\Delta_{R_{max}} = 1\%$ using eq. (5.39) at 2.95%. Finally, the single-ended input resistance seen at each input is given by:

$$R'_{in} = \frac{R_d R_c}{R_d + R_c} = 1.37 \text{ G}\Omega \tag{5.48}$$

5.2.2 CMRR performance

CMRR of the instrumentation amplifier alone

It can be shown that $CMRR_{op}$, the common-mode rejection ratio contributed by op-amps A_1 to A_5 forming the differential amplification channel, is defined as:

$$\frac{1}{CMRR_{op}} = \frac{1}{CMRR_{A1}} + \frac{1}{CMRR_{A_2}} + \frac{1}{CMRR_{A_3}} + \frac{1}{CMRR_{A_4}} + \frac{1}{\frac{A_{d0}}{2} CMRR_{A_5}} \tag{5.49}$$

In addition, the worst-case $CMRR_{\Delta R}$ due to manufacturing tolerances in the gain-determining resistors is given by:

$$CMRR_{\Delta R_{min}} = \frac{A_{d0}}{2\Delta_{R_{max}}} \tag{5.50}$$

Evaluating eqs. (5.49) and (5.50) with $A_{d0} = 40$ dB, $\Delta_{R_{max}} = 1\%$ and the CMRR parameter values listed in Table 5.1 returns $CMRR_{op_{min}} = 63.7$ dB and $CMRR_{\Delta R_{min}} = 74$ dB. The minimum common-mode rejection ratio of the instrumentation amplifier considering only the effects of $CMRR_{op}$ and $CMRR_{\Delta R}$ is therefore given as:

$$\left.\frac{1}{CMRR_{IA}}\right|_{dB} = \left.\frac{1}{CMRR_{\Delta R}}\right|_{dB} + \left.\frac{1}{CMRR_{op}}\right|_{dB} = -61.4 \text{ dB} \tag{5.51}$$

CMRR of the skin-electrode-interface network

We now consider the ECG preamplifier coupled to imbalanced electrode impedances, $Z_{e1} = Z_e(1 \pm \Delta_e)$ and $Z_{e2} = Z_e(1 \mp \Delta_e)$. The common-mode rejection ratio due to impedance mismatch at the amplifier input has been previously derived as:

$$CMRR_{\Delta Z_{min}}|_{dB} \simeq 20 \log_{10}\left(\frac{R_c}{|Z_{e_{max}}|}\right) + 20 \log_{10}\left(\frac{1 - \Delta_c^2}{2(\Delta_c + \Delta_e)}\right) \tag{5.52}$$

Evaluating eq. (5.52) with $|Z_{e_{max}}| = 4$ MΩ, $R_c = 2$ GΩ, $\Delta_c = 3\%$ and $\Delta_e = 33\%$ returns $CMRR_{\Delta Z_{min}} \simeq 58$ dB. Given $CMRR_{IA_{min}} = 61.4$ dB provided by the IA alone, a worst-case common-mode rejection ratio of 53.7 dB is achieved by the differential amplification channel at the output of the skin-electrode-amplifier network. The overall CMRR of the recording

system is improved by adding the contribution of the right-leg-drive, leading to:

$$CMRR|_{dB} = 20\log_{10}(G_{DRL}) + \left.\frac{1}{\frac{1}{CMRR_{IA}} + \frac{1}{CMRR_{\Delta Z}}}\right|_{dB} \tag{5.53}$$

where G_{DRL} is the gain of the inverting amplifier in the driven-right-leg circuit, which must be greater than 42 dB if $CMRR_{min} = 95$ dB is to be achieved for frequencies ranging from $f_1 = 0.5$ Hz to $f_2 = 100$ Hz. Selecting $R_9 = 20$ MΩ and R_5= 300 kΩ secures a mid-band gain of 42.5 dB for the inverting amplifier. This implies the following values for capacitors C_2 and C_3:

$$C_{2_{min}} = \frac{1}{\pi R_5 f_1} = 2.12\ \mu\text{F} \tag{5.54}$$

$$C_{3_{max}} = \frac{1}{2\pi R_9 f_2} = 35\ \text{pF} \tag{5.55}$$

As shown in Fig. 5.5, the selected capacitance values are $C_2 = 3.3$ μF and $C_3 = 33$ pF. The capacitance of C_2 is greater than the minimum required value to secure a high CMRR value at low frequencies, where the magnitude of the skin-electrode impedance is maximal.

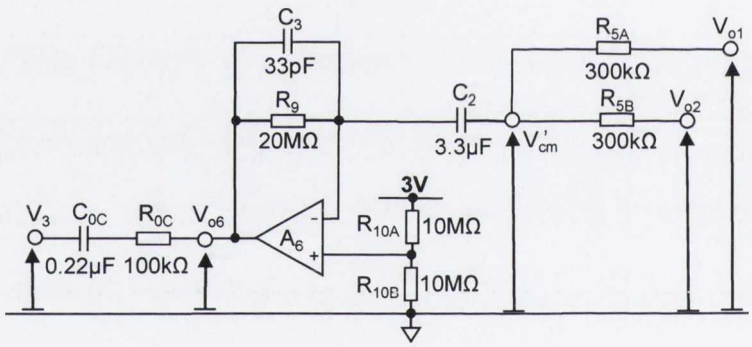

Figure 5.5: Circuit schematic of driven-right-leg circuit including the selected component values.

5.2.3 Frequency response and bandwidth considerations

The amplifier transfer function

The transfer function of the proposed new amplifier is given by:

$$\frac{V_{out}(s)}{V_1(s) - V_2(s)} = \left(1 + \frac{2R_7}{R_6}\right)\left(\frac{s}{s+\omega'_{c1}}\right)\left(\frac{s + \frac{\omega'_{c2}}{1+2R_7/R_6}}{s+\omega'_{c2}}\right) \tag{5.56}$$

with

$$\omega'_{c1} = \frac{1}{\left(\frac{R_c R_d}{2R_c + R_d}\right) C_0} \tag{5.57}$$

and

$$\omega'_{c2} = \frac{1}{R_6 C_1} \tag{5.58}$$

Where C_0 is the capacitance of the three dc-blocking capacitors (C_{0A}, C_{0B} and C_{0C}) connected in series with each electrode. The selection of the component values for R_6 and C_1 must guarantee a low-frequency cutoff $f_c = \omega'_{c2}/2\pi$ of less than 0.05 Hz to prevent amplitude and phase distortion. This is achieved by making the time constant $R_6 C_1 \geq 3.2$ s, as discussed in previous chapters. Non-electrolytic, non-polarised multilayer ceramic chip capacitors providing capacitance of up to 100 µF are commonly available today [208]. Consequently, selecting $R_6 = 200$ kΩ allows the above condition on the time constant to be fulfilled with $C_1 = 22$ µF. A mid-band gain of 100 or 40 dB is therefore obtained with $R_7 = 10$ MΩ. As suggested by Burke & Gleeson [34–36], the combined response of the first and second stages is equivalent to that of a single-pole by making $\omega'_{c1} = \omega'_{c2}/\left(1 + 2R_6/R_7\right)$. This yields the following value for the capacitance C_0 of the dc-blocking capacitors:

$$C_0 = \left(1 + 2\frac{R_7}{R_6}\right) \frac{R_6}{\left(\frac{R_c R_d}{2R_c + R_d}\right)} C_1 = 0.43 \text{ µF} \tag{5.59}$$

$C_0 = 0.47$ µF is selected because this is the closest normalised capacitance value available in ceramic form at low-cost. Thus, eq. (5.56) becomes:

$$\frac{V_{out}(s)}{V_1(s) - V_2(s)} = \left(1 + \frac{2R_7}{R_6}\right)\left(\frac{s}{1 + R_6 C_1 s}\right) \tag{5.60}$$

Stability considerations and frequency compensation

Stray capacitances are present at the op-amp input terminals due to structural parasitics. They cause poles and zeros to occur in the amplifier frequency response which, if not neutralised, can affect the performance of the system by reducing stability or causing peaking in the response [209]. At each stage of the amplification, it is important to assess whether or not the frequency locations of the poles and zeros affect the stability and phase margin of the circuit [210, 211].

Stray capacitances appear at the input of the amplifier in parallel with its input resistances, as illustrated in Fig. 5.6. Input parasitic capacitances modify the amplifier frequency

response as described in eq. (5.61).

$$\frac{V_{in1}(s) - V_{in2}(s)}{V^+(s) - V^-(s)} = \frac{[R_d // (2R_c)] // \left[\frac{1}{sC_d} // \left(\frac{2}{sC_c}\right)\right]}{[R_d // (2R_c)] // \left[\frac{1}{sC_d} // \left(\frac{2}{sC_c}\right)\right] + 2Z_e} = \frac{1}{1 + \frac{4Z_e}{R_d // (2R_c)} + 4Z_e\left(\frac{C_c}{2} + C_d\right)s} \tag{5.61}$$

Given $R_c = 2$ GΩ, $R_d = 4$ GΩ and $|Z_{e_{max}}| = 4$ MΩ as previously established, eq. (5.61) can be closely approximated in the ECG bandwidth by:

$$\frac{V_{in1}(s) - V_{in2}(s)}{V^+(s) - V^-(s)} \simeq \frac{1}{1 + \tau_0 s} \tag{5.62}$$

with

$$\tau_0 = 4\,|Z_e|\left(\frac{C_c}{2} + C_d\right) \tag{5.63}$$

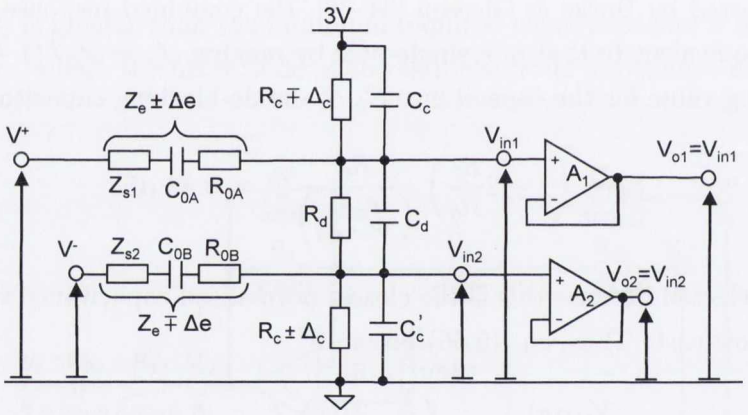

Figure 5.6: Circuit schematic of the front-end stage coupled to the skin-electrode interface that models the effect of the op-amp's input stray capacitances.

The typical value of input capacitance for the front-end op-amps A_1 and A_2 is given in Table 5.1 as $C_c = 6$ pF. C_d is associated with parasitic interconnect capacitance present on the printed circuit board between the two input terminals. The magnitude of C_d can be kept to much less than 1 pF with careful circuit layout and construction [212, 213], resulting in a break frequency $f_0 = 1/(2\pi\tau_0) = 2485$ Hz. This indicates that stray capacitances at the amplifier front-end may limit the obtainable bandwidth to approximately 2.5 kHz, which is well outside the desired amplifier frequency bandwidth as specified by international standards but which covers the amplifier 3-dB bandwidth. The implementation of low-pass filters following the preamplifier allows the risk of instability to be eliminated.

In addition, as reported by Burke & Gleeson, parasitic capacitances at the input of op-amps A_3 and A_4 may also cause instability in the amplifier response [34–36, 50, 51]. Often,

values of phase margin lower than 45° may cause the frequency response to peak up at the bandwidth limit before it rolls off [159]. Closed-loop gain peaking in the amplifier frequency response is generally associated with undershoot and ringing in its impulse response. Since gain peaking increases with increasing closed-loop gain, the risk of instability must be considered in the stage providing amplification for the circuit [159]. Stability can be preserved if the poles and zeros generated by parasitic capacitances are maintained outside the amplifier closed-loop bandwidth. The compensation method suggested by Burke & Gleeson is implemented for preventing instability at the bandwidth limit [34–36] by making $2C_{5A}R_{7A} = 2C_{5B}R_{7B} = C_{4A}R_6 = C_{4B}R_6$, as shown in Fig. 5.7. Capacitances C_{4A} and C_{4B} must be matched and limited to relatively small values to keep the poles outside of the amplifier's operating bandwidth [50, 51]. With $R_6 = 200$ kΩ, selecting $C_{4A} = C_{4B} = C_4 = 100$ pF results in a zero at 16 kHz. Given $R_7 = 10$ MΩ as previously defined, C_{5A} and C_{5B} must be equal to 1 pF to create a pole that cancels the zero at 16 kHz. Frequency compensation implemented this way allows a more consistent flat and stable response at high frequency.

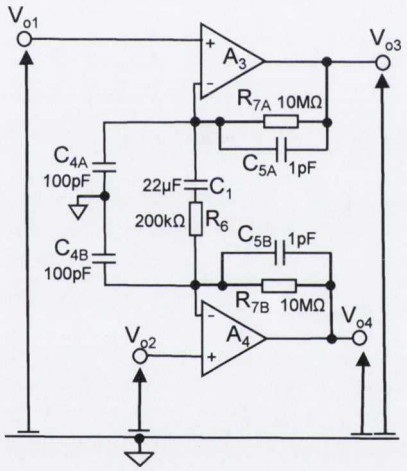

Figure 5.7: Implemented frequency compensation based on the method suggested by Burke & Gleeson [34–36].

5.2.4 DC offset considerations

As previously discussed, the dc operating point at the output of the preamplifier is set at half-rail, $V_{cc}/2$, by selecting R_3=$2R_c$ and keeping the dc-gain to unity in all stages. Nevertheless, the input offset voltage (V_{io}), input bias current (I_B), finite CMRR and finite power supply rejection ratio (PSRR) of op-amps A_1 to A_5 can contribute to variations in the output bias voltage [36]. The PSRR is defined as the ratio of the change in supply voltage to the

corresponding change of voltage at the output of the op-amp:

$$PSRR = \frac{\Delta V_{cc}}{\Delta V_o} \tag{5.64}$$

Fluctuations in the supply voltage of a single battery cell can generally be neglected compared to the other factors [36]. However, given the very high values of input resistances, the effect of bias currents must be taken into account since these may generate offset variations of similar magnitude as the error caused by the op-amp offset voltages.

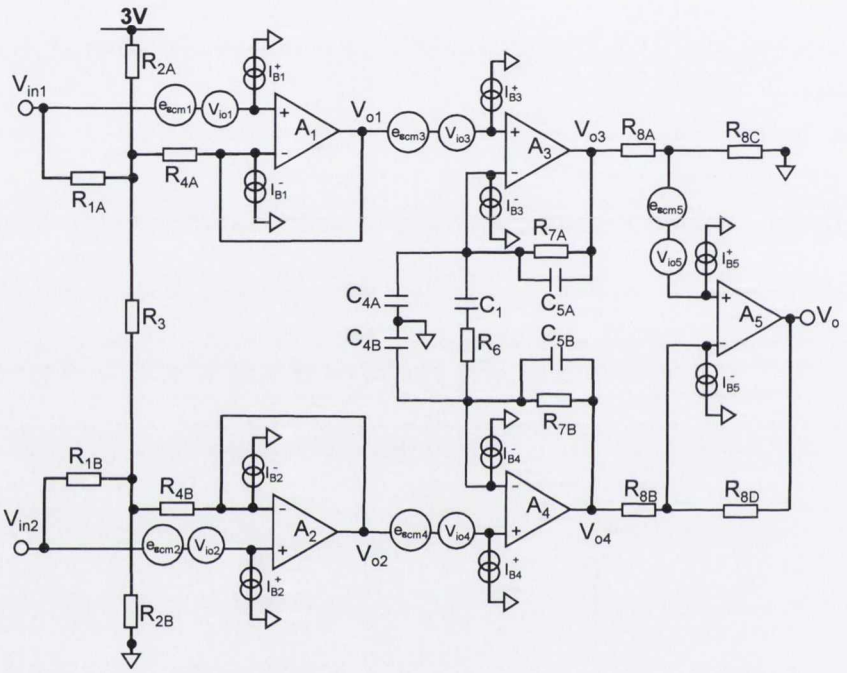

Figure 5.8: Modelling the dc offset sources at the input of each op-amp. $I_{B_k}^-$ and $I_{B_k}^+$ are the bias currents at the inverting and non-inverting input terminals of op-amp A_k, V_{io_k} represents its input offset voltage and $e_{\epsilon cm_k}$ simulates the equivalent input common-mode error voltage due to its limited CMRR.

Fig. 5.8 is a schematic of the differential amplification channel modelling the effects of input offset voltages, bias currents and CMRR of each op-amp. Analysing the circuit of Fig. 5.8, it can be shown that the worst-case error in the differential voltage at the output of the front-end stage resulting from the above effects is given by:

$$\epsilon_{os1} = \left(V_{io1} + \frac{\frac{R_3+R_2}{R_3+2R_2} V_{cc}}{CMRR_{op1}} - V_{io2} - \frac{\frac{R_2}{R_3+2R_2} V_{cc}}{CMRR_{op2}} \right) \left(1 + \frac{R_2}{R_4} \right) + R_1 \left(I_{B1}^+ - I_{B2}^+ \right) \left[1 + \frac{R_2 R_3}{R_4 \left(2R_2 + R_3 \right)} \right] \tag{5.65}$$

The dc-gain of the circuit is unity, preventing amplification of the differential offset error ϵ_{os1}, but small contributions from op-amps A_3, A_4 and A_5 must also be considered, producing an overall dc voltage at the output given by:

$$V_{odc} = \frac{R_3}{R_3 + 2R_2} V_{cc} \pm \Delta V_{odc} \tag{5.66}$$

where

$$\Delta V_{odc} = \epsilon_{os1} + \left(V_{os3} + \frac{\frac{R_3+R_2}{R_3+2R_2} V_{cc}}{CMRR_{op3}} - V_{os4} - \frac{\frac{R_2}{R_3+2R_2} V_{cc}}{CMRR_{op4}} \right) + R_7 \left(I^-_{B3} - I^-_{B4} \right) + \left(V_{os5} + \frac{\frac{R_3}{R_3+2R_2} V_{cc}}{CMRR_{op5}} \right) + R_8 \left(I^+_{B5} - I^-_{B5} \right) \tag{5.67}$$

The front-end op-amps are the principal contributors to dc offset variation since offset voltages and bias currents are multiplied in a similar fashion to the input resistance. The absence of dc gain in the version presented by the author allows variation due to the op-amp input offset voltages to be minimised. Attention must, however, be given to bias currents at the front-end stage due to the very large input resistance at each input. Considering R_1 = 20 MΩ, R_2 = 2.2 MΩ, R_3 = 4.7 MΩ, R_4 = 22 kΩ, V_{io1} = -750 μV and V_{io2} = 750 μV, and the worst-case variations in the bias currents as ±50 pA at the input of op-amps A_1 and A_2, results in a differential offset error ϵ_{os1} of about ± 100 mV. Other stages contribute less 4 mV to dc offset variations at the output, assuming the highest levels of imbalance.

It can be concluded that, despite the implementation of higher input impedance and the use of op-amps with larger bias current, the gain arrangement proposed by the author has reduced dc offset variation at the output, thus preventing the risk of saturation or clipping of the output signal level.

5.2.5 Semiconductor noise

In its passage through the amplifier, the signal quality is degraded by any added intrinsic noise. Fig. 5.9 is a schematic representation of the proposed single-supply instrumentation amplifier that includes the sources of noise internally generated by the circuit. The model comprises three types of noise generators E_{v_k}, E_{i_k} and E_{r_k}, referred to the input of noiseless op-amps. E_{v_k} and E_{i_k} are the noise voltage and noise current generated by op-amp A_k, while E_{r_k} is the noise produced by its equivalent input resistance, R_{in_k} [34, 35, 70, 159, 214]. The resulting mean square white thermal noise voltage generated by the input resistance is defined as:

$$E^2_{r_k} = 4kT \left(f_H - f_L \right) R_{in_k} \tag{5.68}$$

where $k = 1.38\text{x}10^{-23}$ is Boltzmann's constant, T is the temperature of operation, typically 25 °C or 298 K, and f_L and f_H are, respectively, the low-frequency and high-frequency limits of the bandwidth of interest. High-frequency noise is normally eliminated by the low-pass filter following the preamplifier output and consequently noise analysis can be restricted to the ECG signal bandwidth.

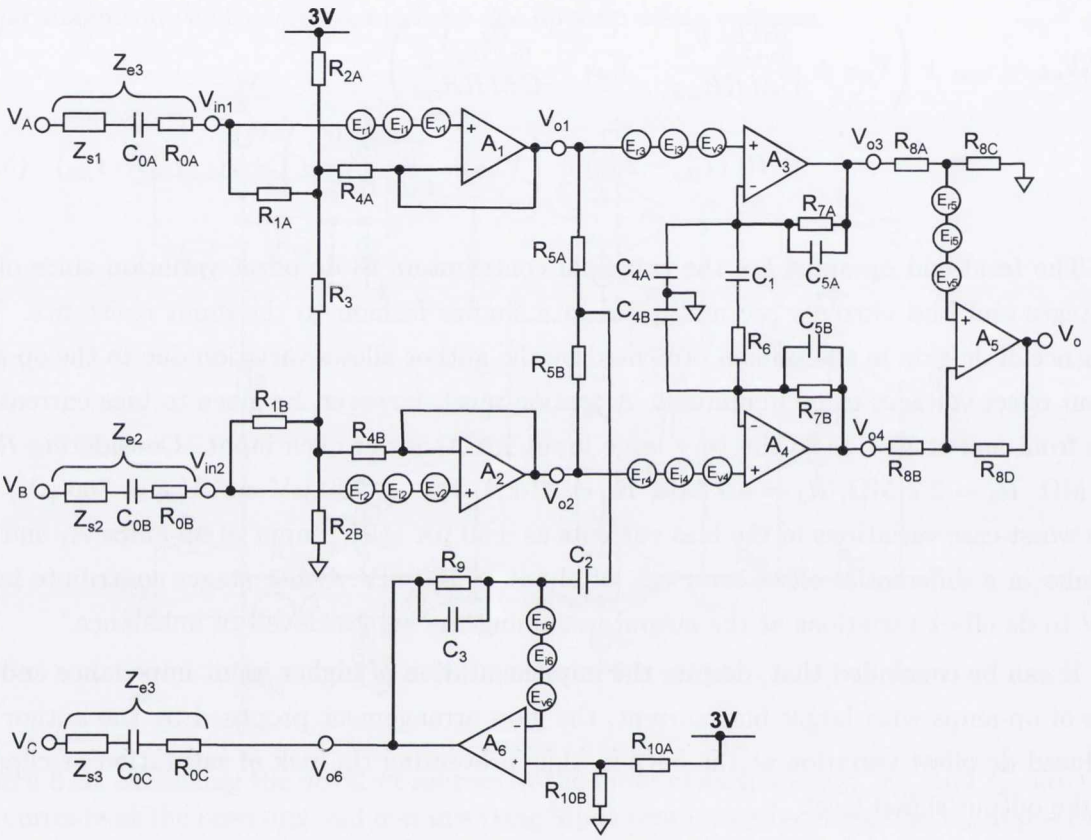

Figure 5.9: Modelling the sources of noise intrinsic to the preamplifier. The r.m.s. value of the noise voltage, E_{v_k}, noise current, E_{i_k}, and the resistor noise, E_{r_k}, are represented at the input of op-amp A_k by three voltage generators in series.

The noise generated by each op-amp is composed of a white thermal noise and a flicker or $1/f$ noise component causing V_{nd}, the spectral density function of the noise voltage, and i_{nd}, the spectral density function of the noise current, of op-amps to vary with frequency [50, 51]. At very low frequencies, the noise amplitude is inversely proportional to frequency but at frequencies above the corner frequencies, f_{cv} and f_{ci}, the noise amplitude is essentially flat [159]. Burke has derived expressions for $E_{v_k}^2$ and $E_{i_k}^2$ by integrating V_{nd}^2 and i_{nd}^2 over the

frequency range f_L to f_H as follows [34, 35, 70]:

$$E_{v_k}^2 = \int_{f_L}^{f_H} V_{nd}^2 \, df = V_{nd0}^2 \left[(f_H - f_L) + 2 \ln \left(\frac{f_H}{f_L} \right) f_{cv} + \left(\frac{f_H - f_L}{f_H f_L} \right) f_{cv}^2 \right] \tag{5.69}$$

and

$$E_{i_k}^2 = R_{in_k}^2 \int_{f_L}^{f_H} i_{nd}^2 \, df = R_{in_k}^2 I_{nd0}^2 \left[(f_H - f_L) + 2 \ln \left(\frac{f_H}{f_L} \right) f_{ci} + \left(\frac{f_H - f_L}{f_H f_L} \right) f_{ci}^2 \right] \tag{5.70}$$

The rms noise voltage referred to the input of op-amp A_k can therefore be estimated as:

$$E_{ni_k} = \sqrt{E_{v_k}^2 + E_{i_k}^2 + E_{r_k}^2} \tag{5.71}$$

The corner frequencies, f_{cv} and f_{ci}, usually lie within the ECG signal spectrum and knowledge of these is required as well as the white noise values, V_{ndo} and I_{ndo}, to allow an accurate estimation of the input noise voltage [50]. Table 5.1 of Section 5.1.3 gives the noise specifications of the selected op-amps as published by the manufacturers. However, several essential characteristics are not disclosed, preventing the rms voltage noise generated internally by the recording system from being accurately estimated. Performance related to semiconductor noise was therefore assessed by measurement on a constructed prototype.

5.3 Results

The proposed ECG amplifier circuit was first simulated with PSpice to allow the predicted worst-case performance in terms of input impedance, frequency response and CMRR to be verified. A prototype was then built and tested using the following equipment:

- A signal analyser: Agilent 35670A;
- A dual channel arbitrary function generator: Tektronix AFG 3022;
- A battery-powered four-channel digital storage oscilloscope: Tektronix TPS 2014.

Fourteen reasonably healthy volunteers were recruited for actual ECG recordings using the wet and dry electrodes depicted in Fig. 5.10. There were 10 males and 4 females, aged between 22 and 41 years.

(a) Standard Ag/AgCl pre-gelled electrode: Schiller Biotabs, 2.3 x 2.3 cm.

(b) Conductive silicon rubber dry electrode: Pro Carbon C5005PF, 2.6 cm in diameter.

Figure 5.10: Photographs showing (a) the wet electrode and (b) dry electrode used for noise measurement and actual ECG recording.

5.3.1 Intrinsic noise measurement

Internally generated noise was evaluated under different configurations for both wet and dry electrodes:

- The input electrodes were connected to one another;
- The equivalent electrical models of the skin-electrode impedance, depicted in Fig. 5.11, were connected between each amplifier input and analogue ground;
- The inputs were connected directly to analogue ground.

Fig. 5.12 shows a sample noise measurement acquired using dry electrodes connected to one another. Table 5.2 lists the value of the peak-to-peak output noise voltage under different input configurations. Noise was measured at about 24 mV p-p in all cases, suggesting that the output noise level is not noticeably affected by the presence of the input electrodes. It can be concluded that the amplifier is the main contributor to the noise observed at the output. Reducing the level of internally generated noise will require the use of op-amps with enhanced noise performance at the expense of an increase in quiescent current.

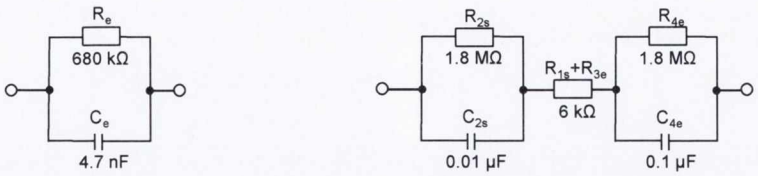

(a) Wet electrode model.

(b) Dry electrode model.

Figure 5.11: Constructed skin-electrode interface models for (a) wet electrodes and (b) dry electrodes.

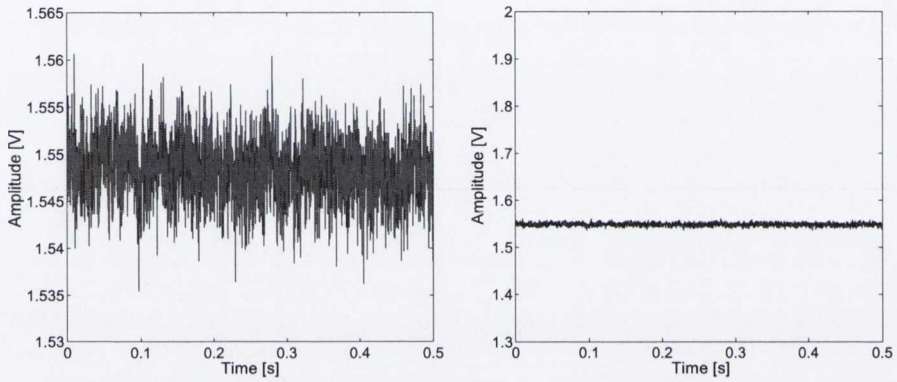

(a) Intrinsic noise level.

(b) The same signal shown on the scale used for ECG recording.

Figure 5.12: Internally generated noise measured at the amplifier output using dry electrodes connected to one another. The recording was acquired with the digital storage oscilloscope at a sampling rate of 5 kHz.

Table 5.2: Intrinsic noise measured at the amplifier output.

	peak-to-peak output noise
specification limit	3 mV
dry electrodes connected to one another	22 to 26 mV
wet electrodes connected to one another	22 to 26 mV
constructed dry electrode models connected to ground	22 to 26 mV
constructed wet electrode models connected to ground	22 to 26 mV
inputs grounded via 100 kΩ resistors and 0.47 μF capacitors	22 to 26 mV

5.3.2 Input impedance performance

Simulation results

Fig. 5.13 presents simulation plots showing the input impedance characteristics of the proposed new amplifier design compared to the performance of the original circuit.

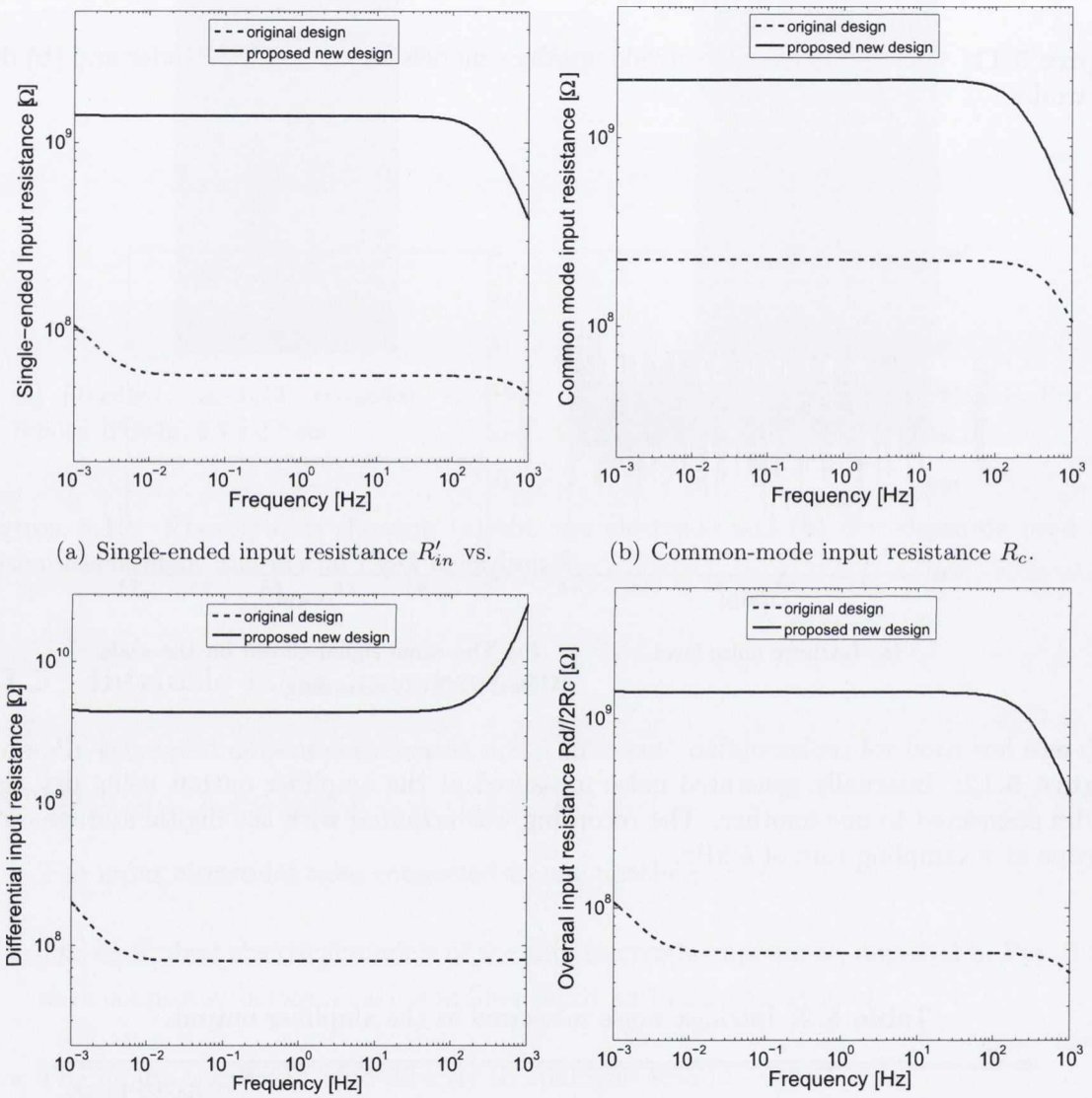

(a) Single-ended input resistance R'_{in} vs.

(b) Common-mode input resistance R_c.

(c) Differential input resistance R_d.

(d) Overall equivalent input resistance $R_d//2R_c$.

Figure 5.13: Simulation plots of the magnitude of the input impedance in (a) single-ended, (b) common-mode, (c) differential configurations and (d) the resulting equivalent impedance seen at amplifier input for the proposed new design compared with the performance of the original design published by Burke & Gleeson.

The magnitude of the single-ended input impedance, R'_{in}, and the common-mode input

impedance, R_c, were measured on the PSpice simulated circuits as the ratio of the potential at the non-inverting input terminal of the front-end op-amps to the current flowing through each input resistor. The differential input impedance is defined as $R_d = R_c R'_{in} / (R_c - R'_{in})$ and the overall input impedance is given by $R_{in} = R_d // (2R_c)$, as indicated in eqs. (5.11) to (5.16). Simulation results, presented in detail in Table 5.3, validate the theoretical values derived in eqs. (5.45) to (5.48). The new circuit arrangement is thus expected to feature enhanced input impedance performance compared to the original solution published by Burke & Gleeson.

Table 5.3: Input impedance characteristics of the proposed new circuit compared to results obtained with the original design simulated with PSpice. The minimum target value is 2 GΩ for $R_d//(2R_c)$. Bold case indicates that target value is not met.

	proposed new design				original design			
frequency [Hz]	0.5	10	50	100	0.5	10	50	100
single-ended input resistance R'_{in} [MΩ]	1386	1385	1367	1316	57	57	57	52
common-mode input resistance R_c [MΩ]	2022	2019	1965	1819	224	224	223	220
differential input resistance R_d [MΩ]	4404	4407	4495	4755	77	77	77	77
overall input resistance $R_d//(2R_c)$ [MΩ]	2108	2108	2097	2061	**66**	**66**	**66**	**66**

Bench test results

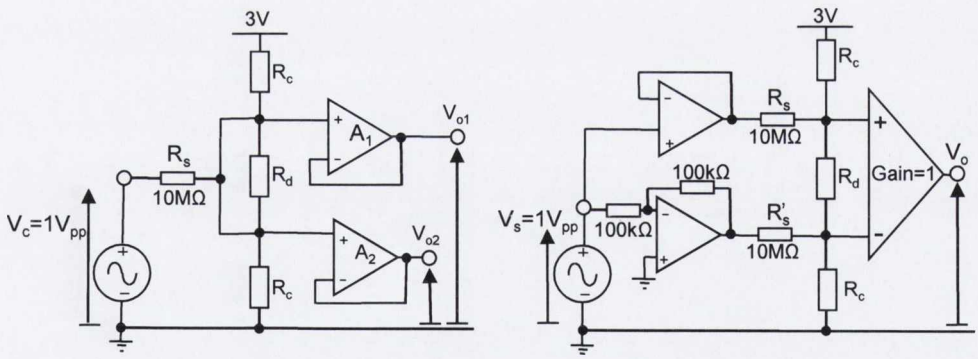

(a) Measurement set-up for estimating R_c. (b) Measurement set-up for estimating R_{in}.

Figure 5.14: Schematic representation of the measurement set-up used for estimating (a) the common-mode input impedance, R_c, and (b) the overall input impedance in a differential configuration $R_{in} = R_d//(2R_c)$. The attenuation caused by the additional series resistance is measured using the signal analyser.

The magnitude of the common-mode input impedance, R_c, and the overall input impedance in a differential configuration, $R_{in} = R_d//(2R_c)$, were estimated from the constructed prototype

in the frequency range 0.5 Hz - 10 kHz by measuring the attenuation caused by the insertion of a 10 MΩ resistor between the source signal and the amplifier inputs, as shown in Fig. 5.14. Measurement results, presented in Table 5.4 and Fig. 5.15, confirm that the bootstrapping mechanism at the amplifier front-end stage allows the target input impedance of 2 GΩ to be achieved at low frequency. However, as frequency increases the magnitude of the input impedance drops. This is believed to be caused by stray capacitance, the value of which is higher than that predicted in simulation. The presence of parasitic capacitance in parallel with R_c and R_d reduces the effective input impedance and limits the amplifier bandwidth.

Table 5.4: Input impedance measurement compared with simulation results.

	measurement						simulation					
freq. [Hz]	0.5	10	50	100	1000	2000	0.5	10	50	100	1000	2000
R_c [MΩ]	2060	1960	2270	1700	178	60	2022	2019	1967	1819	403	197
R_{in} [MΩ]	2140	2010	1750	1520	265	131	2108	2108	2097	2061	780	394

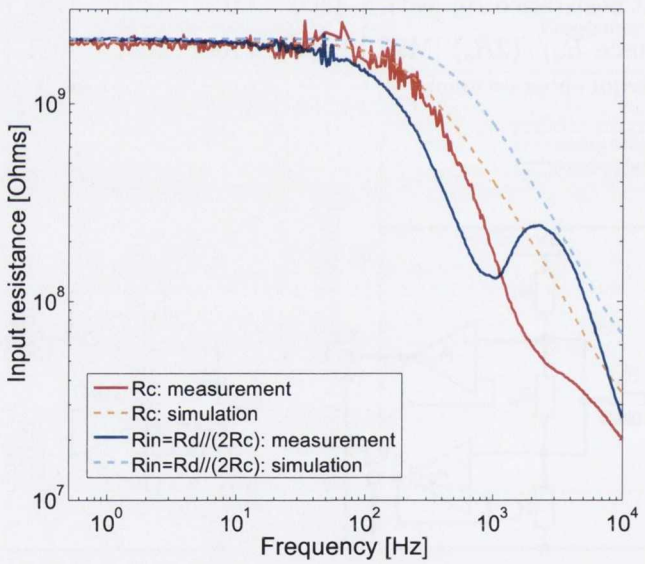

Figure 5.15: Measured input impedance characteristics compared with simulation plots.

5.3.3 Frequency response and impulse response performance

Simulation results

Plots of the simulated amplitude, phase and impulse responses, together with the recovery slope of the proposed new circuit are shown in Fig. 5.16. Results are compared with the responses obtained for the original design presented by Burke & Gleeson considering first the

instrumentation amplifier alone. The simulated circuits are then coupled to the corresponding skin-electrode interface models to determine the effect of the worst-case source impedance on the response of both recording systems. A summary of the predicted frequency response performance is given in Table 5.5.

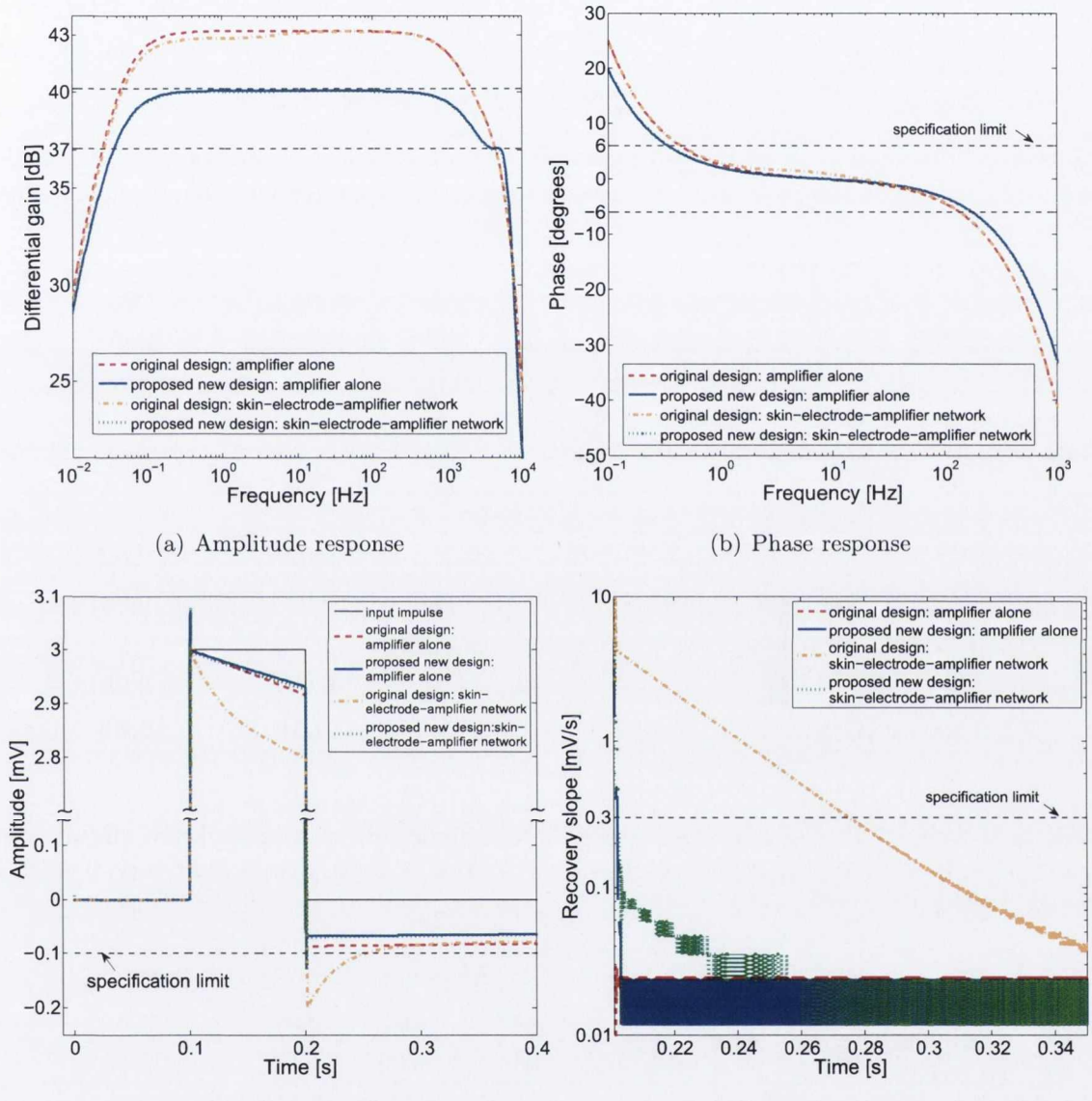

(a) Amplitude response

(b) Phase response

(c) Impulse response

(d) Recovery slope

Figure 5.16: Simulation plots of (a) the amplitude response, (b) phase response, (c) impulse response and (d) recovery slope of the proposed new amplifier and the skin-electrode-amplifier network compared with results obtained with the original design.

The Common Standards for Quantitative Electrocardiography (CSE) issued by the European Union defines the presence of a QRS deflection as a waveform having an amplitude greater than or equal to 20 μV and a duration greater than or equal to 6 ms [104]. Consequently deflections associated with an undershoot and a recovery slope greater than the specification limits after 6 ms following the end of the impulse might be falsely interpreted as valid QRS components. Impulse response characteristics are therefore presented in Table 5.5 beginning at 6 ms after the input impulse.

Table 5.5: Simulated low-frequency response of the proposed new circuit compared to results obtained with the original design. Bold case indicates that performance requirement is not met.

	max. variation in magnitude resp. from 0.14Hz to 30 Hz [dB]	phase @ 0.5 Hz [°]	max. undershoot after 6 ms following impulse [mV]	max. slope [mVs^{-1}]
specification limit	±0.5	6	-0.1	0.3
Performance of the instrumentation amplifier alone:				
proposed new design	-0.29	4.1	-0.07	0.02
original design	-0.42	5.3	-0.09	0.02
Performance with the skin-electrode-amplifier network:				
proposed new design	-0.30	4.2	-0.07	0.08
original design	**−0.77**	5.4	**−0.18**	**3.68**

Table 5.6: Simulated amplitude and phase characteristics of the proposed new circuit compared to results obtained with the original design. Bold case indicates that target value is not met.

	mid-band gain	3-dB bandwidth		±6° phase bandwidth	
	typical [dB]	low [Hz]	high [Hz]	low [Hz]	high [Hz]
target value	≥ 40	≤ 0.05	≥ 2500	≤ 0.5	≥ 250
Performance of the instrumentation amplifier alone:					
proposed new design	40	0.04	5248	0.34	**177**
original design	43	0.04	**2187**	0.45	**138**
Performance of the skin-electrode-amplifier network:					
proposed new design	40	0.04	5128	0.34	**177**
original design	43	0.04	**2187**	0.45	**138**

As indicated in the summary given in Table 5.6, the mid-band gain of the new circuit is 40 dB, compared to 43 dB for the solution presented by Burke & Gleeson. The 3-dB bandwidth of the proposed circuit extends from 0.04 Hz to 5.2 kHz while the magnitude response of the original design ranges from 0.04 Hz to 2.2 kHz. The increase in the bandwidth is mainly due to the use of op-amps with higher gain-bandwidth product and the implementation of a reduced differential gain. The phase shift introduced by the amplifier alone is within $\pm 6°$ from 0.34 Hz to 177 Hz for the new circuit design and from 0.45 Hz to 138 Hz for the original solution. There is no noticeable change in the bandwidth of the amplitude and phase response when the skin-electrode impedance is taken into account. The new circuit implementation falls short of meeting the target maximum phase shift of $-6°$ at 250 Hz to secure linear amplification of ECG components within the bandwidth recommended by the AHA for monitoring infants in non-ambulatory conditions. Nonetheless, the phase shift within the less stringent bandwidth of 150 Hz required by the ANSI is within specification.

PSpice simulation results confirm previous findings reported in Chapter 3 which were obtained by implementing models of skin-electrode-amplifier networks using MATLAB.

Bench test: frequency response results

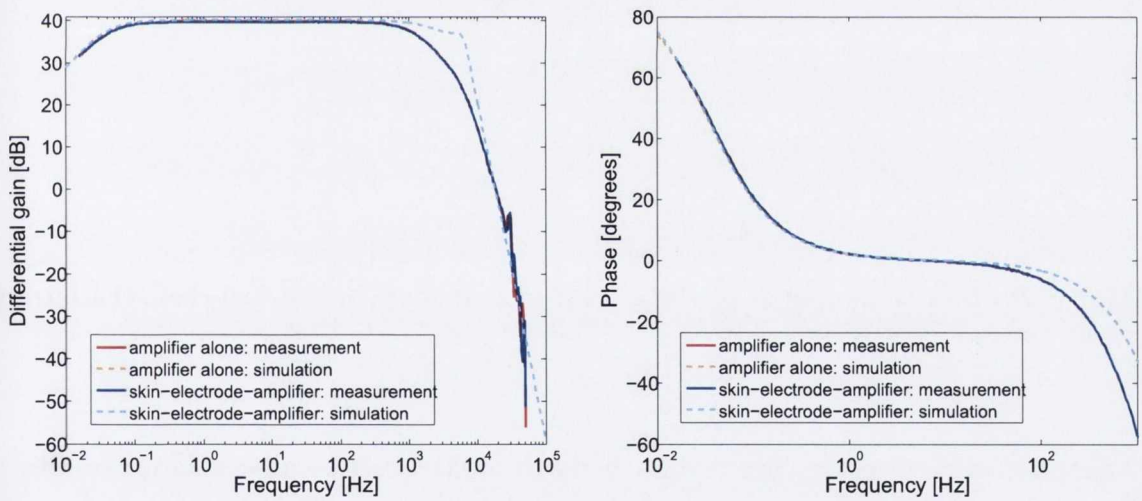

(a) Amplitude response

(b) Phase response

Figure 5.17: Measurement plots of (a) amplitude response and (b) phase response compared with simulation results.

Plots of the differential amplitude and phase response measured using the signal analyser are shown in Fig. 5.17 and data is given in Table 5.7. Bench test results confirm that the measured response is in accordance with simulation results at low frequencies. However, the

performance of the amplifier is limited at high frequency by the effect of stray capacitance on the board, as seen previously.

Table 5.7: Measured amplitude and phase characteristics compared with simulation results.

	mid-band gain	3-dB bandwidth		±6° phase bandwidth	
	typical	low	high	low	high
Performance of the instrumentation amplifier alone:					
measurement	40 dB	0.04 Hz	1250 Hz	0.38 Hz	98 Hz
simulation	40 dB	0.04 Hz	5248 Hz	0.34 Hz	177 Hz
Performance of the skin-electrode-amplifier network:					
measurement	40 dB	0.04 Hz	1200 Hz	0.38 Hz	94 Hz
simulation	40 dB	0.04 Hz	5128 Hz	0.34 Hz	177 Hz

Bench test: impulse response results

The impulse response was tested with an input pulse of 3 mV in amplitude and 100 ms in duration repeated every 2 s.

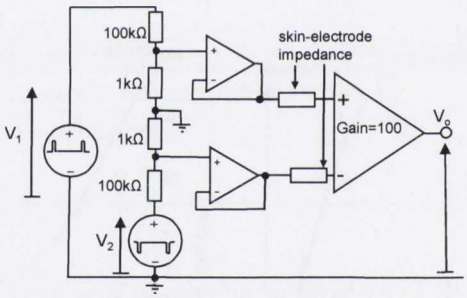

Figure 5.18: Circuit used for attenuating the signal produced by the dual-channel arbitrary function generator.

Table 5.8: Measured impulse response performance compared with simulation results.

	max. undershoot referred to input	max. recovery slope referred to input
specification limit	-0.1 mV	0.3 mVs^{-1}
Performance of the instrumentation amplifier alone:		
measurement	-0.09 mV	0.04 mVs^{-1}
simulation	-0.07 mV	0.02 mVs^{-1}
Performance of the skin-electrode-amplifier network:		
measurement	-0.09 mV	0.06 mVs^{-1}
simulation	-0.07 mV	0.08 mVs^{-1}

The dual-channel arbitrary function generator was used to generate two symmetrical pulses of 150 mV in amplitude, which were then attenuated by a factor of 100 using the circuit shown in Fig. 5.18. The resulting differential input signal is given in Fig. 5.19(a). Fig. 5.19(b) shows the response of the amplifier alone, while Fig. 5.19(c) gives the response of the worst-case skin-electrode-amplifier network. Measurement results, summarised in Table 5.8, indicate that the maximum undershoot and recovery slope measured after the impulse are within the specification limits.

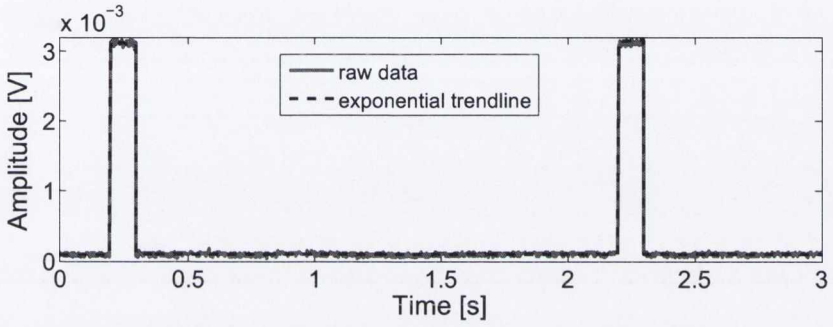

(a) Input impulse.

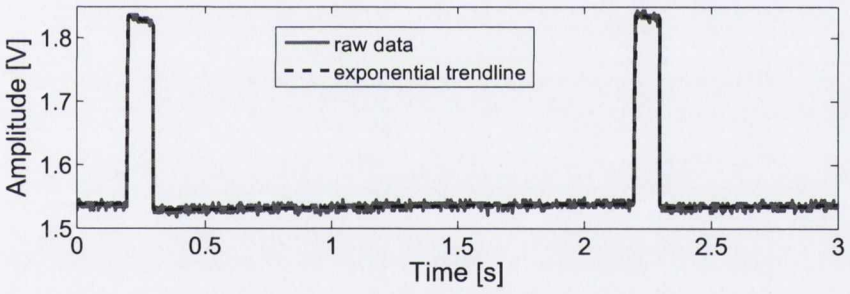

(b) Impulse response of the amplifier alone.

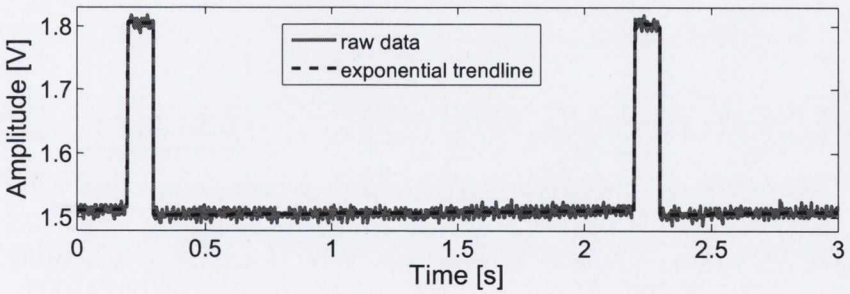

(c) Impulse response of the worst case skin-electrode-amplifier network.

Figure 5.19: Impulse response measurement acquired with the digital storage oscilloscope at 500 samples per s. An exponential trendline is superimposed to raw measurement data to allow the undershoot and recovery slope to be estimated in the presence of baseline noise.

5.3.4 CMRR performance

Simulation results

Fig. 5.20 and Table 5.9 present the simulated CMRR response of the proposed circuit compared with that of the original design. The overall CMRR of the simulated new recording system is 114 dB at 10 Hz and 108 dB at 50 Hz. Performance greater than 100 dB is expected at 0.5 Hz and 100 Hz.

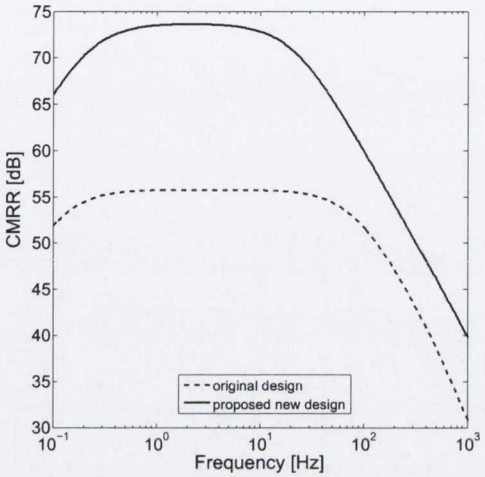

(a) Worst-case CMRR of the IA alone.

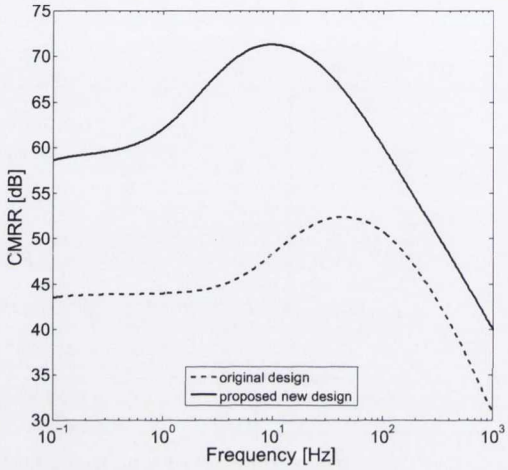

(b) Worst-case CMRR of the skin-electrode-amplifier network.

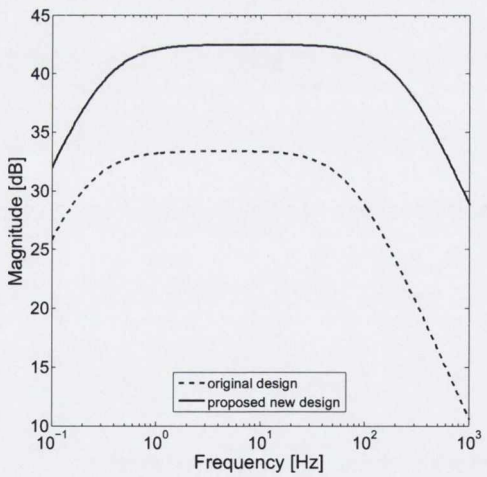

(c) Magnitude response of the driven-right-leg circuit.

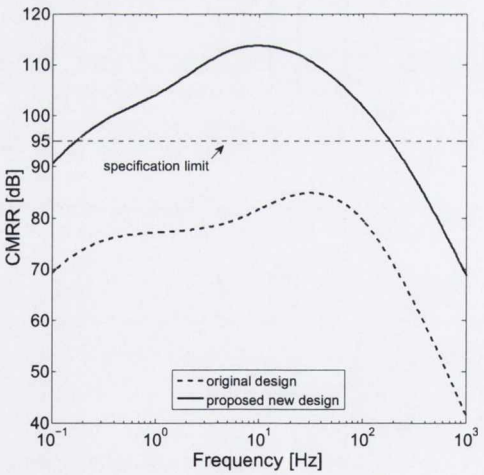

(d) Overall worst-case CMRR

Figure 5.20: Simulation plots of (a) the CMRR of the proposed amplifier alone, (b) the CMRR of the skin-electrode-amplifier network, (c) the gain of the driven-right-leg-circuit and (d) the overall worst-case CMRR of the recording system compared with results obtained with the original amplifier design.

Table 5.9: Simulated worst-case CMRR performance of the proposed new circuit compared with results obtained from the original design. The minimum target value is 95 dB in the bandwidth 0.5 to 100 Hz. Bold case indicates that target value is not met.

	proposed new design				original design			
frequency [Hz]	0.5	10	50	100	0.5	10	50	100
CMRR of the amplifier alone [dB]	73	73	65	60	56	56	54	52
CMRR of the skin-electrode-amplifier [dB]	60	71	65	60	44	48	52	51
CMRR provided by the right-leg-drive [dB]	41	42	42	42	33	33	32	29
CMRR of the overall recording system [dB]	101	114	108	102	**77**	**82**	**84**	**80**

Bench test results

Instability was experienced during actual ECG recording when the driven electrode was connected to the body. It was speculated that saturation of the driven-right-leg circuit may be the cause of the problem and its gain was progressively reduced from 41 dB down to approximately 17 dB for which stable ECG recordings were observed.

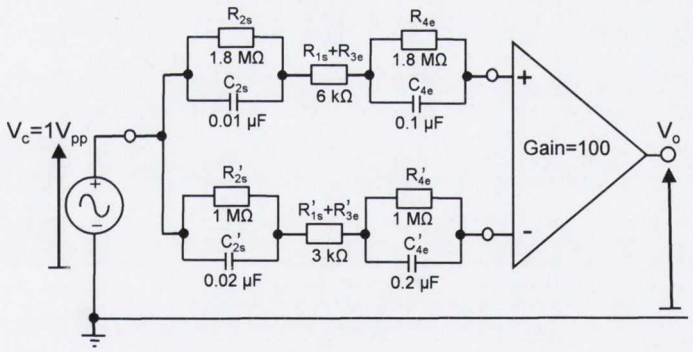

Figure 5.21: Set-up for measuring the common-mode gain of the skin-electrode-amplifier network assuming worst-case skin-electrode impedance and mismatch.

Fig. 5.21 shows the measurement set-up for measuring the common-mode gain of the skin-electrode-amplifier network. The elements of the skin-electrode impedance were mismatched in a 2:1 ratio. The CMRR was then calculated by adding the differential gain and the gain of the driven-right-leg circuit to the inverse of the common-mode gain in the frequency range 0.5 Hz - 10 kHz.

Table 5.10: CMRR measurement compared with simulation results. The mid-band gain of the driven-right-leg circuit is reduced from 41 dB to 17 dB. Bold case indicates that target value of 95 dB from 0.5 Hz to 100 Hz is not met.

	measured CMRR [dB]					simulated CMRR [dB]				
freq. [Hz]	0.5	10	50	100	1000	0.5	10	50	100	1000
amplifier alone	108	103	97	**89**	79	**86**	**89**	**81**	**76**	56
skin-electrode-amplifier	**78**	**86**	**74**	**82**	73	**73**	**73**	**87**	**81**	56

Measurement results are shown in Fig. 5.22 and listed in Table 5.10. The CMRR response of the amplifier was measured at 97 dB at mains frequency, which fulfills the requirement specified by international standards. However, imbalance introduced at the skin-electrode interface makes the skin-electrode-amplifier network fall short of reaching the target value. A detailed analysis of the source of instability in the driven-right-leg circuit is necessary to allow higher gain to be implemented.

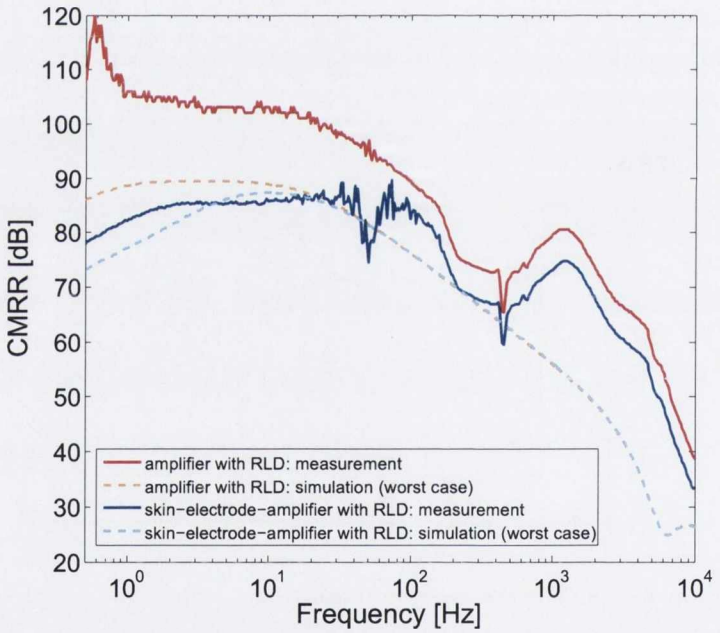

Figure 5.22: Measured CMRR characteristics compared with worst case simulation plots.

5.3.5 Response to a test ECG waveform

Simulation results

Fig. 5.23(a) is a sample lead II ECG recording extracted from the Physionet database "Challenge 2010 Training Set B" (waveform b84) sampled at 250 Hz [215]. The ECG waveform is

used as a test signal connected at the input of the proposed skin-electrode-amplifier network simulated from a data file with PSpice in a two-electrode configuration. The signal probed at output of the amplifier does not show evidence of distortion, as depicted in Fig. 5.23(b). The differential gain is confirmed as 40 dB and the baseline is set at half-rail.

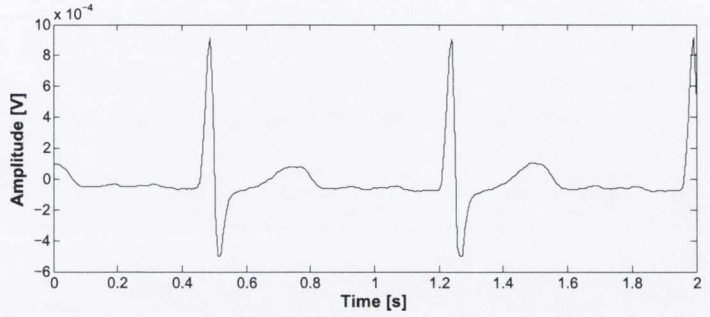

(a) ECG input waveform.

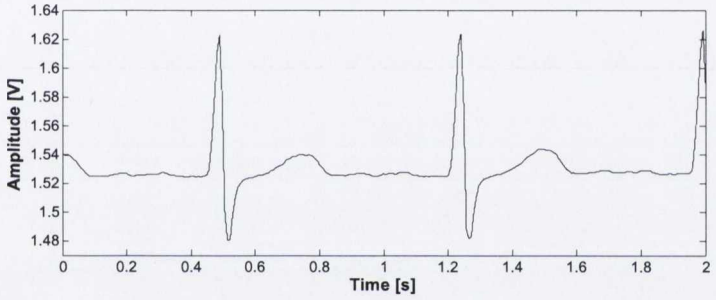

(b) ECG output waveform.

Figure 5.23: Sample ECG waveform shown (a) at the input and (b) at the output of the skin-electrode-amplifier network simulated for the proposed new design.

Bench test results

The arbitrary signal generator was used to generate two symmetrical waveforms of amplitude 500 mV pp, repeated every 2 s. The waveforms were attenuated by 100 using the circuit depicted previously in Fig. 5.18 to produce a 10 mV differential input signal, illustrated in Fig. 5.24(a). The output signal recorded from the amplifier alone and the response acquired using the worst-case skin-electrode-amplifier network are shown in Figs. 5.24(b) and 5.24(c), respectively. The recordings confirm that the input signal features are preserved despite the presence of the simulated skin-electrode interface. This can be explained by the high input impedance implemented at the front-end stage. It must be noted, however, that the quality of the signals shown is limited by the low sampling frequency of 250 Hz used in the original Physionet recording.

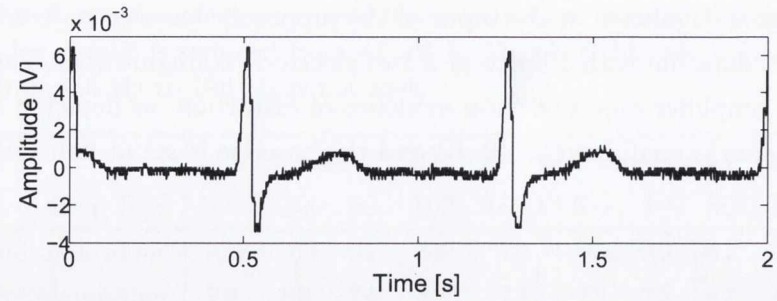

(a) Sample ECG waveform used as input test signal.

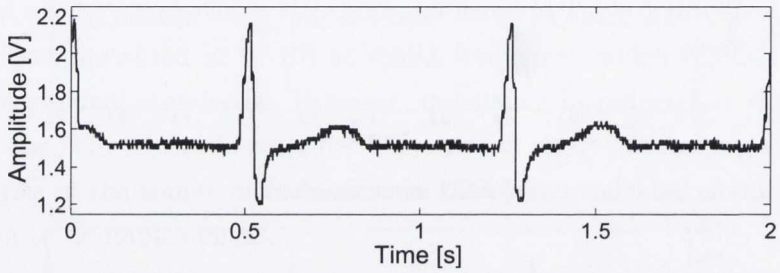

(b) Waveform recorded at the output of the amplifier alone.

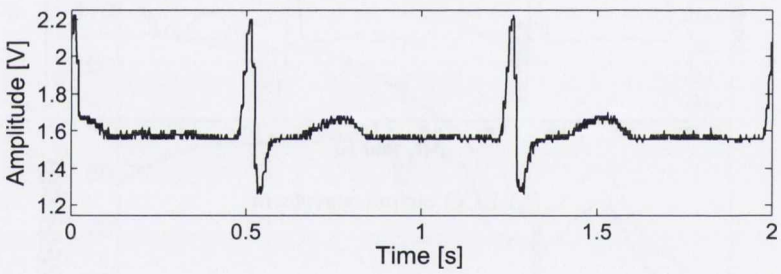

(c) Waveform recorded at the output of the worst case skin-electrode-amplifier network.

Figure 5.24: Waveforms showing (a) the input test ECG signal, (b) the signal at the output of the amplifier alone and (c) the signal at the output of the worst case skin-electrode-amplifier network. The waveforms were acquired at different times using the digital storage oscilloscope at 500 samples per s.

5.3.6 Power dissipation

Simulation results

Power consumption from a 3 V supply was calculated at 43.45 μW in circuit simulation. The circuit implementation proposed by Burke & Gleeson is more power-efficient since the total dissipated power was estimated at 27.15 μW using PSpice. Nonetheless, power consumption is well below the maximum target value of 150 μW specified in Section 2.6.

Bench test results

The power dissipated by the circuit was measured on the constructed prototype by inserting a 100 Ω resistor between the 3 V battery and the amplifier. Initially, no signal was connected to the amplifier inputs and the voltage across the resistor was measured at 1.2 mV, suggesting a quiescent current of 12 μA. With the 10 mV pp test ECG signal shown in Fig. 5.24(a) connected to the inputs, the voltage drop was measured at 1.5 mV, corresponding to a total quiescent current of 15 μA drawn from the battery. Power dissipation for the preamplifier is therefore 45 μW, which is in accordance with the value returned from circuit simulation.

5.3.7 Actual ECG recordings

Practical tests were carried out *in vivo* by comparing ECG recordings obtained using dry and wet electrodes under the following conditions:

- Resting ECG (Fig. 5.26): the subject was sitting still and breathing normally.
- Pseudo-ambulatory ECG (Fig. 5.27): the subject was required to walk on the spot at a normal rhythm.
- Harvard step test (Fig. 5.28): the subject was required to step up onto and down from an 42-cm platform, 30 times per minute.
- Arms high up and down to knees (Fig. 5.29): the subject repeatedly raised both arms above the head and then lowered them down to the knees.

Electrodes were held in contact with the skin using surgical adhesive tape, as shown in Fig. 5.25. The dry electrodes were disinfected with an alcohol wipe before being applied to the skin, but the skin was not cleaned, rubbed or prepared in any way.

(a) Male subject having a hairy chest. (b) Female subject.

Figure 5.25: Photographs showing the placement of electrodes for lead II ECG measurement for (a) a male subject and (b) a female subject.

Resting ECG recording (sitting still)

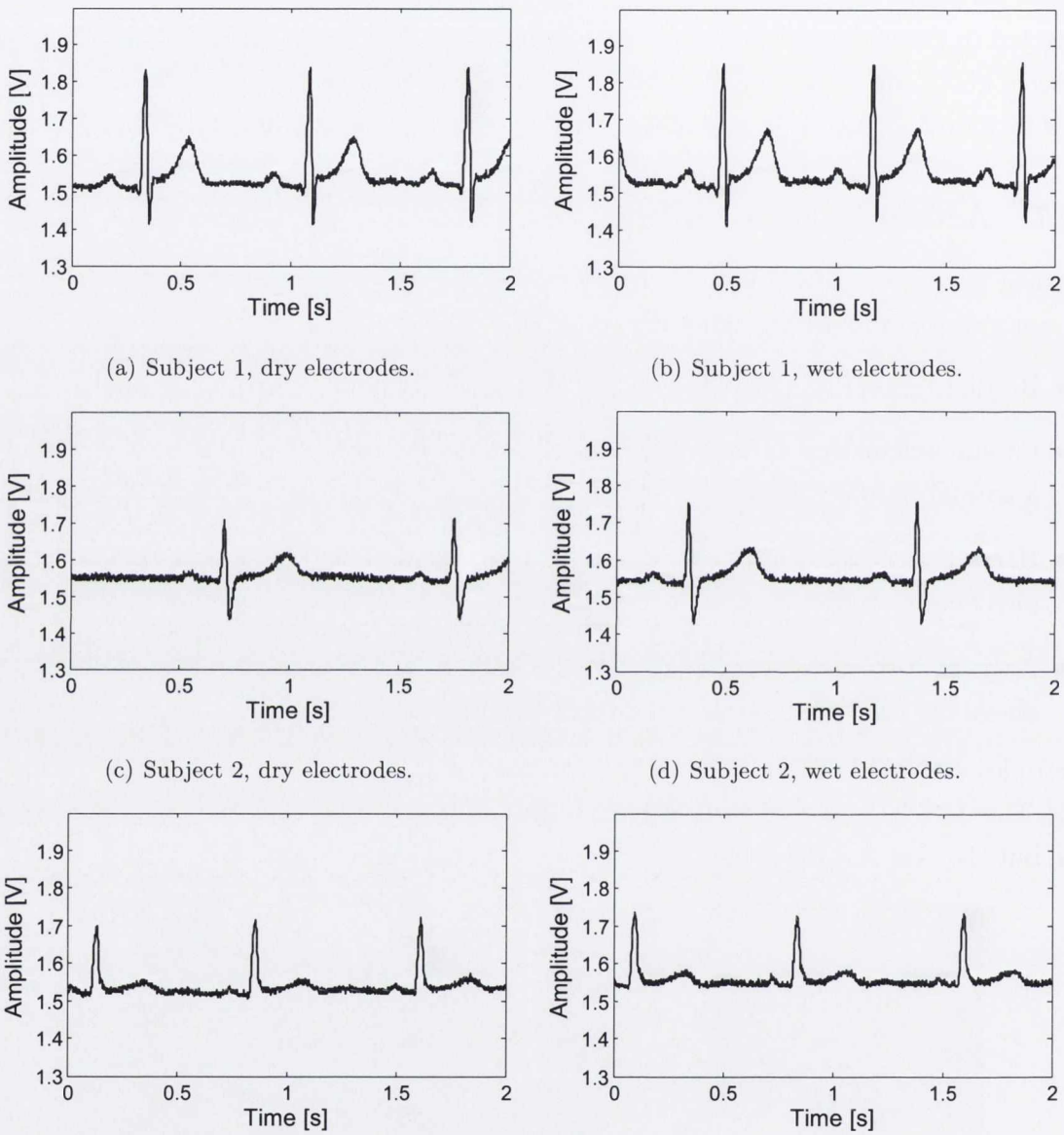

(a) Subject 1, dry electrodes.

(b) Subject 1, wet electrodes.

(c) Subject 2, dry electrodes.

(d) Subject 2, wet electrodes.

(e) Subject 3, dry electrodes.

(f) Subject 3, wet electrodes.

Figure 5.26: Sample resting ECG recordings for three subjects using dry electrodes (left hand side waveforms) and wet electrodes (right hand side waveforms). Subject 1 is a male, aged 23, having no hair at the electrode sites. Subject 2 is a male, aged 40, having a hairy chest. Subject 3 is a female, aged 33. The waveforms were acquired with the digital storage oscilloscope at a rate of 1000 samples per s.

Pseudo-ambulatory ECG (walking on spot)

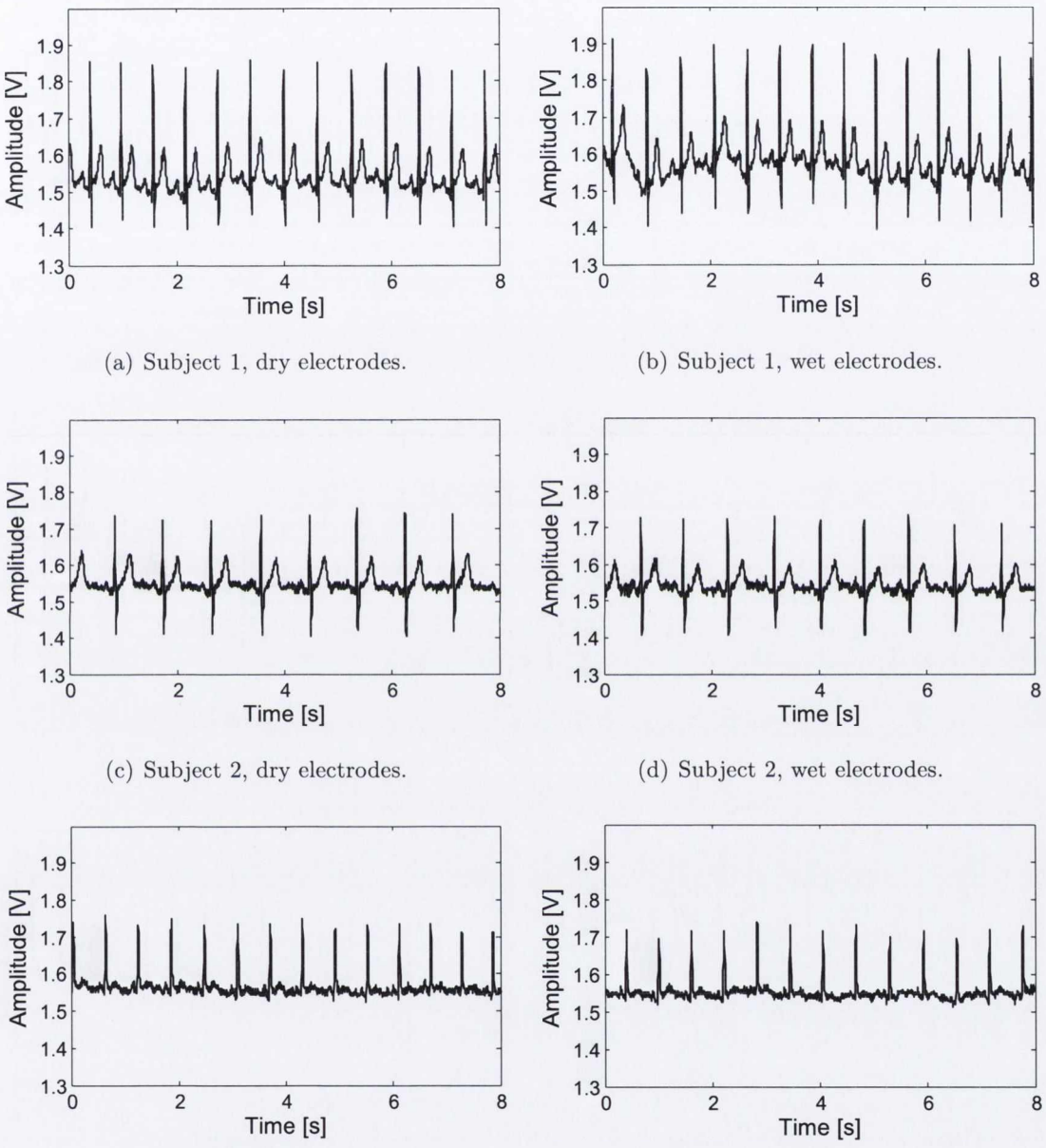

(a) Subject 1, dry electrodes.

(b) Subject 1, wet electrodes.

(c) Subject 2, dry electrodes.

(d) Subject 2, wet electrodes.

(e) Subject 3, dry electrodes.

(f) Subject 3, wet electrodes.

Figure 5.27: Sample ECG recordings for three subjects measured while walking on the spot using dry electrodes (left hand side waveforms) and wet electrodes (right hand side waveforms). The waveforms were acquired with the digital storage oscilloscope at a rate of 250 samples per s.

Harvard step test

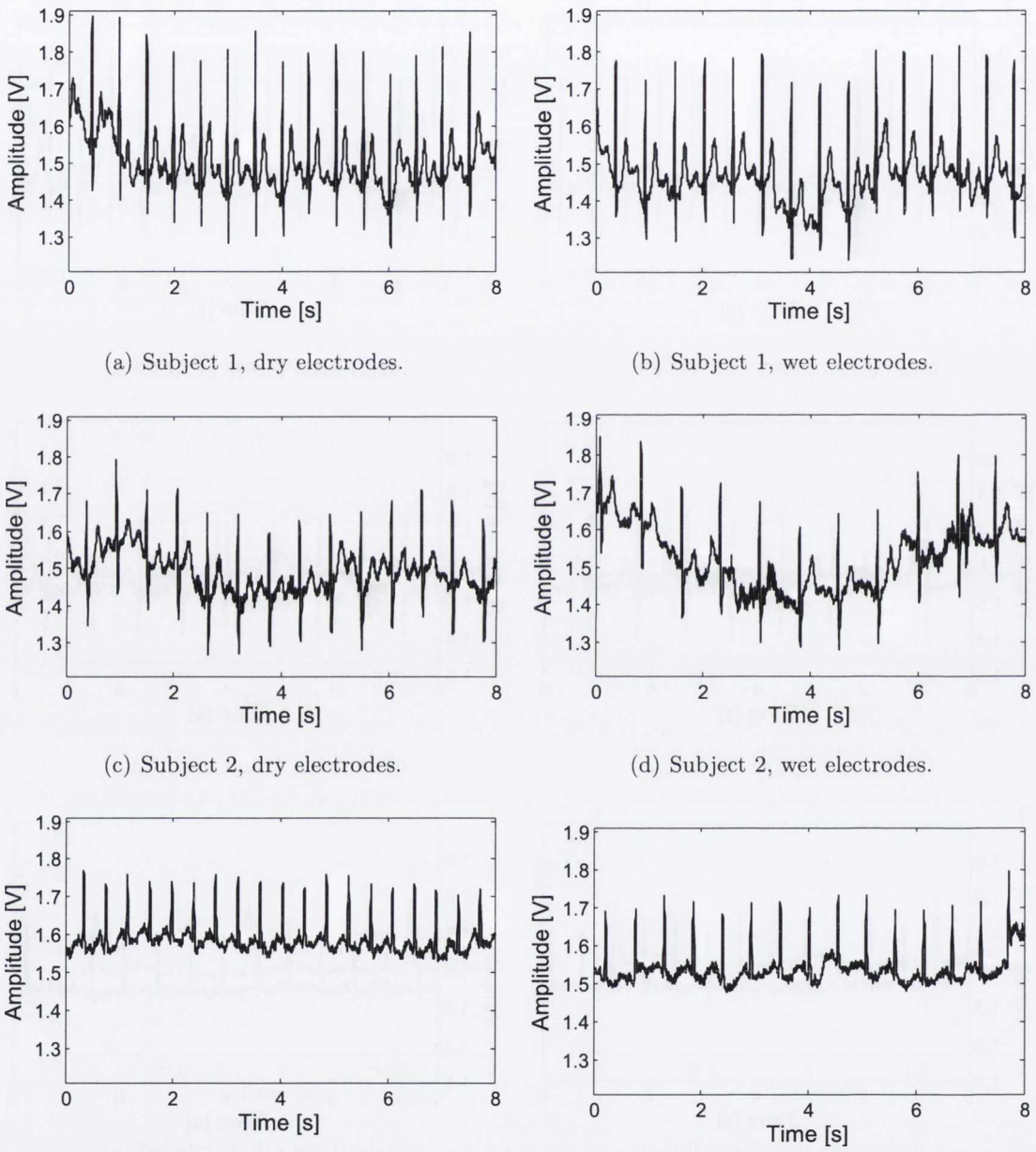

(a) Subject 1, dry electrodes.

(b) Subject 1, wet electrodes.

(c) Subject 2, dry electrodes.

(d) Subject 2, wet electrodes.

(e) Subject 3, dry electrodes.

(f) Subject 3, wet electrodes.

Figure 5.28: Sample ECG recordings for three subjects measured during a step test using dry electrodes (left hand side waveforms) and wet electrodes (right hand side waveforms). The waveforms were acquired with the digital storage oscilloscope at a rate of 250 samples per s.

Arms up high and down to knees

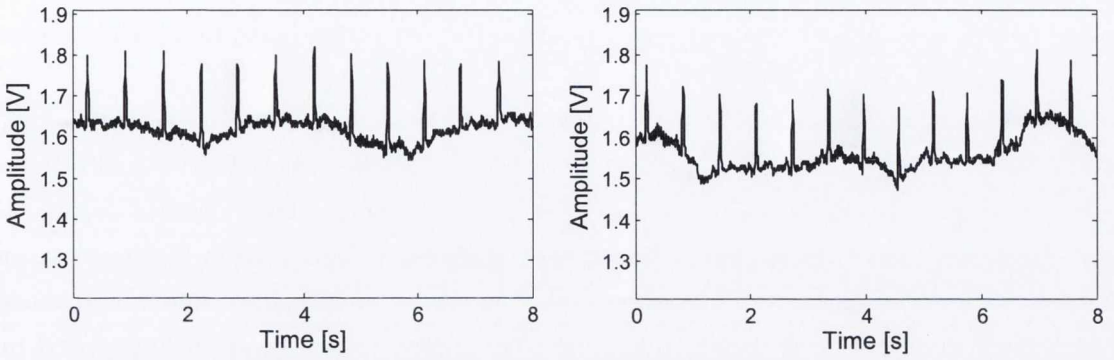

(a) Subject 3, dry electrodes.

(b) Subject 3, wet electrodes.

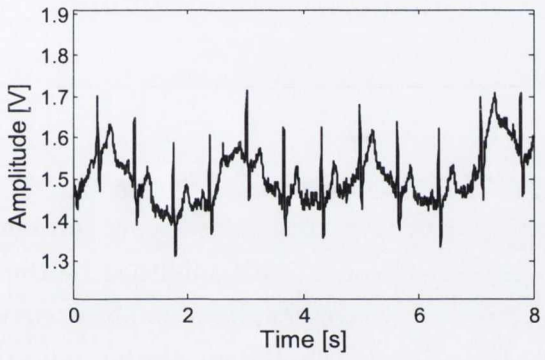

(c) Subject 4, dry electrodes.

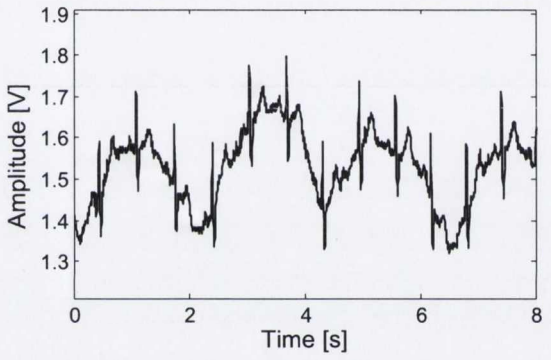

(d) Subject 4, wet electrodes.

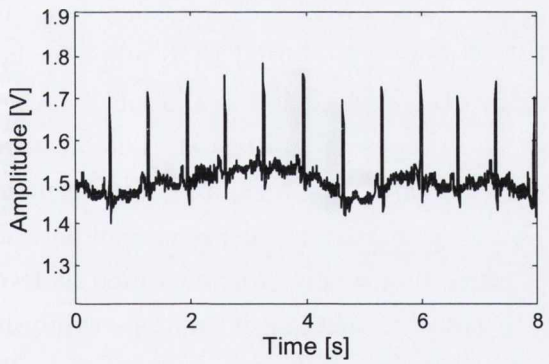

(e) Subject 5, dry electrodes.

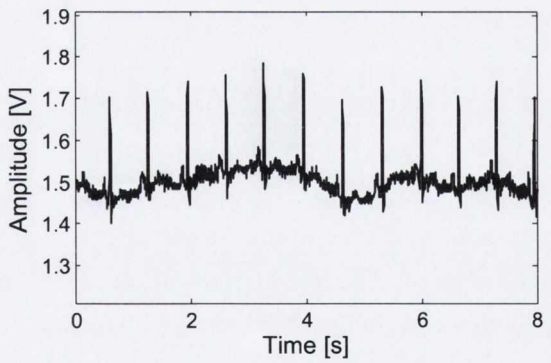

(f) Subject 5, wet electrodes.

Figure 5.29: Sample ECG recordings for three subjects measured while having their arms up high and down to knees using dry electrodes (left hand side waveforms) and wet electrodes (right hand side waveforms). Subject 3 female, aged 33. Subjects 4 and 5 are two males aged 28 and 29, respectively, having no hair at the electrode sites. The waveforms were acquired with the digital storage oscilloscope at a rate of 250 samples per s.

5.3.8 Discussion

ECG recordings for all fourteen subjects are shown in Appendix B. Figs. 5.26 to 5.29 present sample results obtained from three male subjects having no hair at the electrode sites (subjects 1, 4 and 5), a male participant with hairy chest (subject 2) and a female volunteer (subject 3).

The quality of the recorded ECG waveforms is comparable for measurements taken with dry and wet electrodes. The ECG signal can be clearly identified apart from the interference present in recordings. Semiconductor noise affects all waveforms but does not occlude the signal. However, baseline variation and motion artefact can be observed in tracings recorded while the subjects were moving or exercising. The effect of baseline wander and motion artefact is expected to be reduced by having a complete recording system integrated in a body-fit vest securing good contact between skin and electrodes and preventing leads from moving.

5.4 Conclusion

The design procedure has concentrated on essential performance requirements related to frequency response, immunity to external interfering signals, dc conditions, power consumption and intrinsic noise, as defined in previous chapters. A prior work published by Burke & Gleeson in 2000 has allowed a suitable ultra-low-power instrumentation amplifier circuit structure operating from a single-rail supply to be selected. Simulation results indicated that the original recording system designed by Burke & Gleeson provides an overall input impedance of 66 MΩ and a worst-case CMRR greater than 77 dB in the frequency range 0.5 to 100 Hz, for a power consumption of 27.15 μW. However, the initial ECG amplifier falls short of meeting the new performance specifications defined in Chapters 2, 3 and 4. A new amplifier circuit dissipating 45 μW of power was designed, built and tested. The measured low-frequency characteristics are in accordance with simulation results and fulfil performance requirements. Performance at high frequency is, however, limited by the presence of parasitic capacitance on the circuit board. In addition, semiconductor noise was measured at levels above the specification limit. Nevertheless, improvement is possible if op-amps exhibiting enhanced noise performance are used, at the expense of increased power consumption. The common-mode rejection ratio (CMRR) was measured at 97 dB at mains frequency, 50 Hz, and 89 dB at 100 Hz for the amplifier alone, meeting requirements. Finally, real ECG signals were acquired using dry and wet electrodes, returning waveforms of similar quality.

Chapter 6

A novel instrumentation amplifier circuit structure

The design strategy undertaken by the author began with the identification of the principal sources of recording error in Chapters 2, 3 and 4. New performance requirements for dry-electrode electrocardiography were then established, allowing the amplifier specifications in terms of input impedance and immunity to common-mode interference to be redefined. Consequently, the instrumentation amplifier presented in Chapter 5 has been designed to meet the requirements specified by international standards and to provide diagnostic quality ECG measurement with the dry electrodes characterised. CMRR performance was, however, limited by the magnitude of the skin-electrode impedance. New opportunities are expected in the near future with the development of ultra-low-impedance dry contact electrodes reported in May 2010 by Chang et al. [19]. Therefore, immunity to external unwanted voltages will no longer be dictated primarily by impedance imbalance at the amplifier input but will reside to a greater extent in the ability of the circuit to deal with other sources of imbalance to reject more efficiently common-mode signals in the measurement chain.

In this chapter, the author presents a novel instrumentation amplifier circuit structure that allows enhanced CMRR performance without requiring trimming or high-precision resistors. The solution is obtained by revisiting the fundamental theory that underlies the operation of the "classical" instrumentation amplifier. The circuit configuration is then modified to allow common-mode voltages to be rejected further. Circuit simulations are run with PSpice to assess improvement when worst-case mismatch in resistor values is considered. The limitations imposed by imperfections of real op-amps are taken into account and two circuit implementations are then presented and simulated.

6.1 Standard approaches

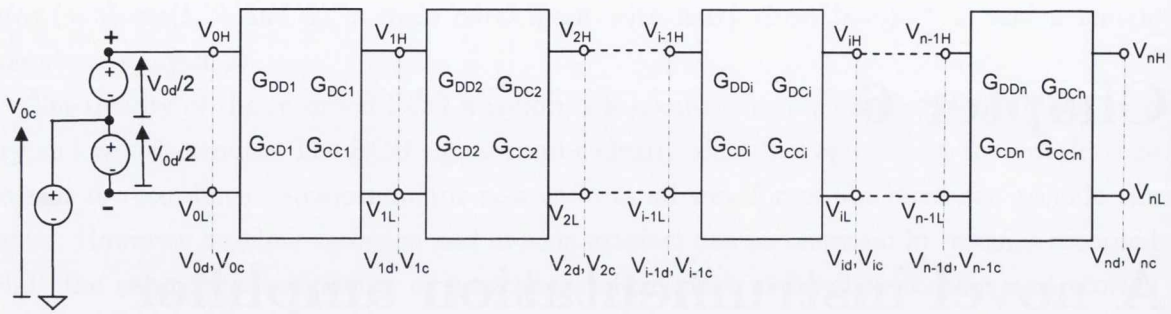

Figure 6.1: Cascaded amplifier network composed of n differential stages.

Fig. 6.1 is a generic representation of a differential measurement chain composed of n stages. For $1 \leq i \leq n$, each stage i is characterised by a transfer function that comprises four parameters G_{DD_i}, G_{CC_i}, G_{DC_i} and G_{CD_i}, defined in eqs. (6.1) to (6.4). The differential-to-differential gain G_{DD_i} is given by:

$$G_{DD_i} = \left.\frac{V_{id}}{V_{i-1d}}\right|_{V_{i-1c}=0} \tag{6.1}$$

G_{CC_i} is the common-mode-to-common-mode gain determined as:

$$G_{CC_i} = \left.\frac{V_{ic}}{V_{i-1c}}\right|_{V_{i-1d}=0} \tag{6.2}$$

The conversion of a common-mode input signal into a differential component is characterised by:

$$G_{DC_i} = \left.\frac{V_{id}}{V_{i-1c}}\right|_{V_{i-1c}=0} \tag{6.3}$$

G_{CD_i} represents the gain associated with the conversion of a differential input signal into a common-mode component and is defined as:

$$G_{CD_i} = \left.\frac{V_{ic}}{V_{i-1d}}\right|_{V_{i-1c}=0} \tag{6.4}$$

V_{kd} and V_{kc} are differential and common-mode composite signals, respectively, defined in eqs. (6.5) and (6.6) for $0 \leq k \leq n$ as:

$$V_{kd} = V_{kH} - V_{kL} \tag{6.5}$$

and

$$V_{kc} = \frac{V_{kH} + V_{kL}}{2} \tag{6.6}$$

Taking $k = 0$, the composite signals at the input of front-stage are the differential input signal, usually reffered to as e_d, and the common-mode interfering signal, generally labeled e_c.

Pallás-Areny and Webster [153–155] have shown that the overall CMRR of the cascaded differential system is given by:

$$\frac{1}{CMRR_T} \simeq \sum_{i=1}^{n} \frac{1}{CMRR_i} \tag{6.7}$$

with

$$CMRR_i = \frac{G_{DD_i}}{G_{DC_i}} \prod_{j=1}^{j<i} \frac{G_{DD_j}}{G_{CC_j}} \tag{6.8}$$

Eq. (6.7) suggests that for a given stage i, $CMRR_i$ is ideally infinite if any of the two following conditions is fulfilled:

1. $G_{DC_i} = 0$, corresponding to the absence of conversion of input common-mode signals into a differential component at the output of stage i.

2. $G_{CC_j} = 0$ for at least one preceding stage j. This implies the cancellation the common-mode component at the output of stage j.

Most CMRR enhancement techniques reviewed so far have relied on dedicated channels for dealing with common-mode signals. The cross-coupling mechanism specific to the "classical" instrumentation amplifier has, however, rarely been modified because a primary advantage of this structure is the ability of the fully differential stage to secure $G_{DC_1} = 0$. Its common-mode gain is unity, $G_{CC_1} = 1$, thus the implementation of large differential gain and the use of high-precision resistors or trimming techniques is necessary to secure high CMRR performance at the single-ended output. There are, however, several factors limiting the differential gain obtainable including:

- the differential dynamic range of the ECG signal at the amplifier input, e_d;
- the supply voltage, V_{cc};
- the gain-bandwidth product of the op-amps, GBP;
- the dynamic input range of the subsequent conditioning stages such as low-pass filters, automatic gain control circuits, threshold detectors and analogue-to-digital converters (ADCs).

International standards specify an input dynamic range $e_d = 10$ mV for non-ambulatory ECG recording. Therefore, for a low-power amplifier operating from a single supply voltage $V_{cc} = 3$ V, the maximum differential gain is determined by $A_{d_{max}} = V_{cc}/e_d = 300$ or 49 dB. Variation in dc bias voltage prevents the maximum gain from being achieved since "headroom" problems may be experienced. Consequently, A_d is generally not much greater than 200 or 46 dB for portable ECG recording systems powered from a 3-V battery. For ambulatory ECG monitoring, the International Electrotechnical Commission (IEC) specifies a lower signal input range as $e_d = 6$ mV, which allows higher gain to be envisaged. This, however, comes at the expense of a reduction in the amplifier bandwidth due to the limited GBP of ultra-low-power op-amps. Nevertheless, the use of op-amps with extended bandwidth or the distribution of the differential gain among several amplification stages does not generally permit a significant increase in the overall differential gain since the dynamic signal range at the preamplifier output must be compatible with the input range of subsequent stages composing the measurement chain. For example, several low-voltage ADCs have input dynamic ranges restricted to 1 V or less [216].

High-precision resistors are manufactured using laser trimming techniques requiring additional resources in time, equipment and labour, which come with increased cost. Generally for high CMRR values to be obtained, fully differential ADCs are used because they allow the differential dynamic range to be doubled and they present superior immunity to common-mode signals compared to difference amplifiers relying on highly matched resistors. Spinelli et al. proposed in January 2010 [173] a conditioning circuit that allows the common-mode voltage at the output of a fully differential amplifier to be attenuated so that it is compatible with differential ADCs having limited common-mode input range. The suggested circuit can be adjusted to achieve $G_{CC} << 1$. However, residual common-mode elements are reproduced at the output due to the conversion of common-mode signals into differential components, limiting the overall CMRR obtainable. In addition, high-resolution fully differential ADCs available today consume more power than their single-ended counterparts. Therefore single-ended circuits are preferred for designs aiming at ultra-low power consumption but mismatch in resistor values becomes a primary source of imbalance in the instrumentation amplifier circuit and degrades the CMRR.

Fig. 6.2 is a schematic diagram of the standard three-op-amp IA in which a switch is inserted in the feedback paths at the front-end stage and the gain-defining resistance at the input is separated into two resistances R_{1A} and R_{1B} to allow the common-mode input signal to be sensed. Referring to Fig. 6.2, the following potentials can be defined:

$$V_x = e_c + G_{DD_1}\frac{e_d}{2} \tag{6.9}$$

$$V_y = e_c - G_{DD_1}\frac{e_d}{2} \tag{6.10}$$

$$V_{cm} = e_c + \left(\frac{\Delta_{1B} - \Delta_{1A}}{\Delta_{1B} + \Delta_{1A}} \right) \frac{e_d}{2} \tag{6.11}$$

where G_{DD_1} is the nominal differential gain of the standard IA circuit defined as:

$$G_{DD_1} = 1 + \frac{R_2}{R_1} \tag{6.12}$$

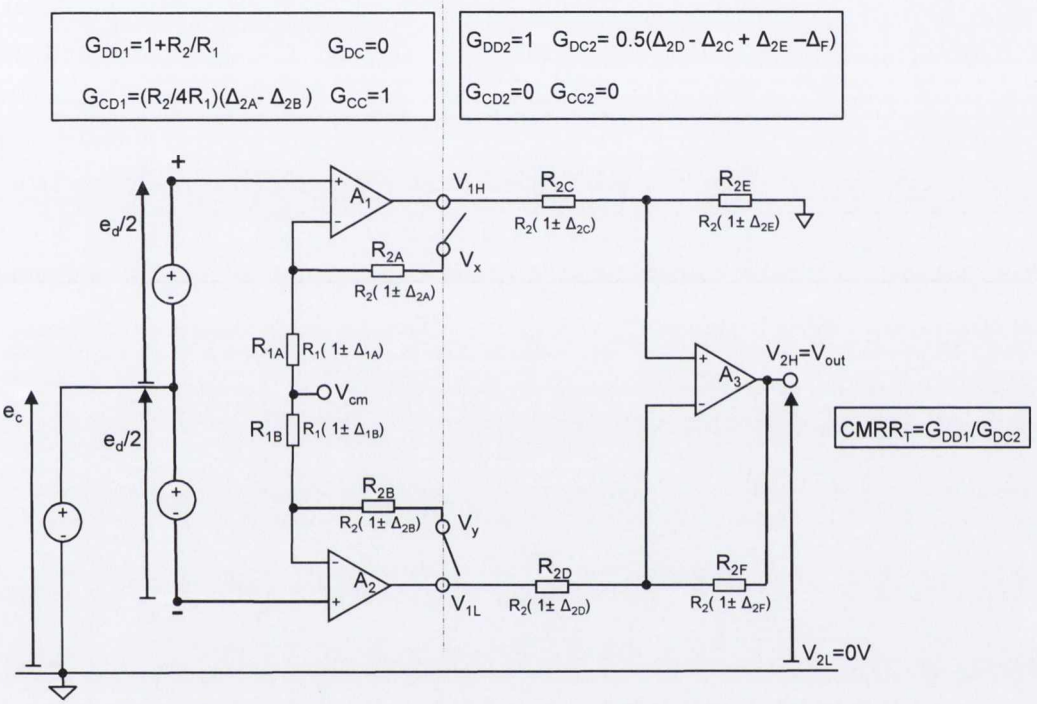

Figure 6.2: Circuit schematic of the "classical" three-op-amp IA that includes a switch in the feedback paths at the front-end stage. A measure of the common-mode input voltage can be obtained at the mid-point between resistors R_{1A} and R_{1B}.

Instead of connecting V_{1H} to V_x and V_{1L} to V_y, as for the standard IA, a more effective solution should aim at feeding back at V_x a potential in the form $\pm V_{1H} + e_c$ and at V_y a potential such as $\pm V_{1L} + e_c$. This would permit the common-mode component e_c to be cancelled on both sides of the amplifier, as indicated in eqs. (6.9) and (6.10). Implementing such functions requires a circuit that senses the common-mode signal, sums it to the output voltages $\{V_{1H}, V_{1L}\}$ and feeds the resulting voltages back to the inverting input terminals of op-amps A_1 and A_2.

6.2 The proposed instrumentation amplifier circuit structure

Several circuit arrangements have been considered by the author for reducing the nominal common-mode voltage in a fully differential configuration, but imbalance on either side of the amplifier generally restricts the obtainable CMRR at the single-ended output. This can be explained by the fact that attenuation or subtraction of the common-mode signal normally relies on op-amp-based voltage amplifiers, the closed-loop gain of which is set by resistor ratios. Any difference in these ratios results in a conversion of the common-mode signal into a differential signal that is amplified in the differential channel and cannot be eliminated at output stage. To be successful in rejecting unwanted common-mode voltages, amplification must be achieved without introducing imbalance in the common-mode component seen on either side of the amplifier before it is cancelled or attenuated. This involves a structure that allows subtraction or attenuation without introducing an error in the common-mode voltage sensed. The following sections outline the design of such an instrumentation amplifier structure.

6.2.1 The novel circuit concept

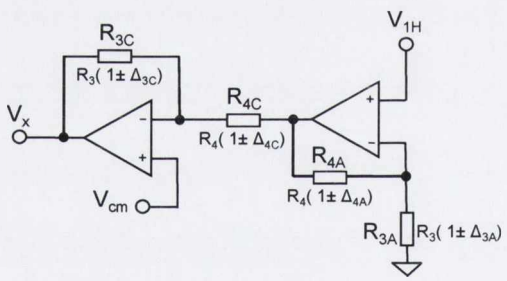

Figure 6.3: Circuit schematic of the standard two-op-amp IA.

Fig. 6.3 is the circuit schematic of the standard two-op-amp instrumentation amplifier for which the output voltage V_x can be expressed as follows:

$$V_x = \left(1+\frac{R_{3C}}{R_{4C}}\right)V_{cm} - \left(\frac{R_{3C}R_{4A}}{R_{4C}R_{3A}}+\frac{R_{3C}}{R_{4C}}\right)V_{1H}$$
$$\simeq \left(1+\frac{R_3}{R_4}\right)(V_{cm}-V_{1H}) + \frac{R_3}{R_4}(\Delta_{3C}-\Delta_{4C})V_{cm} + \left[\left(1+\frac{R_3}{R_4}\right)(\Delta_{3C}-\Delta_{4C})+\Delta_{3A}-\Delta_{4A}\right]V_{1H} \tag{6.13}$$

Eq. (6.13) reveals a particular feature of the two-op-amp IA for which errors in the gain-defining resistors do not affect both input terminals symmetrically. The error affecting the input signal V_{cm} is scaled by the resistor ratio R_3/R_4. Therefore making $R_4 >> R_3$ allows the effect of resistor mismatch to be reduced proportionally.

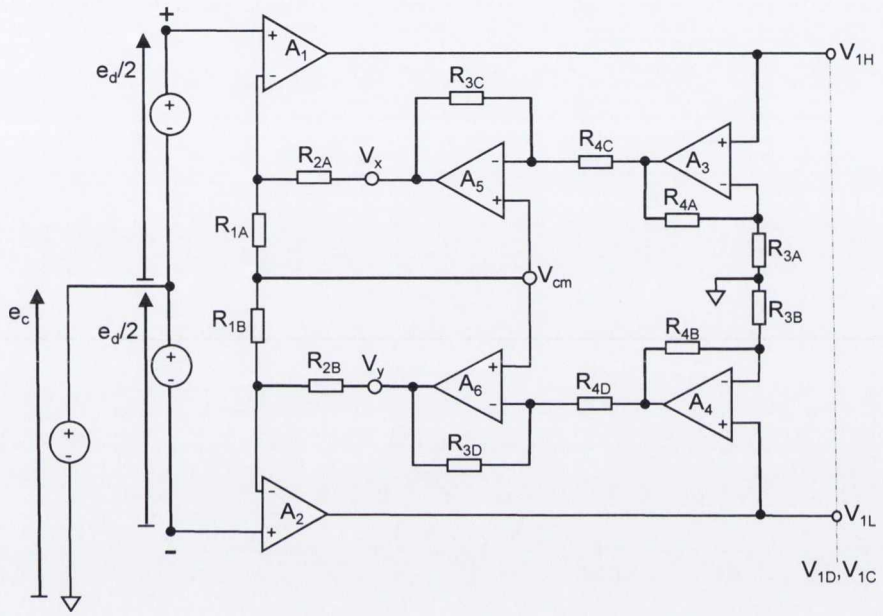

Figure 6.4: Proposed circuit arrangement allowing the reduction of the common-mode gain at the output of a fully differential amplification stage. High CMRR value can be obtained by making $R_4 >> R_3$.

Fig. 6.4 is a schematic of the circuit arrangement proposed by the author that includes a two-op-amp instrumentation amplifier in the feedback paths of a fully differential cross-coupled stage, resulting in:

$$e_c + G_{DD_1}\frac{e_d}{2} = \left[e_c + \left(\frac{\Delta_{1B} - \Delta_{1A}}{\Delta_{1B} + \Delta_{1A}}\right)\frac{e_d}{2} - V_{1H}\right]$$
$$+\frac{R_3}{R_4}(\Delta_{3C} - \Delta_{4C})\left[e_c + \left(\frac{\Delta_{1B} - \Delta_{1A}}{\Delta_{1B} + \Delta_{1A}}\right)\frac{e_d}{2}\right] + \left[\left(1 + \frac{R_3}{R_4}\right)(\Delta_{3C} - \Delta_{4C}) + \Delta_{3A} - \Delta_{4A}\right]V_{1H} \tag{6.14}$$

and

$$e_c - G_{DD_1}\frac{e_d}{2} = \left[e_c + \left(\frac{\Delta_{1B}-\Delta_{1A}}{\Delta_{1B}+\Delta_{1A}}\right)\frac{e_d}{2} - V_{1L}\right]$$
$$+\frac{R_3}{R_4}(\Delta_{3D}-\Delta_{4D})\left[e_c + \left(\frac{\Delta_{1B}-\Delta_{1A}}{\Delta_{1B}+\Delta_{1A}}\right)\frac{e_d}{2}\right] + \left[\left(1+\frac{R_3}{R_4}\right)(\Delta_{3D}-\Delta_{4D}) + \Delta_{3B} - \Delta_{4B}\right]V_{1L} \tag{6.15}$$

Neglecting second order differences, eqs. (6.14) and (6.15) allow the potentials at the output of op-amps A_1 and A_2 to be defined as:

$$V_{1H}\left(1+\frac{R_3}{R_4}\right) \simeq -G_{DD_1}\frac{e_d}{2} + \frac{R_3}{R_4}\left(1 - \frac{\Delta_{4A}-\Delta_{3A}}{1+\frac{R_3}{R_4}}\right)e_c$$
$$-\left[\frac{R_2(\Delta_{2A}-\Delta_{1A}-\Delta_{1B})}{R_1} + 2\Delta_{1B}\left(1+\frac{R_3}{R_4}\right) - \left[\frac{(\Delta_{4A}-\Delta_{3A})}{(1+R_3/R_4)} - \Delta_{3C} + \Delta_{4C}\right]\left(1+\frac{R_1}{R_2}\right)\right]\frac{e_d}{2} \tag{6.16}$$

and

$$V_{1L}\left(1+\frac{R_3}{R_4}\right) \simeq G_{DD_1}\frac{e_d}{2} + \frac{R_3}{R_4}\left(1 - \frac{\Delta_{4B}-\Delta_{3B}}{1+\frac{R_3}{R_4}}\right)e_c$$
$$+\left[\frac{R_2(\Delta_{2B}-\Delta_{1B}-\Delta_{1A})}{R_1} + 2\Delta_{1A}\left(1+\frac{R_3}{R_4}\right) - \left[\frac{(\Delta_{4B}-\Delta_{3B})}{(1+R_3/R_4)} - \Delta_{3D} + \Delta_{4D}\right]\left(1+\frac{R_1}{R_2}\right)\right]\frac{e_d}{2} \tag{6.17}$$

It can be deduced that the differential and common-mode components at the output of the fully differential stage presented in Fig. 6.4 are given by:

$$V_{1d} = V_{1H} - V_{1L} = \frac{G_{DD_1}}{\left(1+\frac{R_3}{R_4}\right)}e_d - \frac{R_3}{R_4}\left[\frac{\Delta_{4B}-\Delta_{4A}+\Delta_{3A}-\Delta_{3B}}{\left(1+\frac{R_3}{R_4}\right)^2}\right]e_c$$
$$+\left[\begin{array}{l}\frac{R_2(\Delta_{2A}+\Delta_{2B})}{2R_1\left(1+\frac{R_3}{R_4}\right)} + \left[1 - \frac{R_2}{R_1\left(1+\frac{R_3}{R_4}\right)}\right](\Delta_{1A}+\Delta_{1B}) \\ +\frac{G_{DD_1}}{2}\left[\frac{(\Delta_{3A}+\Delta_{3B}-\Delta_{4B}-\Delta_{4A})}{\left(1+\frac{R_3}{R_4}\right)} + (\Delta_{4C}+\Delta_{4D}-\Delta_{3D}-\Delta_{3C})\right]\end{array}\right]\frac{e_d}{\left(1+\frac{R_3}{R_4}\right)} \tag{6.18}$$

and

$$V_{1c} = \frac{V_{1H} + V_{1L}}{2} = \left(\frac{R_3}{R_3 + R_4}\right) e_d - \frac{R_3}{R_4}\left[\frac{\Delta_{4B} + \Delta_{4A} - \Delta_{3A} - \Delta_{3B}}{\left(1 + \frac{R_3}{R_4}\right)^2}\right] e_c$$
$$+ \left[\begin{array}{l} \frac{R_2(\Delta_{2B} - \Delta_{2A})}{2R_1\left(1 + \frac{R_3}{R_4}\right)} + \frac{(\Delta_{1A} + \Delta_{1B})}{2} \\ + \frac{G_{DD_1}}{2}\left[\frac{(\Delta_{3B} - \Delta_{3A} - \Delta_{4B} + \Delta_{4A})}{\left(1 + \frac{R_3}{R_4}\right)} + (\Delta_{4D} - \Delta_{4C} - \Delta_{3D} + \Delta_{3C})\right] \end{array}\right] \frac{e_d}{\left(1 + \frac{R_3}{R_4}\right)} \quad (6.19)$$

Eqs. (6.18) and (6.19) suggest that the common-mode signal at the output of the cross-coupled stage is scaled by an attenuation factor equal to $R_3/(R_3 + R_4)$ while the differential component is multiplied by $1/(1 + R_3/R_4)$. This yields a transfer function characterised by the following parameters:

$$G'_{DD_1} = \left.\frac{V_{1d}}{e_d}\right|_{e_c=0} = -\left(\frac{R_4}{R_3 + R_4}\right)\left(1 + \frac{R_2}{R_1}\right)$$
$$+ \left[\begin{array}{l} \frac{R_2(\Delta_{2A} + \Delta_{2B})}{2R_1\left(1 + \frac{R_3}{R_4}\right)} + \left[1 - \frac{R_2}{R_1\left(1 + \frac{R_3}{R_4}\right)}\right](\Delta_{1A} + \Delta_{1B}) \\ + \frac{A_{d0}}{2}\left[\frac{(\Delta_{3A} + \Delta_{3B} - \Delta_{4B} - \Delta_{4A})}{\left(1 + \frac{R_3}{R_4}\right)} + (\Delta_{4C} + \Delta_{4D} - \Delta_{3D} - \Delta_{3C})\right] \end{array}\right] \frac{1}{\left(1 + \frac{R_3}{R_4}\right)} \quad (6.20)$$

$$G'_{CC_1} = \left.\frac{V_{1c}}{e_c}\right|_{e_d=0} = \left(\frac{R_3}{R_3 + R_4}\right) - \frac{R_3}{R_4}\left[\frac{\Delta_{4B} + \Delta_{4A} - \Delta_{3A} - \Delta_{3B}}{\left(1 + \frac{R_3}{R_4}\right)^2}\right] \quad (6.21)$$

$$G'_{DC_1} = \left.\frac{V_{1d}}{e_c}\right|_{e_d=0} = \frac{R_3}{R_4}\left[\frac{\Delta_{4B} - \Delta_{4A} + \Delta_{3A} - \Delta_{3B}}{\left(1 + \frac{R_3}{R_4}\right)^2}\right] \quad (6.22)$$

and

$$G'_{CD_1} = \left.\frac{V_{1c}}{e_d}\right|_{e_c=0} = \left[\begin{array}{l} \frac{R_2(\Delta_{2B} - \Delta_{2A})}{2R_1\left(1 + \frac{R_3}{R_4}\right)} + \frac{(\Delta_{1A} + \Delta_{1B})}{2} \\ + \frac{G_{DD_1}}{2}\left[\frac{(\Delta_{3B} - \Delta_{3A} - \Delta_{4B} + \Delta_{4A})}{\left(1 + \frac{R_3}{R_4}\right)} + (\Delta_{4D} - \Delta_{4C} - \Delta_{3D} + \Delta_{3C})\right] \end{array}\right] \frac{1}{\left(1 + \frac{R_3}{R_4}\right)} \quad (6.23)$$

Eq. (6.20) indicates that the fully differential stage acts as an inverting amplifier, introducing 180° phase shift into the differential response. To avoid inversion, the modification shown in Fig. 6.5 is proposed. The modified circuit is connected to a unity-gain difference amplifier

providing a single-ended output given by:

$$V_{out} \simeq \left(\frac{R_4}{R_3+R_4}\right)\left(1+\frac{R_2}{R_1}\right)e_d$$
$$+\left[\begin{array}{l}\frac{1}{4}\left(-\Delta_{5A}-\Delta_{5B}+\Delta_{5C}+3\Delta_{5D}\right)+\frac{R_2(\Delta_{2A}+\Delta_{2B})}{2R_1\left(1+\frac{R_3}{R_4}\right)}+\left[1-\frac{R_2}{R_1\left(1+\frac{R_3}{R_4}\right)}\right](\Delta_{1A}+\Delta_{1B}) \\ +\frac{\left(1+\frac{R_2}{R_1}\right)}{2}\left[\frac{(\Delta_{3A}+\Delta_{3B}-\Delta_{4B}-\Delta_{4A})}{\left(1+\frac{R_3}{R_4}\right)}+(\Delta_{4C}+\Delta_{4D}-\Delta_{3D}-\Delta_{3C})\right]\end{array}\right]\frac{e_d}{\left(1+\frac{R_3}{R_4}\right)}$$
$$+\frac{R_3}{R_4+R_3}\left[\frac{(\Delta_{5B}-\Delta_{5A}+\Delta_{5C}-\Delta_{5D})}{2}+\frac{\Delta_{4B}-\Delta_{4A}+\Delta_{3A}-\Delta_{3B}}{\left(1+\frac{R_3}{R_4}\right)}\right]e_c \quad (6.24)$$

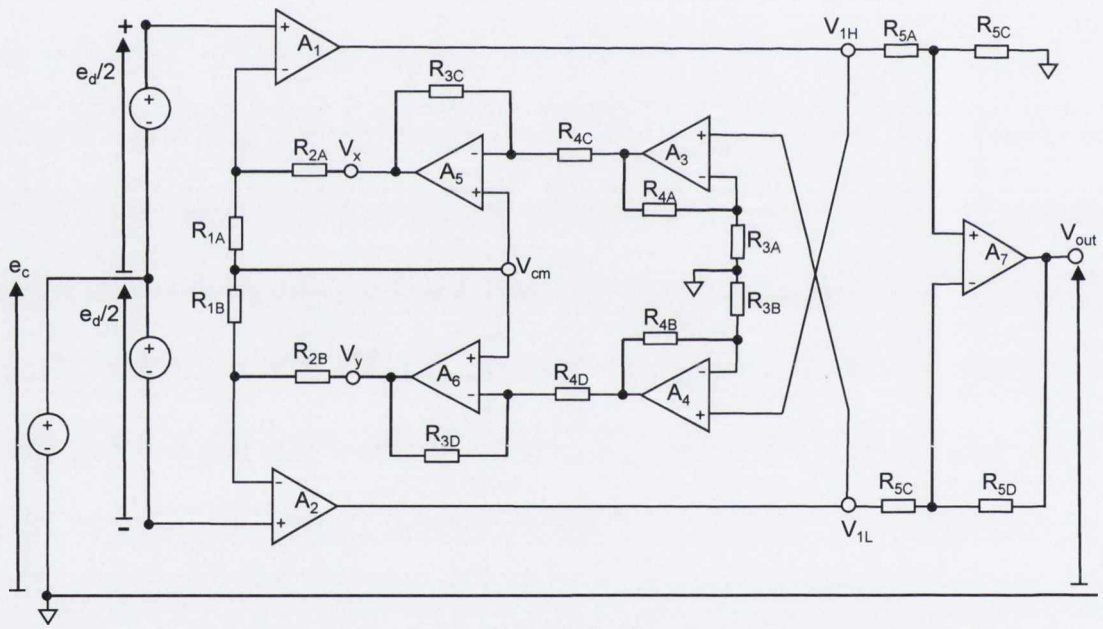

Figure 6.5: Proposed seven-op-amp instrumentation amplifier with enhanced CMRR characteristics providing a single-ended output.

The worst-case scenario corresponds to the mismatch in resistor values that yields the largest common-mode voltage at the single-ended output and is associated with the following combination:

$$\Delta_{1A} = \Delta_{2B} = \Delta_{3A} = \Delta_{3D} = \Delta_{4B} = \Delta_{4C} = \Delta_{5A} = \Delta_{5D} = \Delta_{R_{max}} \quad (6.25)$$

and

$$\Delta_{1B} = \Delta_{2A} = \Delta_{3B} = \Delta_{3C} = \Delta_{4A} = \Delta_{4D} = \Delta_{5B} = \Delta_{5C} = -\Delta_{R_{max}} \tag{6.26}$$

where $\Delta_{R_{max}}$ is the manufacturing tolerance for the resistors used. It results an overall common-mode gain A_c and a differential gain A_d defined is eqs. (6.27) and (6.28) as:

$$A_c \simeq 2\left[\frac{R_3\left(R_3+3R_4\right)}{\left(R_3+R_4\right)^2}\right]\Delta_{R_{max}} \tag{6.27}$$

$$A_d \simeq \left(\frac{R_4}{R_3+R_4}\right)\left(1+\frac{R_2}{R_1}\right)\left[1-\left[3+\left(\frac{R_2}{R_1+R_2}\right)\left(\frac{R_3}{R_4}\right)\right]\Delta_{R_{max}}\right] \tag{6.28}$$

It can then be concluded that the worst-case common-mode rejection ratio due to manufacturing tolerances in the gain-determining resistors is given by:

$$CMRR_{\Delta R_{min}} = \left|\frac{A_d}{A_c}\right| = \left(\frac{R_4}{R_3}\right)\frac{\left(1+\frac{R_2}{R_1}\right)\left[1-\left[3+\left(\frac{R_2}{R_1+R_2}\right)\left(\frac{R_3}{R_4}\right)\right]\Delta_{R_{max}}\right]}{2\left(1+\frac{2R_4}{R_3+R_4}\right)\Delta_{R_{max}}} \tag{6.29}$$

For $R_4 >> R_3$, $CMRR_{\Delta R_{min}}$ can be closely approximated as:

$$CMRR_{\Delta R_{min}} \simeq \frac{R_4}{3R_3}\left(\frac{1+\frac{R_2}{R_1}}{2\Delta_{R_{max}}}\right) \tag{6.30}$$

Detailed derivations demonstrating the effect of manufacturing tolerances in the gain-determining resistors on the CMRR are given in Appendix C.

Improvement compared to the classical three-op-amp IA is determined by the ratio $\alpha = R_4/3R_3$. For example, making $R_4 = 1000R_3$ results in an CMRR increased by 50 dB. The gain of the amplifiers built around op-amps A_3 and A_4 is given by R_4/R_3, which must be large for CMRR performance to be improved. Consequently, the dc bias voltage at the output of op-amps A_1 and A_2 is multiplied by the gain R_4/R_3. A common practice for preventing dc gain is the use of dc-blocking capacitors in series with R_{3A} and R_{3B} but imbalance in capacitance values on either side of the amplifier would degrade the CMRR. In fact, if high performance is to be achieved, R_3 must be several orders of magnitude smaller than R_4. Therefore, taking $R_4 = 10$ MΩ commonly available with 1% tolerance, R_3 must be less than 100 kΩ for a CMRR enhancement of 30 dB or higher. Preserving low-frequency components in the ECG signal would require capacitance values greater than 33 μF, the manufacturing tolerance of which is generally not better than 10%. A capacitance of 330 μF would be required for the CMRR to be improved by 50 dB. The circuit must therefore operate from a dual-rail supply to provide zero dc bias at the output of the fully differential stage.

6.2.2 Validation

In order to verify theoretical results and assess the effect of resistor mismatch on the conversion of common-mode to differential signal at the output of a single-ended amplifier, a Monte Carlo analysis is performed assuming ideal-op-amps and 1% tolerance resistors in the frequency range 1 mHz to 100 kHz with PSpice. Simulation results are shown in Fig. 6.6.

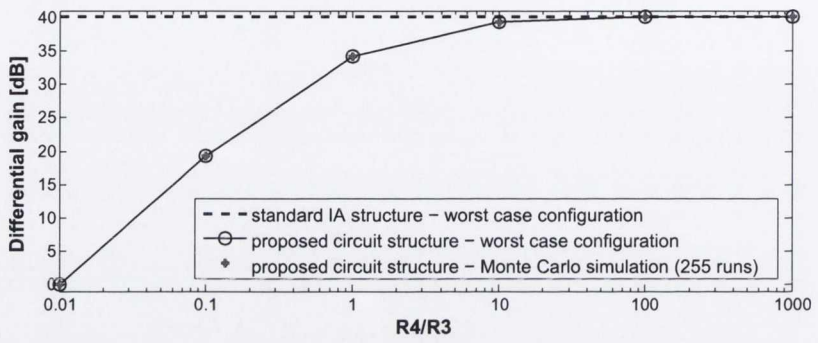

(a) A_d vs. R_4/R_3.

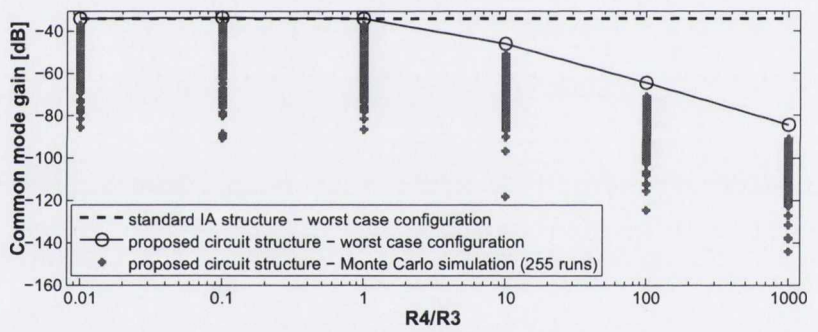

(b) A_c vs. R_4/R_3.

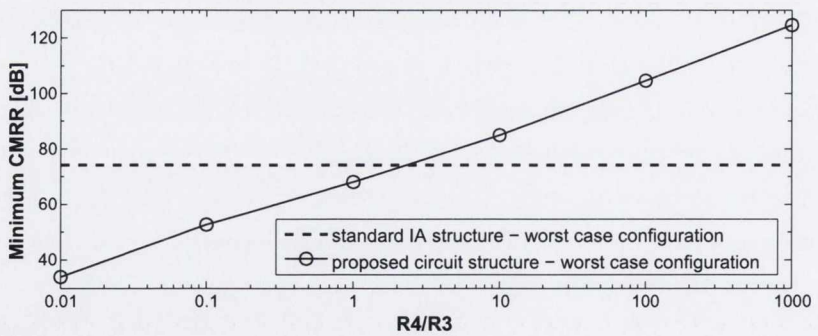

(c) $CMRR$ vs. R_4/R_3.

Figure 6.6: Plots of (a) the differential gain A_d, (b) the common-mode gain A_c and (c) the CMRR of the proposed circuit structure compared with results obtained with the "classical" three op-amp IA structure.

The circuit is simulated using a ±5 V dual supply and with a differential input signal e_d=100 μV in amplitude, because small signals are more noticeably affected by common-mode interference. The amplitude of the common-mode input signal is 1 V. Simulations are carried out for $R_2 = R_4 = R_5 = 10$ MΩ and $R_1 = 100$ kΩ, aiming at a differential gain of 40 dB. Op-amps are powered from a ±5 V supply with the exception of A_3 and A_4 for which $V_{cc} = \pm 6$ V at $R_4/R_3 = 1000$ to prevent saturation. Monte Carlo simulations are run 255 times considering $\Delta_{R_{max}} = 1\%$. The theoretical worst-case configurations are defined in eqs. (6.25) and (6.26).

The differential and common-mode responses of the new circuit concept are compared with results obtained with the standard three-op-amp IA, as depicted in Fig. 6.6. Simulation results demonstrate that for $R_4 >> R_3$, no noticeable difference exists in the differential response of the two circuit structures. However, the amplitude of the common-mode signal measured at the single-ended output is systematically lower for the proposed circuit. The novel instrumentation amplifier circuit structure allows the CMRR due to mismatch in resistor values to be improved by a factor approximately equal to the resistor ratio $\alpha = R_4/3R_3$. When $R_4 \leq R_3$, no improvement is observed in the common-mode response, however, the differential gain is reduced resulting in a decrease in CMRR value. All observations confirm the principle of operation of the novel circuit as described in eqs. (6.27) to (6.30)

6.3 Limitations imposed by op-amp imperfections

Simulations were previously performed assuming ideal op-amps to analyse to effect of tolerances in the gain-defining resistors exclusively. Having identified the worst-case mismatch in resistor values, we now consider some limitations inherent in the use of real op-amps.

6.3.1 Effect of limited CMRR provided by real op-amps

The circuit diagram shown in Fig. 6.7 represents the effects of the limited CMRR provided by real op-amps. For a given op-amp, A_i, a common-mode voltage e_{cmi} applied to its input terminals results in a common-mode error $e_{\epsilon cmi}$ referred to its non-inverting input as:

$$e_{\epsilon cmi} = \frac{e_{cmi}}{CMRR_{opi}} \tag{6.31}$$

The potential V_x at the output of the feedback op-amp A_5 can be expressed in terms the input common-mode voltage e_c and the error introduced by op-amps A_1 and A_2 as follows:

$$V_x = e_c + \left(1 + \frac{R_2}{R_1}\right)(e_{\epsilon cm1} - e_{\epsilon cm2}) \tag{6.32}$$

Considering the two-op-amp instrumentation amplifier built around op-amps A_3 and A_5, a second expression for V_x can be derived in terms of V_{1L}, the gain of the two-op-amp IA and the associated common-mode error voltages:

$$V_x = \left(1 + \frac{R_3}{R_4}\right)\left[e_c + \frac{e_{ecm1} + e_{ecm2}}{2} + e_{ecm5} - V_{1L} - e_{ecm3}\right] \tag{6.33}$$

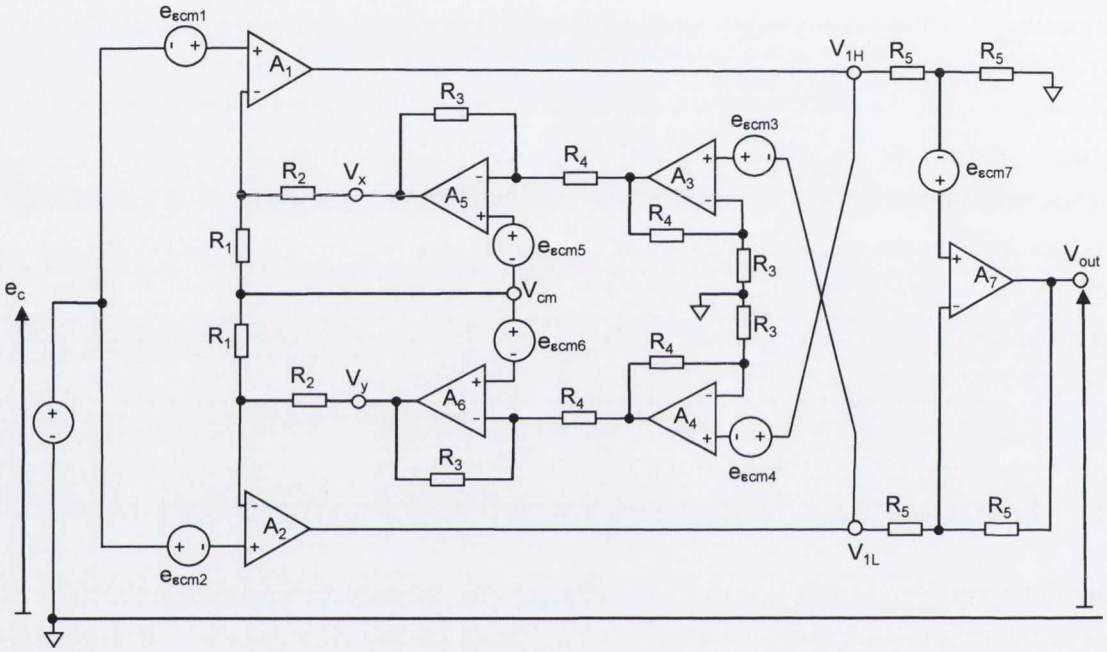

Figure 6.7: Circuit diagram of the novel instrumentation amplifier proposed by the author modelling the effect of limited CMRR of the seven op-amps.

Equating eqs. (6.32) and (6.33) leads to the following expression for V_{1L}:

$$V_{1L} = -\frac{\left[\frac{R_3}{R_4}e_c + \left(1 + \frac{R_2}{R_1}\right)\frac{(e_{ecm1} - e_{ecm2})}{2} - \left(1 + \frac{R_3}{R_4}\right)\left[\frac{e_{ecm1} + e_{ecm2}}{2} + e_{ecm5} - e_{ecm3}\right]\right]}{\left(1 + \frac{R_3}{R_4}\right)} \tag{6.34}$$

A similar approach allows an expression for V_{1H} to be derived as:

$$V_{1H} = -\frac{\left[\frac{R_3}{R_4}e_c - \left(1 + \frac{R_2}{R_1}\right)\frac{(e_{ecm1} - e_{ecm2})}{2} - \left(1 + \frac{R_3}{R_4}\right)\left[\frac{e_{ecm1} + e_{ecm2}}{2} + e_{ecm6} - e_{ecm4}\right]\right]}{\left(1 + \frac{R_3}{R_4}\right)} \tag{6.35}$$

The common-mode error voltages are described in eqs. (6.36) to (6.42) as follows:

$$e_{\epsilon cm1} = \frac{e_c}{CMRR_{op1}} \tag{6.36}$$

$$e_{\epsilon cm2} = \frac{e_c}{CMRR_{op2}} \tag{6.37}$$

$$e_{\epsilon cm3} \simeq \left(\frac{R_3}{R_3 + R_4}\right) \frac{e_c}{CMRR_{op3}} \tag{6.38}$$

$$e_{\epsilon cm4} \simeq \left(\frac{R_3}{R_3 + R_4}\right) \frac{e_c}{CMRR_{op4}} \tag{6.39}$$

$$e_{\epsilon cm5} \simeq \frac{e_c}{CMRR_{op5}} \tag{6.40}$$

$$e_{\epsilon cm6} \simeq \frac{e_c}{CMRR_{op6}} \tag{6.41}$$

and

$$e_{\epsilon cm7} \simeq \left(\frac{R_3}{R_3 + R_4}\right) \frac{e_c}{CMRR_{op7}} \tag{6.42}$$

It can be shown that the potential at the output of the unity-gain difference amplifier built around op-amp A_7 is given by:

$$V_{out} = V_{1H} - V_{1L} + 2e_{\epsilon cm7} = e_c \left[\begin{array}{c} \frac{\left(1+\frac{R_2}{R_1}\right)\left(\frac{1}{CMRR_{op1}} - \frac{1}{CMRR_{op2}}\right)}{1+\frac{R_3}{R_4}} + \frac{1}{CMRR_{op6}} - \frac{1}{CMRR_{op5}} \\ + \left(\frac{R_3}{R_3+R_4}\right)\left(\frac{1}{CMRR_{op4}} - \frac{1}{CMRR_{op3}} + \frac{2}{CMRR_{op7}}\right) \end{array} \right] \tag{6.43}$$

The effect of the limited CMRR of the seven op-amps results at the single-ended output in:

$$CMRR_{op} = \frac{\left.\frac{V_{out}}{e_d}\right|_{e_c=0}}{\left.\frac{V_{out}}{e_c}\right|_{e_d=0}}$$

$$= \frac{1}{\frac{1}{CMRR_{op1}} - \frac{1}{CMRR_{op2}} + \frac{\left(1+\frac{R_3}{R_4}\right)\left(\frac{1}{CMRR_{op5}} - \frac{1}{CMRR_{op6}}\right)}{1+\frac{R_2}{R_1}} + \frac{\left(\frac{R_3}{R_4}\right)\left(\frac{1}{CMRR_{op3}} - \frac{1}{CMRR_{op4}} + \frac{2}{CMRR_{op7}}\right)}{1+\frac{R_2}{R_1}}} \tag{6.44}$$

For $R_4 >> R_3$, $CMRR_{op}$ can be closely approximated by:

$$\frac{1}{CMRR_{op}} \simeq \frac{1}{CMRR_{op1}} - \frac{1}{CMRR_{op2}} + \frac{\frac{1}{CMRR_{op5}} - \frac{1}{CMRR_{op6}}}{1 + \frac{R_2}{R_1}} + \frac{\frac{1}{CMRR_{op3}} - \frac{1}{CMRR_{op4}} + \frac{2}{CMRR_{op7}}}{\frac{R_4}{R_3}\left(1 + \frac{R_2}{R_1}\right)} \quad (6.45)$$

As in the case of the "classical" IA circuit structure, the front-end op-amps A_1 and A_2 must have the highest CMRR characteristics or be closely matched for high performance to be obtained. If $R_2 >> R_1$, the CMRR of op-amps A_5 and A_6 are less critical. In addition, securing $R_4 >> R_3$ allows the effect of the CMRR of op-amps A_3, A_4 and A_7 to be minimised. In practice, it is advisable to select op-amps from the same series and preferably integrated on the same chip in order to obtain better matching in their common-mode responses.

6.3.2 Effect of the op-amp input offset voltages and bias currents

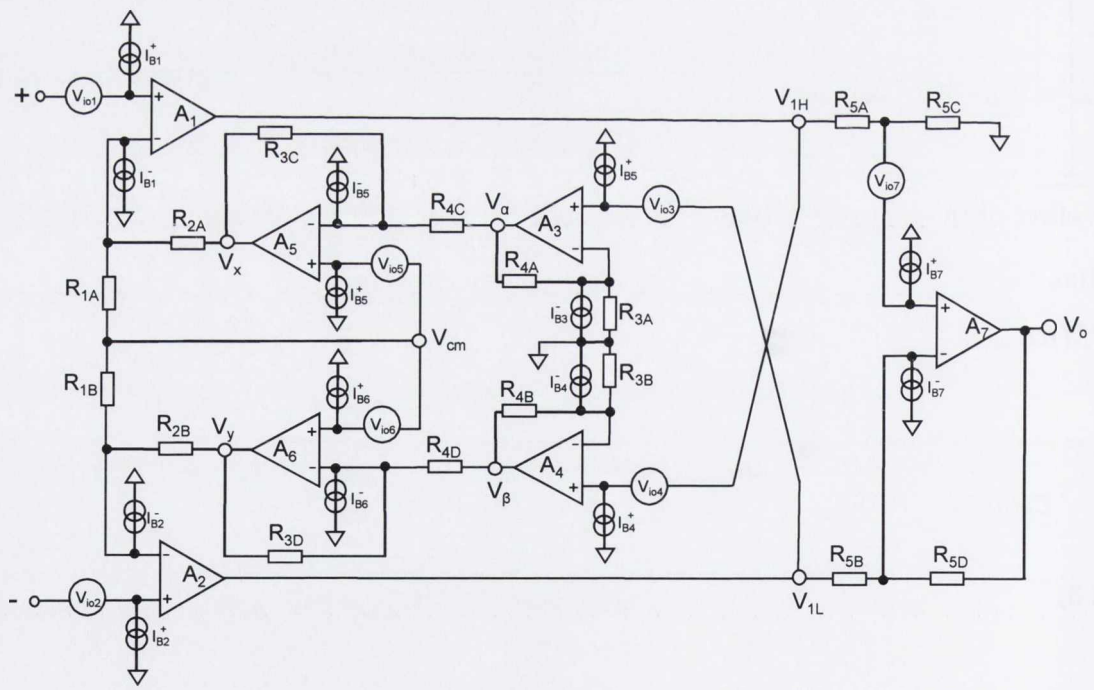

Figure 6.8: Modelling of the dc imperfections of the op-amps. I_{Bk}^- and I_{Bk}^+ are the bias currents at the inverting and non-inverting input terminals of op-amp A_k, respectively. V_{io_k} represents its input offset voltage.

The proposed circuit is dc-coupled, therefore dc components resulting from op-amp imperfections are amplified by the gain of both differential and common-mode channels. Fig. 6.8 is a representation of the new IA circuit concept that includes the unwanted sources of dc signals. Input offset voltages are modelled as constant voltage sources and bias currents are shown as dc current sources at the input terminals of each op-amp.

In the worst-case scenario, input offset voltages and bias currents are imbalanced in a way that results in the highest differential voltage on each side of the amplifier. Following a similar approach as in section 6.3.1, this situation is identified as follows :

$$V_{io1} = V_{io3} = V_{io5} = V_{io7} = V_{io_{max}} \tag{6.46}$$

$$V_{io2} = V_{io4} = V_{io6} = -V_{io_{max}} \tag{6.47}$$

$$I_{B1}^{+} = I_{B2}^{-} = I_{B3}^{+} = I_{B4}^{-} = I_{B5}^{+} = I_{B6}^{-} = I_{B7}^{+} = I_{B_{max}} \tag{6.48}$$

$$I_{B1}^{-} = I_{B2}^{+} = I_{B3}^{-} = I_{B4}^{+} = I_{B5}^{-} = I_{B6}^{+} = I_{B7}^{-} = -I_{B_{max}} \tag{6.49}$$

The most critical sources of error are the offset voltages at the input of op-amps A_1 and A_2. In fact, the difference $V_{io_1} - V_{io_2}$ is amplified by the circuit differential gain at the output of op-amps A_1 and A_2, resulting in:

$$V_{1H_{DC}} = \left(\frac{1 + R_2/R_1}{1 + R_3/R_4}\right)\left(\frac{V_{io1} - V_{io2}}{2}\right) \tag{6.50}$$

and

$$V_{1L_{DC}} = -\left(\frac{1 + R_2/R_1}{1 + R_3/R_4}\right)\left(\frac{V_{io1} - V_{io2}}{2}\right) \tag{6.51}$$

Referring to Fig. 6.8, $V_{1H_{DC}}$ and $V_{1L_{DC}}$ are amplified by a gain that is set by the resistor ratio R_4/R_3, which produces a dc potential at the output of op-amps A_3 and A_4 described respectively in eqs. (6.52) and (6.53) as follows:

$$V_{\alpha_{DC}} = \frac{R_4}{R_3}V_{1H_{DC}} = \frac{R_4}{R_3}\left(\frac{1 + R_2/R_1}{1 + R_3/R_4}\right)\left(\frac{V_{io_1} - V_{io_2}}{2}\right) \tag{6.52}$$

and

$$V_{\beta_{DC}} = \frac{R_4}{R_3}V_{1L_{DC}} = -\frac{R_4}{R_3}\left(\frac{1 + R_2/R_1}{1 + R_3/R_4}\right)\left(\frac{V_{io_1} - V_{io_2}}{2}\right) \tag{6.53}$$

For $R_2/R_1 = R_4/R_3 = 100$ and $V_{cc} = \pm 5$ V, the output of op-amps A_3 and A_4 shall saturate if $V_{io_{max}} \geq 0.5$ mV.

Theoretical results are verified by simulating the amplifier transient response with PSpice considering three differential input voltage levels: 100 µV, 6 mV and 10 mV. Simulation results are shown in Fig. 6.9, where a 1-V input common-mode signal at 50 Hz is superimposed

on the differential input voltage at 1 Hz. The worst-case mismatch in resistor values is also considered so as the maximum variations in input offset voltages and bias currents. $V_{io_{max}}$ is varied between 0.25 mV and 3 mV while $I_{B_{max}}$ ranges from 0.01 pA to 100 pA.

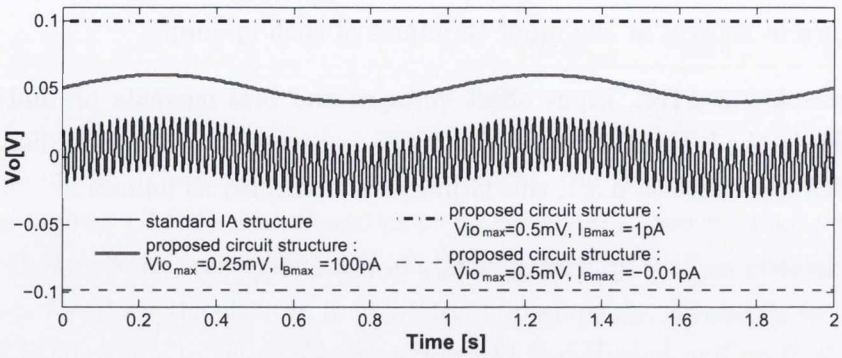

(a) $e_d = 100$ μV, $R_4/R_3 = 100$ and $V_{cc} = \pm 5$ V.

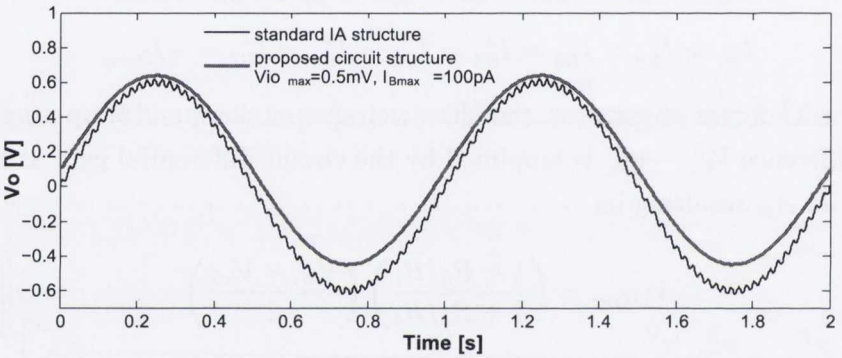

(b) $e_d = 6$ mV, $R_4/R_3 = 10$ and $V_{cc} = \pm 5$ V.

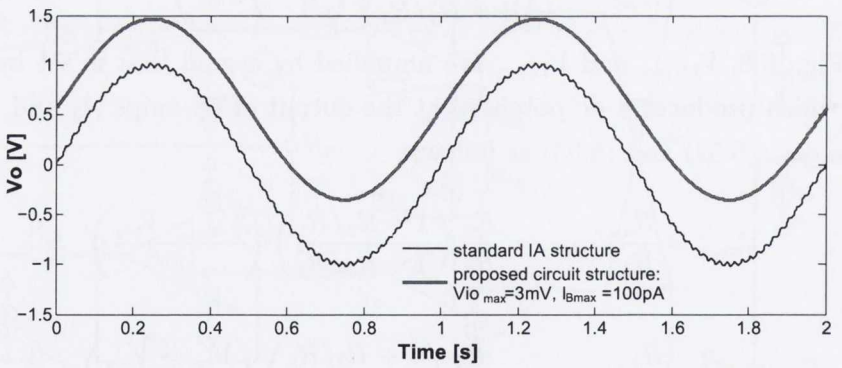

(c) $e_d = 10$ mV, $R_4/R_3 = 10$ and $V_{cc} = \pm 6$ V.

Figure 6.9: Plots of simulated transient responses of the novel circuit proposed by the author compared with those obtained with the standard three-op-amp IA considering worst-case mismatch in resistor values. A 50-Hz common-mode input signal, $e_c = 1$ V, is superimposed on a 1-Hz differential input signal, e_d, that takes three different values: (a) 100 μV, (b) 6 mV and (c) 10 mV. In all cases $R_2/R_1 = 100$, aiming at a differential gain of 40 dB.

In Fig. 6.9(a), $e_d = 100$ μV is chosen to assess the CMRR improvement under worst-case conditions of signal-to-noise ratio. The voltage at the output of the novel circuit concept, simulated for different maximum values of input offset voltage and bias current, is compared to the output obtained from the standard IA structure without any source of dc imperfection. The effect of the 50-Hz interfering common-mode voltage, prominent in the output of the standard IA, is highly attenuated on the signal produced by the novel circuit structure. Nevertheless, a dc-offset is clearly present due to the simulated op-amp imperfections. As expected, the circuit does not return a valid output for $V_{io_{max}} = 0.5$ mV since op-amps A_3 and A_4 reach saturation.

To assess its input dynamic range, the circuit is then tested with $e_d = 6$ mV in Fig. 6.9(b) and with $e_d = 10$ mV in Fig. 6.9(c). The resistor ratio R_4/R_3 is reduced to 10 to prevent "headroom" problems. The simulated transient responses suggest that the circuit proposed by the author provides higher immunity to common-mode signal, however, improvement is less significant than previously because of the reduction in CMRR at the output stage associated with the reduction in R_4/R_3.

6.4 Suggested implementations

Two circuit implementations that target different applications are suggested. The first circuit design utilises op-amps from the MAX400 series that are attractive for their ultra-low power consumption, but op-amp characteristics must be closely matched for the overall CMRR performance to be improved. An alternative solution that secures high CMRR performance in worst-case conditions relies on high-precision, high-voltage op-amps from the OPA140 family introduced by Texas Instruments in October 2010. However, improved performance comes at the expense of a significant increase in power consumption as suggested by the op-amps electrical characteristics summarised in Table 6.1.

Table 6.1: Electrical characteristics of the selected op-amps.

	Ultra-high CMRR high precision high supply voltage			Ultra-low power consumption					
	op-amps A_1 to A_7 OPA140 Texas Instruments Inc.			op-amps A_5 to A_9 MAX406A Maxim Inc.			op-amps A_1 to A_4 MAX409A Maxim Inc.		
Parameter	min.	typ.	max.	min.	typ.	max.	min.	typ.	max.
A_{VOL} (dB)	120	126		106	120		106	120	
GBP (kHz)		11000		4	8		80	150	
Slew rate (Vms^{-1})		20000		3	5		40	80	
Gain stability	1			1			10		
V_{CM} input range	V^-		V^+	V^-		V^+	V^-		V^+
	-0.1 V		-3.5 V			-1.1 V			-1.1 V
CMRR @ dc (dB)	120	140		70	80		70	80	
Com. mode input res.	10^{13} Ω||7 pF			undefined			undefined		
Diff. mode input res.	10^{13} Ω||10 pF			undefined			undefined		
Bias current I_B (pA)		±0.5	±10		< 0.1	10		< 0.1	10
Offset current I_{OS} (pA)		±0.5	±10	undefined			undefined		
In. offset volt. V_{io} (mV)		0.03	0.12		0.25	0.5		0.25	0.5
Volt. noise density V_{nd0}	5.1 nV$\sqrt{Hz}$			150 nV$\sqrt{Hz}$			150 nV$\sqrt{Hz}$		
Cur. noise density I_{nd0}	0.8 fA$\sqrt{Hz}$			undefined			undefined		
Quiescent cur. I_{cc} (μA)		1800	2000		1	1.2		1	1.2
Supply volt. V^+ to V^-	4.5 V		36 V	2.5 V		10 V	2.5 V		10 V

6.4.1 Application to ac-coupled ultra-low-power dry electrode ECG recording

Operating from a dual supply rail ($V_{cc} = \pm 3.3$ V), with common-mode input at dc of zero, a solution optimised for ultra low-power can therefore be implemented using op-amps from the MAX400 series, as shown in Fig. 6.10. The front-end amplifier is a bootstrapped unity-gain buffer stage which is ac-coupled to block large dc offsets generated at the skin-electrode interface. High input impedance can therefore be obtained without requiring unduly large values of resistors.

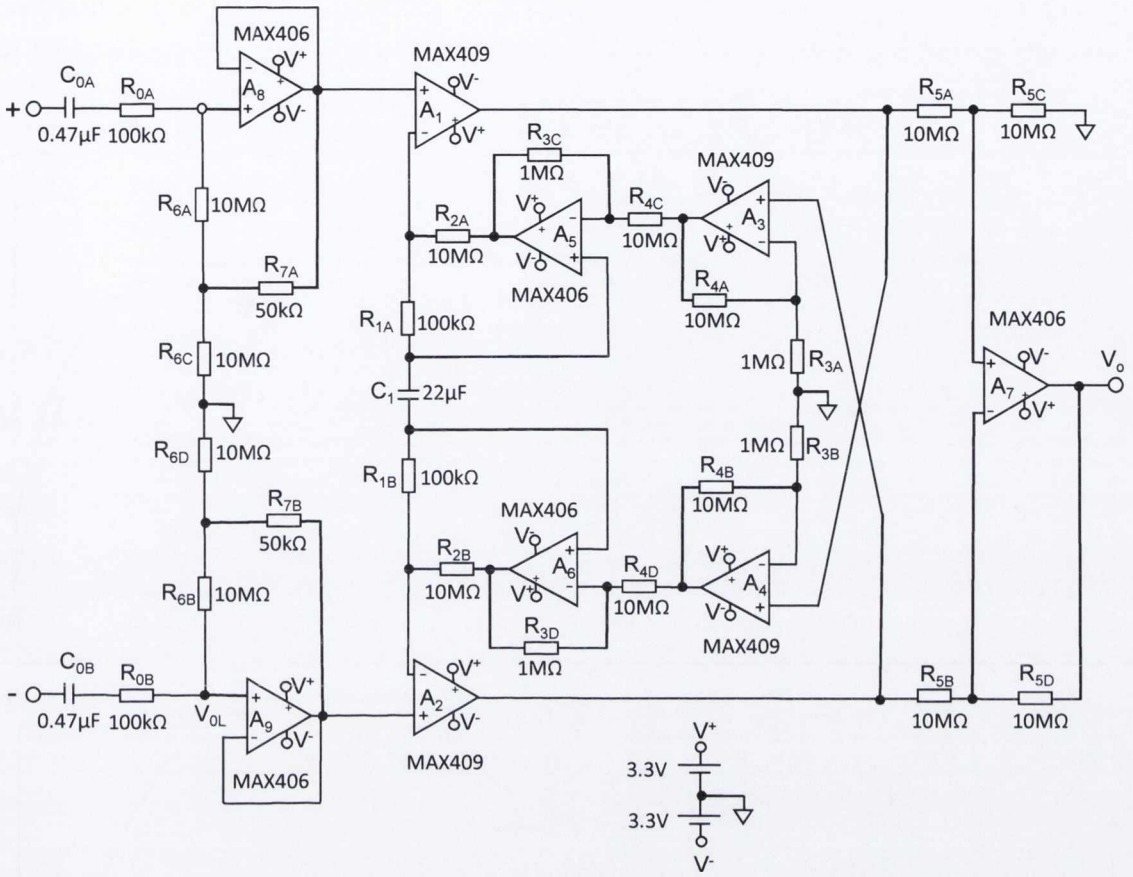

Figure 6.10: Proposed implementation of the novel IA structure optimised for ultra-low-power dry-electrode ECG recording.

The bootstrapped input stage, reviewed in section 4.3.4 in Chapter 4, allows the differential input resistance to be ideally infinite while the common-mode input resistance is given by:

$$R_c = R_{6A} + R_{6C} + \frac{R_{6A}R_{6C}}{R_{7A}} \tag{6.54}$$

Taking $R_{6A} = R_{6B} = R_6 = 10$ MΩ and $R_{7A} = 50$ kΩ, results in $R_c = 2.02$ GΩ. The second stage is built around the novel circuit concept. The differential gain is set at $G_{DD2} = 40$ dB by selecting $R_{2A} = R_{2B} = R_2 = 10$ MΩ and $R_{1A} = R_{1B} = R_1 = 100$ kΩ. The common-mode gain of the fully differential stage is designed to be -20 dB, which is achieved with $R_4 = 10$ MΩ and $R_3 = 1$ MΩ. The final stage is a standard unity-gain difference amplifier obtained with $R_5 = 10$ MΩ. To prevent large dc bias variation caused by the input offset voltages of op-amps A_1 and A_2 as well as the bias currents of the front-end op-amps A_8 and A_9, the differential dc gain is limited to unity by inserting a single dc-blocking capacitor, C_1, in series with the gain-defining resistors R_{1A} and R_{1B}. The low-frequency cutoff of the gain

stage is determined by $f_c = 1/(4\pi R_1 C_1)$, which must be lower than 0.05 Hz for low-frequency components in the ECG signal to be preserved. With $R_1 = 100$ kΩ, selecting $C_1 = 22$ μF allows the performance requirements to be met.

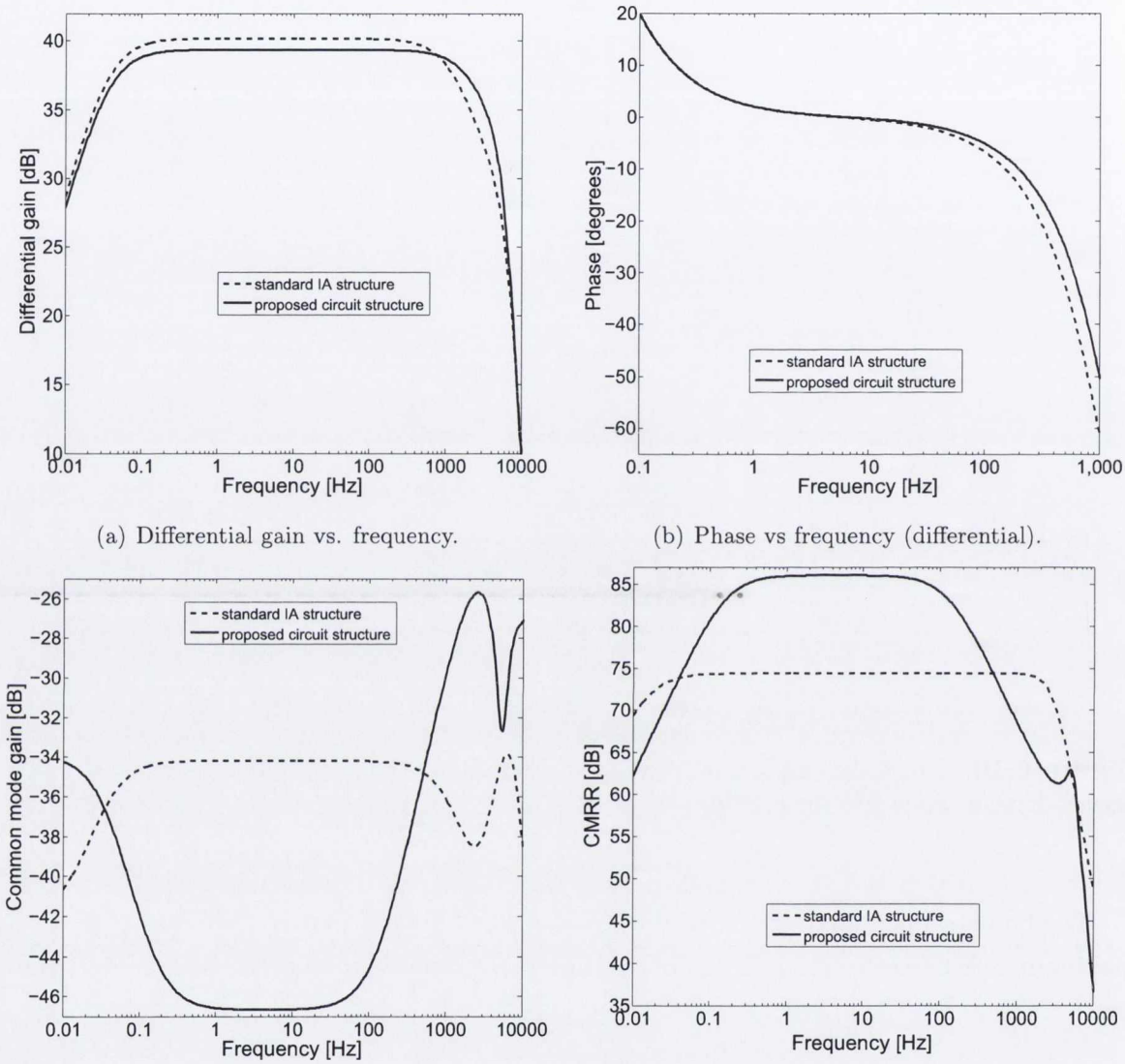

(a) Differential gain vs. frequency.

(b) Phase vs frequency (differential).

(c) Common-mode gain vs. frequency.

(d) CMRR vs frequency.

Figure 6.11: Plots of (a) the differential amplitude response, (b) differential phase response, (c) the common-mode gain and (d) the CMRR of the proposed circuit compared with results obtained from the standard IA structure implemented with op-amps from the MAX400 series.

Fig. 6.11 shows the differential response and common-mode response of the proposed implementation simulated for a differential input signal $e_d = 6$ mV and a common-mode input voltage $e_c = 1$ V. Worst-case imbalance in resistor and capacitor values is considered. The 3-dB differential response ranges from 0.035 Hz to 2.5 kHz and the phase remains between

6° and −6° in the frequency range 0.35 Hz - 117 Hz. The CMRR is greater than 84 dB in the bandwidth 0.2 Hz to 100 Hz and reaches a maximum of 86 dB between 1 Hz and 20 Hz. CMRR improvement is then limited by the performance of the op-amps at higher frequencies. Results confirm that in the frequency range for which the common-mode response of the op-amp is linear, the CMRR of the novel circuit structure is approximately 11 dB greater than that obtained with the standard IA configuration, as predicted by eq. (6.30).

6.4.2 Other applications

The focus of this thesis has concentrated so far on ultra-low-power dry electrode ECG recording but the range of applications of the novel instrumentation amplifier circuit can be extended further. For example, several transducers such as load cells and pressure sensors, among others, provide differential outputs [173]. The small differential signal is generally superimposed on much larger unwanted or interfering common-mode voltages. An instrumentation amplifier is therefore required to carry out amplification selective to the differential signal while rejecting common-mode components.

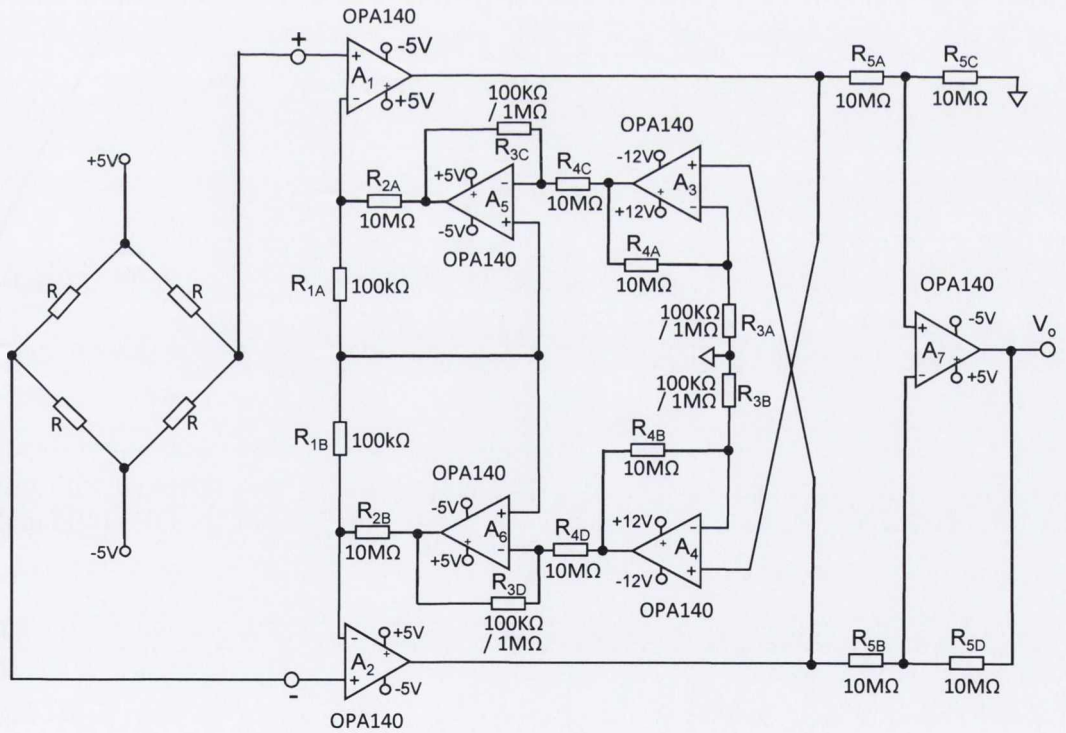

Figure 6.12: A possible utilisation of the novel instrumentation amplifier as a conditioning circuit for bridge sensors.

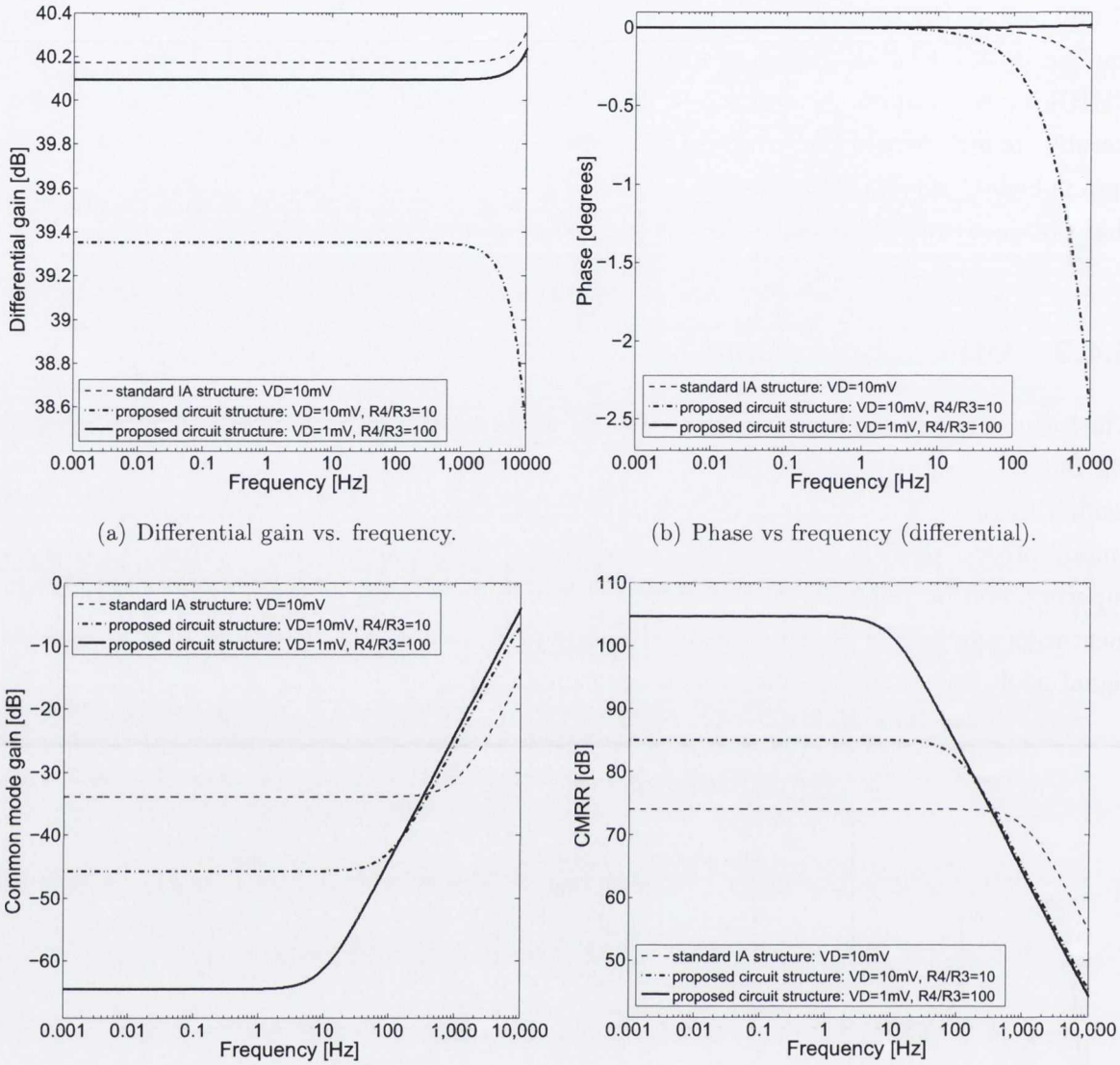

(a) Differential gain vs. frequency.

(b) Phase vs frequency (differential).

(c) Common-mode gain vs. frequency.

(d) CMRR vs frequency.

Figure 6.13: Plots of (a) the differential amplitude response, (b) differential phase response, (c) the common-mode gain and (d) the CMRR of the proposed circuit compared with results obtained from standard IA structure implemented with op-amps from the OPA140 family.

To be effective in worst-case conditions, the novel instrumentation amplifier circuit proposed by the author must employ high-precision op-amps that exhibit excellent CMRR characteristics. The minimum CMRR of the front-end op-amps must be at least 6 dB higher than the minimum CMRR due to tolerances in the gain-determining resistors, in addition, input-offset voltages and bias currents must be as small as possible. In order to secure simultaneously satisfactory input dynamic range, differential gain and improved CMRR performance, the supply voltage must also be raised. The OPA140 is therefore attractive for its

superior CMRR performance (120 dB min.), ultra-low input offset voltage (0.12 mV max.), low bias current level (±10 pA max.) and large supply voltage range (±18 V). Fig. 6.12 is an implementation of the proposed circuit structure based on the OPA140. The circuit is simulated using the component Spice model and the simulation software (TINA-TI) provided by the manufacturer.

Fig. 6.13 shows the differential response and common-mode response of the novel circuit concept compared with the result obtained from the standard three-op-amp structure when worst-case mismatch in the resistor values is assumed. Results are presented for $R_4/R_3 = 100$ and 10. Fig. 6.13(a) demonstrates that there is no significant difference in the differential gain response returned by both structures in frequencies ranging from dc to 3 kHz. Moreover, the phase shift measured at the output is no greater than -2.5° up to 1 kHz, as shown in Fig. 6.13(b). Fig. 6.13(c) indicates that in the linear operating range of the op-amps, the common-mode gain of the novel structure is systematically lower than that obtained from the standard three-op-amp configuration. As expected, Fig. 6.13(d) indicates that the CMRR improvement is 12 dB for $R_4/R_3 = 10$ and 30 dB when R_4/R_3 is increased to 100. Nevertheless, the advantage of the new arrangement is limited to the frequency bandwidth over which the phase of CMRR of the op-amps is small. For CMRR improvement to be secured at higher frequencies, op-amps with extended bandwidth in their common-mode response are required. To the best of the author's knowledge, such components have not been found within the range of high-precision op-amps available.

6.5 Conclusion

In the light of recent development in dry-electrode technology a new circuit structure has been designed for increasing the CMRR performance of the traditional instrumentation amplifier. The proposed solution allows common-mode voltages at the fully differential output to be reduced and the rejection of interfering signals at the single-ended output to be improved without affecting the differential response. Implementations with real op-amps have demonstrated the need to use high-performance amplifiers providing excellent bandwidth of their CMRR response for improvement to be maintained at high frequencies. Ultra-low-power op-amps are generally not designed for simultaneously large bandwidth and very large CMRR and therefore, in order for enhanced CMRR performance to be secured in the worst-case imbalance in component characteristics, op-amps with ultra-high CMRR value are required. A critical limitation exists, however, in the differential input dynamic range which cannot exceed the ratio $V_{cc}G_{CC1}/G_{DD1}$ for the revised fully differential stage. Therefore, considering a differential gain $G_{DD1} \simeq 100$, a common-mode gain $G_{CC1} = 1/100$, and a maximum supply voltage $V_{cc} = \pm 18$ V, the differential input dynamic range is limited to ±1.8 mV. In order to increase the dynamic range to ±5 mV, the level of ECG signals specified in international

standards, G_{DD1} or $1/G_{CC1}$ must be reduced. Nevertheless, the novel circuit concept is suitable for measuring extremely small differential signals contaminated by large common-mode interfering voltages as in the case of the signals sensed by many transducers.

Chapter 7

Conclusion and further work

7.1 Summary

This thesis has presented a rigorous analytical approach to the design of high-performance instrumentation amplifiers with an emphasis on applications in dry-electrode long-term ambulatory ECG recording. The work has highlighted the need to take into account the effect of the time-varying double-time-constant skin-electrode impedance in the model describing the ECG volume conductor in order to accurately relate the voltage sensed at the input of the biopotential amplifier to the signal generated within the heart. The review of international standards and recommendations has allowed essential performance requirements for ECG recorders to be identified but current impedance specifications were shown to be inappropriate for dry electrodes. Performance requirements must therefore be revisited to consider practical recording conditions at the skin-electrode interface. Thus, it is suggested that standards should consider the performance of the recording system as a whole, including a model of the skin and the sensing electrodes in the response of the ECG amplifier. Consequently, new methods of characterisation of the skin-electrode interface were investigated and new input impedance requirements for dry-electrode electrocardiography were derived by using a combination of analytical and numerical methods. This has allowed the ability of the "classical" instrumentation amplifier structure to reject common-mode interfering signals to be assessed. It was concluded that the standard structure must be modified in order to achieve high common-mode rejection ratio in the frequency bandwidth over which additional noise associated with dry electrodes has been measured. A brief review of existing CMRR enhancement techniques has allowed the identification of a suitable instrumentation amplifier structure operating from a single-rail supply that is optimised for ultra-low power consumption and that enables high input impedance and CMRR characteristics to be implemented. In the light of results obtained from the analysis of the skin-electrode-amplifier network in the harshest conditions, a novel instrumentation amplifier circuit was designed,

built and tested. Practical measurements give results which are in accordance with simulation results at low-frequency, suggesting that the modifications presented by the author yield enhanced performance in terms of input impedance and low-frequency response when coupled to the dry electrodes characterised. Fourteen subjects were recruited for actual ECG measurements acquired at rest and while subjects were moving and exercising. No noticeable difference existed between ECG tracings recorded using dry and wet electrodes. Semiconductor noise affected all waveforms but did not significantly degrade the signal. The CMRR was measured at 97 dB at mains frequency, 50 Hz, and 89 dB at 100 Hz for the amplifier alone, meeting requirements. CMRR performance was, however, limited by the magnitude of the skin-electrode impedance when worst-case values were considered. New opportunities are expected in the near future with the development of ultra-low-impedance dry contact electrodes that will offer the possibility of rejecting common-mode signals in the measurement chain more efficiently. A novel instrumentation amplifier circuit structure that permits common-mode voltages at the fully differential output to be reduced and the rejection of interfering signals at the single-ended output to be improved, without affecting the differential response, is finally presented. Worst-case simulation results confirm that the minimum CMRR value obtainable can be augmented by 30 dB compared to that of the "classical" circuit structure without requiring trimming or high precision resistors, but this comes at the expense of increased power consumption. Table 7.1 lists some essential performance characteristics of the three circuit implementations proposed by the author compared with the original dry-electrode amplifier design published by Burke & Gleeson in 2000 [34].

Table 7.1: Essential performance characteristics.

	diff. gain	low freq. cut-off	high freq. cut-off	input impedance	CMRR @ 50 Hz	power dissip.	approx. cost
spec. limits	N.A.	$\leq$0.05 Hz	$\geq$250 Hz	$\geq$10 MΩ	$\geq$95 dB	N.A.	N.A.
Burke & Gleeson	43 dB	0.04 Hz	2200 Hz	66 MΩ	84 dB	27 μW	20 euros
constructed 6 op-amps single-supply low-power design (Fig. 5.2):							
	40 dB	0.04 Hz	1250 Hz	2 GΩ	97 dB	45 μW	10 euros
simulated 9 op-amps dual-supply low-power design (Fig. 6.10):							
	40 dB	0.04 Hz	2500 Hz	2 GΩ	85 dB	60 μW	20 euros
simulated dc-coupled 7 op-amps dual-supply design (Fig. 6.12):							
	40 dB	N.A.	3000 Hz	10^{13} Ω	95 dB	200 mW	7 euros

7.2 Limitations of the proposed approach

The work presented in this thesis has relied heavily on analytical models and numerical methods for the design and assessment of the proposed amplifiers. However, while the approach undertaken by the author has focused on low-frequency response and CMRR of the skin-electrode-amplifier network, other problems inherent to the use of dry electrode in ECG recording remain unsolved.

To begin with, the implementation of an ultra-high input impedance of 2 GΩ in magnitude in series with a dc-blocking capacitance of 0.47 μF yields a time constant of 940 s for the front-end stage, resulting in long time delay before an ECG can be recorded when the system is powered-up. A mechanism allowing "fast recovery" that consists of inserting a switch at the input stage allowing resistors having low value values to be connected in parallel with the impedance-defining input resistors was first considered. This approach, suggested by Spinelli et al. in 2004 [117], necessitates the switch to be manually operated by the patient, which may not be advisable in the case of the very elderly. The investigation of automatic switching mechanisms has not been possible within the duration of this project.

The approach taken has systematically aimed at the most stringent performance requirements under the worst-case scenario, while minimising cost and power consumption. However, emphasis must be placed on the fact that excellent CMRR response, wide bandwidth, low noise and exceptionally good dc performance are not commonly combined features found among commercially available op-amps designed for low supply voltage and ultra-low quiescent current. Enhanced performance is therefore generally accompanied by an increase in power consumption. The solution presented in Chapter 6 illustrates the need for compromise. However, the novel approach may not be suitable in applications for which power consumption is critical, as in the case of cardiac pacemakers and other implantable devices [217–219].

Finally, the standards and recommendations related to the low-frequency performance of ECG recorders consider ideal square waves that are not found in real ECG waveforms. The reference test signals used to represent fast changing components in the ECG signal should therefore be replaced by more realistic input waveforms.

7.3 Further work

It is intended as part of future development to improve, construct and test the circuits presented in Chapter 6 to assess performance in real-life conditions. In addition, the stages subsequent to the ECG preamplifier remain to be designed and implemented. These include: low-pass filtering, an automatic gain control stage, threshold detection and analogue-to-digital convertion. Further research is also needed in the design of an elasticated vest, the

optimisation of electrode locations on the body and the development a communication unit for transmuting the ECG signal to a nearby PC-based substation or to a cellular based network.

Difficulties associated with the detection and suppression of motion artefacts will ultimately limit the ability of dry-electrode electrocardiographs to produce a signal of the same diagnostic quality as that of a standard electrode Holter system. The effect of artefacts within the signal bandwidth is generally exacerbated by poor contact between the skin and the electrodes due to the absence of a coupling gel. Extensive research is required in this area before dry-electrode-based recording systems replace traditional heart monitors currently commercialised. Future work might consider new possibilities for the identification of changes in contact due to motion in order to eliminate its effects on the recorded ECG signal. The opportunities offered by new generations of active electrodes that include accelerometers installed at the electrode site could be considered as a starting point [220, 221].

Accelerometers can also be used to convert body motion into energy for powering biomedical devices [217–219]. Results published in August 2010 by Romero et al. indicate that up to 117 μW of power can be produced by a generator positioned on the ankle while walking [219]. These recent developments offer new prospects in long-term telemetric monitoring of physiological signals in the near future.

7.4 Closing remarks

The analytical methods and mathematical models applied in the thesis are applicable to many systems that can be represented in matrix form or as transfer functions. On a personal level, the experience gained during the course of this project has contributed to the development of a wide range of academic interests offering the opportunity to explore new research problems involving mathematical analysis and computational modeling.

Appendix A

Identification of the model parameters of double-time-constant passive networks exhibiting three local extrema in their phase response

This study gives detail of the key derivations associated with the method presented in Section 3.3 Chapter 3 for the identification of the model parameters of the skin-electrode interface based on values published by Mühlsteff et al. in 2004 [39].

Impedance model

Fig. A.1 shows the electrical model of a double-time-constant passive network connected to a purely resistive impedance.

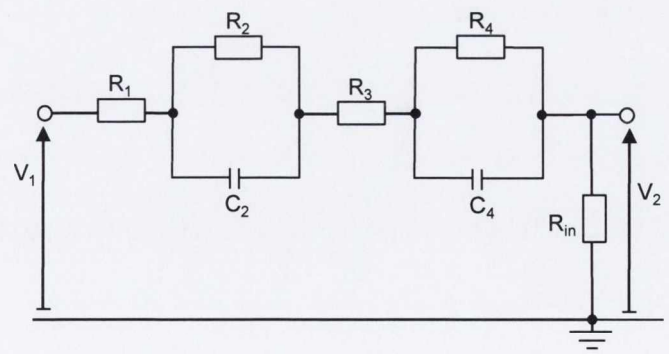

Figure A.1: Model respresenting a double-time-constant system connected to a resistive impedance R_{in}.

Transfer function

The transfer funtion of the network shown in Fig. A.1 is given by:

$$T(s) = \frac{V_2(s)}{V_1(s)} = \frac{R_{in}}{R_{in} + R_1 + \frac{R_2}{sR_2C_2+1} + R_3 + \frac{R_4}{sR_4C_4+1}} \tag{A.1}$$

We introduce the following new variables:

$$\tau_2 = R_2C_2 \tag{A.2}$$

$$\tau_4 = R_4C_4 \tag{A.3}$$

$$R_{13} = R_{in} + R_1 + R_3 \tag{A.4}$$

$$R_{123} = R_{in} + R_1 + R_2 + R_3 \tag{A.5}$$

$$R_{134} = R_{in} + R_1 + R_3 + R_4 \tag{A.6}$$

$$R_T = R_{in} + R_1 + R_2 + R_3 + R_4 \tag{A.7}$$

$$K_0 = \frac{R_{in}}{R_{in} + R_1 + R_2 + R_3 + R_4} \tag{A.8}$$

Eqs. (A.2) to (A.8) allow the transfer function to be expressed as follows:

$$T(s) = K_0 \frac{(1 + s\tau_2)(1 + s\tau_4)}{1 + \left(\frac{\tau_2 R_{134} + \tau_4 R_{123}}{R_T}\right) s + \left(\frac{R_{13}\tau_2\tau_4}{R_T}\right) s^2} \tag{A.9}$$

Eq. (A.9) can be written as a function of the two poles, p_1 and p_2, and the two zeros, z_1 and z_2, associated with the double-time-constant network so that:

$$T(s) = K_0 \frac{\left(1 + \frac{s}{z_1}\right)\left(1 + \frac{s}{z_2}\right)}{\left(1 + \frac{s}{p_1}\right)\left(1 + \frac{s}{p_2}\right)} \tag{A.10}$$

The poles and zeros of $T(s)$ can be derived from eq. (A.9) as:

$$p_1 = \frac{\tau_2 R_{134} + \tau_4 R_{123} - \sqrt{(\tau_2 R_{134} + \tau_4 R_{123})^2 - 4R_T R_{13}\tau_2\tau_4}}{2R_{13}\tau_2\tau_4} \tag{A.11}$$

$$p_2 = \frac{\tau_2 R_{134} + \tau_4 R_{123} + \sqrt{(\tau_2 R_{134} + \tau_4 R_{123})^2 - 4R_T R_{13}\tau_2\tau_4}}{2R_{13}\tau_2\tau_4} \tag{A.12}$$

$$z_1 = \frac{1}{\tau_2} \tag{A.13}$$

and

$$z_2 = \frac{1}{\tau_4} \tag{A.14}$$

Step response

A step input $X(t)$ is ideally modelled using the Heaviside unit step function as:

$$X(t) = \begin{cases} 0 & \text{if t} < 0 \\ 1 & \text{if t} \geq 0 \end{cases} \tag{A.15}$$

Applying Laplace transform to $X(t)$ leads to:

$$X(s) = \mathcal{L}(X(t)) = \frac{1}{s} \tag{A.16}$$

Using the transfer function $T(s)$ defined in eq. (A.10), the frequency response $Y(s)$ of the the double-time-constant network shown in Fig. A.1 to the pulse $X(s)$ is:

$$Y(s) = T(s)X(s) = \frac{T(s)}{s} = K_0 \frac{\left(1 + \frac{s}{z_1}\right)\left(1 + \frac{s}{z_2}\right)}{s\left(1 + \frac{s}{p_1}\right)\left(1 + \frac{s}{p_2}\right)} \tag{A.17}$$

$Y(s)$ can then be expanded by partial fractions as:

$$Y(s) = K_0 \left[\frac{1}{s} + \frac{\frac{p_2}{z_1 z_2}\frac{(z_1 - p_1)(z_2 - p_1)}{(p_1 - p_2)}}{s + p_1} + \frac{\frac{p_1}{z_1 z_2}\frac{(z_1 - p_2)(z_2 - p_2)}{(p_2 - p_1)}}{s + p_2}\right] \tag{A.18}$$

The inverse Laplace transform of $Y(s)$ gives the corresponding response in time, $y(t)$, as:

$$y(t) = \mathcal{L}^{-1}(Y(s)) = K_0 \left[1 + \frac{p_2 (z_1 - p_1)(z_2 - p_1) e^{-t/p_1} - p_1 (z_1 - p_2)(z_2 - p_2) e^{-t/p_2}}{z_1 z_2 (p_1 - p_2)}\right] \tag{A.19}$$

Two asymptotic values can be extracted from the impulse response, $y(t)$, as follows:

$$\lim_{t \to \infty}(y(t)) = \lim_{s \to 0}(sY(s)) = \lim_{\omega \to 0}|T(\omega)| = K_0 = a_4 \tag{A.20}$$

and

$$\lim_{t \to 0}(y(t)) = \lim_{s \to \infty}(sY(s)) = \lim_{\omega \to \infty}|T(\omega)| = K_\infty = a_5 \tag{A.21}$$

Magnitude response

The magnitude response of the system described in Fig. A.1 is given by:

$$|T(j\omega)| = |K_0| \frac{\left|1+\frac{j\omega}{z_1}\right|\left|1+\frac{j\omega}{z_2}\right|}{\left|1+\frac{j\omega}{p_1}\right|\left|1+\frac{j\omega}{p_2}\right|} = |K_0| \frac{|p_1 p_2|\sqrt{z_1^2+\omega^2}\sqrt{z_2^2+\omega^2}}{|z_1 z_2|\sqrt{p_1^2+\omega^2}\sqrt{p_2^2+\omega^2}} \tag{A.22}$$

It can be shown that the limits of $|T(\omega)|$ at low and high frequencies are determined as:

$$\lim_{\omega\to 0}|T(\omega)| = \frac{R_{in}}{R_T} = K_0 = a_4 \tag{A.23}$$

and

$$\lim_{\omega\to\infty}|T(\omega)| = \frac{R_{in}}{R_{13}} = K_\infty = a_5 \tag{A.24}$$

Phase response

The transfer function defined in eq. (A.10) can be rearranged so that real and imaginary parts are more easily identified:

$$T(j\omega) = K_0 \frac{\begin{array}{l}\left[1-\omega^2\left[\frac{1}{p_1p_2}+\frac{1}{z_1z_2}-\left(\frac{z_1+z_2}{z_1z_2}\right)\left(\frac{p_1+p_2}{p_1p_2}\right)\right]+\frac{\omega^4}{z_1z_2p_1p_2}\right] \\ +j\left[\omega\left[\frac{z_1+z_2}{z_1z_2}-\left(\frac{p_1+p_2}{p_1p_2}\right)\right]+\omega^3\left[-\frac{1}{p_1p_2}\left(\frac{z_1+z_2}{z_1z_2}\right)+\frac{1}{z_1z_2}\left(\frac{p_1+p_2}{p_1p_2}\right)\right]\right]\end{array}}{1-\omega^2\left[\frac{2}{p_1p_2}+\left(\frac{p_1+p_2}{p_1p_2}\right)^2\right]+\omega^4\left(\frac{1}{p_1p_2}\right)^2} \tag{A.25}$$

It can be shown that the phase response of the double-time-constant nework considered can be expressed as:

$$\varphi(\omega) = Arg(T(j\omega)) = tan^{-1}\left(\frac{\omega C+\omega^3 D}{1+\omega^2 A+\omega^4 B}\right) \tag{A.26}$$

where

$$A = -\left[\frac{1}{p_1p_2}+\frac{1}{z_1z_2}-\left(\frac{z_1+z_2}{z_1z_2}\right)\left(\frac{p_1+p_2}{p_1p_2}\right)\right] = \frac{\tau_2^2 R_{134}+\tau_4^2 R_{123}}{R_T} \tag{A.27}$$

$$B = \frac{1}{z_1z_2p_1p_2} = \frac{R_{13}(\tau_2\tau_4)^2}{R_T} \tag{A.28}$$

$$C = \frac{z_1+z_2}{z_1z_2}-\left(\frac{p_1+p_2}{p_1p_2}\right) = \frac{R_2\tau_2+R_4\tau_4}{R_T} \tag{A.29}$$

and

$$D = -\frac{1}{p_1p_2}\left(\frac{z_1+z_2}{z_1z_2}\right)+\frac{1}{z_1z_2}\left(\frac{p_1+p_2}{p_1p_2}\right) = \tau_2\tau_4\frac{\tau_2R_4+\tau_4R_2}{R_T} \tag{A.30}$$

Bode diagram

Fig. A.2 shows the asymptotic bode diagram of a double-time-constant network the phase response of which exhibits three local extrema, as suggested by parameter values reported by Mühlsteff et al [39].

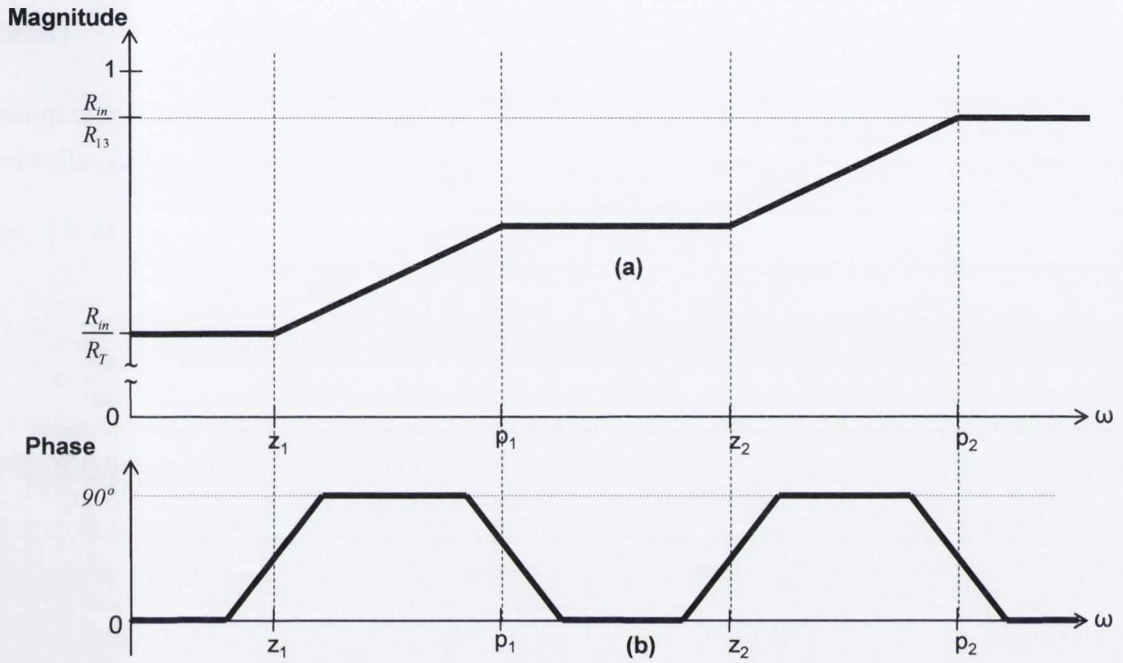

Figure A.2: Bode diagram showing the assymptotic (a) magnitude reponse and (b) phase response of a double-time-constant network that exhibits three local extrama in its phase response.

Parameter Identification method

The the first derivative of the phase with respect to the angular frequency ω is given as:

$$\frac{d\varphi(\omega)}{d\omega} = \frac{C + (3D - AC)\,\omega^2 - (AD - 3BC)\,\omega^4 - BD\omega^6}{(1 + A\omega^2 + B\omega^4)^2 + (C\omega + D\omega^3)^2} \tag{A.31}$$

Eq. A.31 results in the following conditions:

$$\frac{d\varphi(\omega)}{d\omega} = 0 \Rightarrow 1 + \left(3\frac{D}{C} - A\right)\omega^2 + \left(\frac{AD}{C} - 3B\right)\omega^4 - \frac{BD}{C}\omega^6 = 0 \tag{A.32}$$

$$\Rightarrow 1 + a_1\omega^2 + a_2\omega^4 + a_3\omega^6 = 0 \tag{A.33}$$

where a_1, a_2 and a_3 are defined in eqs. A.34 to A.36 as:

$$\begin{cases} a_1 = 3\dfrac{D}{C} - A = \dfrac{3R_T\left(R_4\tau_2 + R_2\tau_4\right)\tau_2\tau_4 - \left(\tau_2^2 R_{134} + \tau_4^2 R_{123}\right)\left(R_2\tau_2 + R_4\tau_4\right)}{R_T\left(R_2\tau_2 + R_4\tau_4\right)} & \text{(A.34)} \\ a_2 = \dfrac{AD}{C} - 3B = \dfrac{\tau_2\tau_4\left(R_{134}\tau_2^2 + R_{123}\tau_4^2\right)\left(\tau_2 R_4 + \tau_4 R_2\right) - 3R_{13}\left(R_2\tau_2 + R_4\tau_4\right)\left(\tau_2\tau_4\right)^2}{R_T\left(R_2\tau_2 + R_4\tau_4\right)} & \text{(A.35)} \\ a_3 = -\dfrac{BD}{C} = -\dfrac{R_{13}\left(R_4\tau_2 + R_2\tau_4\right)}{R_T\left(R_2\tau_2 + R_4\tau_4\right)}\left(\tau_2\tau_4\right)^3 & \text{(A.36)} \end{cases}$$

Up to three local extema can be identified on the plot of phase from the frequency response of the double-time-constant network. They occur at three frequencies ω_1, ω_2 and ω_3, allowing the following system of equations to be obtained:

$$\begin{cases} 1 + a_1\omega_1^2 + a_2\omega_1^4 + a_3\omega_1^6 = 0 & \text{(A.37)} \\ 1 + a_1\omega_2^2 + a_2\omega_2^4 + a_3\omega_2^6 = 0 & \text{(A.38)} \\ 1 + a_1\omega_3^2 + a_2\omega_3^4 + a_3\omega_3^6 = 0 & \text{(A.39)} \end{cases}$$

It can be shown that the system defined in eqs. (A.37) to (A.39) can be rearranged to give the coefficients as:

$$\begin{cases} a_1 = -\dfrac{1}{\omega_1^2} - \dfrac{1}{\omega_2^2} - \dfrac{1}{\omega_3^2} & \text{(A.40)} \\ a_2 = \dfrac{\omega_1^2 + \omega_2^2 + \omega_3^2}{\omega_1^2\omega_2^2\omega_3^2} & \text{(A.41)} \\ a_3 = -\dfrac{1}{\omega_1^2\omega_2^2\omega_3^2} & \text{(A.42)} \end{cases}$$

Eqs. (A.40) to (A.42) indicate that the frequencies at which local extrema in the phase response occur provide valuable information for the characterisation of the double-time-constant network. This requires all three frequencies to be measurable. Considering the two points a_4 and a_5 extracted from the magnitude response, the following system of equations can therefore be derived:

$$\begin{cases} a_1 R_T\left(R_2\tau_2 + R_4\tau_4\right) - 3R_T\tau_2\tau_4\left(R_4\tau_2 + R_2\tau_4\right) + \left(\tau_2^2 R_{134} + \tau_4^2 R_{123}\right)\left(R_2\tau_2 + R_4\tau_4\right) = 0 & \text{(A.43)} \\ a_2 R_T\left(R_2\tau_2 + R_4\tau_4\right) - \tau_2\tau_4\left(R_{134}\tau_2^2 + R_{123}\tau_4^2\right)\left(\tau_2 R_4 + \tau_4 R_2\right) + 3R_{13}\left(R_2\tau_2 + R_4\tau_4\right)\left(\tau_2\tau_4\right)^2 = 0 & \text{(A.44)} \\ a_3 R_T\left(R_2\tau_2 + R_4\tau_4\right) + R_{13}\left(R_4\tau_2 + R_2\tau_4\right)\left(\tau_2\tau_4\right)^3 = 0 & \text{(A.45)} \\ R_T a_4 - R_{in} = 0 & \text{(A.46)} \\ a_5 R_{13} - R_{in} = 0 & \text{(A.47)} \end{cases}$$

The identification problem is now equivalent to the resolution of a non-linear system of five equations with the following five unknowns:

$$x = R_1 + R_3 \tag{A.48}$$

$$y = R_2 \tag{A.49}$$

$$z = R_4 \tag{A.50}$$

$$u = \tau_2 \tag{A.51}$$

$$v = \tau_4 \tag{A.52}$$

Eqs. (A.43) to (A.47) can therefore be rewritten as follows:

$$\begin{cases} a_1 \dfrac{R_{in}}{a_4}(yu+zv) - 3\dfrac{R_{in}}{a_4}uv(zu+yv) + \begin{bmatrix} (R_{in}+x+z)u^2 \\ +(R_{in}+x+y)v^2 \end{bmatrix}(yu+zv) = 0 & \text{(A.53)} \\ a_2 \dfrac{R_{in}}{a_4}(yu+zv) - uv \begin{bmatrix} (R_{in}+x+z)u^2 \\ +(R_{in}+x+y)v^2 \end{bmatrix}(zu+yv) + 3u^2v^2(R_{in}+x)(yu+zv) = 0 & \text{(A.54)} \\ a_3 \dfrac{R_{in}}{a_4}(yu+zv) + u^3v^3(R_{in}+x)(yv+zu) = 0 & \text{(A.55)} \\ a_4(R_{in}+x+y+z) - R_{in} = 0 & \text{(A.56)} \\ a_5(R_{in}+x) - R_{in} = 0 & \text{(A.57)} \end{cases}$$

It can be shown that eq. (A.54) is equivalent to:

$$a_2\frac{R_{in}}{a_4} + \left[\left(\frac{R_{in}}{a_5}+z\right)u^2 + \left(\frac{R_{in}}{a_5}+y\right)v^2\right]\left(\frac{a_3a_5}{u^2v^2a_4}\right) + 3R_{in}\frac{u^2v^2}{a_5} = 0 \tag{A.58}$$

$$\Rightarrow -3\frac{a_3^2a_5^2}{a_4^3} - \frac{a_1a_3a_5}{a_4^2}u^2v^2 + \frac{a_2}{a_4}u^4v^4 + 3\frac{u^6v^6}{a_5} = 0 \tag{A.59}$$

The following change of variable is then proposed:

$$q = uv \tag{A.60}$$

Eq. (A.59) is therefore reduced to that of a single variable q as shown below:

$$-\frac{3a_3^2a_5^2}{a_4^3} - \frac{a_1a_3a_5}{a_4^2}q^2 + \frac{a_2}{a_4}q^4 + \frac{3}{a_5}q^6 = 0 \tag{A.61}$$

Solving eq. A.61 in $\Re^+$ allows the following systems of equation to be derived:

$$\begin{cases} \left[-a_1\dfrac{R_{in}}{a_4} - 3R_{in}\left(\dfrac{a_3a_5}{a_4^2q^2}\right)\right]u^2 = \left[\left(\dfrac{R_{in}}{a_5}+z\right)u^4 + \left(\dfrac{R_{in}}{a_5} + R_{in}\dfrac{a_5-a_4}{a_4a_5} - z\right)q^2\right] & \text{(A.62)} \\ -a_3a_5\left(R_{in}\dfrac{a_5-a_4}{a_4a_5}u - zu + z\dfrac{q}{u}\right) = R_{in}\dfrac{a_5-a_4}{a_5}\dfrac{q^4}{u} - \dfrac{zq^4a_4}{u} + zua_4q^3 & \text{(A.63)} \end{cases}$$

$$\Rightarrow \begin{cases} \left[\left(\dfrac{R_{in}}{a_5}+z\right)u^4 + \left[a_1\dfrac{R_{in}}{a_4} + 3R_{in}\left(\dfrac{a_3a_5}{a_4^2q^2}\right)\right]u^2 + \left(\dfrac{R_{in}}{a_5} + R_{in}\dfrac{a_5-a_4}{a_4a_5} - z\right)q^2\right] = 0 & \text{(A.64)} \\ z = R_{in}\dfrac{\frac{a_5-a_4}{a_5}\frac{q^4}{u} + a_3\frac{a_5-a_4}{a_4}u}{\left[u\left(a_3a_5-a_4q^3\right) - \frac{q}{u}\left(a_3a_5-a_4q^3\right)\right]} = R_{in}\left(\dfrac{a_5-a_4}{a_3a_5-q^3}\right)\dfrac{a_4q^4+a_5a_3u^2}{a_4a_5\left(u^2-q\right)} & \text{(A.65)} \end{cases}$$

$$\Rightarrow \begin{cases} \left[\left(\dfrac{R_{in}}{a_5}+z\right)u^4 + \left[a_1\dfrac{R_{in}}{a_4} + 3R_{in}\left(\dfrac{a_3a_5}{a_4^2q^2}\right)\right]u^2 + \left(R_{in}\dfrac{1}{a_4} - z\right)q^2\right] = 0 & \text{(A.66)} \\ z = R_{in}\dfrac{\frac{a_5-a_4}{a_5}\frac{q^4}{u} + a_3\frac{a_5-a_4}{a_4}u}{\left[u\left(a_3a_5-q^3\right) - \frac{q}{u}\left(a_3a_5-q^3\right)\right]} = R_{in}\left(\dfrac{a_5-a_4}{a_3a_5-a_4q^3}\right)\dfrac{a_4q^4+a_5a_3u^2}{a_4a_5\left(u^2-q\right)} & \text{(A.67)} \end{cases}$$

Eqs. (A.66) and (A.67) are then combined to give the following:

$$\left[\frac{1}{a_5} + \left(\frac{a_5-a_4}{a_3a_5-a_4q^3}\right)\frac{a_4q^4+a_5a_3u^2}{a_4a_5\left(u^2-q\right)}\right]u^4 + \left[\frac{a_1}{a_4} + 3\left(\frac{a_3a_5}{a_4^2q^2}\right)\right]u^2 + \left[\frac{1}{a_4} - \left(\frac{a_5-a_4}{a_3a_5-a_4q^3}\right)\frac{a_4q^4+a_5a_3u^2}{a_4a_5\left(u^2-q\right)}\right]q^2 = 0 \quad \text{(A.68)}$$

$$\Rightarrow \frac{q^2}{a_4} - \left(\frac{a_4-a_5}{a_3a_5-a_4q^3}\right)\frac{q^5}{a_5} + u^2\left[\frac{a_1}{a_4} + 3\left(\frac{a_3a_5}{a_4^2q^2}\right) - \left(\frac{a_4-a_5}{a_3a_5-a_4q^3}\right)\frac{q\left(a_4q^3+a_5a_3\right)}{a_4a_5}\right] + u^4\left[\frac{1}{a_5} - \left(\frac{a_4-a_5}{a_3a_5-a_4q^3}\right)\frac{a_3}{a_4}\right] = 0 \quad \text{(A.69)}$$

Eq. (A.69) permits the following quadratic equation to be established:

$$\rho_0 + \rho_1 U + \rho_2 U^2 = 0 \quad \text{(A.70)}$$

where

$$U = u^2 \quad \text{(A.71)}$$

$$\rho_0 = \frac{q^2}{a_4} - \left(\frac{a_4-a_5}{a_3a_5-a_4q^3}\right)\frac{q^5}{a_5} \quad \text{(A.72)}$$

$$\rho_1 = \left[\frac{a_1}{a_4} + 3\left(\frac{a_3 a_5}{a_4^2 q^2}\right) - \left(\frac{a_4 - a_5}{a_3 a_5 - a_4 q^3}\right)\frac{q\left(a_4 q^3 + a_5 a_3\right)}{a_4 a_5}\right] \tag{A.73}$$

$$\rho_2 = \left[\frac{1}{a_5} - \left(\frac{a_4 - a_5}{a_3 a_5 - a_4 q^3}\right)\frac{a_3}{a_4}\right] \tag{A.74}$$

The solution of eq. (A.70) is the final step of the identification procedure, which returns the model parameters as follows:

$$R_4 = z = R_{in}\left(\frac{a_5 - a_4}{a_3 a_5 - a_4 q^3}\right)\frac{a_4 q^4 + a_5 a_3 u^2}{a_4 a_5\left(u^2 - q\right)} \tag{A.75}$$

$$R_2 = y = R_{in}\frac{a_5 - a_4}{a_4 a_5} - z \tag{A.76}$$

$$C_2 = \frac{u}{y} \tag{A.77}$$

$$C_4 = \frac{q}{uz} \tag{A.78}$$

and

$$R_1 + R_3 = x = R_{in}\frac{1 - a_5}{a_5} \tag{A.79}$$

Appendix B

ECG measurement obtained from the very-low-power single-supply dry-electrode ECG preamplifier outlined in Chapter 5

Table B.1: Subjects recruited for ECG recording.

subject num.	gender	age	noticeable presence of hair at the electrode sites?
1	male	23	no
2	male	40	yes
3	female	33	no
4	male	28	no
5	male	29	no
6	female	33	no
7	male	23	no
8	male	22	no
9	male	39	yes
10	male	33	no
11	male	23	yes
12	female	31	no
13	male	41	yes
14	female	33	no

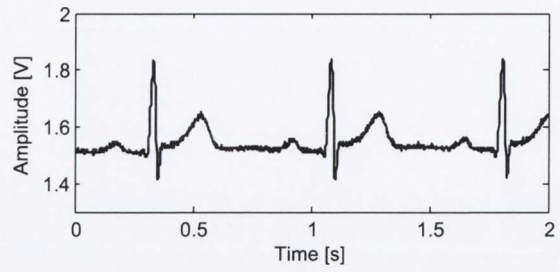

(a) Resting ECG, dry electrodes (1 kSs^{-1}).

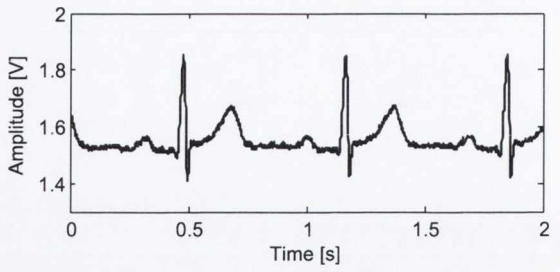

(b) Resting ECG, wet electrodes (1 kSs^{-1}).

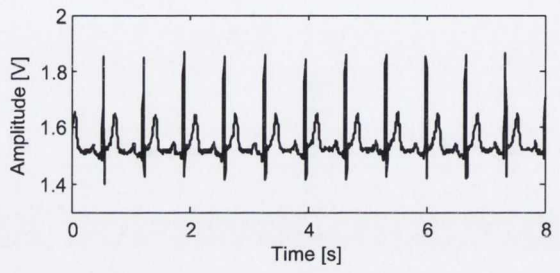

(c) Resting ECG, dry electrodes (250 Ss^{-1}).

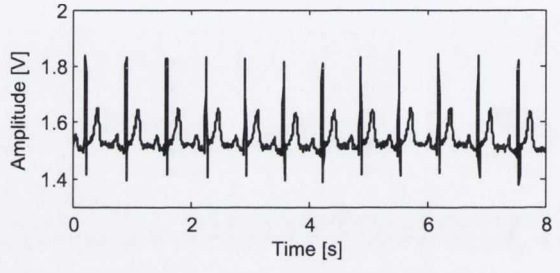

(d) Resting ECG, wet electrodes (250 Ss^{-1}).

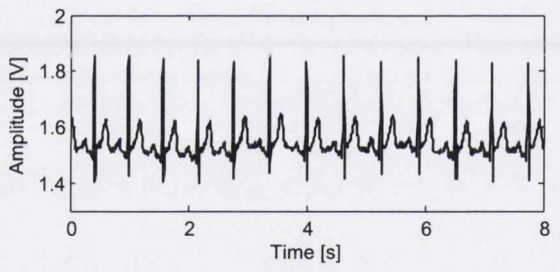

(e) Walking on the spot, dry electrodes (250 Ss^{-1}).

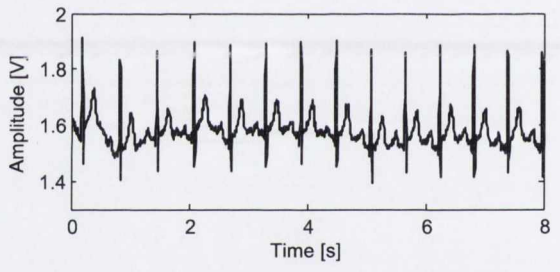

(f) Walking on the spot, wet electrodes (250 Ss^{-1}).

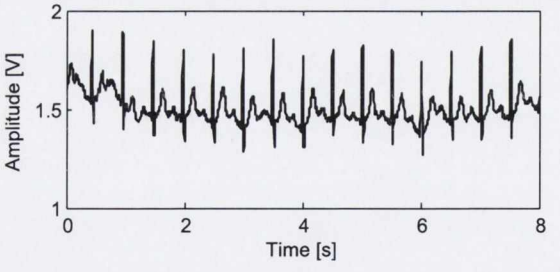

(g) Harvard step test, dry electrodes (250 Ss^{-1}).

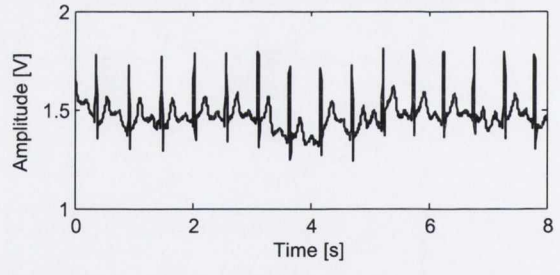

(h) Harvard step test, wet electrodes (250 Ss^{-1}).

Figure B.1: Sample ECG recordings for subject 1 using dry electrodes (left hand side waveforms) and wet electrodes (right hand side waveforms). The sampling rate is given in brackets in samples per s (Ss^{-1}).

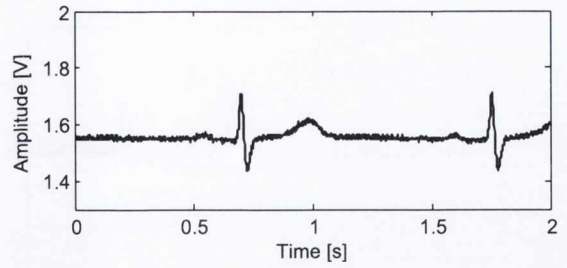

(a) Resting ECG, dry electrodes (1 kSs^{-1}).

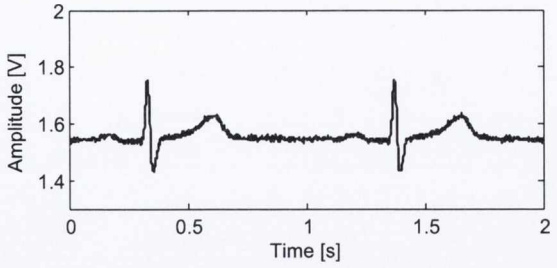

(b) Resting ECG, wet electrodes (1 kSs^{-1}).

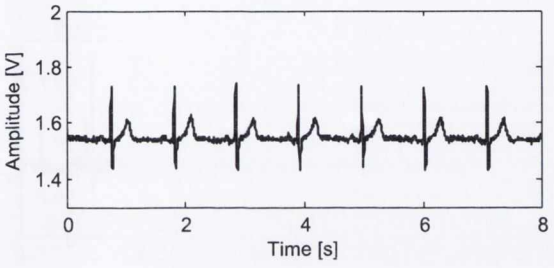

(c) Resting ECG, dry electrodes (250 Ss^{-1}).

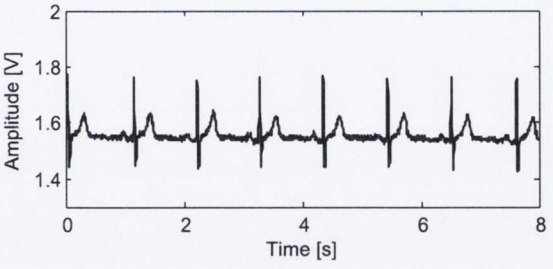

(d) Resting ECG, wet electrodes (250 Ss^{-1}).

(e) Walking on the spot, dry electrodes (250 Ss^{-1}).

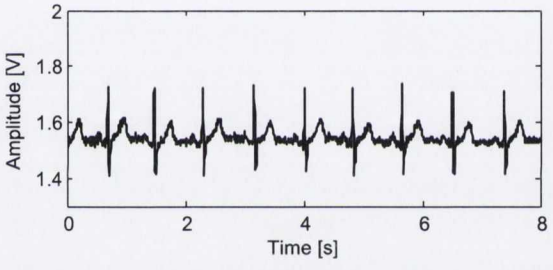

(f) Walking on the spot, wet electrodes (250 Ss^{-1}).

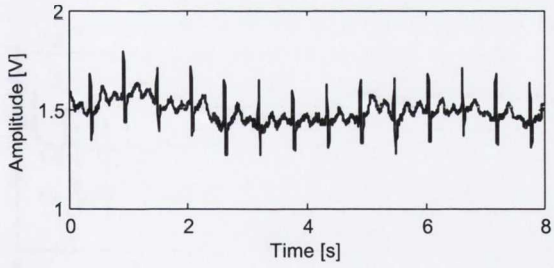

(g) Harvard step test, dry electrodes (250 Ss^{-1}).

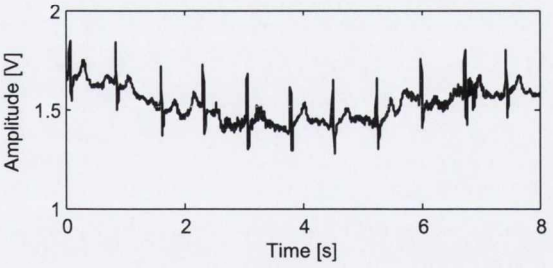

(h) Harvard step test, wet electrodes (250 Ss^{-1}).

Figure B.2: Sample ECG recordings for subject 2 using dry electrodes (left hand side waveforms) and wet electrodes (right hand side waveforms). The sampling rate is given in brackets in samples per s (Ss^{-1}).

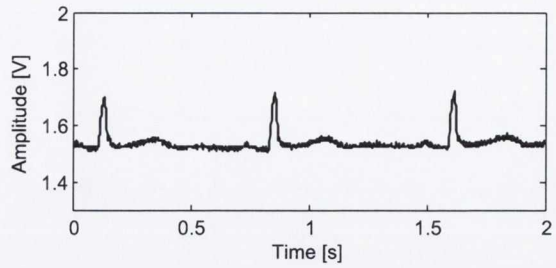

(a) Resting ECG, dry electrodes (1 kSs^{-1}).

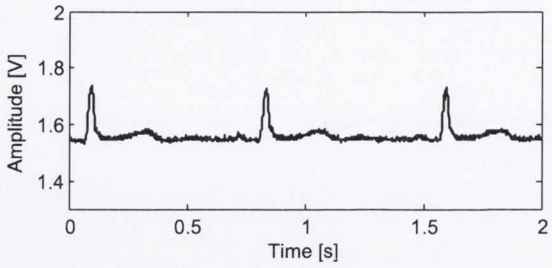

(b) Resting ECG, wet electrodes (1 kSs^{-1}).

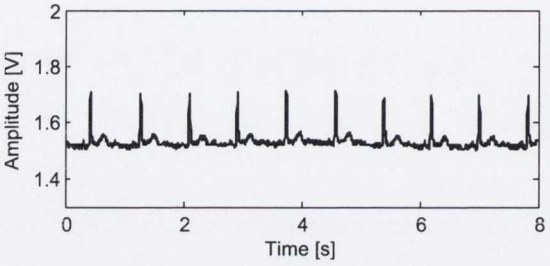

(c) Resting ECG, dry electrodes (250 Ss^{-1}).

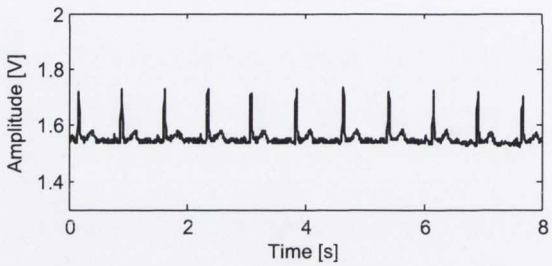

(d) Resting ECG, wet electrodes (250 Ss^{-1}).

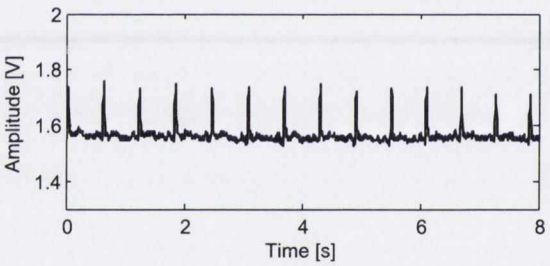

(e) Walking on the spot, dry electrodes (250 Ss^{-1}).

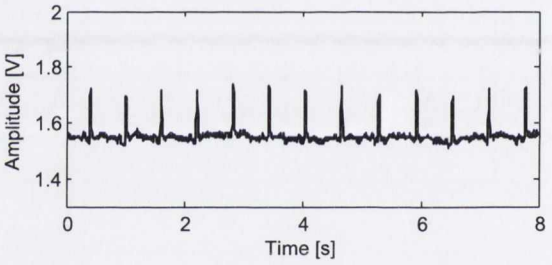

(f) Walking on the spot, wet electrodes (250 Ss^{-1}).

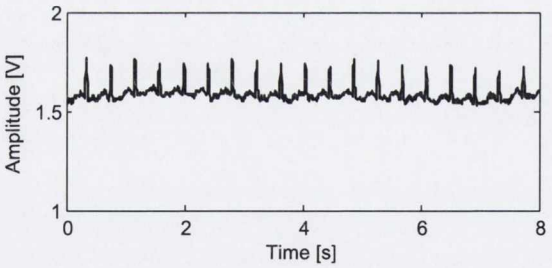

(g) Harvard step test, dry electrodes (250 Ss^{-1}).

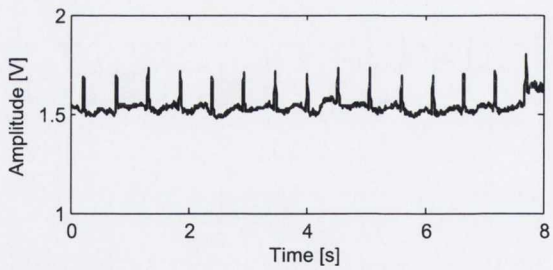

(h) Harvard step test, wet electrodes (250 Ss^{-1}).

Figure B.3: Sample ECG recordings for subject 3 using dry electrodes (left hand side waveforms) and wet electrodes (right hand side waveforms). The sampling rate is given in brackets in samples per s (Ss^{-1}).

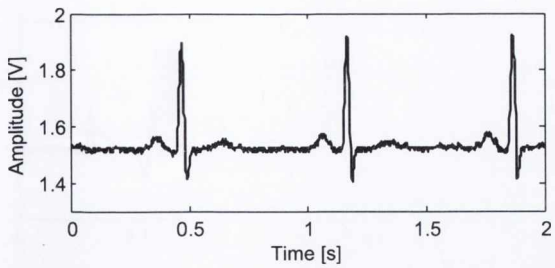

(a) Resting ECG, dry electrodes (1 kSs^{-1}).

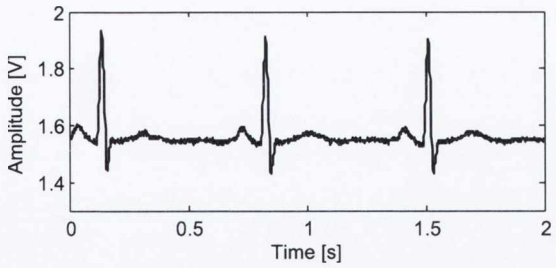

(b) Resting ECG, wet electrodes (1 kSs^{-1}).

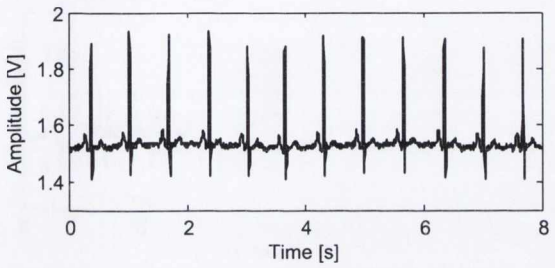

(c) Resting ECG, dry electrodes (250 Ss^{-1}).

(d) Resting ECG, wet electrodes (250 Ss^{-1}).

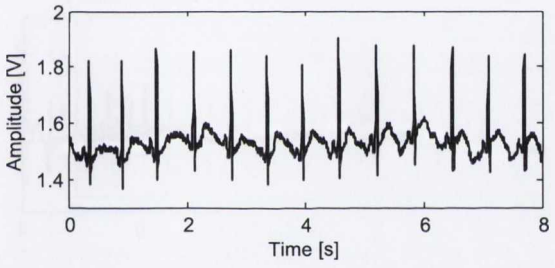

(e) Walking on the spot, dry electrodes (250 Ss^{-1}).

(f) Walking on the spot, wet electrodes (250 Ss^{-1}).

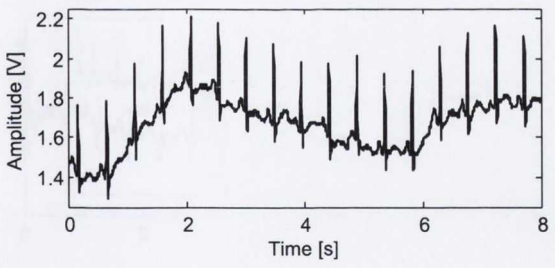

(g) Harvard step test, dry electrodes (250 Ss^{-1}).

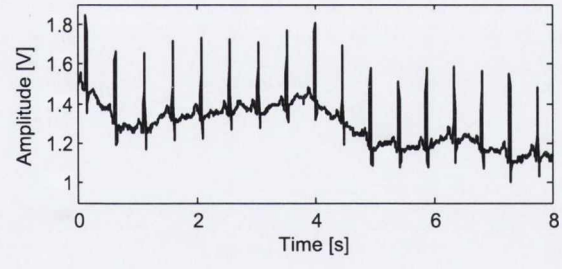

(h) Harvard step test, wet electrodes (250 Ss^{-1}).

Figure B.4: Sample ECG recordings for subject 4 using dry electrodes (left hand side waveforms) and wet electrodes (right hand side waveforms). The sampling rate is given in brackets in samples per s (Ss^{-1}).

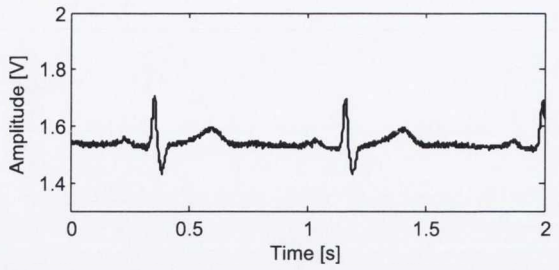

(a) Resting ECG, dry electrodes (1 kSs^{-1}).

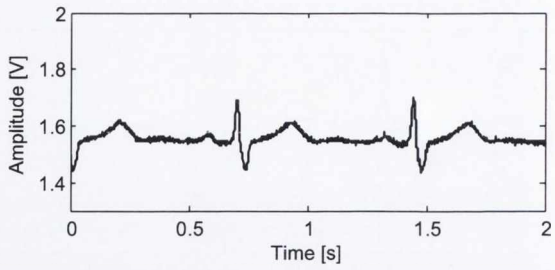

(b) Resting ECG, wet electrodes (1 kSs^{-1}).

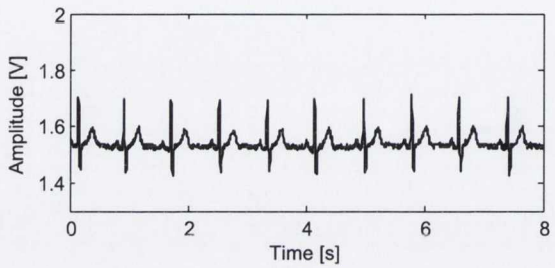

(c) Resting ECG, dry electrodes (250 Ss^{-1}).

(d) Resting ECG, wet electrodes (250 Ss^{-1}).

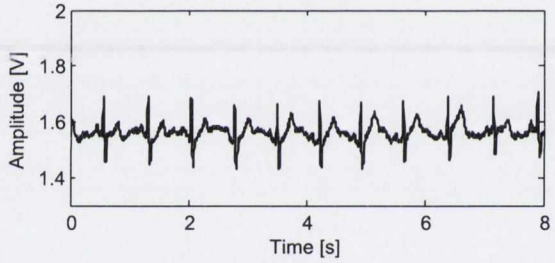

(e) Walking on the spot, dry electrodes (250 Ss^{-1}).

(f) Walking on the spot, wet electrodes (250 Ss^{-1}).

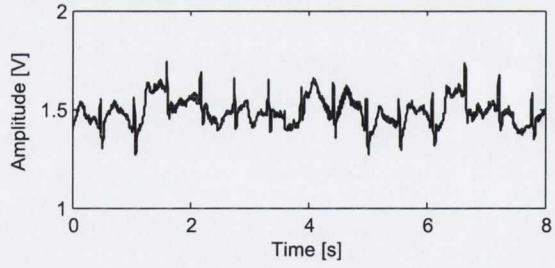

(g) Harvard step test, dry electrodes (250 Ss^{-1}).

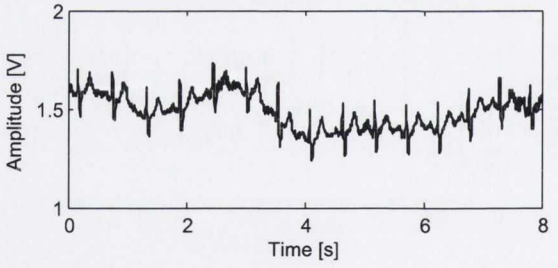

(h) Harvard step test, wet electrodes (250 Ss^{-1}).

Figure B.5: Sample ECG recordings for subject 5 using dry electrodes (left hand side waveforms) and wet electrodes (right hand side waveforms). The sampling rate is given in brackets in samples per s (Ss^{-1}).

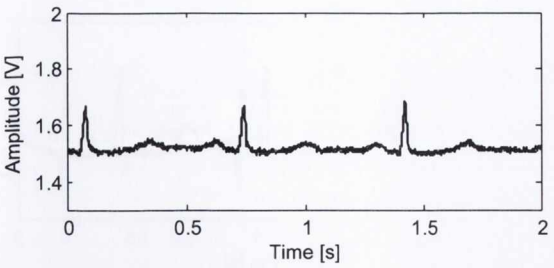

(a) Resting ECG, dry electrodes (1 kSs^{-1}).

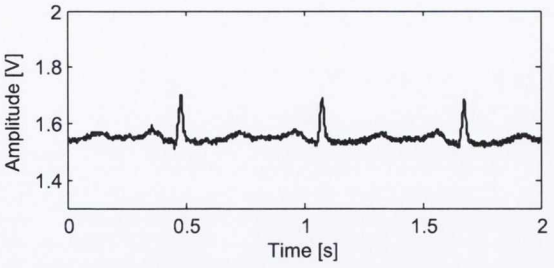

(b) Resting ECG, wet electrodes (1 kSs^{-1}).

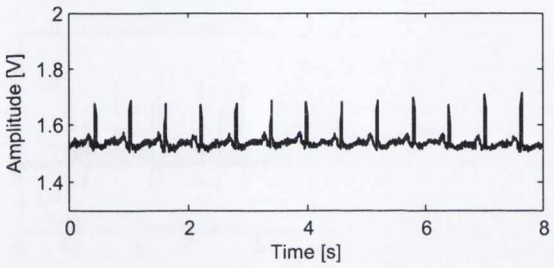

(c) Resting ECG, dry electrodes (250 Ss^{-1}).

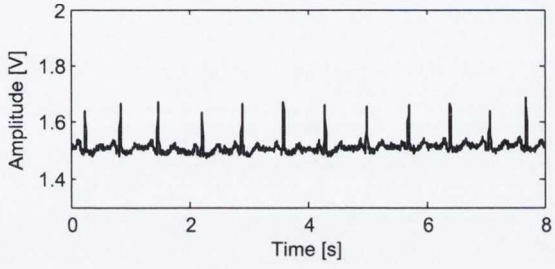

(d) Resting ECG, wet electrodes (250 Ss^{-1}).

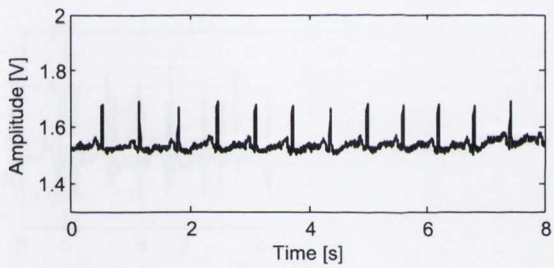

(e) Walking on the spot, dry electrodes (250 Ss^{-1}).

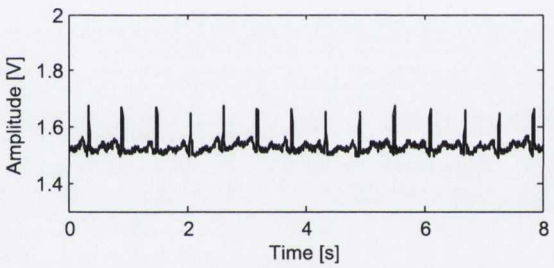

(f) Walking on the spot, wet electrodes (250 Ss^{-1}).

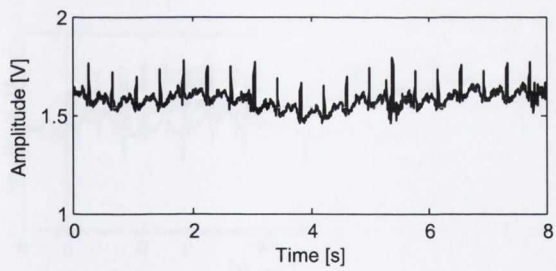

(g) Harvard step test, dry electrodes (250 Ss^{-1}).

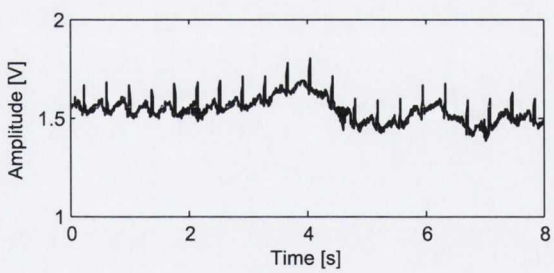

(h) Harvard step test, wet electrodes (250 Ss^{-1}).

Figure B.6: Sample ECG recordings for subject 6 using dry electrodes (left hand side waveforms) and wet electrodes (right hand side waveforms). The sampling rate is given in brackets in samples per s (Ss^{-1}).

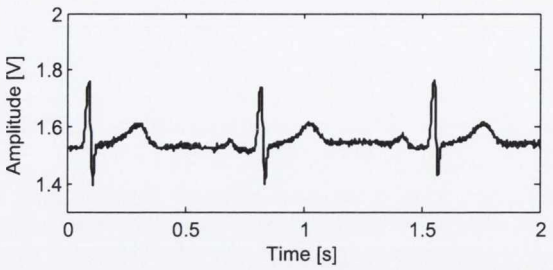

(a) Resting ECG, dry electrodes (1 kSs^{-1}).

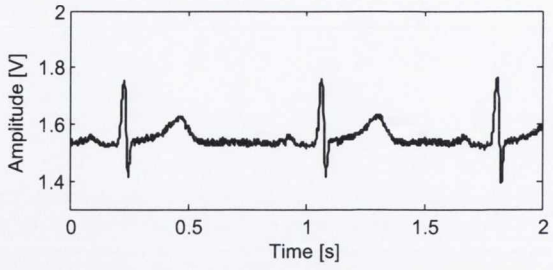

(b) Resting ECG, wet electrodes (1 kSs^{-1}).

(c) Resting ECG, dry electrodes (250 Ss^{-1}).

(d) Resting ECG, wet electrodes (250 Ss^{-1}).

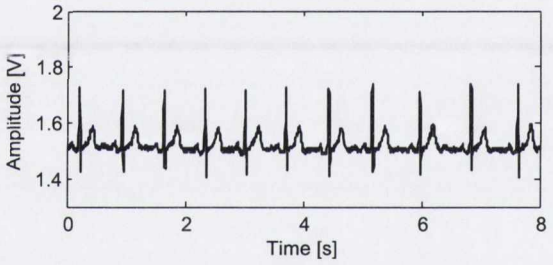

(e) Walking on the spot, dry electrodes (250 Ss^{-1}).

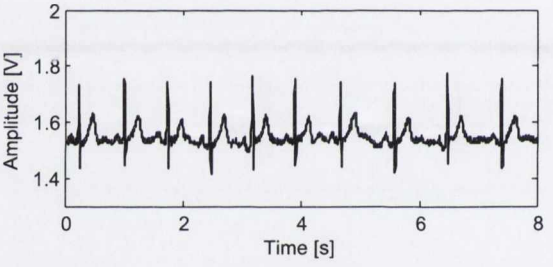

(f) Walking on the spot, wet electrodes (250 Ss^{-1}).

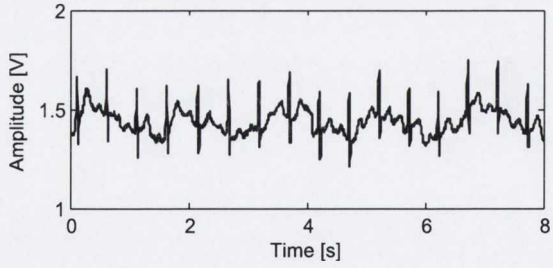

(g) Harvard step test, dry electrodes (250 Ss^{-1}).

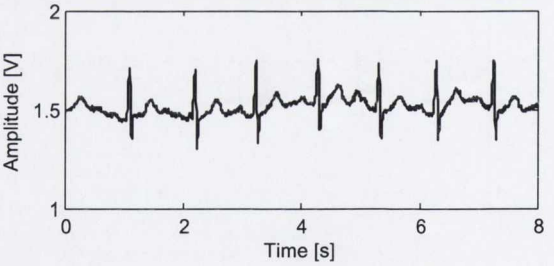

(h) Harvard step test, wet electrodes (250 Ss^{-1}).

Figure B.7: Sample ECG recordings for subject 7 using dry electrodes (left hand side waveforms) and wet electrodes (right hand side waveforms). The sampling rate is given in brackets in samples per s (Ss^{-1}).

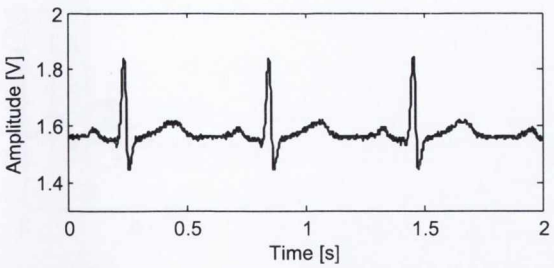

(a) Resting ECG, dry electrodes (1 kSs^{-1}).

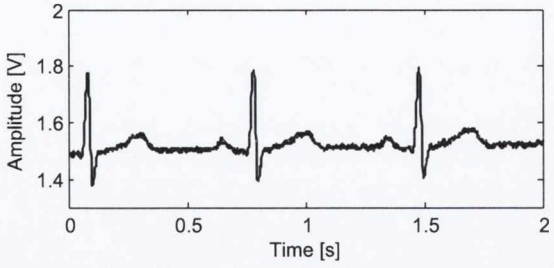

(b) Resting ECG, wet electrodes (1 kSs^{-1}).

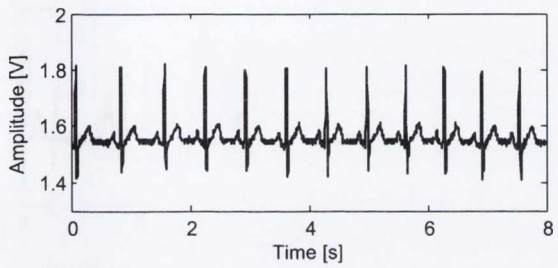

(c) Resting ECG, dry electrodes (250 Ss^{-1}).

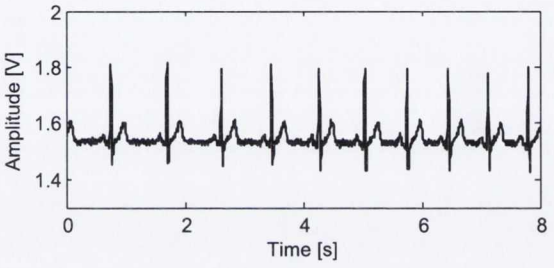

(d) Resting ECG, wet electrodes (250 Ss^{-1}).

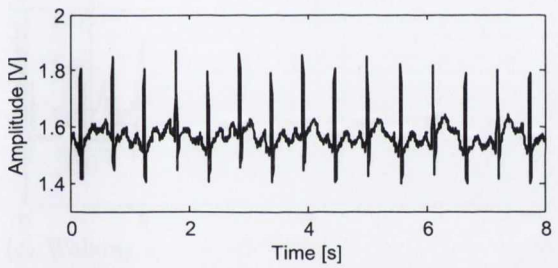

(e) Walking on the spot, dry electrodes (250 Ss^{-1}).

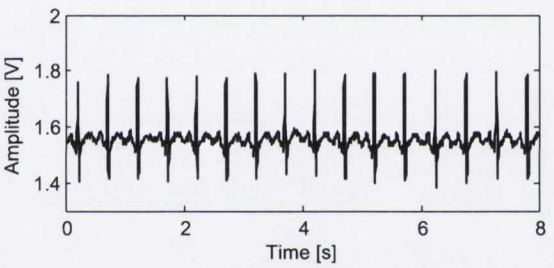

(f) Walking on the spot, wet electrodes (250 Ss^{-1}).

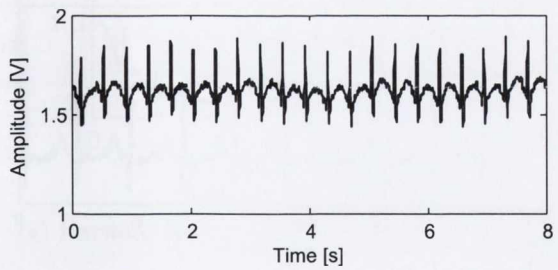

(g) Harvard step test, dry electrodes (250 Ss^{-1}).

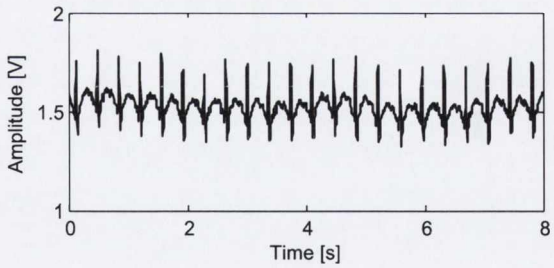

(h) Harvard step test, wet electrodes (250 Ss^{-1}).

Figure B.8: Sample ECG recordings for subject 8 using dry electrodes (left hand side waveforms) and wet electrodes (right hand side waveforms). The sampling rate is given in brackets in samples per s (Ss^{-1}).

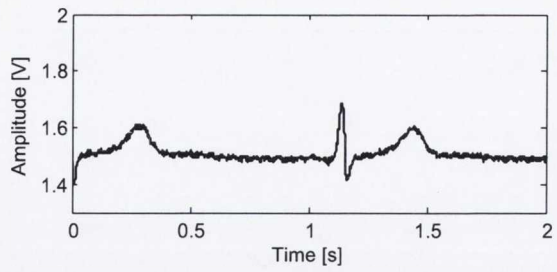

(a) Resting ECG, dry electrodes (1 kSs^{-1}).

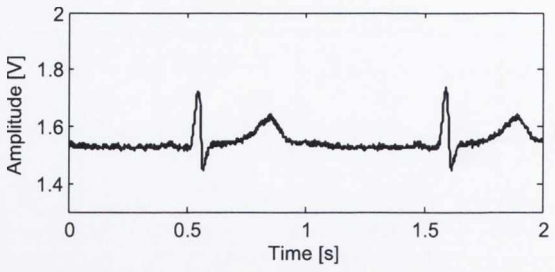

(b) Resting ECG, wet electrodes (1 kSs^{-1}).

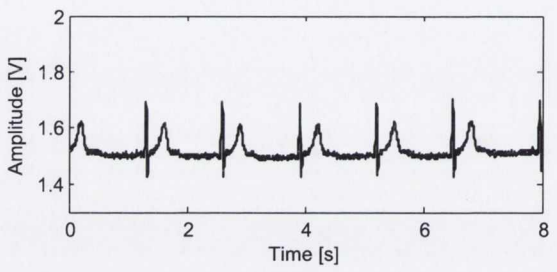

(c) Resting ECG, dry electrodes (250 Ss^{-1}).

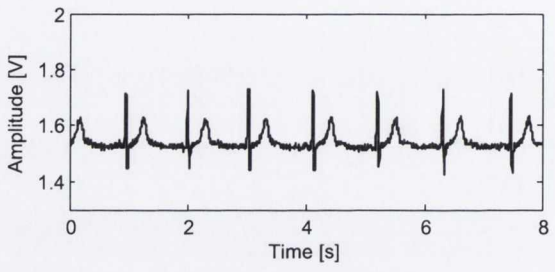

(d) Resting ECG, wet electrodes (250 Ss^{-1}).

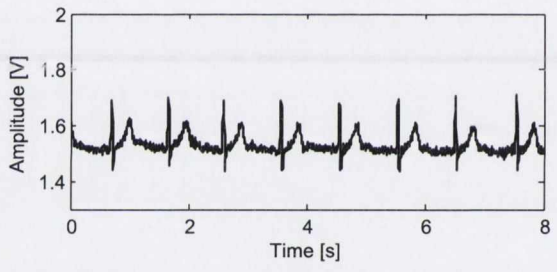

(e) Walking on the spot, dry electrodes (250 Ss^{-1}).

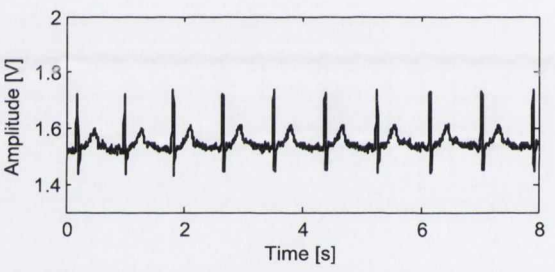

(f) Walking on the spot, wet electrodes (250 Ss^{-1}).

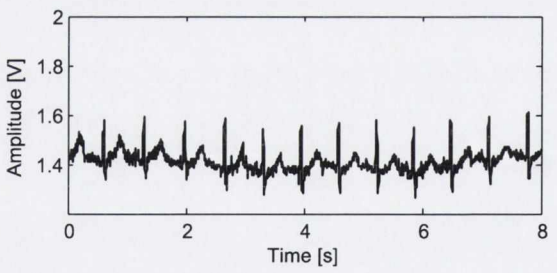

(g) Harvard step test, dry electrodes (250 Ss^{-1}).

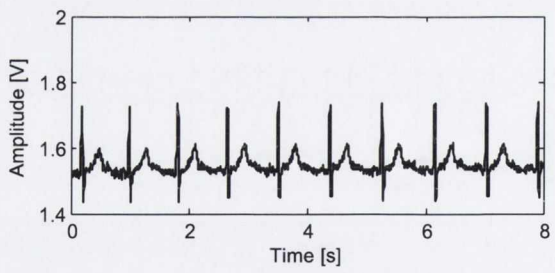

(h) Harvard step test, wet electrodes (250 Ss^{-1}).

Figure B.9: Sample ECG recordings for subject 9 using dry electrodes (left hand side waveforms) and wet electrodes (right hand side waveforms). The sampling rate is given in brackets in samples per s (Ss^{-1}).

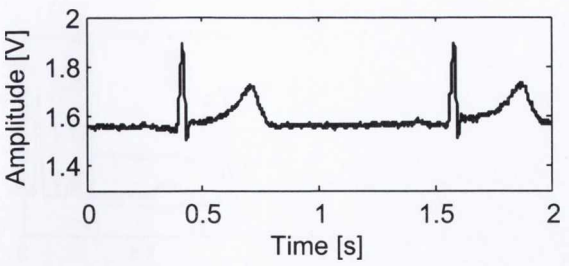

(a) Resting ECG, dry electrodes (1 kSs^{-1}).

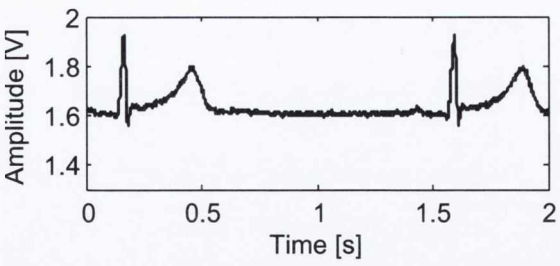

(b) Resting ECG, wet electrodes (1 kSs^{-1}).

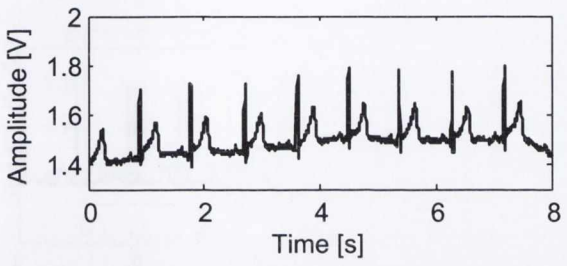

(c) Resting ECG, dry electrodes (250 Ss^{-1}).

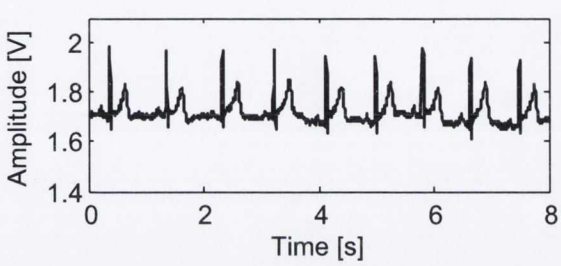

(d) Resting ECG, wet electrodes (250 Ss^{-1}).

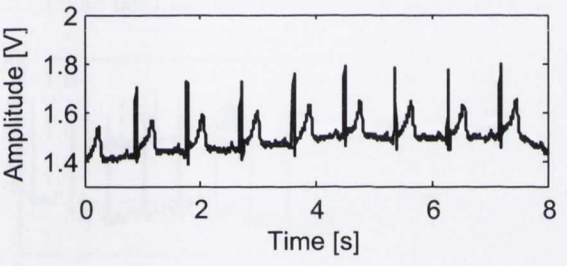

(e) Walking on the spot, dry electrodes (250 Ss^{-1}).

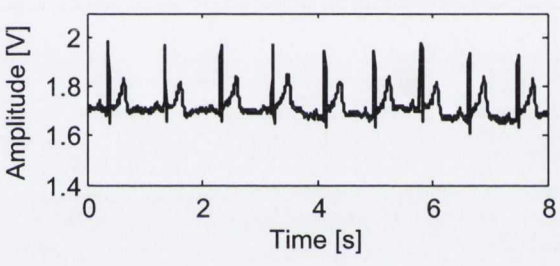

(f) Walking on the spot, wet electrodes (250 Ss^{-1}).

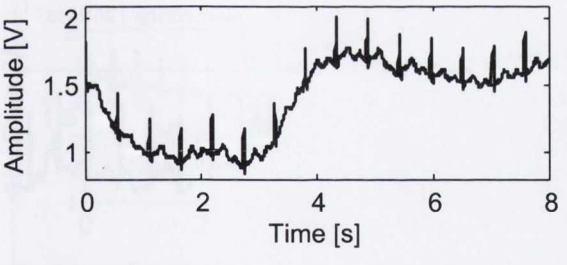

(g) Harward step test, dry electrodes (250 Ss^{-1}).

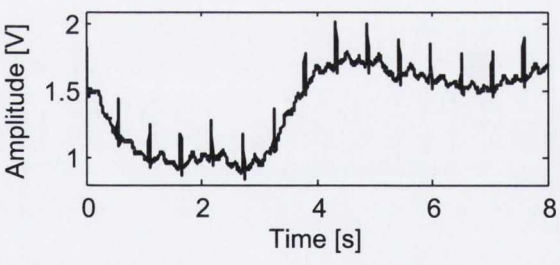

(h) Harward step test, wet electrodes (250 Ss^{-1}).

Figure B.10: Sample ECG recordings for subject 10 using dry electrodes (left hand side waveforms) and wet electrodes (right hand side waveforms). The sampling rate is given in brackets in samples per s (Ss^{-1}).

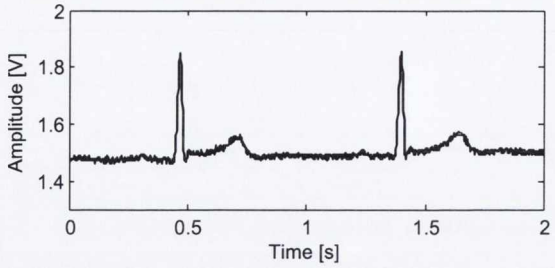

(a) Resting ECG, dry electrodes (1 kSs^{-1}).

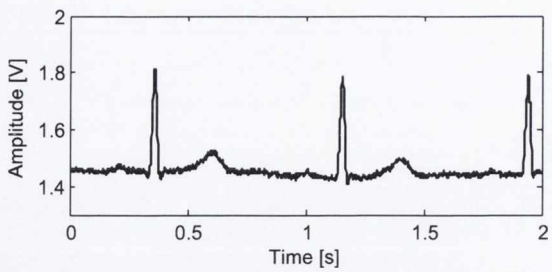

(b) Resting ECG, wet electrodes (1 kSs^{-1}).

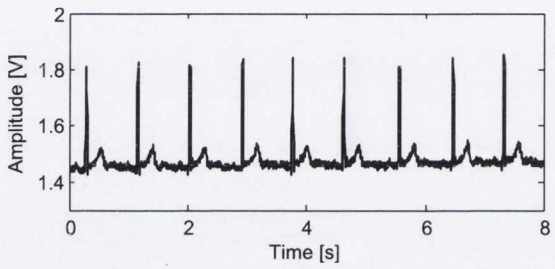

(c) Resting ECG, dry electrodes (250 Ss^{-1}).

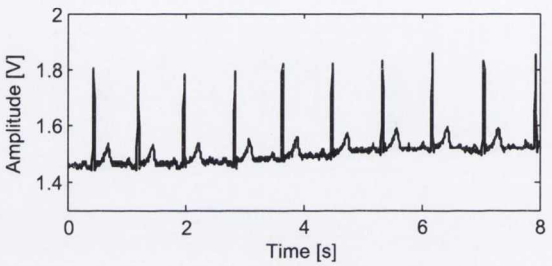

(d) Resting ECG, wet electrodes (250 Ss^{-1}).

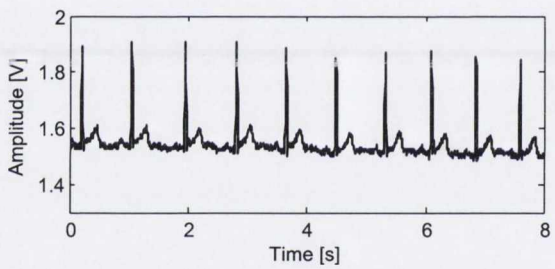

(e) Walking on the spot, dry electrodes (250 Ss^{-1}).

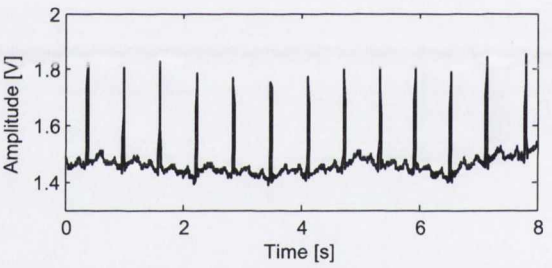

(f) Walking on the spot, wet electrodes (250 Ss^{-1}).

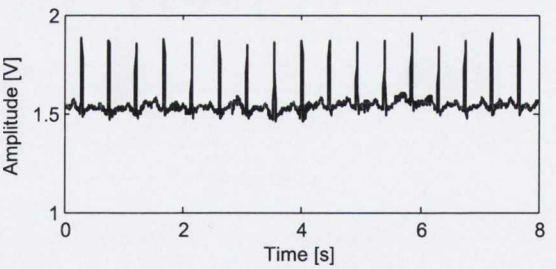

(g) Harvard step test, dry electrodes (250 Ss^{-1}).

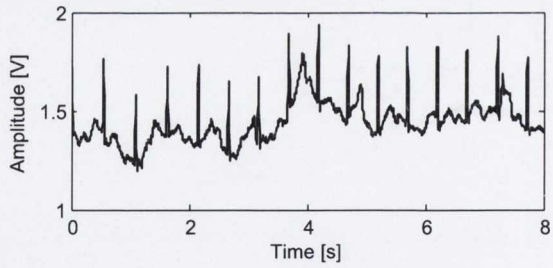

(h) Harvard step test, wet electrodes (250 Ss^{-1}).

Figure B.11: Sample ECG recordings for subject 11 using dry electrodes (left hand side waveforms) and wet electrodes (right hand side waveforms). The sampling rate is given in brackets in samples per s (Ss^{-1}). Significantly higher level of perspiration was observed with subject 11 than with the other thirteen subjects investigated. While sweat can act as an electrolyte in the case of dry electrodes, it was observed that excessive perspiration caused sweat to penetrate pre-gelled electrodes which degraded signal quality.

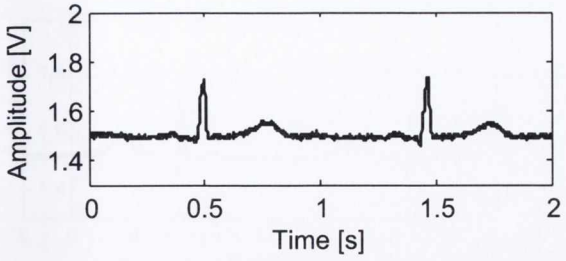

(a) Resting ECG, dry electrodes (1 kSs^{-1}).

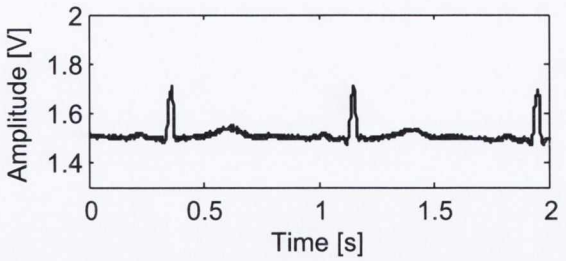

(b) Resting ECG, wet electrodes (1 kSs^{-1}).

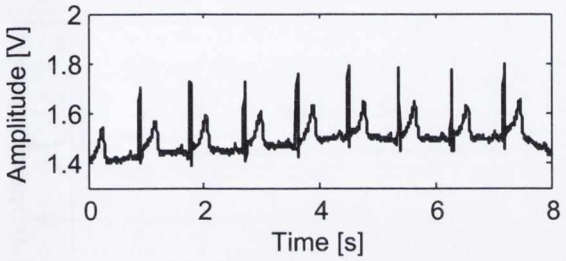

(c) Resting ECG, dry electrodes (250 Ss^{-1}).

(d) Resting ECG, wet electrodes (250 Ss^{-1}).

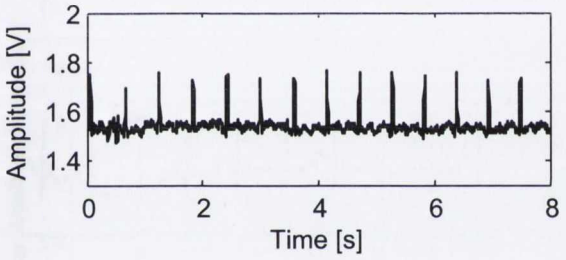

(e) Walking on the spot, dry electrodes (250 Ss^{-1}).

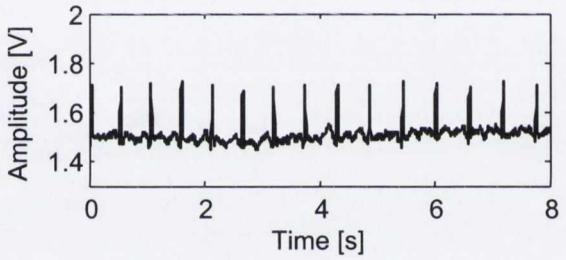

(f) Walking on the spot, wet electrodes (250 Ss^{-1}).

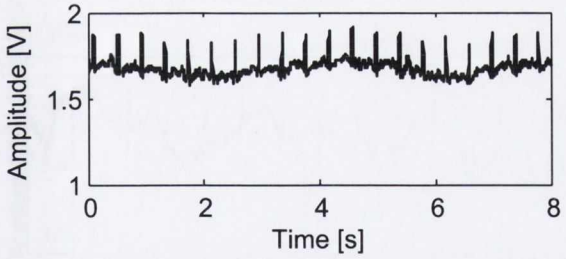

(g) Harward step test, dry electrodes (250 Ss^{-1}).

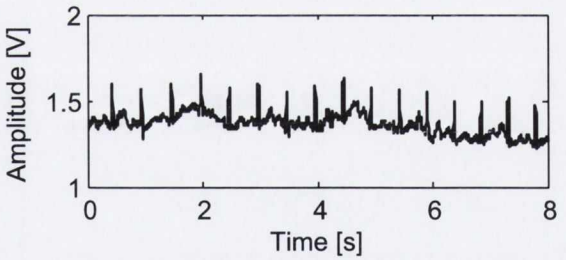

(h) Harward step test, wet electrodes (250 Ss^{-1}).

Figure B.12: Sample ECG recordings for subject 12 using dry electrodes (left hand side waveforms) and wet electrodes (right hand side waveforms). The sampling rate is given in brackets in samples per s (Ss^{-1}).

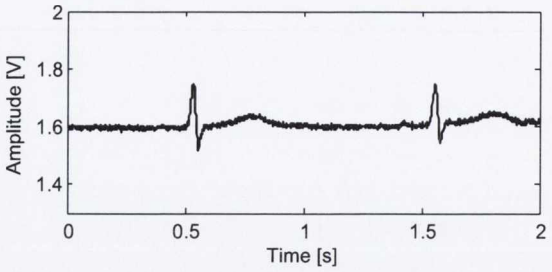

(a) Resting ECG, dry electrodes (1 kSs^{-1}).

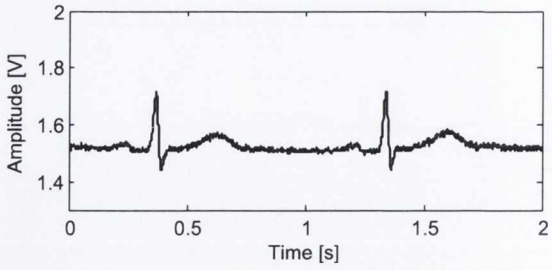

(b) Resting ECG, wet electrodes (1 kSs^{-1}).

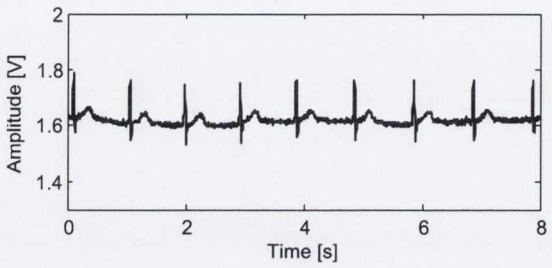

(c) Resting ECG, dry electrodes (250 Ss^{-1}).

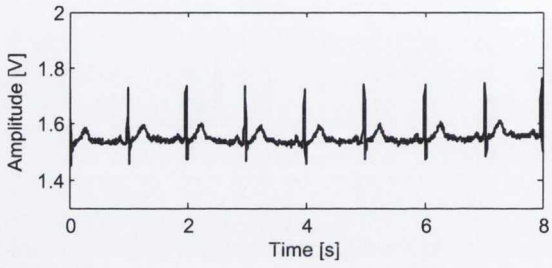

(d) Resting ECG, wet electrodes (250 Ss^{-1}).

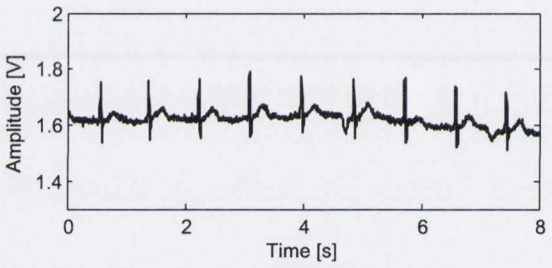

(e) Walking on the spot, dry electrodes (250 Ss^{-1}).

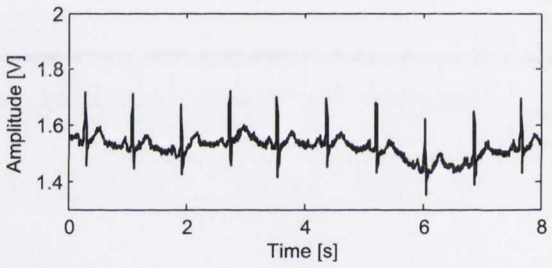

(f) Walking on the spot, wet electrodes (250 Ss^{-1}).

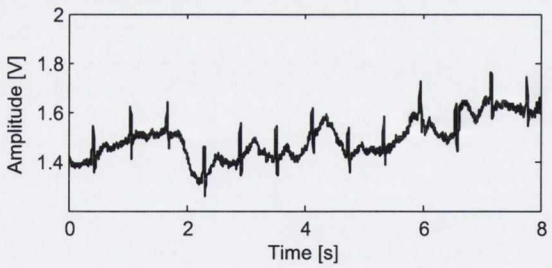

(g) Harvard step test, dry electrodes (250 Ss^{-1}).

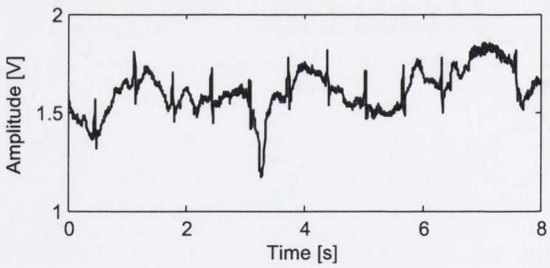

(h) Harvard step test, wet electrodes (250 Ss^{-1}).

Figure B.13: Sample ECG recordings for subject 13 using dry electrodes (left hand side waveforms) and wet electrodes (right hand side waveforms). The sampling rate is given in brackets in samples per s (Ss^{-1}).

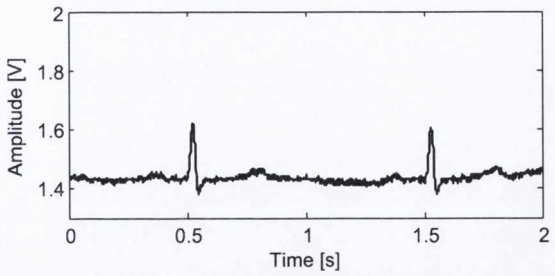

(a) Resting ECG, dry electrodes (1 kSs^{-1}).

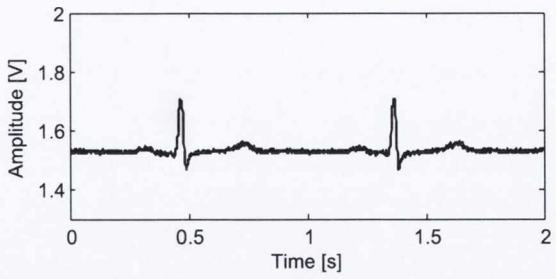

(b) Resting ECG, wet electrodes (1 kSs^{-1}).

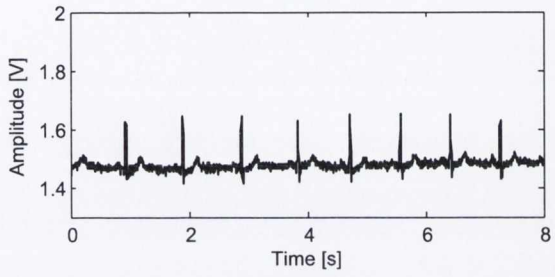

(c) Resting ECG, dry electrodes (250 Ss^{-1}).

(d) Resting ECG, wet electrodes (250 Ss^{-1}).

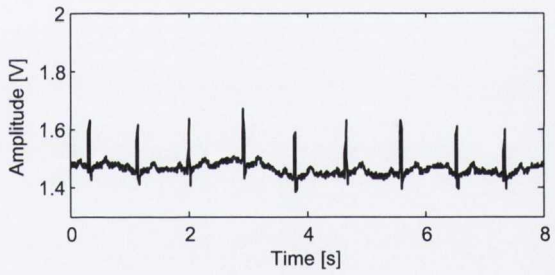

(e) Walking on the spot, dry electrodes (250 Ss^{-1}).

(f) Walking on the spot, wet electrodes (250 Ss^{-1}).

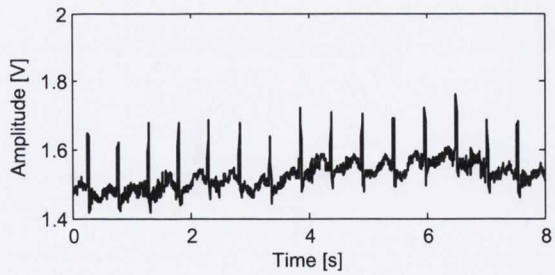

(g) Harvard step test, dry electrodes (250 Ss^{-1}).

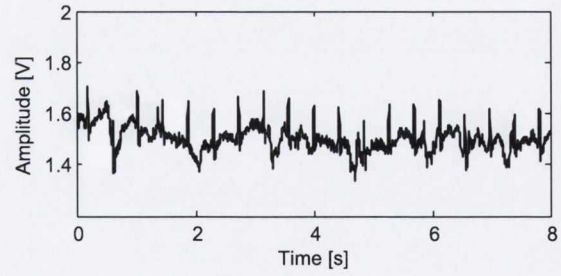

(h) Harvard step test, wet electrodes (250 Ss^{-1}).

Figure B.14: Sample ECG recordings for subject 14 using dry electrodes (left hand side waveforms) and wet electrodes (right hand side waveforms). The sampling rate is given in brackets in samples per s (Ss^{-1}).

Appendix C

Effect of manufacturing tolerances in the gain-determining resistors on the CMRR of the proposed novel IA structure presented in Chapter 6

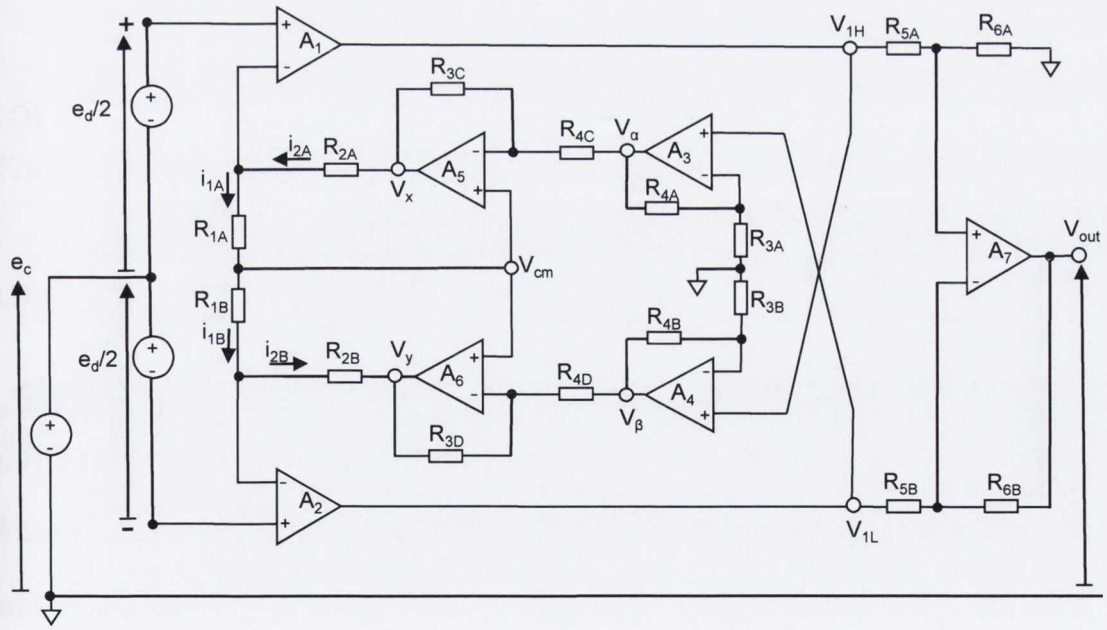

Figure C.1: Circuit schematics of the proposed new instrumentation amplifier circuit concept that features enhanced CMRR performance.

Referring to Fig. C.1, the following voltages and currents can be defined:

$$i_{1A} = i_{1B} = i_{2A} = i_{2B} = \frac{e_d}{R_{1A} + R_{1B}} \tag{C.1}$$

$$V_{cm} = e_c - \frac{e_d}{2} + R_{1B} i_{1B} = e_c + \left(\frac{R_{1B} - R_{1A}}{R_{1A} + R_{1B}}\right) \frac{e_d}{2} \tag{C.2}$$

$$V_x = \left(e_c + \frac{e_d}{2}\right) + R_{2A} i_{2A} = e_c + \left(1 + \frac{2R_{2A}}{R_{1A} + R_{1B}}\right) \frac{e_d}{2} \tag{C.3}$$

and

$$V_y = \left(e_c - \frac{e_d}{2}\right) - R_{2B} i_{2B} = e_c - \left(1 + \frac{2R_{2B}}{R_{1A} + R_{1B}}\right) \frac{e_d}{2} \tag{C.4}$$

Considering the two-op-amp instrumentation amplifier built around A_3 and A_5 in the feedback path of the fully differential stage, the following relationships can be established:

$$\frac{-V_{1L}}{R_{3A}} = \frac{V_{1L} - V_\alpha}{R_{4A}} \Rightarrow V_\alpha = \left(1 + \frac{R_{4A}}{R_{3A}}\right) V_{1L} \tag{C.5}$$

and

$$\frac{V_\alpha - V_{cm}}{R_{4C}} = \frac{V_{ec} - V_x}{R_{3C}} \Rightarrow V_x = \left(1 + \frac{R_{3C}}{R_{4C}}\right) V_{cm} - \frac{R_{3C}}{R_{4C}} V_\alpha \tag{C.6}$$

Eqs. (C.5) and (C.6) allow the following expression for V_x to be derived:

$$V_x = \left(1 + \frac{R_{3C}}{R_{4C}}\right) V_{cm} - \frac{R_{3C}}{R_{4C}} \left[\left(1 + \frac{R_{4A}}{R_{3A}}\right) V_{1L}\right] \tag{C.7}$$

Equating eqs. (C.3) and (C.7) yields:

$$e_c + \left(1 + \frac{2R_{2A}}{R_{1A} + R_{1B}}\right) \frac{e_d}{2} = \left(1 + \frac{R_{3C}}{R_{4C}}\right) V_{cm} - \frac{R_{3C}}{R_{4C}} \left[\left(1 + \frac{R_{4A}}{R_{3A}}\right) V_{1L}\right] \tag{C.8}$$

$$\Rightarrow -\left(\frac{R_{3C}}{R_{4C}} + \frac{R_{4A}}{R_{3A}} \frac{R_{3C}}{R_{4C}}\right) V_{1L} = \left[1 + \frac{2R_{2A}}{R_{1A} + R_{1B}} + \left(1 + \frac{R_{3C}}{R_{4C}}\right) \left(\frac{R_{1A} - R_{1B}}{R_{1A} + R_{1B}}\right)\right] \frac{e_d}{2} - \frac{R_{3C}}{R_{4C}} e_c \tag{C.9}$$

Imbalance introduced in the circuit by mismatch in the values of the gain-defining resistors is considered by expressing each paired resistor, R_{xy}, in terms of its nominal value, R_x, and an error due to manufacturing tolerances, Δ_{xy}, so that:

$$R_{xy} = R_x \left(1 + \Delta_{xy}\right)\big|_{x=\{1,2,3,4,5,6\}, y=\{A,B,C,D\}} \tag{C.10}$$

This results in an expression for V_{1L} given by:

$$V_{1L} = \frac{-\left[1+\frac{R_2}{R_1}+\frac{R_2}{R_1}\left(\Delta_{2A}-\Delta_{1A}-\Delta_{1B}\right)+2\Delta_{1B}\left(1+\frac{R_3}{R_4}\right)\right]\frac{e_d}{2}+\frac{R_3}{R_4}\left(1+\Delta_{3C}-\Delta_{4C}\right)e_c}{\left[1+\frac{R_3}{R_4}+\Delta_{4A}-\Delta_{3A}+\left(1+\frac{R_3}{R_4}\right)\left(\Delta_{3C}-\Delta_{4C}\right)\right]}$$

$$= \frac{-\left[\begin{array}{l}1+\frac{R_2}{R_1}+\frac{R_2(\Delta_{2A}-\Delta_{1A}-\Delta_{1B})}{R_1}\\ +2\Delta_{1B}\left(1+\frac{R_3}{R_4}\right)\end{array}\right]\frac{e_d}{2}+\frac{R_3(1+\Delta_{3C}-\Delta_{4C})}{R_4}e_c}{1+\frac{R_3}{R_4}}\left[1-\frac{\left[\begin{array}{l}\Delta_{4A}-\Delta_{3A}\\ +\left(1+\frac{R_3}{R_4}\right)\left(\Delta_{3C}-\Delta_{4C}\right)\end{array}\right]}{1+\frac{R_3}{R_4}}\right] \tag{C.11}$$

Neglecting second order terms allow eq. (C.11) to be be closely approximated as:

$$V_{1L} \simeq \frac{-\left[\begin{array}{l}1+\frac{R_2}{R_1}+\frac{R_2\left(\Delta_{2A}-\Delta_{1A}-\Delta_{1B}-\frac{\Delta_{4A}-\Delta_{3A}}{1+\frac{R_3}{R_4}}-\Delta_{3C}+\Delta_{4C}\right)}{R_1}\\ +2\Delta_{1B}\left(1+\frac{R_3}{R_4}\right)-\frac{\Delta_{4A}-\Delta_{3A}}{1+\frac{R_3}{R_4}}-\Delta_{3C}+\Delta_{4C}\end{array}\right]\frac{e_d}{2}+\frac{R_3}{R_4}\left(1-\frac{\Delta_{4A}-\Delta_{3A}}{1+\frac{R_3}{R_4}}\right)e_c}{1+\frac{R_3}{R_4}} \tag{C.12}$$

A similar approach yields the following expression for V_{1H}:

$$V_{1H} \simeq \frac{\left[\begin{array}{l}1+\frac{R_2}{R_1}+\frac{R_2\left(\Delta_{2B}-\Delta_{1B}-\Delta_{1A}-\frac{\Delta_{4B}-\Delta_{3B}}{1+\frac{R_3}{R_4}}-\Delta_{3D}+\Delta_{4D}\right)}{R_1}\\ +2\Delta_{1A}\left(1+\frac{R_3}{R_4}\right)-\frac{\Delta_{4B}-\Delta_{3B}}{1+\frac{R_3}{R_4}}-\Delta_{3D}+\Delta_{4D}\end{array}\right]\frac{e_d}{2}+\frac{R_3}{R_4}\left(1-\frac{\Delta_{4B}-\Delta_{3B}}{1+\frac{R_3}{R_4}}\right)e_c}{1+\frac{R_3}{R_4}} \tag{C.13}$$

The differential and common-mode voltages at the output of the fully differential stage can be derived from eqs. (C.12) and (C.13) as:

$$V_{1d} = V_{1H} - V_{1L}$$

$$\simeq \frac{\left(\frac{R_1+R_2}{R_1}\right)\left[\begin{array}{l}1+\frac{R_2\left(\frac{\Delta_{2A}+\Delta_{2B}}{2}\right)}{R_1+R_2}+\frac{\left[R_1\left(1+\frac{R_3}{R_4}\right)-R_2\right](\Delta_{1A}+\Delta_{1B})}{R_1+R_2}\\ -\frac{\Delta_{4B}+\Delta_{4A}-\Delta_{3A}-\Delta_{3B}}{2\left(1+\frac{R_3}{R_4}\right)}+\frac{-\Delta_{3D}-\Delta_{3C}+\Delta_{4C}+\Delta_{4D}}{2}\end{array}\right]e_d-\frac{R_3\left(\frac{\Delta_{4B}-\Delta_{4A}+\Delta_{3A}-\Delta_{3B}}{1+\frac{R_3}{R_4}}\right)}{R_4}e_c}{1+\frac{R_3}{R_4}} \tag{C.14}$$

and

$$V_{1c} = \frac{V_{1H} + V_{1L}}{2}$$
$$\simeq \left(\frac{R_3}{R_3 + R_4}\right)\left(1 - \frac{\Delta_{4B} + \Delta_{4A} - \Delta_{3A} - \Delta_{3B}}{1 + \frac{R_3}{R_4}}\right) e_c$$
$$+ \frac{\left(\frac{R_1+R_2}{R_1}\right)\left[\begin{array}{l} \frac{R_2\left(\frac{-\Delta_{2A}+\Delta_{2B}+\Delta_{1A}-\Delta_{1B}}{4}\right)}{R_1+R_2} + \frac{\left[2R_1\left(1+\frac{R_3}{R_4}\right)-R_2\right]\left(\frac{\Delta_{1A}-\Delta_{1B}}{4}\right)}{R_1+R_2} \\ -\frac{\Delta_{4B}-\Delta_{4A}+\Delta_{3A}-\Delta_{3B}}{4\left(1+\frac{R_3}{R_4}\right)} + \frac{-\Delta_{3D}+\Delta_{3C}-\Delta_{4C}+\Delta_{4D}}{4} \end{array}\right] e_d}{1 + \frac{R_3}{R_4}} \quad \text{(C.15)}$$

The output stage transforms V_{1H} and V_{1L} into a single-ended signal V_{out} defined as follows:

$$V_{out} \simeq \frac{R_6}{R_5}\left[1 + \frac{R_5\left(-\Delta_{5A} - \Delta_{5B} + \Delta_{6A} + \Delta_{6B}\right) + 2R_6\left(\Delta_{6B} - \Delta_{5B}\right)}{2\left(R_5 + R_6\right)}\right]\left(V_{1H} - V_{1L}\right)$$
$$+ \frac{R_6\left(\Delta_{5B} - \Delta_{5A} + \Delta_{6A} - \Delta_{6B}\right)}{R_5 + R_6}\left(\frac{V_{1H} + V_{1L}}{2}\right) \quad \text{(C.16)}$$

Eqs. (C.14) to (C.16) allow V_{out} to be closely approxmated as:

$$V_{out} \simeq \frac{R_6}{R_5\left(1 + \frac{R_3}{R_4}\right)}\left[\begin{array}{l} \left(1 + \frac{R_2}{R_1}\right)\left[\begin{array}{l} 1 + \frac{R_5(-\Delta_{5A}-\Delta_{5B}+\Delta_{6A}+\Delta_{6B})+2R_6(\Delta_{6B}-\Delta_{5B})}{2(R_5+R_6)} \\ +\frac{R_2\left(\frac{\Delta_{2A}+\Delta_{2B}}{2}\right)}{R_1+R_2} + \frac{\left[R_1\left(1+\frac{R_3}{R_4}\right)-R_2\right](\Delta_{1A}+\Delta_{1B})}{R_1+R_2} \\ -\frac{\Delta_{4B}+\Delta_{4A}-\Delta_{3A}-\Delta_{3B}}{2\left(1+\frac{R_3}{R_4}\right)} + \frac{-\Delta_{3D}-\Delta_{3C}+\Delta_{4C}+\Delta_{4D}}{2} \end{array}\right] e_d \\ +\frac{R_3}{R_4}\left[\frac{R_5(\Delta_{5B}-\Delta_{5A}+\Delta_{6A}-\Delta_{6B})}{R_5+R_6} + \frac{\Delta_{4B}-\Delta_{4A}+\Delta_{3A}-\Delta_{3B}}{1+\frac{R_3}{R_4}}\right] e_c \end{array}\right] \quad \text{(C.17)}$$

The CMRR measured at the single-ended output is therefore derived from eq. (C.17) as:

$$CMRR_{\Delta R}$$
$$\simeq \frac{\frac{R_4}{R_3}\left(1 + \frac{R_2}{R_1}\right)\left[\begin{array}{l} 1 + \frac{R_5(-\Delta_{5A}-\Delta_{5B}+\Delta_{6A}+\Delta_{6B})+2R_6(\Delta_{6B}-\Delta_{5B})}{2(R_5+R_6)} + \frac{R_2}{R_1+R_2}\left(\frac{\Delta_{2A}+\Delta_{2B}}{2}\right) \\ +\frac{\left[R_1\left(1+\frac{R_3}{R_4}\right)-R_2\right](\Delta_{1A}+\Delta_{1B})}{R_1+R_2} - \frac{\Delta_{4B}+\Delta_{4A}-\Delta_{3A}-\Delta_{3B}}{2\left(1+\frac{R_3}{R_4}\right)} + \frac{-\Delta_{3D}-\Delta_{3C}+\Delta_{4C}+\Delta_{4D}}{2} \end{array}\right]}{\frac{R_5(\Delta_{5B}-\Delta_{5A}+\Delta_{6A}-\Delta_{6B})}{R_5+R_6} + \frac{\Delta_{4B}-\Delta_{4A}+\Delta_{3A}-\Delta_{3B}}{1+\frac{R_3}{R_4}}}$$
$$\text{(C.18)}$$

The worst-case scenario corresponds to the mismatch in resistor values that yields the largest common-mode voltage at the single-ended output and is associated with the following combination:

$$\Delta_{1A} = \Delta_{2B} = \Delta_{3A} = \Delta_{3D} = \Delta_{4B} = \Delta_{4C} = \Delta_{5A} = \Delta_{6B} = \Delta_{R_{max}} \quad \text{(C.19)}$$

and

$$\Delta_{1B} = \Delta_{2A} = \Delta_{3B} = \Delta_{3C} = \Delta_{4A} = \Delta_{4D} = \Delta_{5B} = \Delta_{6A} = -\Delta_{R_{max}} \tag{C.20}$$

where $\Delta_{R_{max}}$ is the manufacturing tolerance for the resistors used. It can then be concluded that the minimum common-mode rejection ratio due to manufacturing tolerances in the gain determining resistors is given by:

$$CMRR_{\Delta R_{min}} = \frac{\frac{R_4}{R_3}\left(1+\frac{R_2}{R_1}\right)\left[1-\left[2\frac{R_6}{R_5+R_6}+\frac{R_1\left(1+\frac{R_3}{R_4}\right)}{R_1+R_2}+2\right]\Delta_{R_{max}}\right]}{4\Delta_{R_{max}}\left(\frac{R_5}{R_5+R_6}+\frac{1}{1+\frac{R_3}{R_4}}\right)} \tag{C.21}$$

Taking $R_5 = R_6$ and $R_4 >> R_3$, $CMRR_{\Delta R_{min}}$ can be closely approximated by:

$$CMRR_{\Delta R_{min}} \simeq \frac{R_4}{3R_3}\left(\frac{1+\frac{R_2}{R_1}}{2\Delta_{R_{max}}}\right) \tag{C.22}$$

Bibliography

[1] S. M. Munir *et al.*, "Devices in heart failure, potential methods for device-based monitoring of congestive heart failure," *Tex Heart I J*, vol. 35, pp. 166–173, 2008.

[2] G. Boriani *et al.*, "Telecardiology and remote monitoring of implanted electrical devices: The potential for fresh clinical care perspectives." *J Gen Intern Med*, vol. 35, pp. 166–173, 2008.

[3] M. J. Alberts and J. D. Easton, "Stroke best practice: a team approach to evidence-based care," *J Natl Med Assoc*, vol. 96(4 Suppl), pp. 5S–20S, 2004.

[4] J. Hoogsteen and J. Bennekers, "Recommendations and cardiological evaluation of athletes with arrhythmias part 2," *Neth Heart J*, vol. 12(4), pp. 157–164, 2004.

[5] N. J. Holter, "New method for heart studies: Continuous electrocardiography of active subjectsover long periods is now practical," *Science*, vol. 134, pp. 1214–1220, 1961.

[6] J. Gilson, N. J. Holter, and W. Glasscock, "Continuous ambulant electrocardiograms and their analysis: Clinical observations using the electrocardiocorder and avsep analyzer," *Am J Cardiol*, vol. 14, pp. 204–217, 1964.

[7] N. J. Holter, *Historical Background and Development of Ambulatory Monitoring: The Nature of Research, in N.K. Jacobsen & S.R. Yarnall (eds.): Ambulatory ECG Monitoring*, 1st ed. Seattle, WA, USA: MCSA, 1976, pp. 1–9.

[8] A. A. McLeod *et al.*, "A report of a working group of the bcs: cardiology in the district hospital," *Br Heart J*, vol. 72 (3), pp. 303–308, 1994.

[9] D. Reid, "The electrocardiogram in the assessment of the effect of drugs on cardiac arrhthmias," *Br J Clin Pharmacol*, vol. 6(6), pp. 473–485, 1978.

[10] J. Coosemans, B. Hermans, and R. Puers, "Integrating wireless ecg monitoring in textiles," in *Proc IEEE Transducer*, vol. 1, Seoul, Korea, June 2005, pp. 228–232.

[11] C. Y. Ryu, S. H. Nam, and S. Kim, "Conductive rubber electrode for wearable health monitoring," in *Conf Proc IEEE Eng Med Biol Soc*, vol. 35, Shanghai, China, Sept. 2005, pp. 3479–3481.

[12] A. Searle and L. Kirkup, "A direct comparison of wet, dry and insulating bioelectric recording electrodes," *Physiol Meas*, vol. 21(2), pp. 271–283, May 2000.

[13] H. Tam and J. G. Webster, "Minimizing electrode motion artifact by skin abrasion," *IEEE T Bio-Med Eng*, vol. BME-24(2), pp. 134 – 139, March 1977.

[14] J. G. Webster, "Reducing motion artifacts and interference in biopotential recording," *IEEE T Bio-Med Eng*, vol. BME-31(2), pp. 823–826, Dec. 1984.

[15] D. P. Burbank and J. G. Webster, "Reducing skin potential motion artifact by skin abrasion," *Med Biol Eng Comput*, vol. 16, pp. 31–38, 1978.

[16] G. Gargiulo *et al.*, "An ultra-high input impedance ecg amplifier for long-term monitoring of athletes," *Med Dev Evid Res*, vol. 2010:3, pp. 1–9, July 2010.

[17] G. Gargiulo *et al.*, "Dry electrode bio-potential recordings," in *Conf Proc IEEE Eng Med Biol Soc*, Buenos Aires, Argentina, Aug. 2010, pp. 6493–6496.

[18] S. Fuhrhop *et al.*, "Ambulant ecg recording with wet and dry electrodes: A direct comparison of two systems," in *IFMBE Proc*, vol. 25 / V, Munich, Germany, 2009, pp. 305–307.

[19] C.-L. Chang *et al.*, "A power-efficient bio-potential acquisition device with ds-mde sensors for long-term healthcare monitoring applications," *Sensors*, vol. 10, pp. 4778–4793, May 2010.

[20] C. W. Chang and J. C. Chiou, "Surface-mounted dry electrode and analog-front-end systems for physiological signal measurement," in *IEEE NIH Life Sci Syst Appl Workshop*, Bethesda, MD, USA, April 2009, pp. 108–111.

[21] C. Figueiredo, K. Becher, K.-P. Hoffmann, and P. Mendes, "Low power wireless acquisition module for wearable health monitoring systems," in *Conf Proc IEEE Eng Med Biol Soc*, Buenos Aires, Argentina, Sept. 2010, pp. 704–707.

[22] H.-J. Yoo, J. Yoo, and L. Yan, "Wireless fabric patch sensors for wearable healthcare," in *Conf Proc IEEE Eng Med Biol Soc*, Buenos Aires, Argentina, Aug. 2010, pp. 5254–5257.

[23] C. R. Merrit, H. T. Nagle, and E. Grant, "Fabric-based active electrode design and fabrication for health monitoring clothing," *IEEE T Inf Technol B*, vol. 13, pp. 274–280, March 2009.

[24] A. Ayyaswamy. (2009) Design of a wearable wireless electrocardiograph (quick doc). [Online]. Available: http://digitalcommons.mcmaster.ca/ee4bi6/2

[25] E. R. Valverde *et al.*, "Effect of electrode impedance in improved buffer amplifier for bioelectric recordings," *J Med Eng Technol*, vol. 28, pp. 217–222, Sept. 2004.

[26] E. S. Valshinov and N. Pallikarakis, "An active electrode for biopotential recording from small localized bio-sources," *Biomed Eng Online*, vol. 3:25, 2004.

[27] N. Taccini, G. Loriga, M. Pacelli, and R. Paradiso, "Wearable monitoring system for chronic cardio-respiratory diseases," in *Conf Proc IEEE Eng Med Biol Soc*, Vancouver, Canada, Aug. 2008, pp. 3690–3693.

[28] G. Ruffini *et al.*, "Enobio dry electrophysiology electrode; first human trial plus wireless electrode system," in *Conf Proc IEEE Eng Med Biol Soc*, Lyon, France, Aug. 2007, pp. 6689–6693.

[29] A. Gruetzmann, S. Hansen, and J. Müller, "Novel dry electrodes for ecg monitoring," *Physiol Meas*, vol. 28, pp. 1375–1390, 2007.

[30] K.-H. Lee *et al.*, "Wearable heart electrical activity monitoring using circular ring electrode," in *IFMBE Proc*, Seoul, Korea, Aug. 2006, pp. 4088–4091.

[31] K.-H. Lee *et al.*, "Asymmetric skin-to-electrode impedance characterisation of concentric circular ring electrode for monitoring of electrical activity of the heart," in *Conf Proc IEEE SICE-ICASE*, Busan, Korea, Oct. 2006, pp. 1135–1136.

[32] M. Catrysse *et al.*, "Towards the integration of textile sensors in a wireless monitoring suit," *Sensors and Actuat A: Phys*, vol. 114, pp. 302–311, Sept. 2004.

[33] R. Puers *et al.*, "A smart suit for the monitoring of physiological parameters," in *Proc IEEE ISOB*, Brisbane, Australia, 2003, pp. 33–47.

[34] M. J. Burke and D. T. Gleeson, "A micropower dry-electrode ecg preamplifier," *IEEE T Bio-Med Eng*, vol. 47, pp. 155–162, Feb. 2000.

[35] M. J. Burke and D. T. Gleeson, "An ultra-low power pre-amplifier for pasteless electrocardiography," in *IEEE I C Elect Circ*, Cyprus, Sept. 1999, pp. 615–619.

[36] D. Gleeson, "Low-power ecg amplifier and detector," Master's thesis, Trinity College Dublin, Dublin, Ireland, 1996.

[37] J. Yoo *et al.*, "An attachable ecg sensor bandage with planar-fashionable circuit board," in *Proc IEEE ISWC*, Linz, Austria, Sept. 2009, pp. 145–146.

[38] L. M. Yu *et al.*, "A mems-based bioelectrode for ecg measurement," in *Proc IEEE Sensors*, Lecce, Italy, Oct. 2008, pp. 1068–1071.

[39] J. Mühlsteff and O. Such, "Dry electrodes for monitoring of vital signs in functional textiles," in *Conf Proc IEEE Eng Med Biol Soc*, San Francisco, CA, USA, Sept. 2004, pp. 2212 – 2215.

[40] J. Mühlsteff *et al.*, "Wearable approach for continuous ecg and activity patient-monitoring," in *Conf Proc IEEE Eng Med Biol Soc*, San Francisco, CA, USA, Sept. 2004, pp. 2184–2187.

[41] J. McLughlin, E. T. McAdam, and J. M. Anderson, "Novel dry electrode ecg sensor system," in *Conf Proc IEEE Eng Med Biol Soc*, Baltimore, MD, USA, Nov. 1994, p. 804.

[42] C. S. Lessard, W. C. Wong, and A. Yee, "Evaluation of noninvasive measurement methods and systems for application in vital signs detection," Texas A and M University College Station, Bioengineering Program, Tech. Rep., March 1986.

[43] G. Gargiulo *et al.*, "Mobile biomedical sensing with dry electrodes," in *Proc IEEE ISSNIP*, Sydney, Australia, Dec. 2008, pp. 261–266.

[44] A. S. Berson and H. V. Pipberger, "The low frequency response of electrocardiographs, a frequent source of recording errors," *Am Heart J*, vol. 71(6), pp. 779–789, July 1966.

[45] D. Tayler and R. Vincent, "Signal distortion in the electrocardiogram due to inadequate phase response," *IEEE Trans Biomed Eng*, vol. 30(6), pp. 352 – 356, June 1983.

[46] C. Assambo and M. J. Burke, *Low-frequency response and the skin-electrode interface in dry-electrode electrocardiography, in: Electrocardiograms.* InTech, 2011 (invited book chapter, to appear).

[47] C. Assambo and M. J. Burke, "Amplifier input impedance in dry electrode ecg recording," in *Conf Proc IEEE Eng Med Biol Soc*, Minneapolis, MN, USA, Sept. 2009, pp. 1774–1777.

[48] R. Dozio, A. Baba, C. Assambo, and M. J. Burke, "Time based measurement of the impedance of the skin-electrode interface for dry electrode ecg recording," in *Conf Proc IEEE Eng Med Biol Soc*, Lyon, France, Aug. 2007, pp. 5001–5004.

[49] C. Assambo and M. J. Burke, "Determination of the parameters of the skin electrode impedance model for ecg measurement," in *Proc WSEAS EHAC*, Feb. 2007, pp. 90–95.

[50] C. Assambo and M. J. Burke, "An improved very-low power pre-amplifier for use with un-gelled electrodes in ecg recording," *Int J Biol Biomed Eng*, vol. 1, pp. 25–31, 2007.

[51] M. J. Burke and C. Assambo, "An improved micro-power pre-amplifier for dry-electrode ecg recording," in *ELE COM ENG*, vol. 11, July 2007, pp. 234–239.

[52] C. Assambo, A. Baba, R. Dozio, and M. J. Burke, "Parameter estimation of the skin-electrode interface model for high-impedance bio-electrodes," *WSEAS T Biol Biomed*, vol. 3, pp. 573–580, Aug. 2006.

[53] D. G. Plonsey, *Bioelectric phenomena.* New York, USA: McGraw-Hill, 1969.

[54] Shane. (2006) The electrical pathway. [Online]. Available: http://www.ambulancetechnicianstudy.co.uk/card.html

[55] D. Noble, *The initiation of the heartbeat.* Oxford, UK: Oxford University Press, 1979.

[56] J. W. Clark, *The origin of biopotentials, in J. G. Webster (ed): Medical instrumentation, New York:*, 3rd ed. Wiley, 1998, pp. 129–151.

[57] D. Kilpatrick and P. Johnston, "Origin of the electrocardiogram," *IEEE Eng Med Biol Mag*, vol. 13, pp. 479–486, 1994.

[58] J. R. Hampton, *The ECG made easy.* Edinburgh, UK: Churchill Livingstone, 1986.

[59] D. B. Geselowitz, "On the theory of the electrocardiogram," *P IEEE*, vol. 77, pp. 857–876, 1989.

[60] M. R. Neuman, *Biopotential Amplifiers, in J.G. Webster (ed): Medical instrumentation :*, 3rd ed. Wiley, 1998, ch. 6, pp. 289–353.

[61] istockphoto.com. (2010, Dec.) Human body with heart for medical study. [Online]. Available: http://www.istockphoto.com

[62] W. Einthoven, "The string galvanometer and the human electrocardiogram," *Proc Royal Netherlands Academy of Arts and Sciences - PRNAS*, vol. 6, pp. 107–115, 1904.

[63] E. E. van der Wall *et al.*, "Major achievements in cardiology in the past century: influence on dutch cardiovascular medicine," *Neth Heart J*, vol. 17(4), pp. 136–139, 2009.

[64] B. F. Hoffman and P. F. Cranefield, *Electrophysiology of the Heart.* New York, USA: McGraw-Hill, 1960.

[65] W. Nesterenko and C. Antzelevitch, "Simulation of the electrocardiographic u wave in heterogeneous myocardium: Effect of local junctional resistance," in *Proc IEEE CinC*, Durham, NC, USA, Oct. 1992, pp. 43–46.

[66] B. Surawicz, "U wave: Facts, hypotheses, misconceptions, and misnomers," *J Cardiovasc Electr*, vol. 9, pp. 1117–1128, October 1998.

[67] J. Wu, J. Wu, and D. P. Zipes, "Early afterdepolarizations, u waves, and torsades de pointes," *Circulation*, vol. 105, pp. 675–676, Feb. 2002.

[68] J. Kors, H. van Eck, and G. van Herpen, "The u wave explained as an intrinsic part of repolarization," in *Proc IEEE CinC*, Lyon, France, Sept. 2005, pp. 101–104.

[69] *Medical electrical equipment Part 2-51: Particular requirements for safety, including essential performance, of recording and analysing single channel and multichannel electrocardiographs*, IEC Std. IEC60 601-2-51:2003, 2003.

[70] M. J. Burke, "A microcontroller based athletic cardiotachometer," Ph.D. dissertation, University of Dublin, Trinity College, 1990.

[71] J. R. Hampton, *The ECG in practice.* Edinburgh, UK: Churchill Livingstone, 1997.

[72] T. A. Buckingham *et al.*, "Effect of conduction defects on the signal-averaged electrocardiographic determination of late potentials," *Am J Cardiol*, vol. 61, pp. 1265–1271, June 1988.

[73] J. D. Symanski and L. S. Gettes, "Drug effects on the electrocardiogram: a review of their clinical importance," *Drugs*, vol. 46, pp. 219 – 248, August 1993.

[74] C. M. Martin and M. D. Furnas, "Identifying drug-induced changes in electrocardiogram results of elderly individuals," *Consult Pharm*, 1997.

[75] J. Malmivuo and R. Plonsey, *Bioelectromagnetism, Principles and Applications of Bioelectric and Biomagnetic Fields.* Oxford University Press, 1995.

[76] D. Brody, "A theoretical analysis of intracavitary blood mass influence on the heart-lead relationship," *Circ Res*, vol. 4, pp. 731–738, 1956.

[77] B. Appleton *et al.*, "An electrical heart model incorporating real geometry and motion," in *Conf Proc IEEE Eng Med Biol Soc*, vol. 1, Shanghai, China, Sept. 2005, pp. 345–348.

[78] J. K. Norian, "An electrical model of the heart," *Int J Elec Eng Educ*, vol. 45, pp. 26–33, 2008.

[79] M. S. Spach and J. M. Kootsey, "The nature of electrical propagation in cardiac muscle," *Am J Physiol-Heart C*, vol. 244, pp. H3–H22, 1983.

[80] H. P. Schwan and C. F. Kay, "Capacitive properties of body tissues," *Circ Res*, vol. 5, pp. 439 – 443, 1957.

[81] J. C. Huhta and J. G. Webster, "60-hz interference in electrocardiography," *IEEE T. Bio-Med. Eng.*, vol. BME-20, pp. 91–101, March 1973.

[82] *Effects of current on human beings and livestock - Part 1: General aspects*, IEC Std. 60 479-1:2005, 2005.

[83] A. Baba and M. J. Burke, "Electrical characterisation of dry electrodes for ecg recording," in *ELE COM ENG*, Crete, Greece, July 2008, pp. 591–596.

[84] A. Baba, "Electrial measurement and characterisation of the properties of ungelled electrodes for ecg recording," Master's thesis, University of Dublin, Trinity College, 2008.

[85] D. K. Swanson and J. G. Webster, *A model for skin electrode impedance, In: Biomedical Electrode Technology - Theory and Practice*, 1st ed. Academic Press, 1974, pp. 117–128.

[86] M. R. Neuman, *Biopotential Electrodes, in J.G. Webster (ed): Medical instrumentation*, 3rd ed. Wiley, 1998, ch. 5, pp. 182–232.

[87] K. A. Kaczmarek and J. G. Webster, "Voltage-current characteristics of the electrotactile skin-electrode interface," in *Conf Proc IEEE Eng Med Biol Soc*, vol. 5, Seattle, WA, USA, 1989, pp. 1526–1527.

[88] T. Zagar and D. Krizaj, "An instrumentation amplifier as a front-end for a four-electrode bioimpedance measurement," *Physiol Meas*, vol. 28, pp. N57–N65, 2007.

[89] Y.-L. Liu, D.-L. Lin, and Y.-D. Lin, "Spice model for computer-aided design of biopotential amplifier," *Biomed Eng-App Bas C*, vol. 16, pp. 43–48, June 2004.

[90] S. Heuer, D. R. Martinez, S. Fuhrhop, and J. Ottenbacher, "Motion artefact correction for capacitive ecg measurement," in *Proc IEEE BioCAS*, Beijing, China, Nov. 2009, pp. 113–116.

[91] T. Pawar and S. P. Duttagupta, "Body movement activity recognition for ambulatory cardiac monitoring," *IEEE T Bio-Med Eng*, vol. 54, pp. 874–882, May 2007.

[92] K. Kearney, C. Thomas, and E. McAdams, "Quantification of motion artifact in ecg electrode design," in *Conf Proc IEEE Eng Med Biol Soc*, Lyon, France, August 2007, pp. 1533–1536.

[93] K.-P. Hoffman and R. Ruff, "Flexible dry surface-electrodes for ecg long-term monitoring," in *Conf Proc IEEE Eng Med Biol Soc*, Lyon, France, Aug. 2007, pp. 5739–5742.

[94] M. L. Wolbarsht and H. Spekreijse, *Advances in Biomedical Engineering and Medical Physics*. Academic Press, 1968, vol. 2.

[95] Y. Z. Ider and H. Koymen, "A new technique for line interference monitoring and reduction in biopotential amplifiers," *IEEE T Bio-Med Eng*, vol. 37, pp. 624–631, June 1990.

[96] M. F. Chimeno and R. Pallás-Areny, "A comprehensive model for power line interference in biopotential measurements," *IEEE T Instrum Meas*, vol. 49, pp. 535–540, June 2000.

[97] Z. M. Nikolić, D. B. Popović, R. B. Stein, and Z. Kenwell, "Instrumentation for eng and emg recording in fes systems," *IEEE T Bio-Med Eng*, vol. 41, pp. 703–706, July 1994.

[98] *Medical electrical equipment Part 2-25: Particular requirements for the safety, including essential performance, of electrocardiographs*, IEC Working Draft Proposed Standard FprEN 60 601-2-25:2009, 2009.

[99] *Medical electrical equipment Part 2-27: Particular requirements for the safety, including essential performance, of electrocardiographic monitoring equipment*, IEC Working Draft Proposed Standard FprEN 60 601-2-27:2009, 2009.

[100] *Medical electrical equipment Part 2-47: Particular requirements for the safety, including essential performance, of ambulatory electrocardiographic systems*, IEC Working Draft Proposed Standard FprEN 60 601-2-47:2009, 2009.

[101] *Medical electrical equipment Part 2-27: Particular requirements for the safety, including essential performance, of electrocardiographic monitoring equipment*, IEC Std. IEC60 601-2-27:2005, 2005.

[102] *Medical electrical equipment Part 2-47: Particular requirements for the safety, including essential performance, of ambulatory electrocardiographic systems*, IEC Std. IEC60 601-2-47:2001, 2001.

[103] *Medical electrical equipement - Part 1: General requirements for basic safety and essential performance*, IEC Std. IEC60 601-1:2006, 2006.

[104] *Diagnostic electrocardiographic devices*, AAMI Std. ANSI/AAMI EC11:1991/(R)2001/(R)2007, 2007.

[105] *Medical electrical equipment - Part 2-47: Particular requirements for the safety, including essential performance, of ambulatory electrocardiographic systems*, AAMI Std. ANSI/AAMI EC38:2007, 2007.

[106] *Safe Current Limits for Electromedical Apparatus*, AAMI Std. ANSI/AAMI ES1-1993, 1993.

[107] P. M. Rautaharju, B. Surawicz, and L. S. Gettes, "Aha/accf/hrs recommendations for the standardization and interpretation of the electrocardiogram: Part iv: The st segment, t and u waves, and the qt interval: A scientific statement from the american heart association electrocardiography and arrhythmias committee, council on clinical cardiology; the american college of cardiology foundation; and the heart rhythm society: Endorsed by the international society for computerized electrocardiology," *Circulation*, vol. 119, pp. e241–e250, March 2009.

[108] P. Kligfield *et al.*, "Recommendations for the standardization and interpretation of the electrocardiogram: Part i: The electrocardiogram and its technology: A scientific statement from the american heart association electrocardiography and arrhythmias committee, council on clinical cardiology; the american college of cardiology foundation; and the heart rhythm society endorsed by the international society for computerized electrocardiology," *Circulation*, vol. 115, pp. 1306–1324, March 2007.

[109] M. H. Crawford *et al.*, "Acc/aha guidelines for ambulatory electrocardiography: Executive summary and recommendations : A report of the american college of cardiology/american heart association task force on practice guidelines (committee to revise the guidelines for ambulatory electrocardiography) developed in collaboration with the north american society for pacing and electrophysiology," *Circulation*, vol. 100, pp. 886–893, Aug. 1999.

[110] J. Bailey *et al.*, "Recommendations for standardization and specifications in automated electrocardiography: bandwidth and digital signal processing. a report for health professionals by an ad hoc writing group of the committee on electrocardiography and cardiac electrophysiology of the council on clinical cardiology, american heart association," *Circulation*, vol. 81, pp. 730–739, 1990.

[111] S. Knoebel *et al.*, "Guidelines for ambulatory electrocardiography. a report of the american college of cardiology/american heart association task force on assessment of diagnostic and therapeutic cardiovascular procedures," *Circulation*, vol. 79, pp. 206–215, Jan. 1989.

[112] L. T. Sheffield *et al.*, "Aha special reports: Recommendations for standards of instrumentation and practice in the use of ambulatory electrocardiography," *Circulation*, vol. 71, pp. 626A–636A, March 1985.

[113] H. V. Pipberger *et al.*, "Recommendations for standardization of instruments in electrocardiography and vectorcardiography," *IEEE T Bio-Med Eng*, vol. BME-14, pp. 60–68, Jan. 1967.

[114] C. E. Kossmann *et al.*, "Recommendations for standardization of leads and of specifications for instruments in electrocardiography and vectorcardiography," *Circulation*, vol. 35, pp. 583–602, March 1967.

[115] M. Laks *et al.*, "Recommendations for safe current limits for electrocardiographs," *Circulation*, vol. 93, pp. 837–839, 1996.

[116] T. Kugelstadt, "Getting the most out of your instrumentation amplifier design," *Analog Application Journal*, pp. 25–29, 2005. [Online]. Available: http://focus.ti.com/lit/an/slyt226/slyt226.pdf

[117] E. M. Spinelli, N. Martinez, M. A. Mayosky, and R. Pallás-Areny, "A novel fully differential biopotential amplifier with dc suppression," *IEEE T Bio-Med Eng*, vol. 51, pp. 1444–1448, Aug. 2004.

[118] S. Yacoub *et al.*, "Noise analysis of nasicon ceramic dry electrodes," in *Conf Proc IEEE Eng Med Biol Soc*, Montreal, Canada, 1995, pp. 1553–1554.

[119] M. R. Neuman, *Biopotential Amplifiers, in J.G. Webster (ed): Medical instrumentation*, 2nd ed. Wiley, 1995, ch. 6, pp. 288–353.

[120] E. Simonson, J. Brozek, and A. Keys, "Variability of the electrocardiogram in normal men," *Am Heart J*, vol. 38, pp. 407–422, 1949.

[121] E. Simonson, *Differentiation Between Normal and Abnormal in Electrocardiography.* CV Mosby Co, 1961.

[122] M. Bluejay. (2009) Battery guide. [Online]. Available: http://michaelbluejay.com/batteries/recommendations

[123] Microship. (2010) nanowatt xlp. [Online]. Available: http://www.microship.com

[124] I. Zepeda-Carapia, A. Marquez-espionaza, and C. Alvarado-Serrano, "Measurement of the skin-electrode impedance for a 12-lead electrocardiogram," in *Proc IEEE ICEEE*, 2005, pp. 193–195.

[125] S. Nishimura, Y. Tomita, and T. Horiuchi, "Clinical application of an active electrode using an operational amplifier," *IEEE T Bio-Med Eng*, vol. 39, pp. 1096–1099, Oct. 1992.

[126] A. C. M. van Rijn, A. P. Kuiper, T. E. Dankers, and C. A. Grimbergen, "Low-cost active electrode improves the resolution in biopotential recordings," in *Conf Proc IEEE Eng Med Biol Soc*, Amsterdam, The Netherlands, Oct. 1996, pp. 101–102.

[127] G. E. Bergey, R. D. Aquires, and W. C. Sipple, "Electrocardiogram recording with pasteless electrodes," *IEEE T Bio-Med Eng*, vol. BME-18, pp. 206–211, May 1971.

[128] R. J. Prance *et al.*, "Biological and medical applications of a new electric field sensor," in *Proc ESA Ann Meeting Electrostatics*, 2008, pp. N2 1–2.

[129] B. A. Taheri, R. T. Knight, and R. L. Smith, "A dry electrode for eeg recording," *Electroencephalogr Clin Neurophy*, vol. 90, pp. 376–383, 1994.

[130] M. E. Griffith, "Hybrid integrated electrocardiogram electrodes," Master's thesis, Texas Tech University, TX, USA, 1978.

[131] W. Portnoy, R. David, and L. Akers, *Insulated ECG electrodes, in H.A. Miller & D.C. Harrison (eds): Biomedical Electrode Technology:*, 1st ed. Academic Press, 1974, ch. 1, pp. 7–39.

[132] W. H. Ko, M. R. Neuman, R. N. Wolfson, and E. T. Yon, "Insulated active electrodes," *IEEE Transactions on Industrial Electronics and Control Instrumentation*, vol. IECI-17, pp. 195–198, 1970.

[133] R. P. Betts and B. H. Brown, "Method for recording electrocardiograms with dry electrodes applied to unprepared skin," *Med Biol Eng Comput*, vol. 14, pp. 313–315, May 1976.

[134] A. Wolfe and H. Reinhold, *A Flexible, quick application ECG electrode system, in H.A. Miller & D.C. Harrison (eds): Biomedical Electrode Technology:*, 1st ed. Academic Press, 1974, ch. 2, pp. 183–192.

[135] P. Lynch, H. Dargie, S. Krickler, and D. Krickler, "Objective assessment of anti-anginal treatment: A double blind comparison of propranolol, nifedipine, and their combination," *British Medical Journal*, pp. 184 – 187, July 1980.

[136] Y. G. Lim, K. K. Kim, and K. S. Park, "Ecg measurement on a chair without conductive contact," *IEEE Trans Biomed Eng*, vol. 53, pp. 956–959, May 2006.

[137] Y. G. Lim, K. K. Kim, and K. S. Park, "Ecg recording on a bed during sleep without direct skin-contact," *IEEE Trans Biomed Eng*, vol. 54, pp. 718–725, April 2007.

[138] Y. G. Lim *et al.*, "Monitoring physiological signals using nonintrusive sensors installed in daily life equipment," *Biomed Eng Lett*, vol. 1, pp. 11–20, Feb. 2011.

[139] H. J. Baek, J. S. Kim, K. K. Kim, and K. S. Park, "System for unconstrained ecg measurement on a toilet seat using capacitive coupled electrodes : The efficacy and practicality," in *Conf Proc IEEE Eng Med Biol Soc*, Vancouver, Canada, Aug. 2008, pp. 2326–2328.

[140] E. Spinelli and M. Haberman, "Insulating electrodes: a review on biopotential front ends for dielectric skinelectrode interfaces," *Physiol Meas*, vol. 31, pp. S183–S198, Sept. 2010.

[141] J. Rosell *et al.*, "Skin impedance from 1 hz to 1 mhz," *IEEE T Bio-Med Eng*, vol. 35, pp. 649–651, Aug. 1988.

[142] D. Prutchi and M. Norris, *Biopotential Amplifiers in: Design and Development of Medical Electronic Instrumentation.* Wiley-Interscience, 2005.

[143] R. Pallás-Areny and J. G. Webster, "Composite instrumentation amplifier for biopotentials," *Ann Biomed Eng*, vol. 18, pp. 251–262, 1990.

[144] J. J. Carr and J. M. Brown, *Bioelectric amplifiers*, 4th ed. Prentice Hall, 2001, ch. 7, pp. 126–196.

[145] R. L. Shoenfeld, "Common-mode rejection ratio - two definitions," *IEEE T Bio-Med Eng*, vol. BME-17, pp. 73 – 74, 1970.

[146] W. H. Ko and J. Hynecek, *Dry Electrodes and Electrode Amplifiers, in H.A. Miller & D.C. Harrison (eds): Biomedical Electrode Technology*, 1st ed. Academic Press, 1974, ch. 2, pp. 169–181.

[147] A. C. MeetingVanRijn, "Amplifiers for bioelectric events: a design with a minimal number of parts," *Med Biol Eng Comput*, vol. 32, pp. 305–310, May 1994.

[148] J. H. Nagel, *Biopotential Amplifiers, in J.D. Bronzino (ed): The Biomedical Engineering Handbook*, 2nd ed. CRC Press, 2000, ch. 70.

[149] Intersil, "Instrumentation amplifier application note," *Intersil Application Notes*, May 2009.

[150] D. Chevallier. (2010) L'ampli d'instrumentation. [Online]. Available: http://www.bedwani.ch/electro/ch27/

[151] O. Français. (2000) Amplificateur d'instrumentation. [Online]. Available: www.esiee.fr

[152] O. Casas and R. Pallás-Areny, "Basics of analog differential filters," *IEEE T Instrum Meas*, vol. 45, pp. 275–279, Feb. 1996.

[153] R. Pallás-Areny and J. G. Webster, *Analog signal processing.* John Wiley & Sons, 1999.

[154] R. Pallás-Areny and J. G. Webster, "Common mode rejection ratio for cascaded differential amplifier stages," *IEEE T Instrum Meas*, vol. 40, pp. 677–681, Aug. 1991.

[155] R. Pallás-Areny and J. G. Webster, "Common mode rejection ratio in differential amplifiers," *IEEE T Instrum Meas*, vol. 40, pp. 669–676, Aug. 1991.

[156] R. Pallás-Areny, "Interference-rejection characteristics of biopotential amplifiers: A comparative analysis," *IEEE T Bio-Med Eng*, vol. 35, pp. 953 – 959, Nov. 1988.

[157] J. Szynowski, "Cmrr analysis of instrumentation amplifiers," *Electron Lett*, vol. 19, pp. 547 – 549, July 1983.

[158] M. Smither, D. Pugh, and L. Woolard, "C.m.r.r. analysis of the 3-op-amp instrumentation amplifier," *Electron Lett*, vol. 13, p. 594, Sept. 1977.

[159] G. Clayton and S. Winder, *Real op-amp performance parameters*, 5th ed. Newnes, 2003, ch. 1, pp. 49–50.

[160] P. E. Allen and D. R. Holberg, *CMOS operational amplifiers*, 2nd ed. Oxford University Press, 2002, ch. 6, pp. 246–248.

[161] J. R. Kellogg, "Wideband instrumentation amplifier with high commom mode rejection," USA Patent 4,206,416, June, 1980.

[162] N. Jorgovanović, D. Bojanić, V. Ilić, and D. Stanišić, "An improved ac-amplifier for electrophysiology," *J Automatic Control, University of Belgrade*, vol. 19, pp. 7–12, 2009.

[163] A. Istanbullu, P. Oner, I. Kocaturk, and I. Ozcan, "Low cost ecg monitoring experiment set-up for nonclinical applications," in *Proc IEEE OPTIM*, Brasov, Romania, May 2008, pp. 229–234.

[164] I.-D. Hwang and J. G. Webster, "Direct interference canceling for two-electrode biopotential amplifier," *IEEE T. Bio-Med. Eng.*, vol. 55, pp. 2620–2627, Nov. 2008.

[165] T. Degen and H. Jäckel, "Enhancing interference rejection of preamplified electrodes by automated gain adaption," *IEEE T Bio-Med Eng*, vol. 51, pp. 2031–2039, Nov. 2004.

[166] E. M. Spinelli, R. Pallás-Areny, and M. A. Mayosky, "Ac-coupled front-end for biopotential measurements," *IEEE T Bio-Med Eng*, vol. 50, pp. 391–395, March 2003.

[167] G. Gargiulo *et al.*, "A mobile eeg system with dry electrodes," in *Conf Proc IEEE Biomedical Circuits & Systems - BioCAS*, Baltimore, MD, USA, Nov. 2008, pp. 273–276.

[168] A. N. Bermúdez, E. M. Spinelli, and C. H. Muravchik, "Bio-potential amplifier for potential gradient measurements," *JPCS*, vol. 90, Dec. 2007.

[169] E. M. Spinelli, N. H. Martinez, and M. A. Mayosky, "A single supply biopotential amplifier," *Med Eng Phys*, vol. 23, pp. 235–238, April 2001.

[170] E. M. Spinelli and M. A. Mayosky, "Ac coupled three op-amp biopotential amplifier with active dc suppression," *IEEE T Bio-Med Eng*, vol. 47, pp. 1616–1619, 2000.

[171] Q. Huang and M. Oberle, "A 0.5mw passive telemetry ic for biomedical applications," in *Proc Eur Solid-State*, Southampton, UK, Sept. 1997, pp. 172–175.

[172] P. Nickolls. (2002) Electrocardiogram. [Online]. Available: http://www.eelab.usyd.edu.au/ELEC3801/notes/ecg.pdf

[173] E. M. Spinelli, P. A. Garcia, and D. O. Guaraglia, "A dual-mode conditioning circuit for differential analog-to-digital converters," *IEEE T Instrum Meas*, vol. 59, pp. 195 – 199, 2010.

[174] O. Casas, E. M. Spinelli, and R. Pallás-Areny, "Fully differential ac-coupling networks: A comparative study," *IEEE T Instrum Meas*, vol. 58, pp. 94–98, 2009.

[175] E. Spinelli, M. Mayosky, and C. Christiansen, "Dual-mode design of fully differential circuits using fully balanced operational amplifiers," *IET Circ Device Syst*, vol. 2, pp. 243–248, April 2008.

[176] E. Spinelli and M. Mayosky, "Un amplificador operacional equilibrado," *IEEE Latin America T*, vol. 5, pp. 557–560, Dec. 2007.

[177] E. Spinelli, M. Mayosky, and R. J. Mantz, "Independent common-mode and differential-mode design of fully differential analog filters," *IEEE T Circuits-II*, vol. 53, pp. 572–576, July 2006.

[178] M. Mollazadeh and K. Murari, "Micropower cmos integrated low-noise amplification, filtering, and digitization of multimodal neuropotentials," *IEEE T Biomed Circuits Syst*, vol. 3, pp. 1–10, Feb. 2009.

[179] I. Technologies. (2010, Sept.) Rha1016: Fully integrated 16 channel biopotential amplifier array. [Online]. Available: http://www.intantech.com

[180] M. Gasulla, . Casas, and R. Pallas-Areny, "On the common mode response of fully differential circuits," in *IEEE IMTC P*, vol. 2, Baltimore, MD, USA, May 2000, pp. 1045–1049.

[181] R. Casas, O. Casas, and V. Ferrari, "Single-ended input to differential output circuits: a comparative analysis," in *IEEE IMTC P*, Sorrento, Italy, 2006, pp. 548–551.

[182] A. Devices. (2010, Dec.) Input buffer amplifier requirements. [Online]. Available: http://www.analog.com

[183] J. Hbribik, S. Lanyi, and M. Hruskovic, "A high-input-impedance buffer," in *Conf Proc IEEE Radioelektronika*, Prague, Czech Republic, April 2008, pp. 1–4.

[184] D. Dobrev, T. Neycheva, and N. Mudrov, "Bootstrapped two-electrode biosignal amplifier," *Med Biol Eng Comput*, vol. 46, pp. 613–619, Feb. 2008.

[185] S. Lányi and M. Pisani, "A high-input-impedance buffer," *IEEE T Circuits-I*, vol. 49, pp. 1209–1211, August 2002.

[186] H. Huang, S. Karthikeyan, and E. K. Lee, "A 1 v instrumentation amplifier," in *Midwest Symp Circuit*, Las Cruces, NM, USA, Aug. 1999, pp. 170–173.

[187] B. Whitlock, "A new balanced audio input circuit for maximum common-mode rejection in real-word environments," Jensen Transformers Inc., Van Nuys, CA, USA, Tech. Rep., 1996.

[188] R. Pallás-Areny, J. Colominas, and J. Rosell, "An improved buffer for bioelectric signals," *IEEE T Bio-Med Eng*, vol. 36, pp. 490–493, April 1989.

[189] B. Winter and J. G. Webster, "Reduction of interference due to common mode voltage in biopotential amplifiers," *IEEE T Bio-Med Eng*, vol. BME-30, pp. 58–62, Jan. 1983.

[190] G. Mpitsos and A. D. McClellan, "Extracellular amplifier with bootstrapped input stage results in high common-mode rejection," *Med Biol Eng Comput*, vol. 19, pp. 657–658, 1981.

[191] T. Degen and H. Jäckel, "A pseudodifferential amplifier for bioelectric events with dc-offset compensation using two-wired amplifying electrodes," *IEEE T Bio-Med Eng*, vol. 53, pp. 300–310, Feb. 2006.

[192] A. C. M. van Rijn, A. Peper, and C. A. Grimbergen, "The isolation mode rejection ratio in bioelectric amplifiers," *IEEE T Bio-Med Eng*, vol. 38, pp. 1154–1157, Nov. 1991.

[193] A. C. M. van Rijn, A. Peper, and C. A. Grimbergen, "High-quality recording of bioelectric events. part 1: Interference reduction, theory and practice," *Med Biol Eng Comput*, vol. 28, pp. 389–397, Sept. 1990.

[194] B. Winter and J. G. Webster, "Driven-right-leg circuit design," *IEEE T Bio-Med Eng*, vol. BME-30, pp. 62–66, Jan. 1983.

[195] D. Dobrev, T. Neycheva, and N. Mudrov, "Simple two-electrode biosignal amplifier," *Med Biol Eng Comput*, vol. 43, pp. 725–730, Nov. 2005.

[196] E. M. Spinelli and M. A. Mayosky, "Two-electrode biopotential measurements: power line interface analysis," *IEEE T Bio-Med Eng*, vol. 52, pp. 1436 – 1442, August 2005.

[197] D. Dobrev, "Two-electrode low supply voltage electrocardiogram signal amplifier," *Med Biol Eng Comput*, vol. 42, pp. 272–276, March 2004.

[198] D. Dobrev, "Two-electrode non-differential biopotential amplifier," *Med Biol Eng Comput*, vol. 40, pp. 546–549, Sept. 2002.

[199] M. I. Products, "Application note 656: Design trade-offs for single-supply op amps," MAXIM, Tech. Rep., April 2000.

[200] B. Baker, "Using single supply operational amplifiers in embedded systems," Microchip Technology Inc., Tech. Rep., 2000.

[201] B. Carter, "A single-supply op-amp circuit collection," Texas Instruments Incorporated, Tech. Rep., Nov. 2000.

[202] B. Clarke, "Maximizing battery life in communications systems," *Analogue Dialogues*, vol. 29, pp. 7–8, 1995.

[203] J. Firth and P. Errico, "Low-power, low-voltage ic choices for ecg system requirements," *Analog Dialogues*, vol. 29, pp. 9–10, 1995.

[204] S. Guinta, "Considerations in designing low-power, single-supply systems part i : Designs using ac line power," *Analog Dialogue*, vol. 29, pp. 2–6, 1995. [Online]. Available: http://www.analog.com/library/analogdialogue/cd/vol29n3.pdf

[205] S. Guinta, "Considerations in designing single supply, low-power systems part ii: Battery powered systems," *Analog Dialogue*, vol. 30, pp. 9–11, 1996.

[206] A. M. van Rijn, A. Peper, and C. Grimbergen, "High-quality recording of bioelectric events - part 1: interferenec reduction, theory and practice," *Med Biol Eng Comput*, vol. 28, pp. 389–397, Sept. 1990.

[207] D. R. White, "Phase compensation of the three op amp instrumentation amplifier," *IEEE T Instrum Meas*, vol. IM-36, pp. 842 – 844, Sept. 1987.

[208] J. Cain, "Comparison of multilayer ceramic and tantalum capacitors," AVX Corporation, Tech. Rep., 2007. [Online]. Available: http://www.avx.com/docs/techinfo/mlctant.pdf

[209] K. H. Lundberg, "Internal and external op-amp compensation: a control-centric tutorial," in *P Amer Contr Conf*, vol. 6, Boston, MA, USA, 2004, pp. 5197–5211.

[210] A. A. Khan and A. Kumar, "A novel instrumentation amplifier with reduced magnitude and phase errors," *IEEE T Instrum Meas*, vol. 40, pp. 1035–1038, Dec. 1991.

[211] M. B. Amer, "Novel design of a bioelectric amplifier with minimized magnitude and phase errors," *J Electronics (China)*, vol. 18, July 2001.

[212] J. Ardizzoni, "A practical guide to high-speed printed-circuit-board layout," *Analog Dialogue*, vol. 39, Sept. 2005. [Online]. Available: http://www.analog.com/library/analogdialogue/archives/39-09/layout.pdf

[213] J. Karki, "Effect of parasitic capacitance in op amp circuits," *Texas Instrument Application Report*, vol. Application report SLOA013A, Sept. 2000. [Online]. Available: http://focus.ti.com/lit/an/sloa013a/sloa013a.pdf

[214] M. B. Amer, "Analysis of internally generated noise of bioelectric amplifiers," *J Electronics (China)*, vol. 20, pp. 20–28, Jan. 2003.

[215] PhysioNet. (2010, Dec.) Record challenge/2010/set-b/b84 (ii), from 0:00.000 to 0:10.000. [Online]. Available: http://www.physionet.org/cgi-bin/ATM

[216] M. Inc. (2010, Dec.) Parametric search: Precision adcs. [Online]. Available: http://www.maxim-ic.com/

[217] J. Martinez-Quijada and S. Chowdhury, "Body-motion driven mems generator for implantable biomedical devices," in *Proc IEEE CCECE*, April 2007, pp. 164–167.

[218] E. Romero, R. O. Warrington, and M. R. Neuman, "Body motion for powering biomedical devices," in *Conf Proc IEEE Eng Med Biol Soc*, Minneapolis, MN, USA, 2009, pp. 2752–2755.

[219] E. Romero, R. O. Warrington, and M. R. Neuman, "Powering biomedical devices with body motion," in *Conf Proc IEEE Eng Med Biol Soc*, Buenos Aires, Argentina, Aug. 2010, pp. 3747–3750.

[220] Y.-S. O. Yang *et al.*, "Adaptive reduction of motion artefact in wireless physiological monitoring microsystems," in *Proc IEEE ICST*, Dec. 2008, pp. 523–526.

[221] D. A. Tong, K. A. Bartels, and K. S. Honeyager, "Adaptive reduction of motion artifact in the electrocardiogram," in *Conf Proc IEEE Eng Med Biol Soc*, Houston, TX, USA, Oct. 2002, pp. 1403–1404.